Water Droplet Impact on Functional Surfaces

BROWN, PHILIP,SIMON

Water Droplet Impact on Functional Surfaces

Philip Simon Brown

PhD Thesis

Department of Chemistry

Durham University

2013

DECLARATION

The work described in this thesis was carried out in the Department of Chemistry at Durham University between October 2010 and September 2013. It is the original work of the author except where otherwise acknowledged, and has not been previously submitted for a degree in this or any other university.

Dr. Arganthaël Berson (Department of Engineering, Durham University) helped to develop the MATLAB code used in Chapters 3–7 and derived equations used in Chapter 3. Emma Talbot (Department of Chemistry, Durham University) constructed the droplet rig used in Chapters 3–7. Doug Carswell (Department of Chemistry, Durham University) carried out DSC measurements for Chapter 8. Olivia Atkinson (Department of Chemistry, Durham University) carried out the initial work that inspired Chapter 8.

STATEMENT OF COPYRIGHT

ACKNOWLEDGMENTS

Many thanks to the following: Professor Jas Pal Badyal for three years of excellent supervision; Professor Colin Bain for his insight and suggestions; members of Lab 98 — Tom, Hayley, Suzanne, Matt, James, Mike, and Olivia — for their ideas and support; members of I^4T — in particular Arganthaël, Lisong, and Emma; the glassblowers, Malcolm and Aaron, for fixing the things I broke and making many new items throughout my studies; Neil, Kelvin, Barry, and Omer in the workshops; Doug for DSC measurements; Jun Jie Wu for use of the microindenter; and Tracey Davey at Newcastle University for training me on the SEM.

LIST OF PUBLICATIONS

Arising from Thesis

Work in this thesis has been published as follows:

1. “Impact of Picoliter Droplets on Superhydrophobic Surfaces with Ultralow Spreading Ratios” P. S. Brown, A. Berson, E. L. Talbot, T. J. Wood, W. C. E. Schofield, C. D. Bain and J. P. S. Badyal *Langmuir* **2011**, *27*, 13897.
2. “Superhydrophobic Hierarchical Honeycomb Surfaces” P. S. Brown, E. L. Talbot, T. J. Wood, C. D. Bain and J. P. S. Badyal *Langmuir* **2012**, *28*, 13712.

Collaborative Publications

1. “Nanoplasma surface electrification” S. Morsch, P. S. Brown and J. P. S. Badyal *J. Mater. Chem.* **2012**, *22*, 3922.
2. “Evaporation of picoliter droplets on surfaces with a range of wettabilities and thermal conductivities” E. L. Talbot, A. Berson, P. S. Brown and C. D. Bain *Phys. Rev. E* **2012**, *85*, 061604.
3. “Oxidative Atomized Spray Deposition of Electrically Conductive Poly(3,4-Ethylenedioxythiophene)” T. J. Wood, P. S. Brown and J. P. S. Badyal *Chem. Commun.* **2013**, *49,* 7741.

ABSTRACT

The impact and spreading of picolitre-sized water droplets on a substrate is of importance in many applications such as rapid cooling, delayed freezing, crop spraying, and inkjet printing. In this thesis, the effects of substrate chemistry, roughness, hardness, charge, and porosity on such droplet impact are studied.

The effect of roughness was investigated through the use of superhydrophobic CF_4 plasma fluorinated polybutadiene. Comparison of the maximum spreading ratio and droplet oscillation frequencies with literature models shows that both are found to be lower than theoretically predicted. Further study of the effect of multiple types of surface topography was carried out via the CF_4 plasma texturing of honeycomb surfaces, leading to hierarchical surfaces with roughness on two length scales. This led to the discovery that surfaces with similar static contact angles can give rise to different droplet impact dynamics, governed by the underlying surface topography.

The effect of the mechanical properties of the substrate upon picolitre droplets can be important in microfluidics. The oscillatory dynamics of picolitre droplets following impact were found to depend upon the thickness and elasticity of the substrate. Higher oscillation frequencies are measured for softer and thicker films, which are correlated to larger surface deformations around the contact line.

Static buildup during inkjet printing is known to affect print quality. The role of surface charge on picolitre droplet impact onto polymer substrates is found to give rise to increased droplet impact velocities. Higher surface potentials can result in unexpected behaviour such as droplet bouncing or increased contact area diameters leading to a decrease in print resolution.

Printing on porous materials is important as porosity can aid ink adhesion and durability. CF_4 plasma fluorination of porous membranes can inhibit droplet spreading laterally over a surface, with little change in the imbibition behaviour in the material, leading to printing that is more highly defined. These hydrophobic membranes remain oleophilic and could also find use in oil–water separation. Similarly, a hydrophilic–oleophobic switching surface can be beneficial in a range of applications such as anti-fogging, self-cleaning, and oil–water separation. Polelectroyle–fluorosurfactant complexes were found to exhibit excellent switching, resulting in a surface that quickly becomes hydrophilic whilst remaining oleophobic.

TABLE OF CONTENTS

LIST OF SCHEMES

LIST OF FIGURES

LIST OF TABLES

Chapter 1 Surfaces for Inkjet Printing

1.1 Introduction

Inkjet printing is the creation of a pattern or image through the deposition of small amounts of liquid on a substrate surface. Its major application is in the transferring of data to paper and is used in this respect in households and offices across the world. However, in recent years much work has been carried out to assess the feasibility of inkjet printing technology in manufacturing processes.[1,2,3,4]

There are two different printing processes that are widely used in the industry. In continuous inkjet (CIJ) printing, a liquid jet is formed and subsequently broken up through perturbation, leading to uniform droplets, which are deflected in an electric field to fall to a specific position on the paper. Undeflected, uncharged droplets are captured and recycled.[5] CIJ printing is favoured for its high speed and is utilised in textile labelling. The second technique is known as drop on demand (DOD). In DOD, ink droplets are formed as needed and ejected from nozzles on a moving print head.[5] DOD is favoured for its accuracy and smaller droplet size.

There are numerous reasons why inkjet printing may be considered a more suitable method of pattern fabrication than other techniques. Inkjet printing is a contactless technique, which can be modified to dispense a wide variety of materials onto a range of substrates. This versatility is the main reason why inkjet printing has been studied for use in many different applications. Such applications include microelectronics,[1,2,3,4] pharmaceutical dosing or screening,[6,7,8] tissue engineering,[9,10] and optics.[11,12] Another advantage is the additive aspect of inkjet printing, droplets can easily be overprinted onto dried dots which were printed earlier, this can result in the creation of patterned three-dimensional structures.[9,13]

However, there are several problems that limit the use of inkjet technology. It is simply not a case of dissolving or suspending material in a liquid and depositing it on the surface, numerous interactions must first be taken into account. Previous work has investigated the behaviour of inks during storage in the print head, jetting, and after impact, spreading, and eventual

drying on the substrate surface. All these considerations lead to ink that is a complex mixture of biocides, polymeric additives, humectants, low-volatility water miscible liquids, and more.[13]

There are numerous review articles of inks and their interactions.[5,13,14,15] In this introductory chapter, the focus will instead be placed on the substrate. The ink has to land somewhere, and the substrate properties can greatly affect the final outcome of the printing process.

1.2 Contact Angle Theory

When a droplet lands on a substrate, in addition to the liquid parameters (surface tension, viscosity, etc.), the amount to which it spreads is determined by the chemistry and roughness of the surface. These two characteristics determine the most favourable shape a droplet of a particular liquid will adopt.

When a surface is created, the disruption of the intermolecular bonds causes the interface to exhibit an intrinsic energy. It is less favourable for a substrate molecule to be at the surface than to be in the bulk hence there is a difference in energies. Liquids can interact favourably or unfavourably with a solid surface; the wetting of a solid surface by a liquid depends upon their respective surface free energies. Liquids commonly adopt shapes that minimise their surface area as this ensures the most number of interactions with neighbouring molecules. The shape of a droplet on a surface is dictated by the balance of surface tensions at the contact line, giving rise to a contact angle between the drop and the substrate

$$\cos\theta = \frac{\gamma_{sv} - \gamma_{ls}}{\gamma_{lv}}, \qquad (1.1)$$

where γ_{sv}, γ_{sl}, and γ_{lv} are the solid–vapour, solid–liquid, and liquid–vapour surface tensions respectively, and θ is the contact angle of the droplet, Figure 1.1.

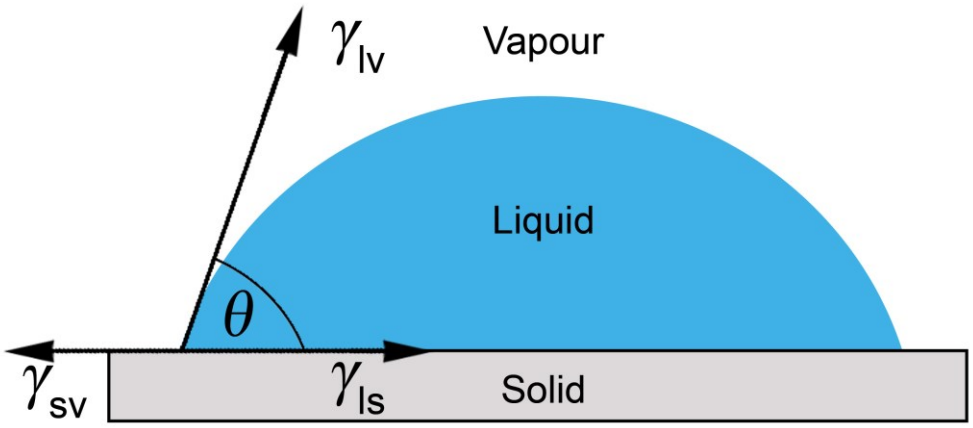

Figure 1.1: Balance of surface tensions resulting in a contact angle, θ.

Favourable liquid–solid interactions cause the liquid to spread to minimise the surface energy, this results in a low contact angle. If water spreads on or wets a surface, the surface is termed hydrophilic. Hydrophilic surfaces tend to have water contact angles from ≈ 0° (completely wets) up to 90°. Hydrophilic surfaces typically contain polar groups capable of hydrogen bonding.[16] Water contact angles above 90° and the surface is considered hydrophobic (unfavourable liquid–solid interactions).

Equation 1.1 is known as the Young's equation.[17] This equation assumes a perfectly flat surface, which in many situations results in a disparity between the actual contact angle and that predicted by Equation 1.1. This is due to the roughness of the surface. As shown in Figure 1.2, on a rough surface, the liquid can either penetrate into the fine structure at the surface, or the droplet can be suspended on the 'spikes' creating air pockets underneath. These are the Wenzel[18] and Cassie-Baxter[19] states respectively. In the Wenzel state

$$\cos\theta^* = r\frac{\gamma_{sv} - \gamma_{sl}}{\gamma_{lv}}, \tag{1.2}$$

where θ* is the apparent contact angle and r is the roughness ratio

$$r = \frac{surface\ area}{projected\ \ surface\ area}. \tag{1.3}$$

In the Cassie-Baxter state

$$\cos\theta^* = r_f f\cos\theta + f - 1, \tag{1.4}$$

where r_f is the roughness ratio of the wet surface area and f is the fraction of solid surface area wet by the liquid. If $r_f = r$ and $f = 1$ then the Cassie-Baxter equation becomes the Wenzel equation.

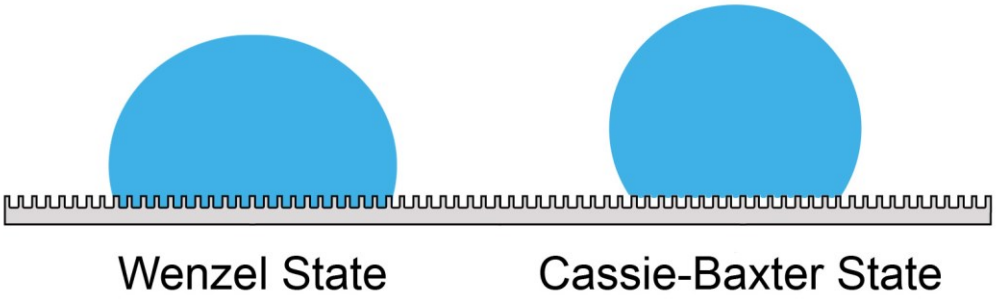

Figure 1.2: Two possible behaviours of a liquid droplet on a rough surface.

Whilst the two theories provide predictions for the contact angle on rough surfaces, there has been much debate as to whether they are relevant, some arguing that the nature of the surface at the contact line is more important than that of the entire surface under the drop.[20,21,22,23,24]

A rough surface can also exhibit contact angle hysteresis. This is where the contact angles of a mobile drop are different for the leading edge and the trailing edge. This hysteresis occurs because a droplet on a surface is occupying a certain metastable state. If a droplet is resting on a rough surface and the surface is tilted, an energy barrier must be overcome for the droplet to start moving. As the leading edge of a droplet moves downhill, it does so with a certain contact angle, this is the advancing contact angle (since the leading edge is advancing on the surface). When the trailing edge begins to move, it will do so with a receding contact angle. Advancing and receding may have different activation energies, resulting in a difference between their respective contact angles;[25,26] this is the contact angle hysteresis, Figure 1.3. Droplets adopting a Cassie-Baxter state on a very rough surface tend to have a low hysteresis as the energy barrier between metastable states is low. This is because the contact line is distorted by the tops of asperities and so further distortion as the droplet moves can occur easily. Droplets adopting a Wenzel state tend to have a high hysteresis as the energy barriers for movement are

high, the contact line needs to engulf the asperities whilst advancing or dewet them whilst receding.

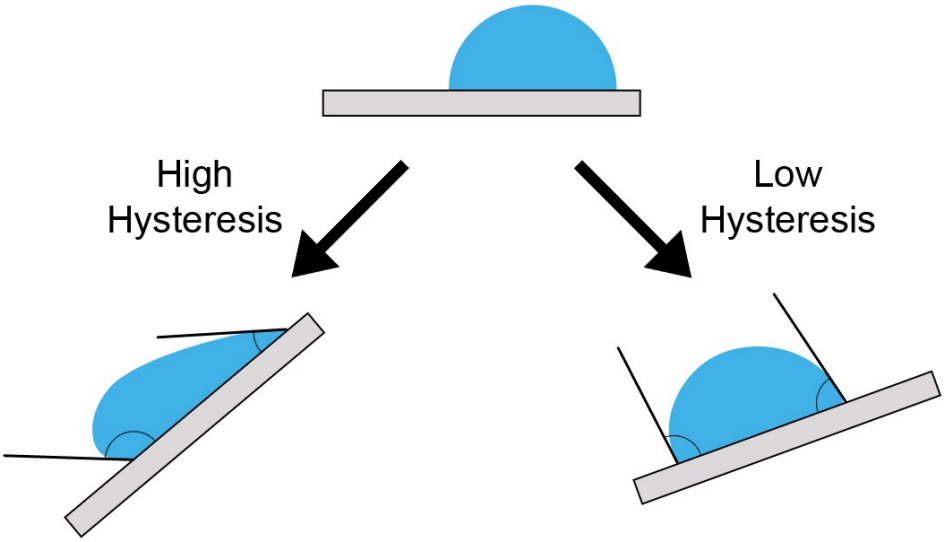

Figure 1.3: The difference between high and low contact angle hysteresis becomes noticeable when the substrate is titled and the droplet begins to move.

Roughening of a hydrophobic substrate usually results in a surface that is more hydrophobic.[18] For instance, polypropylene samples can be made with water contact angles ranging from 104° to 160° simply by changing the fabrication method.[27] It was found that by changing the solvent and lowering the drying temperature, a rougher film could be produced which resulted in a larger contact angle.[27] Mechanically flattened alkylketene dimer displays a contact angle of 107°,[28] however a fractal surface of the same material has a contact angle of 174°. Spin coated polystyrene exhibits a contact angle of 90° whereas electrohydrodynamic films displayed angles as large as 160°.[29] Electrochemical deposition of poly(alkylpyrrole) leads to needle like structures and a water contact angle of 150°.[30] However, none of these studies detail contact angle hysteresis data, which some argue provides a better indication of true superhydrophobicity.[31]

With regards to inkjet printing, both high and low surface energies can be beneficial. With high surface energies, the droplet contact line is pinned and there is no receding during the drying stage. However, droplets on hydrophilic surfaces may not reach their equilibrium diameter immediately. Conversely, deposition on low surface energy surfaces results in droplets that reach their equilibrium diameter quickly. Because the surface is hydrophobic, this diameter

is usually smaller than on hydrophilic surfaces, which means printing can be more highly defined. However, the hydrophobic nature of these surfaces may introduce unfavourable drop behaviour during impact and the larger contact angle can result in a longer droplet drying time.[32,33]

Droplet behaviour is also dependent on the constituent liquid, the size of the droplet formed, and its velocity. These properties form the basis of a group of dimensionless numbers commonly used to describe a particular droplet. [34,35] The Weber (We) number

$$We = \frac{\rho D_0 U_0^2}{\sigma}, \tag{1.5}$$

the Ohnesorge (Oh) number

$$Oh = \frac{\mu}{\sqrt{D_0 \sigma \rho}}, \tag{1.6}$$

and the Reynolds (Re) number

$$Re = \frac{\rho D_0 U_0}{\mu} = \frac{\sqrt{We}}{Oh}. \tag{1.7}$$

D_0 and U_0 are the diameter and velocity before impact respectively, both of which can be varied experimentally. Whilst ρ, σ, and μ are properties of the fluid, its density, surface tension, and viscosity respectively. Weber numbers are useful for categorising liquids into groups that would experience similar impact regimes.[35]

1.3 Hydrophilic Surfaces

Making surfaces more hydrophilic will increase the spreading of water-based droplets and increase the diameter of the drop on the surface. This is favourable in pigment-based inks when printing on materials not normally suitable for deposition, such as textiles.[36] Hydrophilic surfaces also help to pin the contact line of a drying droplet. This is where the droplet spreads to an equilibrium diameter, which then remains constant as the height and contact angle of the droplet decrease during drying.

There are numerous surface treatment techniques to improve the wettability of a surface, such as O_2 plasma.[37] O_2 plasma treatment increases the surface energy of a substrate by installing oxygen functionalities at the surface. Printing on these substrates resulted in an average dot size that was three

times that of the nozzle diameter. Furthermore, it was reported that overprinting (printing of further drops on dried dots) on these substrates did not cause the diameter of the dried dot to increase significantly, thanks to contact line pinning.[37] Similar results can be achieved through the use of UV/ozone[38] or an air plasma.[36] In the latter study, polyester fabrics were treated with an atmospheric pressure air/Ar plasma. Water droplets completely wet the treated substrate surface after 2 seconds, whereas droplets on the untreated substrate still had a finite contact angle after 90 seconds.[36] This improved wettability was found to improve the anti-bleed performance of the substrates; however the rougher surfaces resulted in a lower luminance due to a smaller amount of light being reflected. Similar results have been reported on silk fabrics using O_2 plasma.[39]

A further way to achieve better wetting is through thermal oxidation. Untreated silicon wafer has a water contact angle of around 70°. After treatment in a furnace containing dry O_2 this can be reduced to 30°.[40] Droplets on these surfaces were found to spread to up to 2.5 times the droplet diameter prior to impact (known as the spreading ratio), though this was also dependent on the velocity of the droplet.

Whilst the use of hydrophilic surface treatments for inkjet printing is prevalent in the textile industry, their applications are somewhat limited in other areas. Although contact line pinning can be advantageous in certain scenarios, especially additive printing, the large spread of droplets means that the use of hydrophilic surfaces is not feasible in applications where print resolution is important.

1.4 Hydrophobic Surfaces

A surface is said to be hydrophobic when the contact angle of a water drop is greater than 90°. Hydrophobic surfaces are of interest to the inkjet printing field because they will inhibit droplet spreading, allowing for a smaller printed dot size, and a higher resolution. Hydrophobic surfaces are also beneficial because the contact line of a deposited liquid is not usually pinned, unlike on hydrophilic surfaces. This lack of pinning results in a more even deposit for particulate-based inks, overcoming problems such as the coffee ring effect.[14]

Recently, work has been carried out to determine how plasma treatment can create hydrophobic surfaces for control of inkjet printed droplet size.[41] In this study, polyimide (PI) surfaces were exposed to C_4F_8 plasma treatment using varying RF power and gas pressures. Unsurprisingly, the smallest droplet spreading diameters are found on the substrates that contain the greatest F content.[41] However, some of the experiments utilised an extremely high RF power. It would not be unreasonable to assume that ablation is also occurring alongside fluorination in these high-energy plasmas, resulting in varying nanoscale morphology. However, no study into the morphology was carried out. Similar results can be achieved using CF_4 plasma treatment.[38]

In a second study by the same group it was found that whilst C_4F_8 treated substrates offered smaller dot diameters, overprinting resulted in significant increases in the dot size.[37] This was attributed to the de-pinning of the contact line and is contrary to high-energy substrates, where overprinting does not cause an increase in the dot diameter.[37]

Hydrophobic surfaces are usually created through the adsorption of a self-assembled monolayer (SAM).[42,43,44,45,46] 1-Octadecanethiol can be used to form a SAM on gold coated silicon wafers, the resulting surface was found to have a contact angle of 110°.[47] Drop impact on these substrates resulted in a spreading ratio (D/D_0) of around 1; the droplets also reached their equilibrium diameter up to 4 times quicker than those dropped on more hydrophilic substrates.[47]

The coffee ring effect is where a higher amount of solute is deposited at the contact line as the droplet dries and is caused by contact line pinning.[14] It was found that by utilising a perfluorinated substrate and a mixture of good solvents, this phenomenon can be eliminated.[14] In this case, a perfluorinated silane was deposited on glass. Dried polymer dots on the hydrophobic surface were not only more uniform than those on untreated glass, but were also much smaller than the nozzle diameter; leading the authors to postulate that lower energy surfaces could provide a route to the printing of sub-micrometre features.[14] A separate report also utilised a hydrophobic silane deposited on aluminium foil.[46] This resulted in water/ethylene glycol contact angles of 75° and droplets which were used for the templating of microsieves.[46]

In addition to adsorption onto flat substrates, SAMs have also been employed in conjunction with rough surfaces to achieve superhydrophobicity.[48] The term superhydrophobic (or ultraphobic) is commonly used to describe surfaces which display a water contact angle of 150° or more.[49] One such example involved the creation of patterned silicon surfaces using photolithography. Surfaces containing silicon 'posts' of varying shapes and sizes were fabricated and coated with hydrophobic silanes.[31] This method resulted in contact angles as high as 174°; however significant hysteresis, up to 40° in some cases, was reported. This was attributed to the regular array of 'posts' resulting in a straight contact line over large length scales.[31] This would seem to be supported by work done on randomly rough surfaces, which exhibits a much lower hysteresis.[50] Alteration of the post height or surface chemistry seemed to have little effect on the contact angle, though changing the post shape to a star or indented square contorted the contact line, resulting in a decreased hysteresis.[31]

There are various examples in the literature of designing patterned rough surfaces with an aim of superhydrophobicity.[51,52,53] One novel surface comprised an array of undercut pillars of silicon or "micro-hoodoos".[54] Treated with a hydrophobic silane, these surfaces displayed a contact angle above 150°. Patterned silicon substrates treated with a hydrophobic silane is a common method for creation of superhydrophobic surface.[55,56,57,58] Silanes have also been used to coat films of aligned carbon nanotubes, the combination of nanostructures and a hydrophobic layer resulting in a contact angle of 174°.[59,60]

Another study involved the deposition of two silanes on micron-sized patterned surfaces.[61] One silane was deposited in the vapour phase, resulting in a smooth coating. The other was deposited in solution resulting in nanoscale roughness on top of the microscale features. It was found that surfaces with only one length scale of roughness exhibited a high contact angle hysteresis of 20°, which was attributed to pinning at the tops of the features.[61] Surfaces with both micro and nanoscale roughness appeared to exhibit no hysteresis with advancing and receding angles both being measured at 176°. It was theorised that the lack of hysteresis was down to the nanoscale roughness lowering the transition energy between metastable droplet states, suggesting that two length scales can lead to true superhydrophobicity.[61]

Whilst the use of SAMs, on their own or combined with a separate roughening step, is common, there are several drawbacks which limit the more widespread use of these surfaces. Many silanes used to make a surface more hydrophobic are sensitive to moisture, forming insoluble polymers in solution.[62,63,64] In the case of thiol systems, these display long term instability toward oxidation,[65] and only assemble on specific surfaces such as gold,[66] platinum,[67] or palladium.[68]

Taking into account these drawbacks, there has been a push to utilise other methods to create hydrophobic and superhydrophobic surfaces. One such example involves the fluorination of polybutadiene films via plasma treatment.[69] Through this technique, surfaces could be fabricated with water contact angles over 170°, with low hysteresis. It was found that by varying the treatment time or plasma discharge power, the root-mean-squared roughness could be altered, which altered the surface energy of the substrate.[69] However, there was no study into how the hysteresis varied with roughness.

A similar study involved the plasma deposition of a fluorocarbon onto paper sheets giving a contact angle of over 150°.[70] If this was preceded by an etching step, the resulting contact angle hysteresis was found to be low. If the plasma deposition was carried out without the etching step, the hysteresis was much higher. The authors concluded that the rougher surfaces allowed for the droplet to occupy metastable states, which were separated by a low energy barrier; the effect of which was a low contact angle hysteresis and “roll off” of the droplet.[70]

Other studies have attempted to couple a fluoropolymer with roughness. Zinc nanopowder mixed with a fluoropolymer has been shown to exhibit contact angles of 150°.[71] It was found that altering the fabrication method could modify the contact angle hysteresis. By spray coating the suspension, a low root-mean-square roughness was achieved, resulting in a high hysteresis. However if the suspension was spin coated a much rougher surface was created and the contact angle hysteresis was significantly lower. AFM analysis confirmed that the spin coated samples contained more peaks than valleys, and the sample was approaching a perfectly random roughness, both of these factors favour a Cassie-Baxter state of wetting and a low hysteresis.

Another study found that rough surfaces with needle like structures displayed a lower hysteresis than those with smaller features.[72] This was attributed to the larger features being able to trap air more effectively, resulting in a composite solid-air interface as in the Cassie-Baxter state of wetting. Surfaces with lower features were unable to trap air and droplets adopted the Wenzel state, resulting in a much higher hysteresis.[72]

1.5 Drop Impact

Droplet impact upon solid surfaces is a prevalent phenomenon in our environment and naturally has been studied for over a century.[73] Whilst the equilibrium contact angle is vital for inkjet printing, how a droplet behaves upon impact is also important; there are several drop impact behaviours that would be detrimental to printing. Such behaviours include bouncing, splashing, and roll-off.

Typically, the impact of a droplet onto a solid surface can be divided into four regimes. The first involves the initial impact and is largely dependent upon the compressibility of the drop. During the second phase, the droplet spreads to a maximum diameter on the surface, which is determined by a balance between the inertia of the drop (governed by its diameter, velocity, viscosity, and density) and surface tension forces. The third phase entails the dissipation of the droplet inertia, as seen by oscillations in the height, width, and contact area diameter of the drop on the surface. This phase is highly dependent upon the fluid and substrate surface energies, which determine the static and dynamic contact angles. The final stage encompasses the relaxation of the drop towards its equilibrium diameter.

The magnitude of the effect of surface chemistry on the equilibrium position of a droplet after impact is disputed. Some studies have concluded that changing the surface energy of a substrate does not change the equilibrium diameter of a drop,[74] arguing that fluid viscosity and impact velocity are more important parameters, especially for millimetre sized droplets. Whilst the liquid properties are crucial in drop impact, there are numerous studies that suggest that surface energy can affect not only the equilibrium diameter, but other aspects of the impact regime too.[40,75,76,77]

One way to control the surface energy involves the adsorption of two different alkanethiols, one with hydrophilic tail groups, and the other, hydrophobic. By changing the ratio of the two organic molecules, the surface energy of the resulting monolayer can be altered.[78] This group were able to create four different water contact angles, from 55° up to 113°. This change in contact angle resulted in a dramatic difference in the spreading regime of the droplets. After impact, the droplets spread to an initial diameter, largely determined by the fluid properties. Therefore during the first few moments of impact, the spreading scenarios are similar for different surface energies.[78] After this, the surfaces behave differently. In the case of the hydrophilic surfaces, the contact line is pinned and so there is little or no retraction or change in the droplet shape and height. In the case of the hydrophobic surface, the contact line recedes and the height and shape of the droplet change dramatically as the droplet tries to avoid interacting with the surface. After the kinetic energy from impact has been fully dissipated, the droplet spreads to its equilibrium diameter. In the case of the hydrophobic surface, this does not take long as the diameter would have already started to move to this value because of the mobile contact line. In the hydrophilic case, the droplet continues to spread over the surface. It was found that on the hydrophilic surface, the droplet took over twice as long to reach its equilibrium diameter.[78]

A similar technique involved the partial oxidation of a hydrophobic SAM to control the surface energy of the substrate.[79,80] OTS was adsorbed onto a glass slide and then exposed to UV-ozone plasma treatment. This technique resulted in a range of contact angles from 110° (no UV treatment) to 10° (300 seconds UV).[75,79] This work revealed that not only did the hydrophobic substrate cause the droplet to recede after impact, but the drop shape and deformation history of the droplet were different when compared to those dropped on the hydrophilic surface. Exposure of silica nanoparticles to UV radiation can also result in a range of wettabilities.[81] Contact angles from 10° to 165° were reported, with low contact angle hysteresis for the latter, though no drop impact study was carried out.[81]

Droplet impact onto rough superhydrophobic surfaces usually results in bouncing of the drop.[82,83] The situation is further complicated in that the inertia may be sufficient to impale the droplet on the surface features, forcing a Wenzel

configuration.[84] Indeed, if the velocity is high enough, droplets have been known to bounce off a superhydrophobic substrate before landing back on the surface and forming a homogenous solid-liquid interface (i.e. Wenzel state).[85] If the substrate is sufficiently rough, droplets can also fragment (or splash) upon high-speed impact,[86,87,88,89] Figure 1.4.

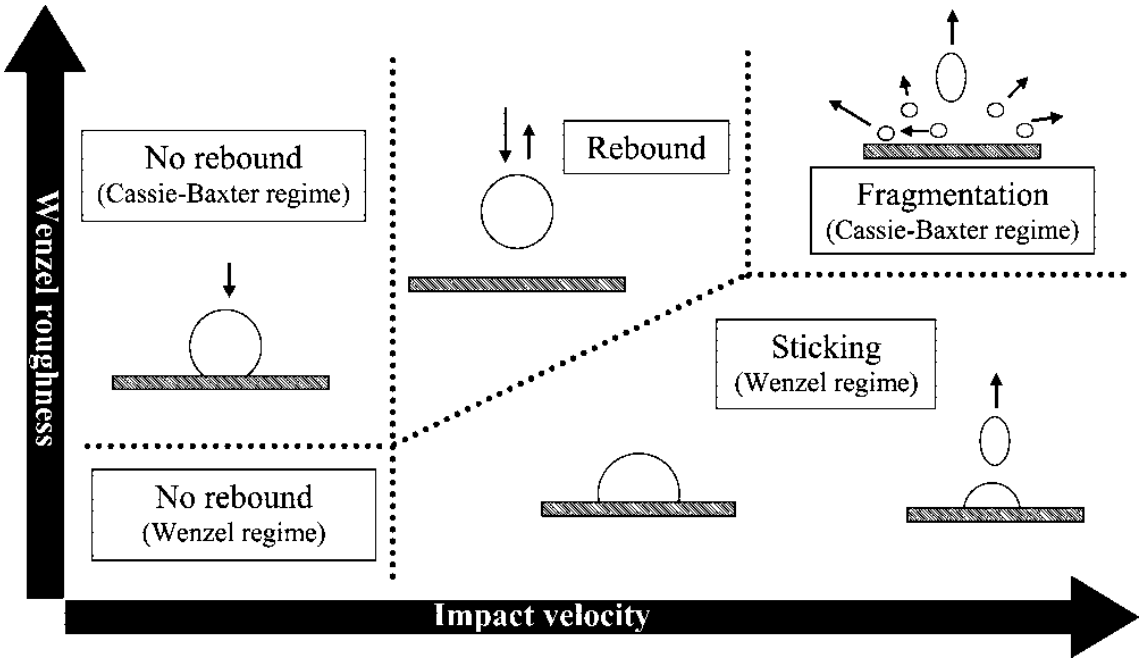

Figure 1.4: Drop impact outcomes on a superhydrophobic surface. Reprinted with permission from (84). Copyright (2008) American Chemical Society.

The impact of water droplets on superhydrophobic carbon nanofiber jungles showed that droplet behaviour could be changed from complete rebound (bouncing) to deposition (non-bouncing) by simply decreasing the Weber number of the droplet.[90] This can be achieved by decreasing the size or velocity of the water droplet, or altering the fluid properties. This behaviour was similar to that of a separate microstructured polymer surface with a similar contact angle, indicating that the precise nature of the surface roughness may have little effect on impact regimes, though they may still affect drop behaviour within a certain regime.[90]

Studies of droplet impact over a range of roughness's are rare, as surface roughness is difficult to define.[91] Many papers use root-mean-squared roughness values, the average magnitude of the peaks and valleys typically determined via atomic force microscopy, however these do not adequately describe the actual topography of a surface, which may be crucial for droplet

impact. For instance two surfaces may have similar root-mean-square values of roughness but different distribution of asperities. A droplet will behave differently on a surface with large scale infrequent features than on a surface with frequent smaller scale features.

1.6 Conclusions

Both hydrophilic and hydrophobic surface treatments can be beneficial for inkjet printing depending upon the underlying substrate and application. Hydrophilic treatments are more suitable on substrates for which inkjet printing would not normally be feasible. Treatment of man-made textiles improves the wettability, leading to a more vivid print albeit at lower resolution.

If resolution is important, a hydrophobic coating can improve the definition of the inkjet printing technique by inhibiting the spread of a droplet and hence decreasing the size of deposit on the substrate. Because on hydrophobic surfaces liquid–solid interactions are unfavourable, the contact line is usually de-pinned. This invariably leads to a more even deposit for particulate based inks and can help to eliminate the coffee ring effect. Application of a hydrophobic treatment is easier than trying to improve performance through modification of the ink itself, since other interactions must be considered, including those in the bulk, at the meniscus, and whilst jetting.

Whilst the equilibrium position of a drop is important for assessing surface treatments for their suitability for inkjet printing, drop impact behaviour is also vital. A rough superhydrophobic surface may help improve resolution by decreasing the diameter of the drop, but it may also introduce unfavourable impact events such as bouncing, splashing, or roll off.

1.7 Scope of Thesis

There has been a range of work carried out on the wettability of surfaces and the role this can play in inkjet printing. However, in many cases the droplet sizes utilised are not inkjet-relevant. In this thesis, the effect of substrate chemistry, roughness, hardness, charge, and porosity on inkjet-sized picolitre droplets is studied and compared to microlitre droplets more commonly used to characterise surface wettability.

Chapter 3 investigates the impact of picolitre droplets on CF_4 plasma fluorinated polybutadiene. Such surfaces are determined to be superhydrophobic for microlitre droplets, resulting in high contact angles and low hysteresis. In the case of picolitre droplets however, the impact and spreading is determined not only by the extent of surface roughness (RMS value) but also the average feature size relative to the size of the drop. A comparison of the maximum spreading ratio and droplet oscillation frequencies with literature models shows that both are found to be lower than theoretically predicted.

Chapter 4 describes CF_4 plasma texturing of honeycomb surfaces, leading to hierarchical surfaces with roughness on two length scales. For picolitre droplets, it is found that surfaces with similar static contact angles can give rise to different droplet impact dynamics, governed by the underlying surface topography.

In Chapter 5, the oscillatory dynamics of picolitre droplets following impact is found to be influenced by the mechanical properties of the substrate. Higher oscillation frequencies are measured for oscillating droplets on softer and thicker films, which correlates to a larger surface deformation around the contact line.

Chapter 6 investigates picolitre droplet impact onto charged polymer substrates, which is found to give rise to increased droplet impact velocities. Higher surface potentials can result in the electrostatic attraction of the droplet, causing unexpected behaviour such as increased contact area diameters (decrease in print resolution) or droplet bouncing.

Chapter 7 investigates the effects of CF_4 plasma fluorination on the imbibition behaviour of porous polymer membranes as a function of pore size. These membranes are hydrophobic–oleophilic and efficient oil–water separators.

Finally, Chapter 8 describes the creation of copolymer–fluorosurfactant complex film surfaces, which exhibit hydrophilic–oleophobic behaviour. The time taken for the surface to become hydrophilic is much shorter than in previous studies. Such surfaces are found to display excellent anti-fogging, self-cleaning, and oil–water separation properties.

1.8 References

[1] Sirringhaus, H.; Kawase, T.; Friend, R. H.; Shimoda, T.; Inbasekaran, M.; Wu, W.; Woo, E. P. High-Resolution Inkjet Printing of All-Polymer Transistor Circuits. *Science* **2000**, *290*, 2123.

[2] Wang, J. Z.; Zheng, Z. H.; Li, H. W.; Huck, W. T. S.; Sirringhaus, H. Dewetting of conducting polymer inkjet droplets on patterned surfaces. *Nat. Mater.* **2004**, *3*, 171.

[3] Sele, C. W.; von Werne, T.; Friend, R. H.; Sirringhaus, H. Lithography-Free, Self-Aligned Inkjet Printing with Sub-Hundred-Nanometer Resolution. *Adv. Mater.* **2005**, *17*, 997.

[4] Doggart, J.; Wu, Y.; Liu, P.; Zhu, S. Facile Inkjet-Printing Self-Aligned Electrodes for Organic Thin-Film Transistor Arrays with Small and Uniform Channel Length. *ACS Appl. Mater. Interfaces* **2010**, *2*, 2189.

[5] Croucher, M. D.; Hair, M. L. Design criteria and future directions in ink-jet ink technology. *Ind. Eng. Chem. Res.* **1989**, *28*, 1712.

[6] Barbulovic-Nad, I.; Lucente, M.; Sun, Y.; Zhang, M.; Wheeler, A. R.; Bussmann, M. Bio-Microarray Fabrication Techniques—A Review. *Crit. Rev. Biotechnol.* **2006**, *26*, 237.

[7] Tan, C. P.; Cipriany, R.; Lin, D. M.; Craighead, H. G. Nanoscale Resolution, Multicomponent Biomolecular Arrays Generated By Aligned Printing With Parylene Peel-Off. *Nano Lett.* **2010**, *10*, 719.

[8] Arrabito, G.; Pignataro, B. Inkjet Printing Methodologies for Drug Screening. *Anal. Chem.* **2010**, *82*, 3104.

[9] Mironov, V.; Boland, T.; Trusk, T.; Forgacs, G.; Markwald, R. R. Organ printing: computer-aided jet-based 3D tissue engineering. *Trends Biotechnol.* **2003**, *21*, 157.

[10] Xu, T.; Jin, J.; Gregory, C.; Hickman, J. J.; Boland, T. Inkjet printing of viable mammalian cells. *Biomaterials* **2005**, *26*, 93.

[11] Bharathan, J.; Yang, Y. Polymer electroluminescent devices processed by inkjet printing: I. Polymer light-emitting logo. *Appl. Phys. Lett.* **1998**, *72*, 2660.

[12] Chang, S.-C.; Bharathan, J.; Yang, Y.; Helgeson, R.; Wudl, F.; Ramey, M. B.; Reynolds, J. R. Dual-color polymer light-emitting pixels processed by hybrid inkjet printing. *Appl. Phys. Lett.* **1998**, *73*, 2561.

[13] Calvert, P. Inkjet Printing for Materials and Devices. *Chem. Mater.* **2001**, *13*, 3299.

[14] De Gans, B.; Schubert, U. S. Inkjet Printing of Well-Defined Polymer Dots and Arrays. *Langmuir* **2004,** *20*, 7789.

[15] Tekin, E.; Smith, P. J.; Schubert, U. S. Inkjet printing as a deposition and patterning tool for polymers and inorganic particles. *Soft Matter* **2008**, *4*, 703.

[16] Drelich, J.; Chibowski, E.; Meng, D. D.; Terpilowski, K. Hydrophilic and superhydrophilic surfaces and materials. *Soft Matter* **2011**, *7*, 9804.

[17] Young, T. An Essay on the Cohesion of Fluids. *Philos. Trans. R. Soc.* **1805**, *95*, 65.

[18] Wenzel, R, N. Resistance of Solid Surfaces to Wetting by Water. *Ind. Eng. Chem.* **1936**, *28*, 988.

[19] Cassie, A. B. D.; Baxter, S. Wettability of porous surfaces. *Trans. Faraday Soc.* **1944**, *40*, 546.
[20] Gao, L.; McCarthy, T. J. How Wenzel and Cassie Were Wrong. *Langmuir* **2007**, *23*, 3762.
[21] McHale, G. Cassie and Wenzel: Were They Really So Wrong? *Langmuir* **2007**, *23*, 8200.
[22] Panchagnula, M. V.; Vedantam, S. Comment on How Wenzel and Cassie Were Wrong by Gao and McCarthy. *Langmuir* **2007**, *23*, 13242.
[23] Gao, L.; McCarthy, T. J. Reply to "Comment on How Wenzel and Cassie Were Wrong by Gao and McCarthy". *Langmuir* **2007**, *23*, 13243.
[24] Kwon, Y.; Choi, S.; Anantharaju, N.; Lee, J.; Panchagnula, M. V.; Patanka, N. A. Is the Cassie−Baxter Formula Relevant? *Langmuir* **2010**, *26*, 17528.
[25] Extrand, C. W. Model for Contact Angles and Hysteresis on Rough and Ultraphobic Surfaces. *Langmuir* **2002**, *18*, 7991.
[26] Extrand, C. W. Contact Angles and Hysteresis on Surfaces with Chemically Heterogeneous Islands. *Langmuir* **2003**, *19*, 3793.
[27] Erbil, H. Y.; Demirel, A. L.; Avci, Y.; Mert, O. Transformation of a Simple Plastic into a Superhydrophobic Surface. *Science* **2003**, *299*, 1377.
[28] Onda, T.; Shibuichi, S.; Satoh, N.; Tsujii, K. Super-Water-Repellent Fractal Surfaces. *Langmuir* **1996**, *12*, 2125.
[29] Jiang, L.; Zhao, Y.; Zhai, J. A Lotus-Leaf-like Superhydrophobic Surface: A Porous Microsphere/Nanofiber Composite Film Prepared by Electrohydrodynamics. *Angew. Chem. Int. Ed.* **2004**, *43*, 4338.
[30] Yan, H.; Kurogi, K.; Mayama, H.; Tsujii, K. Environmentally Stable Super Water-Repellent Poly(alkylpyrrole) Films. *Angew. Chem. Int. Ed.* **2005**, *44*, 3453.
[31] Öner, D.; McCarthy, T. J. Ultrahydrophobic Surfaces. Effects of Topography Length Scales on Wettability. *Langmuir* **2000**, *16*, 7777.
[32] Picknett, R. G.; Bexon, R. The evaporation of sessile or pendant drops in still air. *J. Colloid Interface Sci.* **1977**, *61*, 336.
[33] Talbot, E. L.; Berson, A.; Brown, P. S.; Bain, C. D. Evaporation of picoliter droplets on surfaces with a range of wettabilities and thermal conductivities. *Phys. Rev. E* **2012**, *85*, 061604.
[34] Bridgman, P. W. *Dimensional Analysis*; Yale University Press: New Haven, 1931.
[35] Schiaffino, S.; Sonin, A. A. Molten droplet deposition and solidification at low Weber numbers. *Phys. Fluids* **1997**, *9*, 3172.
[36] Zhang, C.; Fang, K. Surface modification of polyester fabrics for inkjet printing with atmospheric-pressure air/Ar plasma. *Surf. Coat. Technol.* **2009,** *203*, 2058.
[37] Lee, D. J.; Oh, J. H. Shapes and morphologies of inkjet-printed nanosilver dots on glass substrates. *Surf. Interface Anal.* **2010,** *42*, 1261.
[38] Duineveld, P. C. *J. Fluid Mech.* **2003,** *477*, 175.
[39] Fang, K.; Wang, S.; Wang, C.; Tian, A. Inkjet printing effects of pigment inks on silk fabrics surface-modified with O2 plasma. *J. Appl. Polym. Sci.* **2008,** *107*, 2949.

[40] Dong, H.; Carr, W. W.; Bucknall, D. G.; Morris, J. F. Temporally-resolved inkjet drop impaction on surfaces. *AIChE J.* **2007,** *53*, 2606.
[41] Oh, J. H.; Lim, S. Y. Precise size control of inkjet-printed droplets on a flexible polymer substrate using plasma surface treatment. *J. Micromech. Microeng.* **2010,** *20*, 015030.
[42] Norton, J. F. Waterproofing Treatment of Materials. U.S. Pat. No. 2,386,259, 1945.
[43] Fadeev, A. Y.; McCarthy, T. J. Trialkylsilane Monolayers Covalently Attached to Silicon Surfaces: Wettability Studies Indicating that Molecular Topography Contributes to Contact Angle Hysteresis. *Langmuir* **1999**, *15*, 3759.
[44] Daniel, S.; Chaudhury, M. K.; Chen, J. C. Fast Drop Movements Resulting from the Phase Change on a Gradient Surface. *Science* **2001**, *291*, 633.
[45] Nakajima, A.; Hashimoto, K.; Watanabe, T.; Takai, K.; Yamauchi, G.; Fujishima, A. Transparent Superhydrophobic Thin Films with Self-Cleaning Properties. *Langmuir* **2000**, *16*, 7044.
[46] Jahn, S. F.; Engisch, L.; Baumann, R. R.; Ebert, S.; Goedel, W. A. Polymer Microsieves Manufactured by Inkjet Technology. *Langmuir* **2009**, *25*, 606.
[47] Dong, H.; Carr, W. W.; Morris, J. F. Visualization of drop-on-demand inkjet: Drop formation and deposition. *Rev. Sci. Instrum.* **2006,** *77*, 085101.
[48] Li, X.; Ma, X.; Lan, Z. Behavioral patterns of drop impingement onto rigid substrates with a wide range of wettability and different surface temperatures. *AIChE J.* **2009**, *55*, 1983.
[49] Li, X.-M.; Reinhoudt, D.; Crego-Calama, M. What do we need for a superhydrophobic surface? A review on the recent progress in the preparation of superhydrophobic surfaces. *Chem. Soc. Rev.* **2007**, *36*, 1350.
[50] Chen, W.; Fadeev, A. Y.; Hsieh, M. C.; Öner, D.; Youngblood, J. P.; McCarthy, T. J. Ultrahydrophobic and Ultralyophobic Surfaces: Some Comments and Examples. *Langmuir* **1999**, *15*, 3395.
[51] Yabu, H.; Takebayashi, M.; Tanaka, M.; Shimomura, M. Superhydrophobic and Lipophobic Properties of Self-Organized Honeycomb and Pincushion Structures. *Langmuir* **2005**, *21*, 3235.
[52] Krupenkin, T. N.; Taylor, J. A.; Wang, E. N.; Kolodner, P.; Hodes, M.; Salamon, T. R. Reversible Wetting−Dewetting Transitions on Electrically Tunable Superhydrophobic Nanostructured Surfaces. *Langmuir* **2007**, *23*, 9128.
[53] Dufour, R.; Harnois, M.; Coffinier, Y.; Thomy, V.; Boukherroub, R.; Senez, V. Engineering Sticky Superomniphobic Surfaces on Transparent and Flexible PDMS Substrate. *Langmuir* **2010**, *26*, 17242.
[54] Tuteja, A.; Choi, W.; Ma, M.; Mabry, J. M.; Mazzella, S. A.; Rutledge, G. C.; Mckinley, G. H.; Cohen, R. E. Designing Superoleophobic Surfaces. *Science* **2007**, *318*, 1618.

[55] Mishchenko, L.; Hatton, B.; Bahadur, V.; Taylor, J. A.; Krupenkin, T.; Aizenberg, J. Design of Ice-free Nanostructured Surfaces Based on Repulsion of Impacting Water Droplets. *ACS Nano* **2010**, *4*, 7699.

[56] Cho, W. K.; Kang, S. M.; Kim, D. J.; Yang, S. H.; Choi, I. S. Formation of Superhydrophobic Surfaces by Biomimetic Silicification and Fluorination. *Langmuir* **2006**, *22*, 11208.

[57] Cao, L.; Jones, A. K.; Sikka, V. K.; Wu, J.; Gao, D. Anti-Icing Superhydrophobic Coatings. *Langmuir* **2010**, *25*, 12444.

[58] Xue, C.-H.; Jia, S.-T.; Zhang, J.; Tian, L.-Q. Superhydrophobic surfaces on cotton textiles by complex coating of silica nanoparticles and hydrophobization. *Thin Solid Films* **2009**, *517*, 4593.

[59] Li, H.; Wang, X.; Song, Y.; Liu, Y.; Li, Q.; Jiang, L.; Zhu, D. Super-"Amphiphobic" Aligned Carbon Nanotube Films. *Angew. Chem. Int. Ed.* **2001**, *40*, 1743.

[60] Feng, L.; Li, S.; Li, Y.; Li, H.; Zhang, L.; Zhai, J.; Song, Y.; Liu, B.; Jiang, L.; Zhu, D. Super-Hydrophobic Surfaces: From Natural to Artificial. *Adv. Mater.* **2002**, *14*, 1857.

[61] Gao, L.; McCarthy, T. J. The "Lotus Effect" Explained: Two Reasons Why Two Length Scales of Topography Are Important. *Langmuir* **2006**, *22*, 2966.

[62] Ulman, A. Formation and Structure of Self-Assembled Monolayers. *Chem. Rev.***1996**, *96*, 1533.

[63] Wang, M.; Liechti, K. M.; Wang, Q.; White, J. M. Self-Assembled Silane Monolayers: Fabrication with Nanoscale Uniformity. *Langmuir* **2005**, *21*, 1848.

[64] Hancer, M. The effect of humidity on the stability of octadecyltrichlorosilane for the self-assembled monolayer coating applications. *Prog. Org. Coat.* **2008**, *63*, 395.

[65] Lee, M.-T.; Hsueh, C.-C.; Freund, M. S.; Ferguson, G. S. Air Oxidation of Self-Assembled Monolayers on Polycrystalline Gold: The Role of the Gold Substrate. *Langmuir* **1998**, *14*, 6419.

[66] Bain, C. D.; Troughton, E. B.; Tao, Y. T.; Evall, J.; Whitesides, G. M.; Nuzzo, R. G. Formation of monolayer films by the spontaneous assembly of organic thiols from solution onto gold. *J. Am. Chem. Soc.* **1989**, *111*, 321.

[67] Tu, W.; Takai, K.; Fukui, K.-I.; Miyazaki, A.; Enoki, T. Interface Effect on the Electronic Structure of Alkanethiol-Coated Platinum Nanoparticles. *J. Phys. Chem. B* **2003**, *107*, 10134.

[68] Stapleton, J. J.; Daniel, T. A.; Uppili, S.; Cabarcos, O. M.; Naciri, J.; Shashidhar, R.; Allara, D. L. Self-Assembly, Characterization, and Chemical Stability of Isocyanide-Bound Molecular Wire Monolayers on Gold and Palladium Surfaces. *Langmuir* **2005**, *21*, 11061.

[69] Woodward, I.; Schofield, W. C. E.; Roucoules, V.; Badyal, J. P. S. Super-hydrophobic Surfaces Produced by Plasma Fluorination of Polybutadiene Films. *Langmuir* **2003**, *19*, 3432.

[70] Balu, B.; Breedveld, V.; Hess, D. W. Fabrication of "Roll-off" and "Sticky" Superhydrophobic Cellulose Surfaces via Plasma Processing. *Langmuir* **2008**, *24*, 4785.

[71] Kulinich, S. A.; Farzaneh, M. How Wetting Hysteresis Influences Ice Adhesion Strength on Superhydrophobic Surfaces. *Langmuir* **2009**, *25*, 8854.
[72] Miwa, M.; Nakajima, A.; Fujishima, A.; Hashimoto, K.; Watanabe, T. Effects of the Surface Roughness on Sliding Angles of Water Droplets on Superhydrophobic Surfaces. *Langmuir* **2000**, *16*, 5754.
[73] Worthington, A. M. On the Forms Assumed by Drops of Liquids Falling Vertically on a Horizontal Plate. *Proc. R. Soc. Lond.* **1876**, *25*, 261.
[74] Mao, T.; Kuhn, D. C. S.; Tran, H. Spread and rebound of liquid droplets upon impact on flat surfaces. *AIChE J.* **1997**, *43*, 2169.
[75] Rioboo, R.; Marengo, M.; Tropea, C. Time evolution of liquid drop impact onto solid, dry surfaces. *Exp. Fluids* **2002**, *33*, 112.
[76] Šikalo, Š.; Marengo, M.; Tropea, C.; Ganić, E. N. Analysis of impact of droplets on horizontal surfaces. *Exp. Therm. Fluid Sci.* **2002**, *25*, 503.
[77] Wang, M.-J.; Lin, F.-H.; Hung, Y.-L.; Lin, S.-Y. Dynamic Behaviors of Droplet Impact and Spreading: Water on Five Different Substrates. *Langmuir* **2009**, *25*, 6772.
[78] Ukiwe, C.; Mansouri, A.; Kwok, D. Y. The dynamics of impacting water droplets on alkanethiol self-assembled monolayers with co-adsorbed CH_3 and CO_2H terminal groups. *J. Coll. Int. Sci.* **2005**, *285*, 760.
[79] Son, Y.; Kim, C.; Yang, D. H.; Ahn, D. J. Spreading of an Inkjet Droplet on a Solid Surface with a Controlled Contact Angle at Low Weber and Reynolds Numbers. *Langmuir* **2008**, *24*, 2900.
[80] Son, Y.; Kim, C.; Spreading of inkjet droplet of non-Newtonian fluid on solid surface with controlled contact angle at low Weber and Reynolds numbers. *J. Non-Newtonian Fluid Mech.* **2009**, *162*, 78.
[81] Han, J. T.; Kim, S.; Karim, A. UVO-Tunable Superhydrophobic to Superhydrophilic Wetting Transition on Biomimetic Nanostructured Surfaces. *Langmuir* **2007**, *23*, 2608.
[82] Jung, Y. C.; Bhushan, B. Dynamic Effects of Bouncing Water Droplets on Superhydrophobic Surfaces. *Langmuir* **2008**, *24*, 6262.
[83] Brunet, P.; Lapierre, F.; Thomy, V.; Coffinier, Y.; Boukherroub, R. Extreme Resistance of Superhydrophobic Surfaces to Impalement: Reversible Electrowetting Related to the Impacting/Bouncing Drop Test. *Langmuir* **2008**, *24*, 11203.
[84] Rioboo, R.; Voué, M.; Vaillant, A.; De Coninck, J. Drop Impact on Porous Superhydrophobic Polymer Surfaces. *Langmuir* **2008**, *24*, 14074.
[85] Jung, Y. C.; Bhushan, B. Dynamic Effects Induced Transition of Droplets on Biomimetic Superhydrophobic Surfaces. *Langmuir* **2009**, *25*, 9208.
[86] Rioboo, R.; Marengo, M.; Tropea, C. Outcomes from a Drop Impact on Solid Surfaces. *Atomization Spray* **2001**, *11*, 155.
[87] Deng, T.; Varanasi, K. K.; Hsu, M.; Bhate, N.; Keimel, C.; Stein, J.; Blohm, M. Nonwetting of impinging droplets on textured surfaces. *Appl. Phys. Lett.* **2009**, *94*, 133109.
[88] Lembach, A. N.; Tan, H.-B.; Roisman, I. V.; Gambaryan-Roisman, T.; Zhang, Y.; Tropea, C.; Yarin, A. L. Drop Impact, Spreading, Splashing, and Penetration into Electrospun Nanofiber Mats. *Langmuir* **2010**, *26*, 9516.

[89] Tsai, P.; van der Veen, R. C. A.; van de Raa, M.; Lohse, D. How Micropatterns and Air Pressure Affect Splashing on Surfaces. *Langmuir* **2010**, *26*, 16090.
[90] Tsai, P.; Pacheco, S.; Pirat, C.; Lefferts, L.; Lohse, D. Drop Impact upon Micro- and Nanostructured Superhydrophobic Surfaces. *Langmuir* **2009**, *25*, 12293.
[91] Apel-Paz, M.; Marmur, A. Spreading of liquids on rough surfaces. *Colloid Surface A* **1999**, *146*, 273.

Chapter 2 Experimental Techniques

2.1 Introduction

Throughout this thesis, a range of surface fabrication and analysis techniques are utilised to modify and characterise various substrate properties such as chemistry, morphology, and roughness as well as determine their effect on droplet impact. This chapter includes a brief summary of the experimental techniques used in this thesis.

2.2 Plasma Processing

Plasma is commonly referred to as the 'fourth state of matter'. The term, first coined in the late 1920s by Irving Langmuir[1] is now used to describe a gas composed of mostly ionised particles, such as charged ions, electrons metastables, and neutrals. Plasma discharge occurs when electrons accelerated by an applied electric field undergo collisions, which lead to ionisation and excitation processes causing the acceleration of secondary electrons and resulting in a cascade, Figure 2.1. Plasma discharge can be used in the deposition, treatment, and etching of polymer films. Non-polymerising plasmas such as O_2 or CF_4 plasmas can be used to treat existing polymer surfaces improving the wettability or hydrophobicity respectively. Such treatments can be used to alter the properties of the substrate surface whilst maintaining those of the bulk.[2] CF_4 plasma treatment results in fluorination of the polymer surface, which has been shown to dominate over polymer deposition.[3]

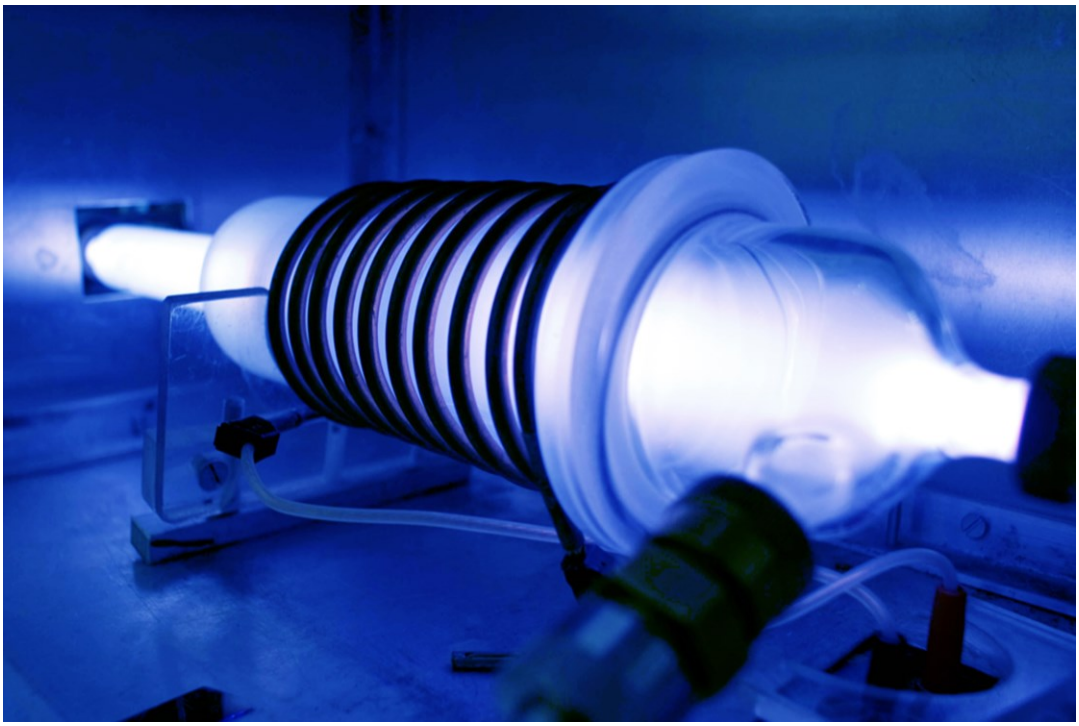

Figure 2.1: Plasma chamber during CF_4 plasma discharge.

2.2.1 Plasma Treatment

The treatment of a sample with a non-polymerising plasma can result in modification of the chemical and morphological properties of the surface. One example is the fluorination and texturing of polymer surfaces treated with CF_4 plasma. The presence of an alternating RF electromagnetic field causes electron acceleration, which in turn leads to bond cleavage and ionization of CF_4 molecules. Surface roughening takes place through the etching of volatile, low molecular weight species formed via the cleavage of polymer chains by ion bombardment,[4] vacuum ultraviolet (VUV) irradiation,[5] and chemical attack by fluorine atoms during electrical discharge treatment. Such polymer chain scission increases their mobility to enable topographical rearrangement[6,7] so as to minimise the surface free energy.[8,9] The extent of this polymer chain rearrangement results in different surface topographies, and is dependent upon the degree of chain scission and etching (i.e. the parameters employed during plasma processing such as plasma power and exposure time).[10] VUV irradiation can also penetrate below the polymer film surface. In this subsurface region, permeation of gaseous species is limited, and hence any photo-initiated reaction will proceed along different reaction pathways compared to those at the surface. Such reactions may include the efficient dissociation of polymer chain

σ-bonds,[11] leading to increased cross-linking of the subsurface, to create regions more resistant to ablation, which eventually become uncovered following prolonged or energetic surface etching.[12] VUV irradiation however does not affect the bulk properties of the polymer because the penetration depth is typically <100 nm.[11,12,13]

2.2.2 Plasma Polymerisation

Traditionally, continuous wave (CW) plasma polymerisation has yielded films bearing very little structural resemblance to the parent precursor and is highly influenced by process parameters such as: electrode configuration,[14] power input,[15] temperature,[16] precursor pressure,[17] and flow rate.[14] CW plasma polymerisation is often described as consisting of two distinct reaction processes, namely plasma-induced polymerisation and plasma-state polymerisation.[18] The former is a conventional polymerisation mechanism requiring double bonds or cyclic rings to be present within the monomer structure which get initiated by electrons or radicals contained within the electrical discharge.[19] Whereas the latter only takes place in the vicinity of a plasma,[18] where precursor fragmentation produces radicals and electrons which then reform into larger molecular species. This process repeats itself until macromolecular chains are formed. Therefore, the monomer for CW plasma polymerisation does not necessarily need to contain conventional polymerisable functional groups (such as double bonds). Subsequently, CW plasma polymerisation yields polymeric films that are highly cross-linked[20] and often display little resemblance to the precursor originally used to form them.

These shortcomings can be resolved by utilising pulsed plasmas comprising short on-periods (typically μs–ms) followed by extended off-periods (typically ms). This leads to lower fragmentation of the precursor molecule, less damage to the growing film, and allows the propagation of conventional reaction pathways, for example monomer carbon-carbon double bond polymerisation during each plasma duty cycle off-period.[21,22,23,24,25] As a consequence, polymer films can be produced which are structurally very similar to those produced by conventional polymerisation mechanisms.

2.3 Atom Transfer Radical Polymerisation (ATRP)

ATRP is an example of a controlled radical polymerisation technique. The technique takes advantage of the oxidation states of a metal, typically copper, to transfer atoms (X, typically halides) between the metal centre and the growing polymer chain, Figure 2.2. This transfer results in a cycling of the polymer chain between active and dormant states. In the active state, the polymer chain contains a radical centre, which is able to undergo further reaction with monomer units (i.e. propagation). By tethering halide-containing groups onto a surface, it is possible to grow surface-immobilised polymer chains using this technique.[26]

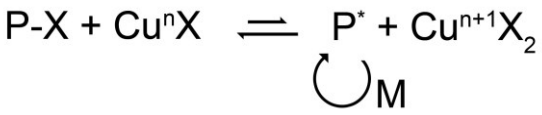

Figure 2.2: Schematic of typical ATRP reaction pathway. P denotes growing polymer chain, X is a halide, and M is a monomer unit.

2.4 X-Ray Photoelectron Spectroscopy (XPS)

XPS is a surface sensitive technique that provides quantitative information about the chemical composition of a sample. Photo-irradiation of a sample using soft X-rays results in the emission of core-level electrons from the sample surface, typically the top 5 nm.[27] The measured kinetic energy of the emitted electron can be related to its binding energy[28]

$$E_k = h\nu - E_b - \phi, \qquad (2.1)$$

where E_k is the kinetic energy of the emitted electron, E_b is the binding energy, $h\nu$ is the excitation energy, and ϕ is the work function.

The core electron binding energies are sensitive to the surrounding chemical environment. Therefore XPS spectra can contain broad envelopes containing individual peaks from elements in slightly different environments.[29] To prevent contamination or scatter of photo-electrons, XPS analysis is carried out in ultra-high vacuum conditions.

X-ray photons are created via the impaction of thermionic electrons on magnesium (Mg Kα: 1253.6 eV) or aluminium (Al Kα: 1486.6 eV) coated anodes. These photons have sufficient energy to eject core electrons for a range of elements. Ejected electrons are captured by a concentric

hemispherical analyser operating under constant analyser energy, permitting electrons of a certain pass energy (20 eV).

2.5 Infrared Analysis

Infrared analysis is a common technique used to identify chemical groups present in a liquid or solid sample. Infrared radiation is used to excite vibrational modes of molecules, which occur at characteristic group frequencies dependent upon the covalent bond being excited.

Fourier transform infrared spectroscopy (FTIR) is based on analysis of the absorbance of light containing many frequencies at once. This is achieved by taking a broadband source (containing the full spectrum of wavelengths to be measured) and passing it through an interferometer. This contains fixed and movable mirrors, which results in the blocking and transmission of various wavelengths of light due to interference between two separate beams passed through the mirrors. As the movable mirror is adjusted, the wavelengths that are blocked or transmitted vary, resulting in a different spectrum of light leaving the interferometer. This is then passed through the sample to be measured and to a detector where the raw data (an interferogram of light absorption/transmission at each position of the movable mirror) must be processed into an infrared spectrum (light absorption/transmission at each wavelength).

Infrared analysis of solid samples is generally carried out in two ways. The first is reflection absorption infrared spectroscopy (RAIRS), which entails the bouncing of the beam off the surface of a reflective substrate upon which the film of interest is coated. Silicon is typically used as the reflective substrate and this technique is able to measure the infrared spectra of thin films deposited on top. As the beam passes through the coating (before and after being reflected by the silicon below) excitation of the molecular vibrations within the film can occur, resulting in an infrared spectrum being recorded.

For thick films (typically >2 μm) or liquid samples, attenuated total reflectance (ATR) can be used. In this case, the beam is passed through a diamond crystal where it undergoes total internal reflection at the crystal–sample interface. At the point of internal reflectance, an evanescent wave extends several microns into the sample; this allows an infrared spectrum of the sample to be captured.

2.6 Atomic Force Microscopy (AFM)

Atomic Force Microscopy (AFM) is a surface analysis technique commonly used to determine the topography of a sample. This is achieved by scanning the sample with a sharp tip located on the end of a cantilever. As the tip responds to the topography of the surface, it deflects a laser beam positioned at the end of the cantilever. This deflection is monitored by a photodiode and fed into a feedback loop, which controls the sample stage, Figure 2.3. Three imaging modes are possible using this setup.

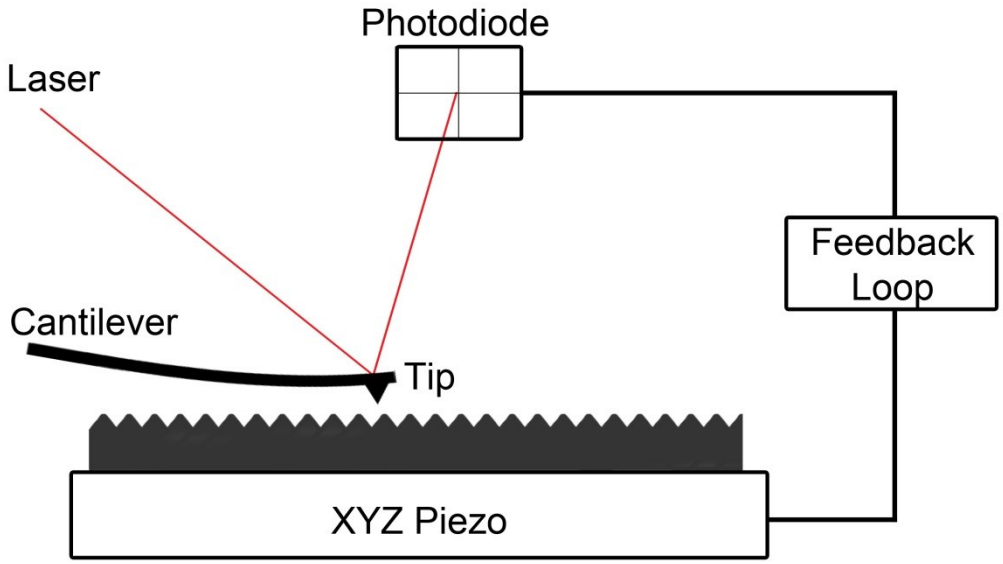

Figure 2.3: Schematic diagram showing the key components of an atomic force microscope.

2.6.1 Contact Mode

In contact mode, the tip is brought into close proximity with the surface so that the repulsive forces are dominant. As it is scanning, the tip–surface height is varied so as to maintain a constant force between the two; determined by maintaining a constant laser deflection. Changes in Z height through the sample piezo are collected to build a topographic image of the surface. This is preferable to a 'constant height' contact mode as this would risk crashing the tip in to the sample. However, contact mode still involves strong repulsive forces, which can cause damage to soft samples.

2.6.2 Non-Contact Mode

Non-contact mode relies on the oscillation of the cantilever near its resonant frequency just above the sample surface with an amplitude of around 10 nm. Long range forces between the sample and the tip reduce the resonant frequency of the cantilever. The feedback loop keeps the tip frequency constant by altering the tip–sample distance. Non-contact mode can be used with soft samples without the risk of damage, however the weak interactions involved mean the resulting images can contain a greater amount of noise. Any adsorbed liquid on the surface of the sample will also reduce the sensitivity of this mode due to hydro-dynamic damping.

2.6.3 Tapping Mode

In tapping mode, the cantilever is oscillated near its resonance frequency as in non-contact mode. However in tapping mode, the amplitude of this oscillation is far greater, typically 100 to 200 nm. When the tip moves closer to the sample surface, the interactive forces cause the oscillation amplitude to decrease. By adjusting the tip–sample distance, a constant oscillation amplitude can be achieved and a topographic image produced. This mode lessens the damage caused to both the tip and the sample compared to contact mode and also does not suffer from the same problems as non-contact mode with regards to adsorbed liquids. It is therefore suitable for the imaging of soft surfaces in ambient conditions.

2.7 Scanning Electron Microscopy (SEM)

Scanning electron microscopy is used to capture a high-resolution image of a sample. A highly focussed beam of electrons is used to excite atoms on the surface, which emit secondary electrons that can be captured. The electron beam is scanned across the surface and this movement is combined with the secondary electron signal to create an image. By coating the sample with an ultra-thin gold coat, the emission of secondary electrons is enhanced and problems arising due to surface charging are mitigated.

2.8 Thickness Measurements

Thickness measurements of thin films can be determined through the use of a spectrophotometer that measures the reflectance and transmittance of light from an irradiated sample, Figure 2.4. Such measurements can help to determine the refractive index (n), extinction coefficient (k), and thickness (d) of a film.

For incoming light of different wavelengths (350–1000 nm), the amount reflected by a sample will vary due to varying amounts of constructive and destructive interference from the reflections at the top and bottom of a deposited film. The refractive index of a film is determined by the speed which light travels through it, relative to the speed of light in a vacuum. This affects the distance travelled and therefore will affect the path length of the light travelling through the film. The extinction coefficient is a measure of the amount of light absorbed by a film which can affect the intensity of the light reflected. The resulting spectrum can be fitted with a Cauchy model[30] (which assumes the extinction coefficient is low) to give values of the refractive index and thickness of the film, Figure 2.5.

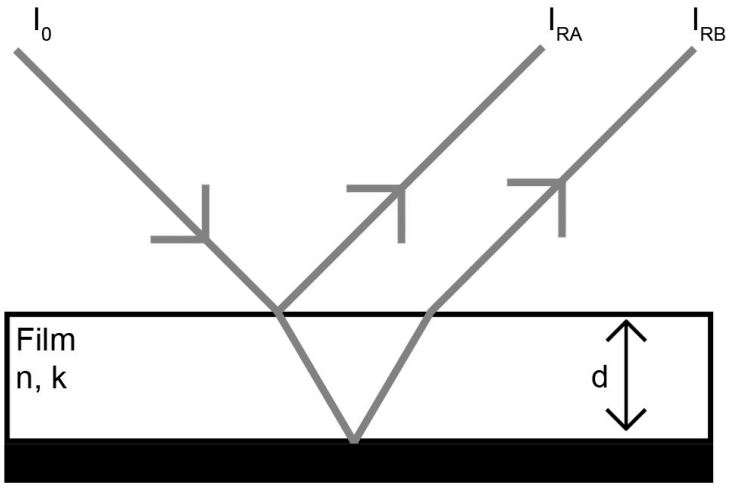

Figure 2.4: Determining film parameters through irradiation of sample with monochromatic light at various wavelengths.

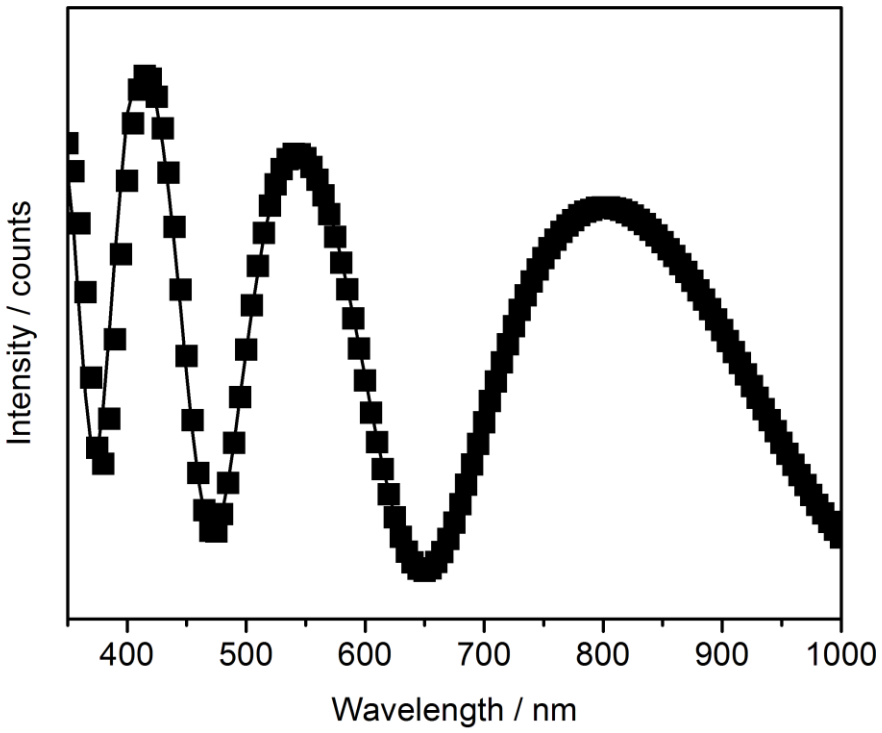

Figure 2.5: Reflectance graph for a polymer film on an opaque substrate. The variation in the amount of reflected light as a function of wavelength can be used to determine the film's refractive index and thickness.

2.9 Water Contact Angle Analysis

The spread of a liquid on a solid sample is highly dependent upon the surface energy and roughness. Contact angle measurements therefore can prove useful in characterising samples.

The angle a liquid droplet makes with a surface is determined by the balance of liquid–solid–vapour interactions at the three phase boundary, Equation 1.1 and Figure 1.1 (pages 17 and 18).

Differences in liquid contact angles can arise due to surface roughness and inhomogeneities, a liquid advancing over a surface can do so with a greater angle than when it is receding. This difference is known as contact angle hysteresis. The more homogenous the surface, the lower the energy difference between different contact line positions and therefore the lower the hysteresis.

Advancing and receding angles can be measured by increasing or decreasing the amount of fluid in a droplet on a surface respectively, and measuring the contact angle when the contact line begins to move.[31]

2.10 Drop Impact Rig

To study the impact and spreading of picolitre-sized droplets, an imaging rig was setup as shown in Figure 2.6. A high-speed camera is required to capture the initial moments following droplet impact. The camera, controlled by computer software, sends a signal to the jetting driver, which in turn sends a pulse to the inkjet nozzle. The size and shape of this pulse is set using accompanying software. A piezo in the nozzle contracts and expands as it responds to the pulse. This causes a pressure change in the filled capillary, which results in the expulsion of an amount of liquid. Through surface tension effects, this portion of fluid forms a droplet, which then impacts upon the substrate below. The jetting driver pulse can be fine-tuned to deliver single droplets with reproducible diameters and velocities. A representative pulse shape is shown in Figure 2.7. The nozzle piezo contracts when a positive voltage is applied during the dwell time of the pulse, expelling a droplet. To prevent satellite droplets from being generated, a negative voltage is applied during the echo time, expanding the piezo and decreasing the pressure in the capillary.

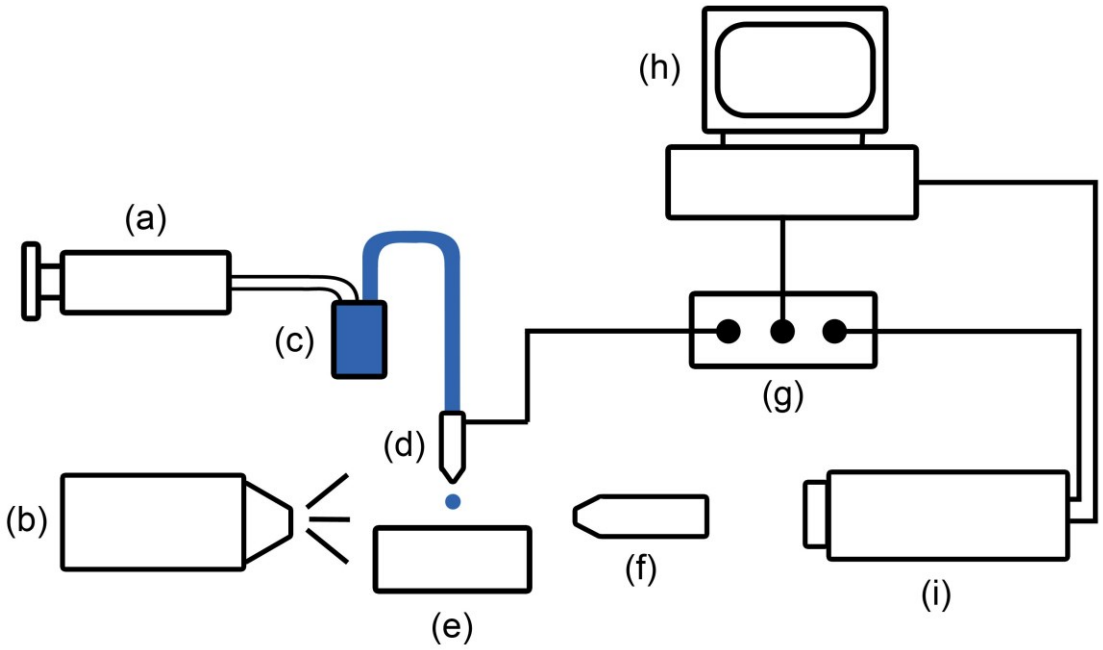

Figure 2.6: Droplet imaging rig: (a) pressure adjustment; (b) illumination source; (c) ink reservoir; (d) inkjet nozzle; (e) substrate; (f) objective lens; (g) jetting driver; (h) computer; (i) high-speed camera.

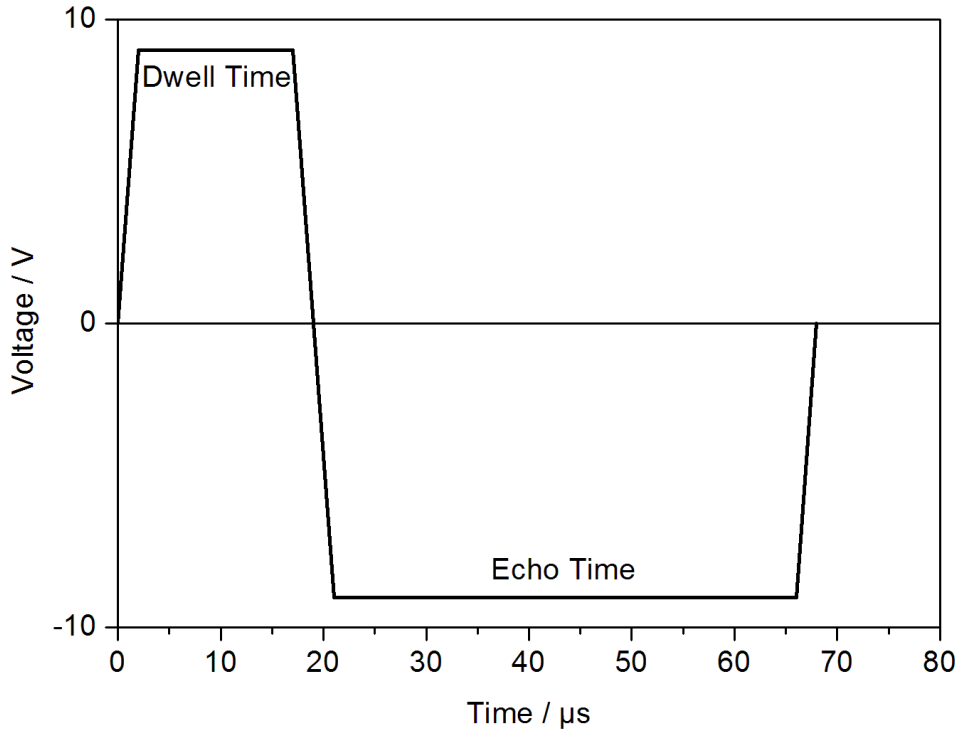

Figure 2.7: Representative waveform sent from the jetting driver to the nozzle piezo.

Images recorded from this setup were post-processed using custom MATLAB code to ascertain the evolution of the droplet shape after impact, Figure 2.8.

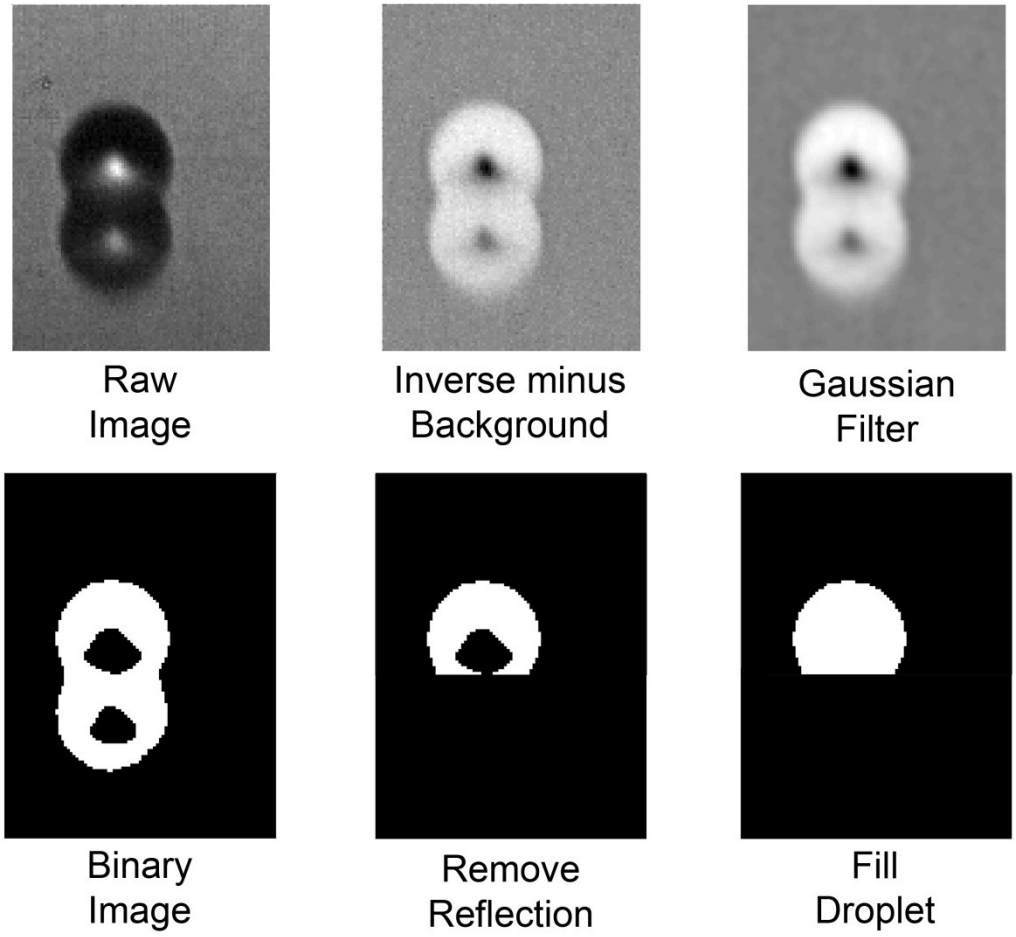

Figure 2.8: Post processing of raw image data using custom MATLAB code.

Binary images were used to determine the height, width, and diameter of the contact line of the droplet by pixel summation. Imaging of the nozzle aperture served as a calibration of the setup and allowed for conversion from pixels to microns. The contact angle of a droplet was obtained through basic trigonometry and verified by assuming a spherical cap fit. By processing images recorded prior to impact, the initial velocity and diameter of a droplet could be determined.

2.11 References

[1] Langmuir, I. The Interaction of Electron and Positive Ion Space Charges in Cathode Sheaths. *Phys. Rev.* **1929**, *33*, 954.

[2] Chan, C. M.; Ko, T. M.; Hiraoka, H. Polymer surface modification by plasmas and photons. *Surf. Sci. Rep.* **1996,** *24,* 1.

[3] Hopkins, J.; Badyal, J. P. S. Nonequilibrium Glow Discharge Fluorination of Polymer Surfaces. *J. Phys. Chem.* **1995**, *99*, 4261.

[4] Yasuda, H., *Plasma Polymerization*. 1985, New York: Academic Press.

[5] Egitto, F. D. Plasma etching and modification of organic polymers*. Pure Appl. Chem*. **1990**, *62*, 1699.

[6] Poncin-Epaillard, F.; Brosse, J. C.; Falher, T. Cold Plasma Treatment: Surface or Bulk Modification of Polymer Films? *Macromolecules* **1997**, *30*, 4415.

[7] Boyd, R. D., Kenwright, A. M.; Badyal, J. P. S.; Briggs, D. Atmospheric Nonequilibrium Plasma Treatment of Biaxially Oriented Polypropylene. *Macromolecules* **1997**, *30*, 5429.

[8] Andrade, J. D. *Polymer surface dynamics*; Springer: New York, 1988.

[9] Occhiello, E.; Morra, M.; Morini, G.; Garbassi, F.; Humphrey, P. Oxygen-plasma-treated polypropylene interfaces with air, water, and epoxy resins: Part I. Air and water. *J. Appl. Polym. Sci.* **1991**, *42*, 551.

[10] Kogelschatz, U.; Esrom, H.; Zhang, J.-Y.; Boyd, I. W. High-intensity sources of incoherent UV and VUV excimer radiation for low-temperature materials processing. *Proc. Eur. Mater. Res.* **2000**, *168*, 29.

[11] Holländer, A.; Wilken, R.; Behnisch, J. Subsurface chemistry in the plasma treatment of polymers. *Surf. Coat. Technol.* **1999**, *116–119*, 788.

[12] Liston, E. M.; Martinu, L.; Wertheimer, M. R. Plasma surface modification of polymers for improved adhesion: a critical review. *J. Adhes. Sci. Technol.* **1993**, 7, 1091.

[13] Poncin-Epaillard, F., B. Chevet, and J.-C. Brosse, Modification of isotactic poly(propylene) with a nitrogen plasma; differences in comparison to the treatment with a carbon dioxide plasma. *Die Makromolekulare Chemie* **1991**, *192*, 1589.

[14] Yasuda, H.; Hirotsu, T. Distribution of polymer deposition in plasma polymerization. II. Effect of reactor design. *J. Polym. Sci. Polym. Chem. Ed.* **1978**, *16*, 313.

[15] Yasuda, H.; Hirotsu, T. Distribution of polymer deposition in plasma polymerization. III. Effect of discharge power. *J. Polym. Sci. Polym. Chem. Ed.* **1978**, *16*, 2587.

[16] Ohkubo, J.; Inagaki, N. Influences of the system pressure and the substrate temperature on plasma polymers. *J. Appl. Polym. Sci.* **1990**, *41*, 349.

[17] Donohoe, K. G.; Wydeven, T. Plasma polymerization of ethylene in an atmospheric pressure-pulsed discharge. *J. Appl. Polym. Sci.* **1979**, 23, 2591.

[18] Yasuda, H. *Plasma Polymerisation;* Academic Press: New York, 1985.

[19] Bradley, A.; Czuha, M., Jr. Analytical Methods for Surface Grafts. *Anal. Chem.* **1975**, *47*, 1838.

[20] O'Kane, D. F.; Rice, D. W. Preparation and Characterization of Glow Discharge Fluorocarbon-Type Polymers. *J. Macromol. Sci., Part A: Pure Appl. Chem.* **1976**, *10*, 567.
[21] Ryan, M. E.; Hynes, A. M.; Badyal, J. P. S. Pulsed Plasma Polymerization of Maleic Anhydride. *Chem. Mater.* **1996**, *8*, 37.
[22] Savage, C. R.; Timmons, R. B.; Lin, J. W. Molecular control of surface film compositions via pulsed radio-frequency plasma deposition of perfluoropropylene oxide. *Chem. Mater.* **1991**, *3*, 575.
[23] Yasuda, H.; Hsu, T. Some aspects of plasma polymerization investigated by pulsed R.F. discharge. *J. Polym. Sci. Polym. Chem. Ed.* **1977**, *15*, 81.
[24] Yasuda, H.; Wang, C. R. Plasma polymerization investigated by the substrate temperature dependence. *J. Polym. Sci. Polym. Chem. Ed.* **1985**, *23*, 87.
[25] Timmons, R. B.; Griggs, A. J. Pulsed Plasma Polymerisations. In *Plasma Polymer Films*; Biederman, H., Ed.; Imperial Collge Press: London, 2004.
[26] Teare, D. O. H.; Barwick, D. C.; Schofield, W. C. E.; Garrod, R. P.; Ward, L. J.; Badyal, J. P. S. Substrate-Independent Approach for Polymer Brush Growth by Surface Atom Transfer Polymerization. *Langmuir* **2005**, *21*, 11425.
[27] Seah, M. P.; Deanch, W. A. Quantitative electron spectroscopy of surfaces: A standard data base for electron inelastic mean free paths in solids. *Surf. Interface Anal.* **1979**, *1*, 2.
[28] Moulder, J. F.; Stickle, W. F.; Sobol, P. E.; Bomben, K. D. *Handbook of X-ray Photoelectron Spectroscopy*; Perkin-Elmer: Minnesota, 1992.
[29] Beamson, G.; Briggs, D. *High-Resolution XPS of Organic Polymers*; John Wiley & Sons: New York, 1992.
[30] Tabet, M. F.; McGahan, W. A. Use of artificial neural networks to predict thickness and optical constants of thin films from reflectance data. *Thin Solid Films* **2000**, *370*, 122.
[31] Johnson, R. E. Jr.; Dettre, R. H. Wetting of Low-Energy Surfaces. In Wettability; Berg J. C., Ed.; Marcel Dekker, Inc.: New York, 1993; Chapter 1, p 13.

Chapter 3 Deposition of Picolitre Droplets on Superhydrophobic Surfaces with Ultra-Low Spreading Ratios

3.1 Introduction

Droplet impact upon solid surfaces is a widespread phenomenon and has been investigated for over a century.[1] Important technological applications include: rapid cooling,[2,3,4] delayed freezing,[5,6,7,8] crop spraying,[9] and inkjet printing. In recent years, work has been carried out to assess the feasibility of inkjet printing technology in manufacturing processes. In the case of the latter, the resolution of impact is critical for patterning applications such as: microelectronics,[10,11,12,13] pharmaceutical dosing or screening,[14,15,16] tissue engineering, [17,18] and optics.[19,20]

Whilst liquid properties are important during drop impact,[21] there exists strong evidence suggesting that surface properties not only affect the final static diameter of the droplet, but other key aspects of the surface impact. [22,23,24,25,26,27,28]

For topographically complex superhydrophobic surfaces, the impacting droplet can either penetrate into the surface fine structure, or become suspended on the asperities creating air pockets underneath giving a composite solid-air interface. These are respectively the Wenzel[29] and Cassie-Baxter[30] states. Droplet impact onto rough superhydrophobic surfaces usually results in bouncing[31,32] or splashing.[33,34,35,36,37] The situation is further complicated in that the inertia may be sufficient to impale the droplet onto surface features forcing a Wenzel configuration.[38,39] Droplet impact studies as a function of surface roughness are rare, because surface roughness is difficult to define and control.[40]

In this chapter, impact of picolitre droplets is investigated across a range of surface roughness values. The superhydrophobic surfaces were prepared by plasmachemical fluorination of polybutadiene films yielding sessile drop water contact angle values exceeding 170°, with negligible contact angle hysteresis.[41,42] The surface roughness was varied whilst maintaining a constant surface chemistry. The influence of the substrate on the static and dynamic

spreading ratio as well as on droplet oscillations has been investigated and the results compared with models from the literature.

3.2 Experimental

3.2.1 Sample Preparation

Polybutadiene (Sigma-Aldrich Inc., M_w = 420,000, 36% cis 1,4 addition, 55% trans 1,4 addition, 9% 1,2 addition) dissolved in toluene (BDH, +99.5% purity) at a concentration of 5% (w/v) was spin coated onto polished silicon (100) wafers (Silicon Valley Microelectronics Inc.) using a photoresist spinner (Cammax Precima) operating at 3000 rpm. These polymer films were subsequently annealed at 90 °C under vacuum for 60 min to remove entrapped solvent.

Plasmachemical fluorination was carried out in a cylindrical glass reactor (5 cm diameter, 470 cm^3 volume) connected to a two stage rotary pump via a liquid nitrogen cold trap with a base pressure of 4 x 10^{-3} mbar and a leak rate better than 6 x 10^{-9} mol s^{-1}. An L-C matching unit was used to minimise the standing wave ratio (SWR) for the power transmitted from a 13.56 MHz radio frequency generator to a copper coil externally wound around the glass reactor. Prior to each plasma treatment, the chamber was scrubbed with detergent, rinsed in propan-2-ol, and further cleaned using a 50 W air plasma for 30 min. A piece of polybutadiene coated substrate was then placed into the centre of the reactor, followed by evacuation to base pressure. Next, CF_4 gas (99.7% purity, Air Products) was admitted into the system via a needle valve at a pressure of 0.2 mbar, and the electrical discharge ignited. Upon completion of surface functionalisation, the gas feed was turned off and the chamber vented to atmosphere.

3.2.2 Surface Characterisation

A VG ESCALAB spectrometer equipped with an unmonochromatised Mg K_α X-ray source (1253.6 eV) and a concentric hemispherical analyser (CAE mode pass energy = 20 eV) was used for X-ray photoelectron spectroscopy (XPS) analysis. The XPS spectra were referenced to the C(1s) peak at 285.0 eV and fitted with a linear background and equal full-width-at-half maximum (FWHM) Gaussian components.[43] Elemental compositions were calculated using

sensitivity factors derived from chemical standards, F(1s): O(1s): C(1s) equals 0.27: 0.40: 1.00.

Microlitre sessile drop contact angle analysis was carried out with a video capture system (VCA2500XE, AST Products Inc.) using 1.0 μL dispensation of de-ionised water (BS 3978 grade 1). Advancing and receding angles were measured by respectively increasing and decreasing the droplet size until the contact line was observed to move.[44]

AFM images were acquired using a Digital Instruments Nanoscope III scanning probe microscope. Damage to the tip and sample surface was minimised by employing Tapping Mode AFM. Root-mean-square (RMS) roughness values were calculated over 50 μm x 50 μm scan areas.

3.2.3 Drop Impact and Imaging

The inkjet nozzle (Horizon Instruments Ltd., MicroFab MJ-ABP-01) was a piezo-type nozzle with a diameter of 30 μm. Water drops of 30 μm diameter were generating using a drive voltage of 9 V and pulse width of 15 μs. The distance between the nozzle tip and the substrate surface was set at 0.4 mm. Impact speeds were typically between 0.8 and 1.2 m s^{-1}. The temperature of the nozzle was 30 °C. A high-speed camera (Photron Europe Ltd., FASTCAM APX RS) in conjunction with a microscopic objective lens (Nikon U.K. Ltd., M Plan) with a magnification of 20x were used to observe the droplet. A back lighting system (Thorlabs Ltd., HPLS-30-02) was used for the illumination source. 90000 frames per second were achieved, to give an image every 11 μs. The shutter speed was set to 1 μs. Each frame consisted of 128 x 96 pixels, with the pixel size equal to 0.73 μm. The jetting driver was triggered by the camera.

Droplet impact can be described using the following three dimensionless numbers.[45,46] The Weber number (We, Equation 1.5, page 21), the Ohnesorge number (Oh, Equation 1.6), and the Reynolds number (Re, Equation 1.7). Undesirable droplet behaviour, such as bouncing or splashing, was supressed by fine-tuning of these dimensionless parameters. Throughout this study, picolitre water droplets with We = 0.3–0.6, Oh = 0.02, and Re = 25–40 were utilised.

3.3 Results

3.3.1 Superhydrophobic Surfaces

The XPS elemental composition of spin coated polybutadiene was 86% C, 14% O, and 0% F. Following CF_4 plasma fluorination, a constant F:C ratio across a range of electrical discharge powers was measured,[41] Figure 3.1. Therefore, any variation in the droplet impact regime can primarily be attributed to a change in surface topography.

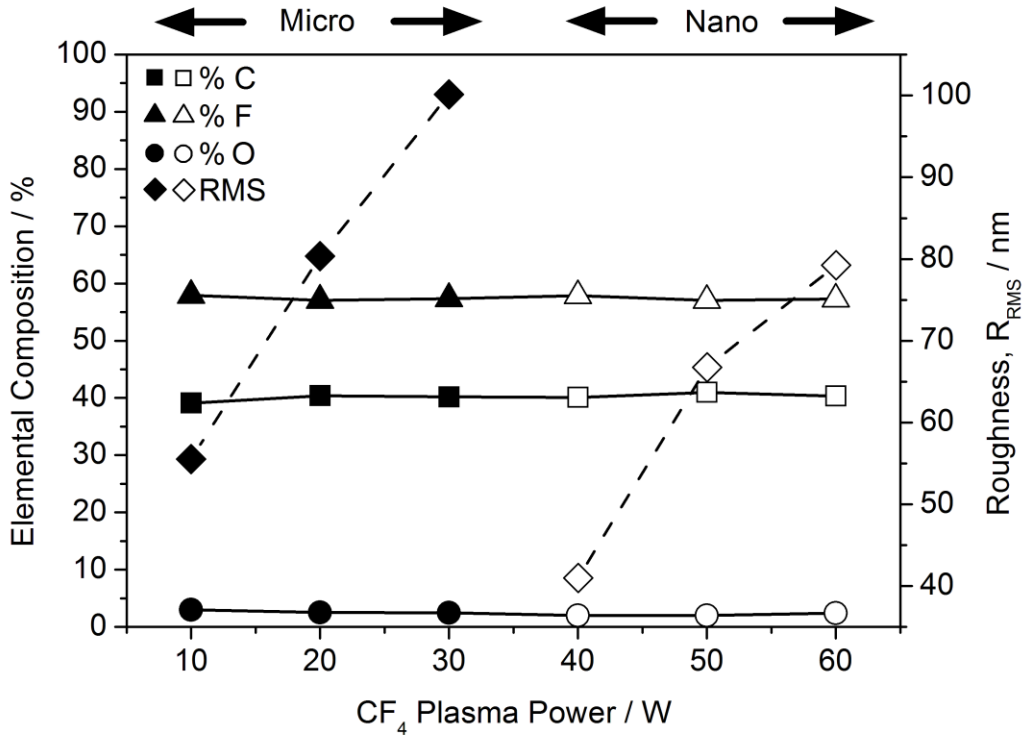

Figure 3.1: XPS and AFM RMS roughness analysis following 5 min CF_4 plasma fluorination of polybutadiene surfaces as a function of power. The lines are guides to the eye. Closed symbols denote microscale features, and open symbols denote nanoscale features. Error values: Elemental Composition = ± 2%; Roughness, R_{RMS} = ± 5 nm.

The surface roughness of the freshly prepared polybutadiene surfaces was measured to be R_{RMS} = 7 ± 1 nm. CF_4 plasma fluorination gave rise to two distinct regimes of surface topography as observed by AFM, Figure 3.1 and Figure 3.2. Large scale (micro) undulating features, observed at low powers, which are replaced by finer scale (nano) roughness at higher powers.[41] Longer treatment times can result in a composite surface exhibiting two roughness length scales.

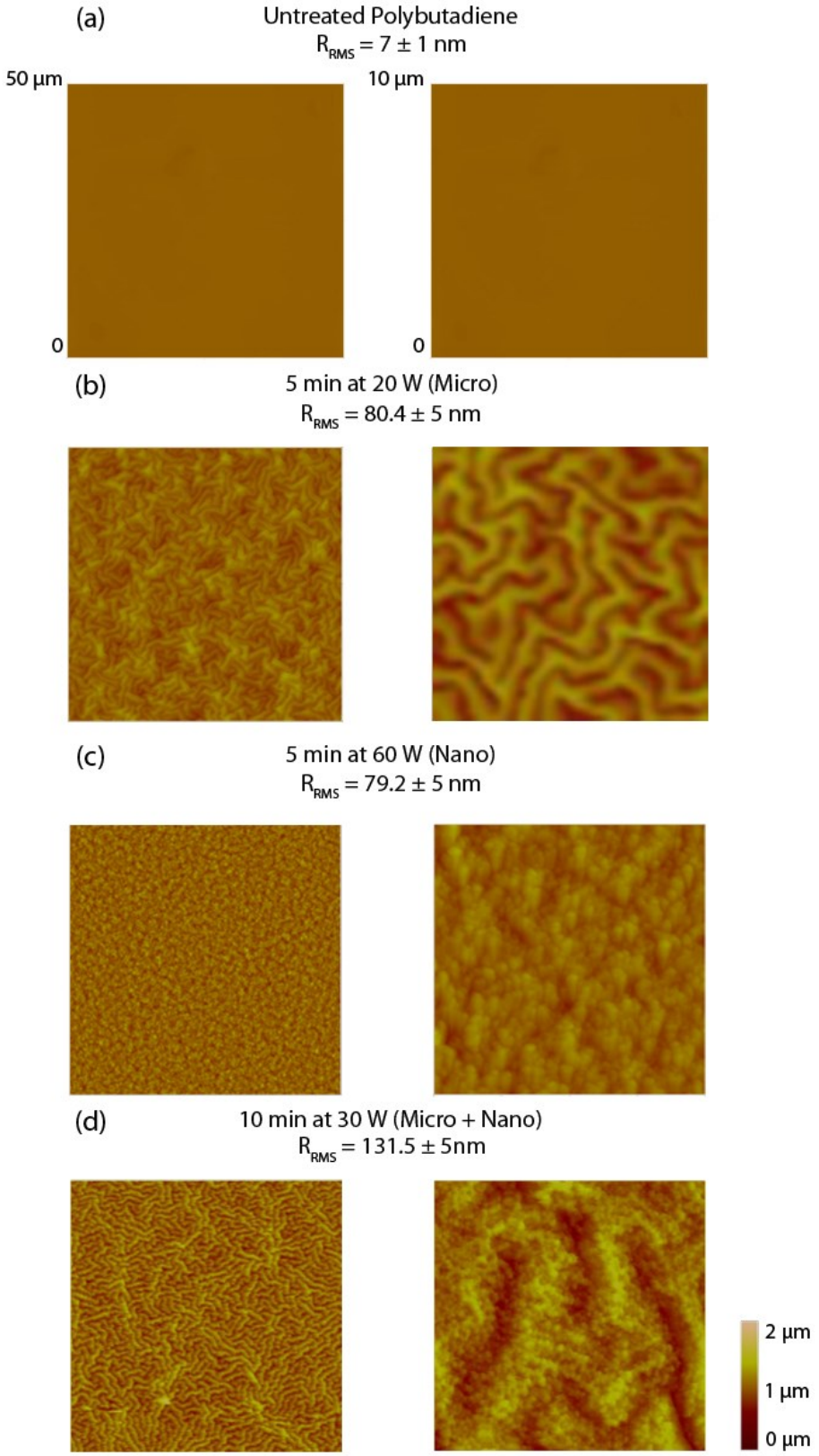

Figure 3.2: AFM height images of the different surface topographies for CF_4 plasma fluorinated polybutadiene surfaces with different distribution of asperities: (a) untreated polybutadiene; (b) microscale features; (c) nanoscale features; and (d) hierarchical surface.

Microlitre droplets placed onto these CF_4 plasma fluorinated polybutadiene surfaces yield contact angles ranging from 140° to 174°, Figure 3.3. With increasing surface roughness, the height of the asperities becomes sufficient to support a composite solid-air interface and the droplet behaviour corresponds to the Cassie-Baxter state.[30] This state is reflected in larger water contact angle values in conjunction with smaller contact angle hysteresis (θ_{adv} - θ_{rec}), Figure 3.3. It is worth noting that both the micro- and nanoscale topography data sit on the same equilibrium contact angle and contact angle hysteresis trend lines for R_{RMS} > 60 nm.

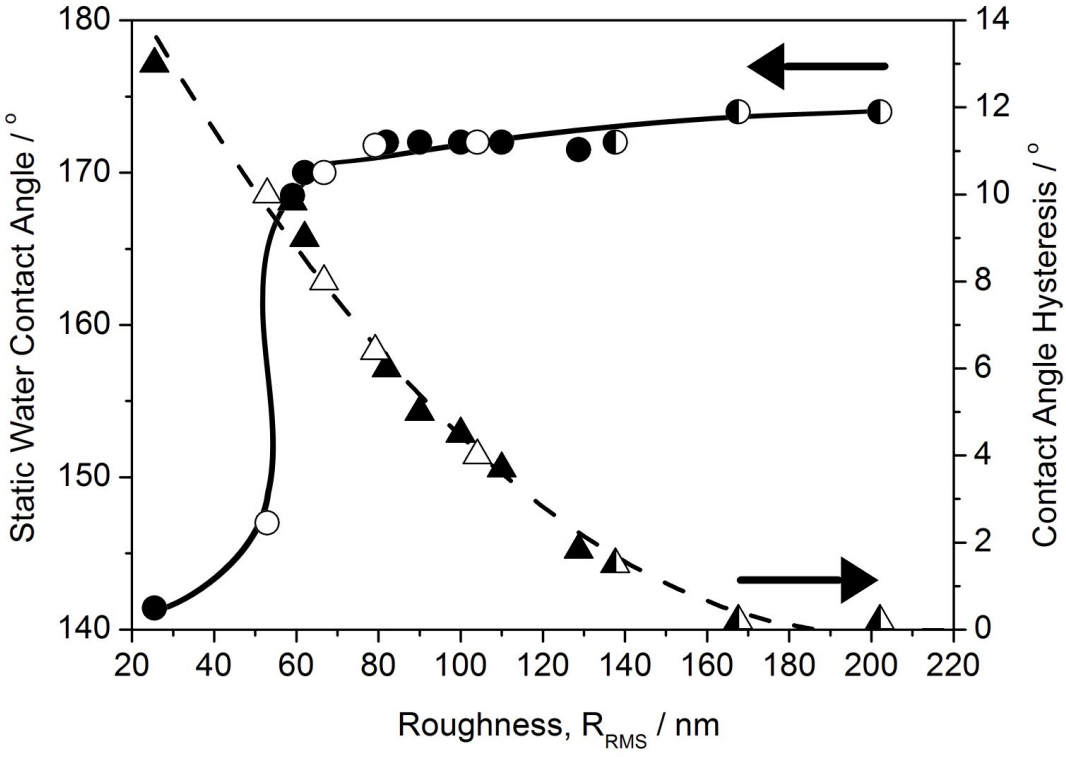

Figure 3.3: Static water contact angle and contact angle hysteresis values for 1.0 µL water drops placed onto CF_4 plasma fluorinated polybutadiene as a function of surface roughness. The lines are guides to the eye. Closed symbols denote microscale features, open symbols denote nanoscale features, and half closed symbols denote microscale+nanoscale features. Error values: Static Water Contact Angle = ± 5°; Contact Angle Hysteresis ± 0.5°; Roughness, R_{RMS} = ± 5 nm.

3.3.2 Picolitre Droplet Impact

High-speed photography of picolitre droplets striking these superhydrophobic surfaces without bouncing or splashing shows that, following initial impact, the droplet spreads outwards to a maximum diameter on the surface, Figure 3.4. Upon reaching this diameter, any excess energy will cause oscillations of the height, width, and contact line of the droplet about their static positions. The fluctuation in droplet height / width is pronounced, but the change in the contact area diameter is much more subtle due to the contact line being partially pinned. The droplet eventually comes to rest at its static position when its inertia is fully expended.

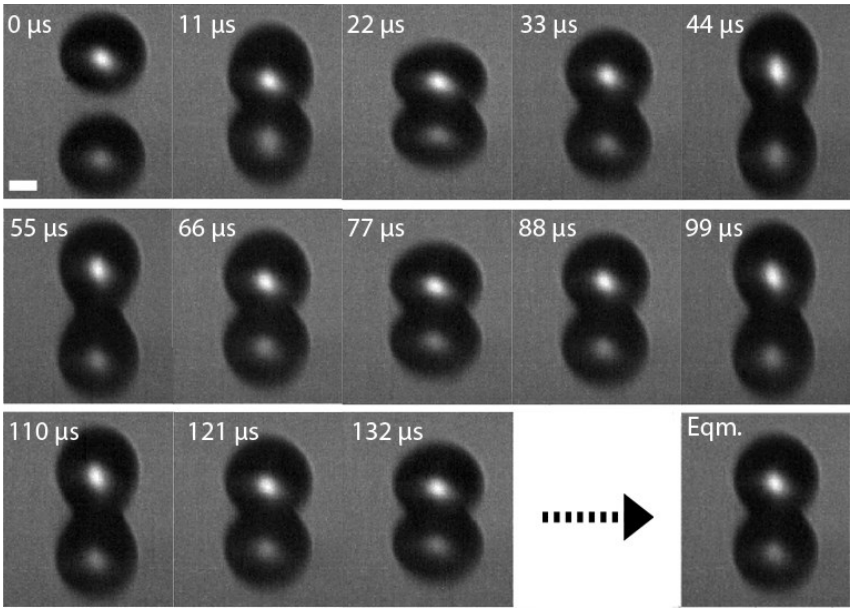

Figure 3.4: Typical high-speed video images of a picolitre size water droplet striking a superhydrophobic CF_4 plasma fluorinated and textured polybutadiene surface (including droplet reflection - lower image). White scale bar = 10 µm.

The higher contact angle values observed for microlitre versus picolitre water droplets resting on CF_4 plasma fluorinated polybutadiene surfaces imply that the smaller droplets experience a Wenzel state of wetting possibly induced by the force of impact, Figure 3.5. Furthermore, in the case of the picolitre size droplets for comparable surface roughness values, they display larger contact angles for the nanoscale surface topography. Whilst picolitre droplets striking surfaces with roughness values exceeding R_{RMS} = 140 nm bounce, Figure 3.5.

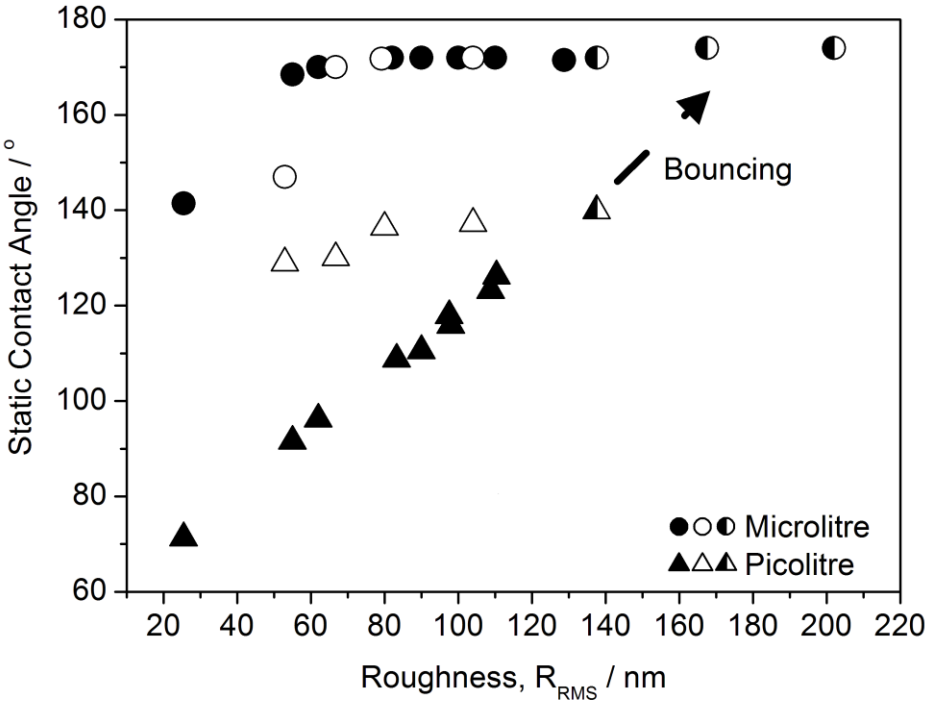

Figure 3.5: Static and equilibrium contact angles of microlitre and picolitre water droplets respectively on CF_4 plasma fluorinated polybutadiene as a function of surface roughness. Closed symbols denote microscale features, open symbols denote nanoscale features, and half closed symbols denote microscale+nanoscale features. Error values: Static Water Contact Angle = ± 5°; Roughness, R_{RMS} = ± 5 nm.

Maximum spreading occurs during the initial stages of droplet impact and is largely dependent upon the properties of the liquid.[22] Numerous attempts have been made to model the maximum spreading ratio. The Pasandideh-Fard model[47] assumes the droplet is thin and the contact angle is low, which is not valid for superhydrophobic surfaces. A modified model by Son[27] relaxes these assumptions but violates volume conservation. The following analysis is based on the model by Attané.[48]

Attané neglects the initial kinetic energy of the droplet and viscous dissipation within the droplet, which is reasonable when both *We* and *Oh* are small. At maximum spreading, all the surface energy of the droplet before impact is equal to the surface energy of the sessile droplet:

$$\sigma\pi D_0^2 = \sigma\left[A - \pi\left(\frac{D_{\max}}{2}\right)^2 \frac{\left(\sigma_{sv} - \sigma_{sl}\right)}{\sigma}\right] \tag{3.1}$$

where σ is the liquid surface tension, σ_{sv} is the surface free energy of the solid–vapour interface, σ_{sl} is the surface free energy of the solid–liquid interface (both per unit geometrical area), A is the area of the air–water interface, D_0 is the initial droplet diameter and D_{max} is the maximum spreading diameter. Young's equation allows the elimination of the solid surface free energies to give:

$$\sigma\pi D_0^2 = \sigma\left[A - \pi\left(\frac{D_{\max}}{2}\right)^2 \cos\theta_{eq}\right], \tag{3.2}$$

where θ_{eq} is the equilibrium contact angle. Assuming that the air–water interface is a spherical cap and that volume is conserved, Equation 3.2 can be rewritten as:

$$\frac{1}{3}\left[2\frac{h^2}{D_0{}^2} + \frac{D_0}{h} - \left(\frac{D_0}{h} - \frac{h^2}{D_0{}^2}\right)\cos\theta_{eq}\right] = 1, \tag{3.3}$$

where h is the height of the spherical cap. The maximum spreading ratio is obtained from the height as follows:

$$\frac{D_{\max}}{D_0} = 2\left[\frac{1}{3}\left(\frac{D_0}{h} - \frac{h^2}{D_0{}^2}\right)\right]^{1/2}. \tag{3.4}$$

Equations 3.3 and 3.4 provide an upper limit for the maximum spreading ratio as they assume there is no dissipation. The practical problem is knowing the value of θ_{eq}. We assume here that θ_{eq} is the same as the static contact angle, θ, when the droplet motion has ceased. A lower limit to D_{max} is given by the static spreading ratio:

$$\frac{D_s}{D_0} = 2\left[\frac{\sin^3\theta}{4 - 6\cos\theta + 2\cos^3\theta}\right]^{1/3}. \tag{3.5}$$

Experimental maximum spreading ratios are compared to the results of Equations 3.4 and 3.5 in Figure 3.6.

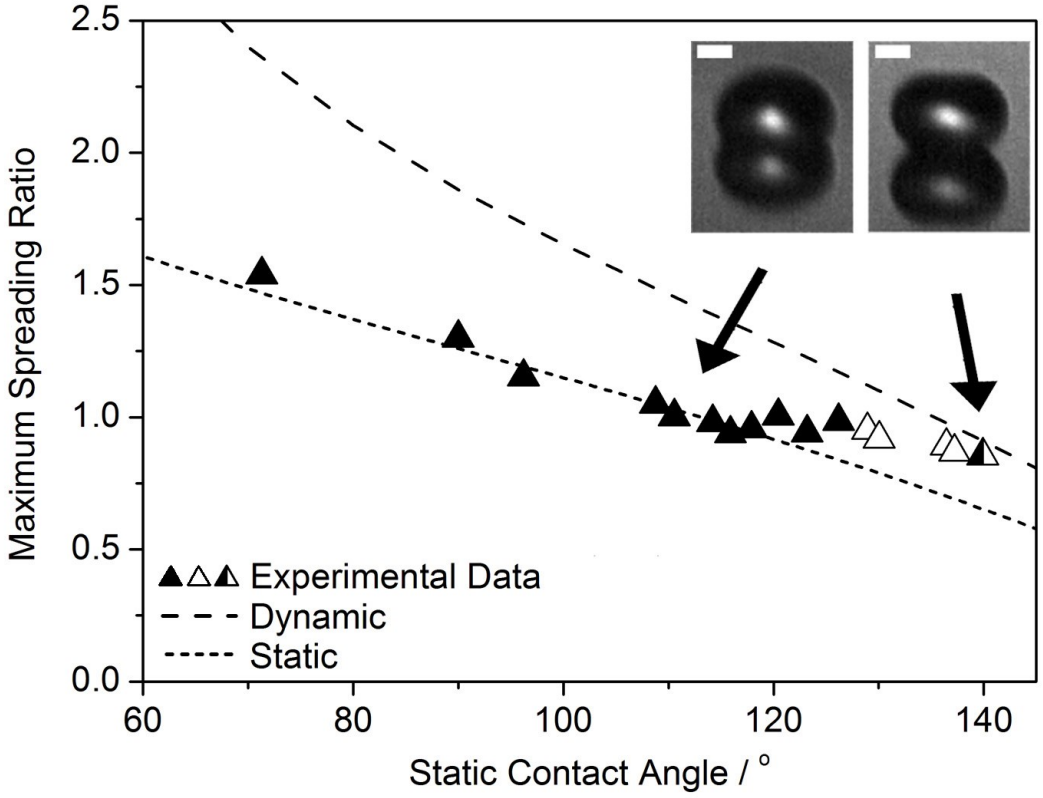

Figure 3.6: Maximum spreading ratios (D_{max}/D_0) as a function of static contact angle for picolitre sized water droplets. Experimental data is compared with the two limiting cases of maximum dynamic spreading (Equation 3.4) and static contact angle (Equation 3.5). Closed symbols denote microscale features, open symbols denote nanoscale features, and half closed symbols denote microscale+nanoscale features. Inset: Images of droplets during maximum spreading on microscale features. White scale bar = 10 μm. Error values: Spreading Ratio = ± 0.05; Static Contact Angle = ± 5°.

The oscillation of the contact diameter for picolitre droplets after impact was fitted to the damped oscillation equation: [49]

$$y = a_0 + a_1 e^{-a_2 t} \cos(a_3 t + a_4), \qquad (3.6)$$

where a_0–a_4 are fitting parameters, t is time, and y is droplet height, width, or contact area diameter. The first oscillation of the droplet was discarded because it is influenced by internal flows arising from the droplet impact.[22] Beyond the first oscillation, a good fit to Equation 3.6 was obtained, Figure 3.7.

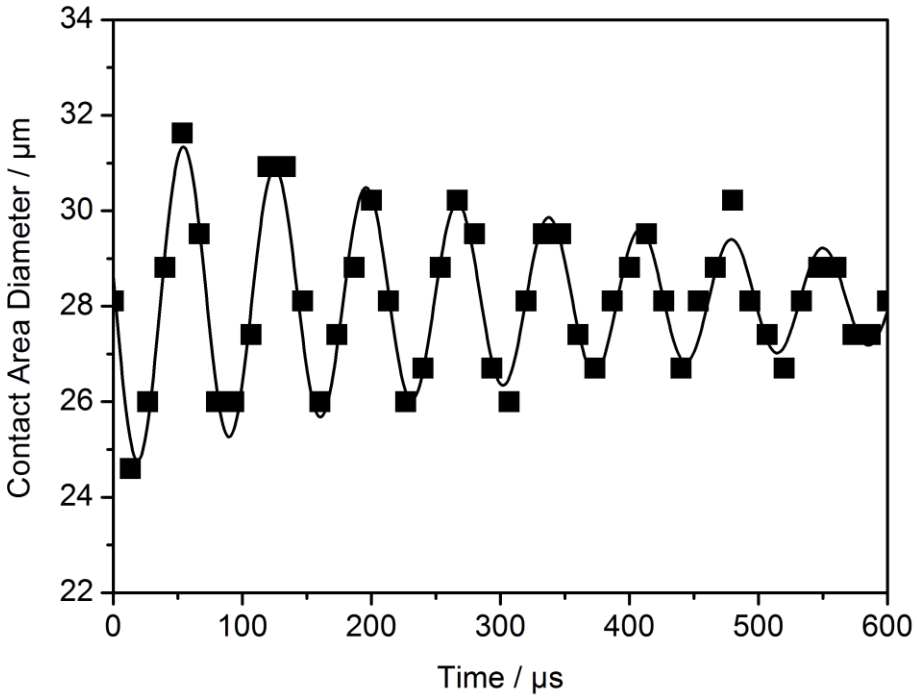

Figure 3.7: Typical damped oscillating curve (Equation 3.6) fitted to the experimental data for picolitre water droplet fluctuation following impact.

Figure 3.8 plots the oscillation frequency and half-life ($\ln(2/a_2)$) as a function of static contact angle of picolitre droplets. The higher the static water contact angles, the lower the frequency of oscillation and the longer the half-life.

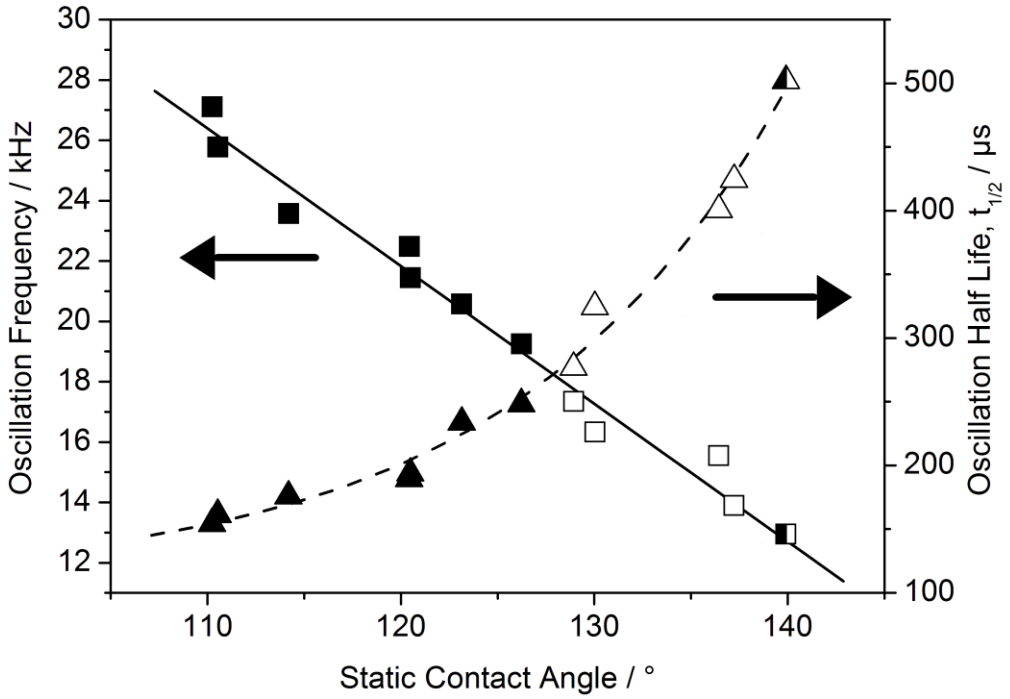

Figure 3.8: Frequency and half-life of the oscillation in height, contact area and diameter of picolitre sized water droplets following surface impact as a function of measured static contact angle. The lines are guides to the eye. Closed symbols denote microscale features, open symbols denote nanoscale features, and half closed symbols denote microscale+nanoscale features. Error values: Oscillation Frequency = ± 0.5 kHz; Oscillation Half Life = ± 20 µs; Static Contact Angle = ± 5°.

The static spreading ratio (D_s/D_0) is found to decrease with increasing surface roughness, Figure 3.9. However, two distinct regimes are evident which correspond to the two different types of surface roughness features (micro or nano), Figure 3.2. Where the two regimes meet corresponds to droplet impact on a surface featuring both roughness length scales (micro and nano).

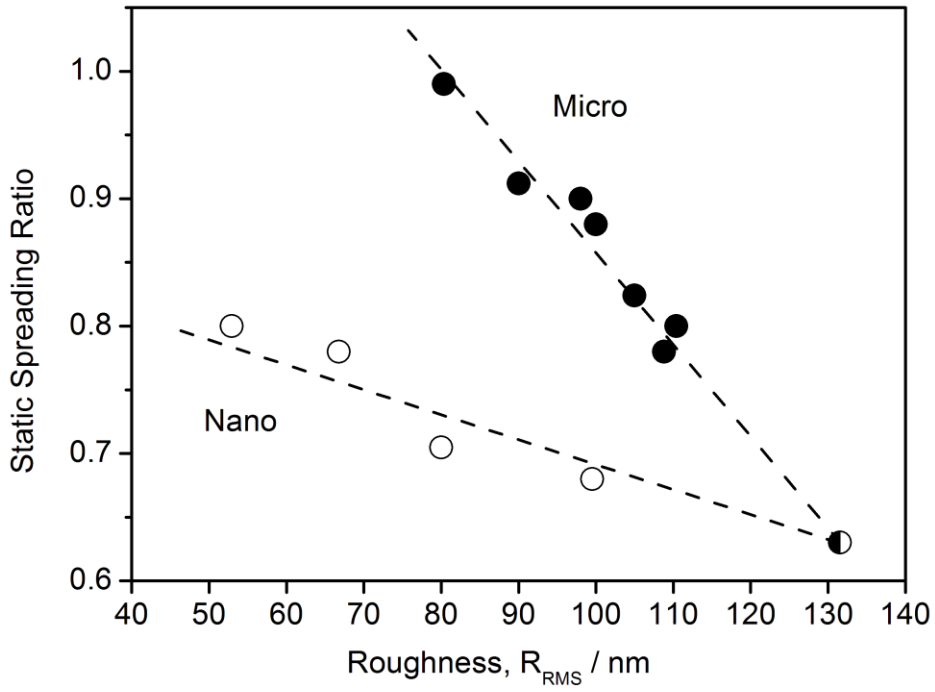

Figure 3.9: Static spreading ratio (D_s/D_0) of picolitre sized water droplets as a function of RMS surface roughness. The lines are guides to the eye. Closed symbols denote microscale features, open symbols denote nanoscale features, and half closed symbols denote microscale+nanoscale features. Highlighted data points denote composite surface. Error values: Static Spreading Ratio = ± 0.05; Roughness, R_{RMS} = ± 5nm.

3.4 Discussion

Plasmachemical fluorination of polybutadiene yields superhydrophobic surfaces[41,42] as predicted by previously derived structure-behaviour relationships.[50] The high level of sp^2 carbon centres leads to a large F:C ratio as a consequence of atomic fluorine addition to carbon-carbon double bonds being the major reaction pathway as well as straightforward hydrogen substitution.[50] Concurrently there is phase induced surface roughening. The differences in the resulting roughness morphology at varying plasma power and treatment time are attributed to the various competing etching regimes outlined in Section 2.2.1 (page 38), including ion bombardment,[51] vacuum ultraviolet (VUV) irradiation,[52] and chemical attack by fluorine atoms. Large undulating features give way to finer scale roughness features at higher plasma powers and through variation of the plasma parameters it is possible to achieve a hierarchical surface with both length scales of roughness combined.

Static contact angle measurements show that a surface roughness of R_{RMS} = 60 nm is sufficient to promote a hydrophobic state for microlitre size water droplets, Figure 3.3. For a truly superhydrophobic state, a small contact angle hysteresis is usually required (2° or less);[53,54,55] this is achieved for microlitre size droplets on plasma fluorinated substrates with a surface roughness value of a least R_{RMS} = 120 nm, Figure 3.3.

Experiments were conducted at low Weber and Ohnesorge numbers where the spreading model of Attané, based on conservation of surface free energy, might be expected to hold. For final (static) contact angles $\theta \leq 110°$, the maximum spreading ratio for picolitre drops coincides with the static ratio: in other words, the contact line does not retract. The maximum spreading ratio is much less than that predicted by the Attané model. There are two plausible explanations for this discrepancy, both of which may act simultaneously. First, the excess surface free energy is dissipated in the motion of the contact line across the surface. Evidence to support this explanation is that these droplets do not show observable oscillations from the excess energy of the droplet. Second, it is not appropriate to use the static contact angle in place of the equilibrium contact angle in Equation 3.3. If a surface exhibits large contact angle hysteresis then, provided that the contact angle at maximum spreading is greater than the receding angle, the contact line will not retract. The equilibrium contact angle on surfaces with hysteresis lies between the maximum advancing and minimum receding contact angles. Evidence to support this view is that static contact angles of 60–100° reported in Figure 3.6 are low for water on flat fluorinated surfaces. If $\theta_{eq} > \theta$, the discrepancy between the theoretical prediction and the experimental data is reduced.

For static contact angles $\theta \geq 110°$, the maximum spreading ratio is larger than the static one (the contact line recedes) and oscillations are observed in the shape of the droplet demonstrating that spreading does not dissipate all the excess surface energy. The experimental maximum spreading ratios tend towards the Attané prediction as the static contact angle increases. However, we note that the assumption of a spherical cap does not hold for drops with static contact angles greater than 120° (see Figure 3.6, inset). Instead, the droplet flattens to minimise unfavourable spreading, thus reducing the maximum spreading ratio measured.

As noted above, impacting droplets with static contact angles > 110° undergo damped oscillations after spreading. There are very few models or experimental data in the literature on the oscillations of sessile droplets that cover a range of contact angles as wide as explored here. Strani and Sabetta[56,57] derived an analytical model for the free oscillations of spherical droplets sitting in a solid, spherical cup with a pinned contact line. These models are close to our experimental situation with the exception that the solid is flat, not cupped. The Strani and Sabetta model predicts lower oscillation frequencies for higher contact angles, in agreements with our experimental data. However, theoretical results overestimate the experimental oscillation frequencies by a factor of approximately two. This disparity is most likely due to contact line motion. In the model, the contact line is pinned whereas, in the experimental data, the droplet dynamics include a moving contact line. It is also possible that the rough surfaces inhibit contact line motion,[58] meaning the droplet oscillates at a lower frequency than that expected.

A useful way to describe the deposition of a droplet onto a surface is to use a spreading ratio, which is calculated by dividing the diameter of the contact area by the diameter of the droplet during free flight. For inkjet applications, a small spreading ratio is highly desirable because it minimises the spread of the droplet across the surface leading to high definition printing. Previous studies of substrate wettability in regimes relevant for inkjet printing have reported equilibrium spreading ratios of 1.0 or higher.[23,59] The dotted line in Figure 3.6 shows that for contact angles > 110°, the spreading ratio is less than unity. The minimum value of the spreading ratio that was achieved in this study was 0.63 (Figure 3.9), which is believed to be the smallest spreading ratio reported for picolitre droplets. This spreading ratio was achieved on a composite surface with roughness on two length scales, which is believed to be important for superhydrophobicity.[60] It is envisaged that such smaller contact areas could be utilised to improve the resolution of inkjet printing techniques, without the need to modify the base ink. The limitation of the current surfaces is that picolitre droplets with impact velocities typical of commercial inkjet printers tend to bounce.

By plotting static spreading ratio as a function of surface roughness, Figure 3.9, it is clear that two distinct regimes of roughness (micro or nano)

exist with their corresponding different droplet impact behaviours, Figure 3.2. For microlitre drops, this regime change has no effect on the droplet behaviour observed since the droplet is several orders of magnitude larger than the roughness features. However, in the case of picolitre droplets, the contact area diameter is only an order of magnitude larger than the asperities, making picolitre droplet behaviour more dependent upon the surface topography. These spreading characteristics are influenced by the precise nature of the surface roughness.

3.5 Conclusions

The impact and spreading of picolitre droplets of water onto superhydrophobic CF_4 plasma fluorinated polybutadiene surfaces is strongly influenced by the length-scale of surface topography (for similar roughness values). Large differences are observed between the behaviour of microlitre and picolitre drops, implying that measurements made with conventional contact angle instruments are unlikely to be good predictors of inkjet behaviour. Impacting droplet oscillation frequency is found to decrease with increasing static contact angle providing a good qualitative agreement, albeit a poor quantitative one, with available models. A static spreading ratio of 0.63 has been measured which is lower than previously reported values.

3.6 References

[1] Worthington, A. M. On the Forms Assumed by Drops of Liquids Falling Vertically on a Horizontal Plate. *Proc. R. Soc. Lond.* **1876**, *25*, 261.

[2] Yao, S. C.; Choi, K. J. Heat transfer experiments of mono-dispersed vertically impacting sprays. *Int. J. Multiphase Flow* **1987**, *13*, 639.

[3] Pasandideh-Fard, M.; Aziz, S. D.; Chandra, S.; Mostaghimi, J. Cooling effectiveness of a water drop impinging on a hot surface. *Int.J. Heat and Fluid Flow* **2001**, *22*, 201.

[4] Chen, R.-H.; Chow, L. C.; Navedo, J. E. Effects of spray characteristics on critical heat flux in subcooled water spray cooling. *Int. J. Heat Mass Tran.* **2002**, *45*, 4033.

[5] Tourkine, P.; Le Merrer, M.; Quéré, D. Delayed Freezing on Water Repellent Materials. *Langmuir* **2009**, *25*, 7214.

[6] Kulinich, S. A.; Farzaneh, M. How Wetting Hysteresis Influences Ice Adhesion Strength on Superhydrophobic Surfaces. *Langmuir* **2009**, *25*, 8854.

[7] Cao, L.; Jones, A. K.; Sikka, V. K.; Wu, J.; Gao, D. Anti-Icing Superhydrophobic Coatings. *Langmuir* **2009**, *25*, 12444.

[8] Mishchenko, L.; Hatton, B.; Bahadur, V.; Taylor, J. A.; Krupenkin, T.; Aizenberg, J. Design of Ice-free Nanostructured Surfaces Based on Repulsion of Impacting Water Droplets. *ACS Nano* **2010**, *4*, 7699.

[9] Reichard, D. L. Drop formation and impaction on the plant. *Weed Technol.* **1988**, *2*, 82.

[10] Sirringhaus, H.; Kawase, T.; Friend, R. H.; Shimoda, T.; Inbasekaran, M.; Wu, W.; Woo, E. P. High-Resolution Inkjet Printing of All-Polymer Transistor Circuits. *Science* **2000**, *290*, 2123.

[11] Wang, J. Z.; Zheng, Z. H.; Li, H. W.; Huck, W. T. S.; Sirringhaus, H. Dewetting of conducting polymer inkjet droplets on patterned surfaces. *Nat. Mater.* **2004**, *3*, 171.

[12] Sele, C. W.; von Werne, T.; Friend, R. H.; Sirringhaus, H. Lithography-Free, Self-Aligned Inkjet Printing with Sub-Hundred-Nanometer Resolution. *Adv. Mater.* **2005**, *17*, 997.

[13] Doggart, J.; Wu, Y.; Liu, P.; Zhu, S. Facile Inkjet-Printing Self-Aligned Electrodes for Organic Thin-Film Transistor Arrays with Small and Uniform Channel Length. *ACS Appl. Mater. Interfaces* **2010**, *2*, 2189.

[14] Barbulovic-Nad, I.; Lucente, M.; Sun, Y.; Zhang, M.; Wheeler, A. R.; Bussmann, M. Bio-Microarray Fabrication Techniques—A Review. *Crit. Rev. Biotechnol.* **2006**, *26*, 237.

[15] Tan, C. P.; Cipriany, R.; Lin, D. M.; Craighead, H. G. Nanoscale Resolution, Multicomponent Biomolecular Arrays Generated By Aligned Printing With Parylene Peel-Off. *Nano Lett.* **2010**, *10*, 719.

[16] Arrabito, G.; Pignataro, B. Inkjet Printing Methodologies for Drug Screening. *Anal. Chem.* **2010**, *82*, 3104.

[17] Mironov, V.; Boland, T.; Trusk, T.; Forgacs, G.; Markwald, R. R. Organ printing: computer-aided jet-based 3D tissue engineering. *Trends Biotechnol.* **2003**, *21*, 157.

[18] Xu, T.; Jin, J.; Gregory, C.; Hickman, J. J.; Boland, T. Inkjet printing of viable mammalian cells. *Biomaterials* **2005**, *26*, 93.
[19] Bharathan, J.; Yang, Y. Polymer electroluminescent devices processed by inkjet printing: I. Polymer light-emitting logo. *Appl. Phys. Lett.* **1998**, *72*, 2660.
[20] Chang, S.-C.; Bharathan, J.; Yang, Y.; Helgeson, R.; Wudl, F.; Ramey, M. B.; Reynolds, J. R. Dual-color polymer light-emitting pixels processed by hybrid inkjet printing. *Appl. Phys. Lett.* **1998**, *73*, 2561.
[21] Mao, T.; Kuhn, D. C. S.; Tran, H. Spread and rebound of liquid droplets upon impact on flat surfaces. *AIChE J.* **1997**, *43*, 2169.
[22] Rioboo, R.; Marengo, M.; Tropea, C. Time evolution of liquid drop impact onto solid, dry surfaces. *Exp. Fluids* **2002**, *33*, 112.
[23] Dong, H.; Carr, W. W.; Bucknall, D. G.; Morris, J. F. Temporally-resolved inkjet drop impaction on surfaces *AIChE J.* **2007,** *53*, 2606.
[24] Šikalo, Š.; Marengo, M.; Tropea, C.; Ganić, E. N. Analysis of impact of droplets on horizontal surfaces. *Exp. Therm. Fluid Sci.* **2002**, *25*, 503.
[25] Wang, M.-J.; Lin, F.-H.; Hung, Y.-L.; Lin, S.-Y. Dynamic Behaviors of Droplet Impact and Spreading: Water on Five Different Substrates. *Langmuir* **2009**, *25*, 6772.
[26] Ukiwe, C.; Mansouri, A.; Kwok, D. Y. The dynamics of impacting water droplets on alkanethiol self-assembled monolayers with co-adsorbed CH3 and CO2H terminal groups. *J. Coll. Int. Sci.* **2005**, *285*, 760.
[27] Son, Y.; Kim, C.; Yang, D. H.; Ahn, D. J. Spreading of an Inkjet Droplet on a Solid Surface with a Controlled Contact Angle at Low Weber and Reynolds Numbers. *Langmuir* **2008**, *24*, 2900.
[28] Son, Y.; Kim, C. Spreading of inkjet droplet of non-Newtonian fluid on solid surface with controlled contact angle at low Weber and Reynolds numbers. *J. Non-Newtonian Fluid Mech.* **2009**, *162*, 78.
[29] Wenzel, R, N. Resistance of Solid Surfaces to Wetting by Water. *Ind. Eng. Chem.* **1936**, *28*, 988.
[30] Cassie, A. B. D.; Baxter, S. Wettability of porous surfaces. *Trans. Faraday Soc.* **1944**, *40*, 546.
[31] Jung, Y. C.; Bhushan, B. Dynamic Effects of Bouncing Water Droplets on Superhydrophobic Surfaces. *Langmuir* **2008**, *24*, 6262.
[32] Brunet, P.; Lapierre, F.; Thomy, V.; Coffinier, Y.; Boukherroub, R. Extreme Resistance of Superhydrophobic Surfaces to Impalement: Reversible Electrowetting Related to the Impacting/Bouncing Drop Test. *Langmuir* **2008**, *24*, 11203.
[33] Tsai, P.; Pacheco, S.; Pirat, C.; Lefferts, L.; Lohse, D. Drop Impact upon Micro- and Nanostructured Superhydrophobic Surfaces. *Langmuir* **2009**, *25*, 12293.
[34] Rioboo, R.; Marengo, M.; Tropea, C. Outcomes from a drop impact on solid surfaces. *Atomization Sprays* **2001**, *11*, 155.
[35] Deng, T.; Varanasi, K. K.; Hsu, M.; Bhate, N.; Keimel, C.; Stein, J.; Blohm, M. Nonwetting of impinging droplets on textured surfaces. *Appl. Phys. Lett.* **2009**, *94*, 133109.
[36] Lembach, A. N.; Tan, H.-B.; Roisman, I. V.; Gambaryan-Roisman, T.; Zhang, Y.; Tropea, C.; Yarin, A. L. Drop Impact, Spreading, Splashing,

and Penetration into Electrospun Nanofiber Mats. *Langmuir* **2010**, *26*, 9516.
[37] Tsai, P.; van der Veen, R. C. A.; van de Raa, M.; Lohse, D. How Micropatterns and Air Pressure Affect Splashing on Surfaces. *Langmuir* **2010**, *26*, 16090.
[38] Rioboo, R.; Voué, M.; Vaillant, A.; De Coninck, J. Drop Impact on Porous Superhydrophobic Polymer Surfaces. *Langmuir* **2008**, *24*, 14074.
[39] Jung, Y. C.; Bhushan, B. Dynamic Effects Induced Transition of Droplets on Biomimetic Superhydrophobic Surfaces. *Langmuir* **2009**, *25*, 9208.
[40] Apel-Paz, M.; Marmur, A. Spreading of liquids on rough surfaces. *Colloid Surface A* **1999**, *146*, 273.
[41] Woodward, I.; Schofield, W. C. E.; Roucoules, V.; Badyal, J. P. S. Super-hydrophobic Surfaces Produced by Plasma Fluorination of Polybutadiene Films. *Langmuir* **2003**, *19*, 3432.
[42] Woodward, I. S.; Schofield, W. C. E.; Roucoules, V.; Badyal, J. P. S. Micropatterning of Plasma Fluorinated Super-hydrophobic Surfaces. *Plasma Chem. Plasma Process.* **2006**, *26*, 507.
[43] Evans, J. F.; Gibson, J. H.; Moulder, J. F.; Hammond, J. S.; Goretzki, H. Angle resolved ESCA analysis of plasma modified polystyrene. *Fresenius J. Anal. Chem*. **1984**, *841*, 319.
[44] Johnson, R. E. Jr.; Dettre, R. H. Wetting of Low-Energy Surfaces. In Wettability; Berg J. C., Ed.; Marcel Dekker, Inc.: New York, 1993; Chapter 1, p 13.
[45] Bridgman, P. W. *Dimensional Analysis*; Yale University Press: New Haven, 1931.
[46] Schiaffino, S.; Sonin, A. A. Molten droplet deposition and solidification at low Weber numbers. *Phys. Fluids* **1997**, *9*, 3172.
[47] Pasandideh-Fard, M.; Qiao, Y. M.; Chandra, S.; Mostaghimi, J. Capillary effects during droplet impact on a solid surface. *Phys. Fluids* **1996**, *8*, 650.
[48] Attané, P.; Girard, F.; Morin, V. An energy balance approach of the dynamics of drop impact on a solid surface. *Phys. Fluids* **2007**, *19*, 012101.
[49] van Dam, D. B.; Le Clerc, C. Experimental study of the impact of an ink-jet printed droplet on a solid substrate. *Phys. Fluids* **2004**, *16*, 3403.
[50] Hopkins, J.; Badyal, J. P. S. Nonequilibrium Glow Discharge Fluorination of Polymer Surfaces. *J. Phys. Chem.* **1995**, *99*, 4261.
[51] Yasuda, H., *Plasma Polymerization*. 1985, New York: Academic Press.
[52] Egitto, F. D. Plasma etching and modification of organic polymers. *Pure Appl. Chem*. **1990**, *62*, 1699.
[53] Murase, H.; Fujibayashi, T. Characterization of molecular interfaces in hydrophobic systems. *Prog. Org. Coat.* **1997**, *31*, 97.
[54] Miwa, M.; Nakajima, A.; Fujishima, A.; Hashimoto, K.; Watanabe, T. Effects of the Surface Roughness on Sliding Angles of Water Droplets on Superhydrophobic Surfaces. *Langmuir* **2000**, *16*, 5754.
[55] Öner, D.; McCarthy, T. J. Ultrahydrophobic Surfaces. Effects of Topography Length Scales on Wettability. *Langmuir* **2000**, *16*, 7777.

[56] Strani, M.; Sabetta, F. Free vibrations of a drop in partial contact with a solid support. *J. Fluid Mech.* **1984**, *141*, 233.
[57] Strani, M.; Sabetta, F. Viscous oscillations of a supported drop in an immiscible fluid. *J Fluid Mech.* **1988**, *189*, 397.
[58] Fetzer, R.; Ralston, J. J. Influence of Nanoroughness on Contact Line Motion. *Phys. Chem. C* **2010**, *114*, 12675.
[59] Kannangara, D.; Shen, W. Roughness effects of cellulose and paper substrates on water drop impact and recoil. *Colloids Surf., A* **2008**, *330*, 151.
[60] Gao, L.; McCarthy, T. J. The “Lotus Effect” Explained: Two Reasons Why Two Length Scales of Topography Are Important. *Langmuir* **2006**, *22*, 2966.

Chapter 4 Superhydrophobic Hierarchical Honeycombs

4.1 Introduction

In the previous chapter, the effect of plasma-induced roughening of a polymer surface on the impact of picolitre droplets was carried out using flat, spin-coated polybutadiene as the starting substrate. An additional level of surface topography can be added to such surfaces by utilising a different solvent casting technique. One such example is to utilise breath figures[1,2] (which are two-dimensional hexagonally packed arrays of water droplets condensed onto a cooled surface) as a means for templating polymer film surfaces.[3] This entails dissolving a polymer into a water immiscible, volatile solvent, and then film casting onto a surface under a controlled humid environment. Subsequent solvent evaporation gives rise to cooling of the solution surface, which culminates in water condensation[4,5] and the formation of a breath figure array of hexagonally ordered water droplets,[6] Scheme 4.1. The coalescence of these water droplets is avoided either by the occurrence of Marangoni convection or due to the precipitation of a polymer layer at the water-solvent interface.[7] Effectively, the water droplets serve as a template for the drying polymer solution leading to the formation of a honeycomb-like surface structure following complete evaporation of the solvent and water. Well-defined surface pore arrays are of significant interest for numerous applications including proteomics,[8] tissue engineering,[9] photonics,[10,11] sensors,[12,13] and catalysis.[14]

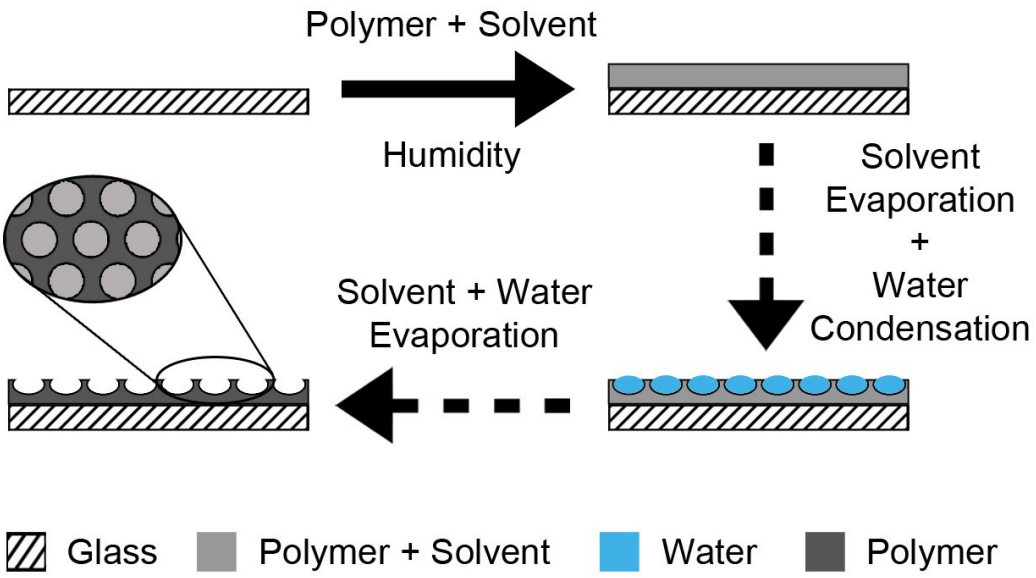

Scheme 4.1: Casting of a polymer dissolved in a water immiscible solvent under controlled humidity. Solvent evaporation leads to surface cooling and water condensation to form a hexagonal breath figure array, which acts as a template for the drying polymer solution.

In the past, such honeycomb surfaces have predominantly been prepared using block copolymers[15] or branched polymers[16] because of their ability to more readily precipitate out at the solvent / water interface, and thereby negating undesired water droplet coalescence.[17,18,19,20] A few linear homopolymers with high chain densities such as polyphenylene oxide[21] and polystyrene[22,23,24,25] have also been shown to form stable breath figure arrays.

However, the aforementioned polymer honeycomb systems typically have limited surface functionality as well as needing a separate cross-linking step (otherwise the honeycomb structure can be unstable towards ageing, aggressive solvents, or elevated temperatures). In the past, this has been addressed by chemical-,[26,27,28,29] thermal-,[30] or photo-cross-linking,[31,32,33,34] which typically entail complex or harsh processing conditions (e.g. intense irradiation or toxic chemicals).

In this chapter, a much simpler and more straightforward approach is described comprising the solvent casting of a readily available and cheap polymer, polybutadiene, under controlled humidity. The resultant hexagonal honeycomb arrays are then simultaneously functionalised (fluorinated),

textured, and cross-linked via CF_4 plasma treatment to yield superhydrophobic surfaces (for microlitre and picolitre droplets) that are both chemically and thermally stable.

4.2 Experimental

4.2.1 Sample Preparation

Control sample preparation comprised spin coating polybutadiene (Sigma-Aldrich Inc., M_w = 420,000, 36% cis 1,4 addition, 55% trans 1,4 addition, 9% 1,2 addition) as described in Section 3.2.1 (page 52).

For the honeycomb surfaces, polybutadiene dissolved at varying concentrations in dichloromethane (Fisher Scientific, +99.9% purity) was cast onto clean glass slides (Smith Scientific Ltd.) under controlled humidity conditions. This entailed placing the glass substrate onto a wire mesh so that is was suspended above a saturated salt solution contained within a 25mL glass bottle fitted with a rubber septum. The salt solutions used were magnesium chloride (Sigma-Aldrich Inc., +98%), potassium carbonate (Sigma-Aldrich Inc., +99%), magnesium nitrate (Sigma-Aldrich Inc., +99%), sodium bromide (Sigma-Aldrich Inc., +99.5%), strontium chloride (Sigma-Aldrich Inc., +99%), sodium chloride (Sigma-Aldrich Inc., +99.5%), and potassium chloride (Sigma-Aldrich Inc., +99.5%) which gave relative humidities of 33%, 43%, 54%, 59%, 73%, 76%, and 85% respectively.[35] For each film, 0.1 mL of polymer solution was deposited onto the glass slide using a microsyringe. Subsequently, these polymer films were annealed at 90 °C under vacuum for 60 min.

Plasmachemical fluorination, texturing, and cross-linking of the polybutadiene films was undertaken in a cylindrical glass reactor of similar design to that used in Section 3.2.1 (page 52). A piece of polybutadiene coated substrate was placed into the reactor (either in the glow region for textured surfaces or 8 cm downstream for smooth surfaces), followed by evacuation to base pressure. CF_4 gas (+99.7% purity, Air Products) was then admitted into the system via a needle valve at a pressure of 0.2 mbar and 2 cm^3 min^{-1} flow rate, and the electrical discharge ignited at a power of 30 W for 5 min duration for textured surfaces or 60 s for smooth surfaces. Upon completion of surface functionalization (and texturing), the gas feed was switched off and the chamber vented to atmosphere.

4.2.2 Surface Characterisation

The obtained honeycomb surfaces were visually examined using an optical microscope (Olympus BX40) fitted with a digital camera and a Euromax fibre optic light source. Pore size distribution, surface coverage, and lattice parameters were measured using image analysis software (ImageJ, public domain, http://rsbweb.nih.gov/ij/). Errors were calculated by analysing numerous images of each surface type.

Surface elemental compositions were determined by X-ray photoelectron spectroscopy (XPS) using a VG ESCALAB II electron spectrometer as described in Section 3.2.2 (page 52). Elemental compositions were calculated using sensitivity factors derived from chemical standards, C(1s): O(1s): F(1s) equals 1.00: 0.34: 0.26.

Atomic force microscopy (AFM) images were collected in tapping mode at 20 °C in ambient air (Nanoscope III, Digital Instruments Inc.). The stiff silicon cantilever had a spring constant of 42–83 N m^{-1} (Nanoprobe, Digital Instruments Inc.). Root-mean-square (RMS) roughness values were calculated over 50 μm x 50 μm scan areas.

Microlitre sessile drop contact angle analysis was carried out with a video capture system (VCA2500XE, AST Products Inc.) using 1.0 μL dispensation of de-ionised water (BS 3978 grade 1). Advancing and receding angles were measured by respectively increasing and decreasing the droplet size until the contact line was observed to move.[36]

Picolitre drop impact studies were carried out using an imaging rig as described in Section 3.2.3 (page 53). The piezo-type nozzle (MicroFab MJ-ABP-01, Horizon Instruments Ltd.) had an aperture diameter of 50 μm, generating water drops of 50 μm diameter (65 pL).

4.3 Results

4.3.1 Honeycomb Formation

Polybutadiene honeycomb surfaces were created across a range of relative humidities (RH), Figure 4.1. It was found that the average pore diameter increased and pore density decreased with rising humidity, Figure 4.2. As previously reported for other polymer systems, honeycombs did not form at 100% RH[23] or below 40% RH.[37]

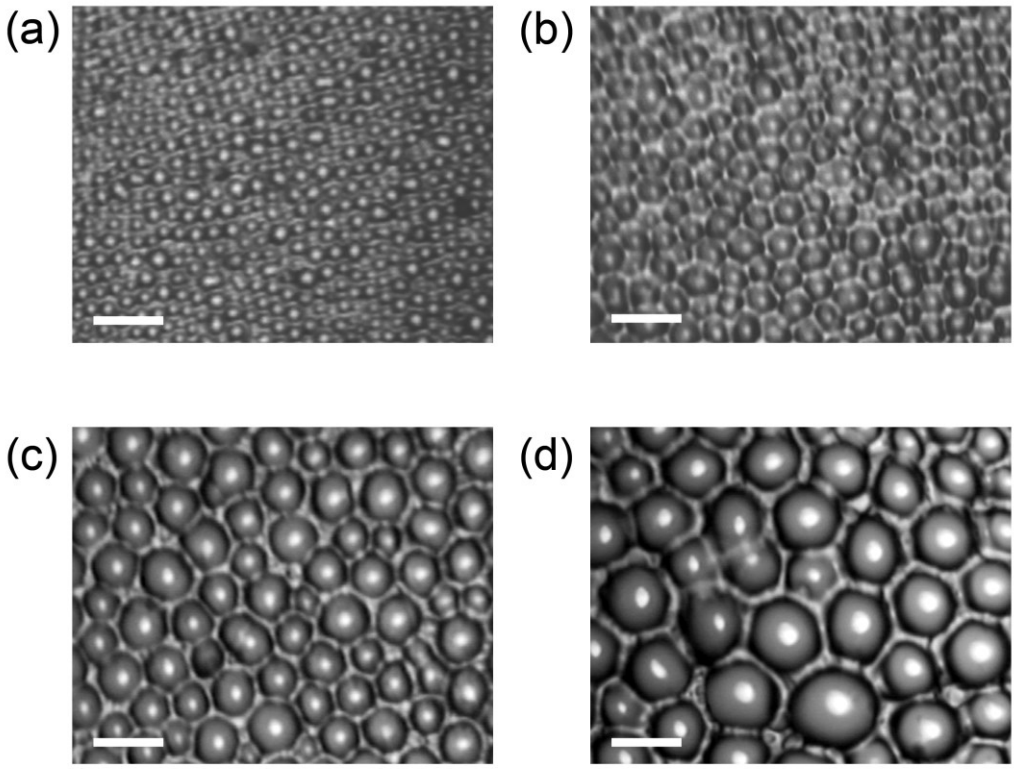

Figure 4.1: Optical microscope images of honeycomb surfaces cast from 1% w/v polybutadiene solution dissolved in dichloromethane under controlled RH of: (a) 43%; (b) 54%; (c) 73%; and (d) 85%. The pores increase in size with rising RH. Scale bar = 50 μm.

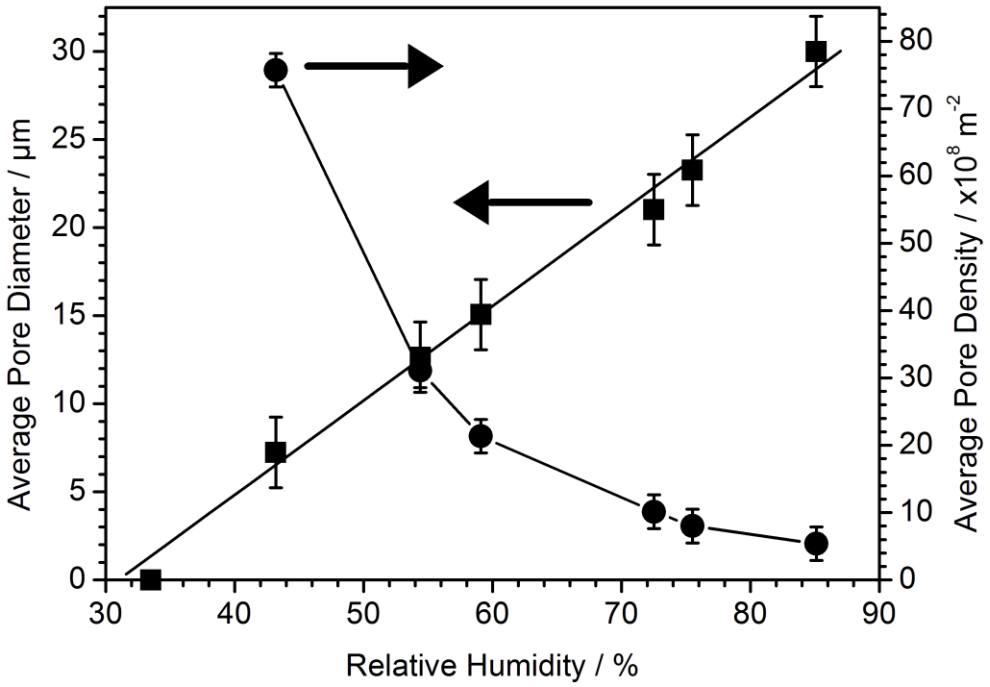

Figure 4.2: Average pore diameter and average pore density in polymer films cast from 1% w/v polybutadiene dissolved in dichloromethane as a function of controlled RH.

The dimensions of the honeycomb arrays could also be varied by changing the concentration of the polybutadiene solution, Figure 4.3. The polymer solution concentration had little effect on the average pore diameter at constant humidity; whilst the flat polymer bridging regions in-between the pores increased in width with rising polymer concentration (albeit still dilute),[38] leading to a concurrent decrease in overall pore surface area and a corresponding drop in average surface pore density, Figure 4.3 and Figure 4.4.

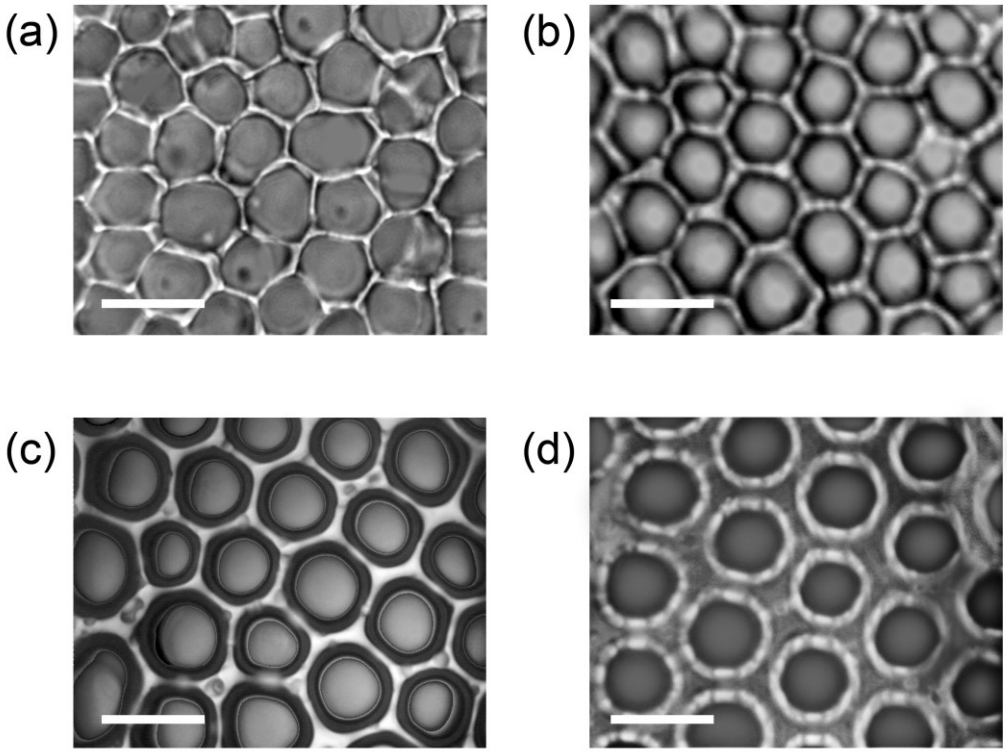

Figure 4.3: Optical microscope images of honeycomb surfaces formed under 54% RH from polybutadiene dissolved in dichloromethane with concentrations of: (a) 0.5% w/v; (b) 1% w/v; (c) 2% w/v; and (d) 3% w/v. The raised plateaus (lighter regions) encircling the pores (darker areas) expand in width with increasing polymer concentration. Scale bar = 25 μm.

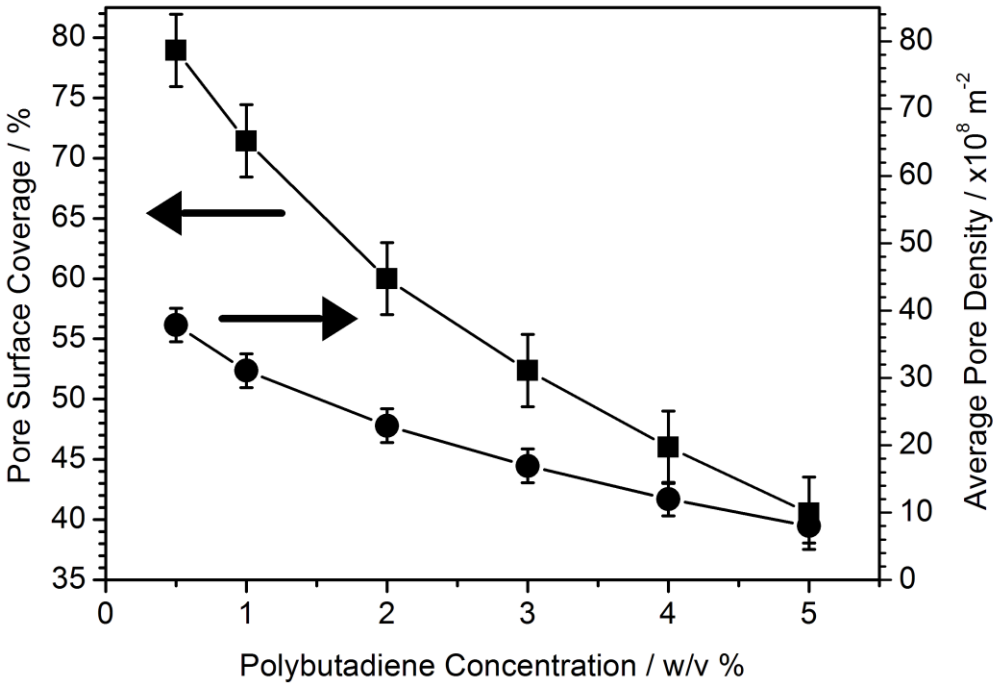

Figure 4.4: Overall surface coverage of honeycomb pores as a function of polybutadiene concentration (dissolved in dichloromethane). Samples were prepared under 54% RH. Average pore size across the polymer concentrations shown remains constant within the range of 12–14 μm.

The breath figure templating process produces an approximate hexagonally ordered two-dimensional array of surface pores. The lattice parameter of these hexagonal arrays increased with both RH and concentration, Figure 4.5.

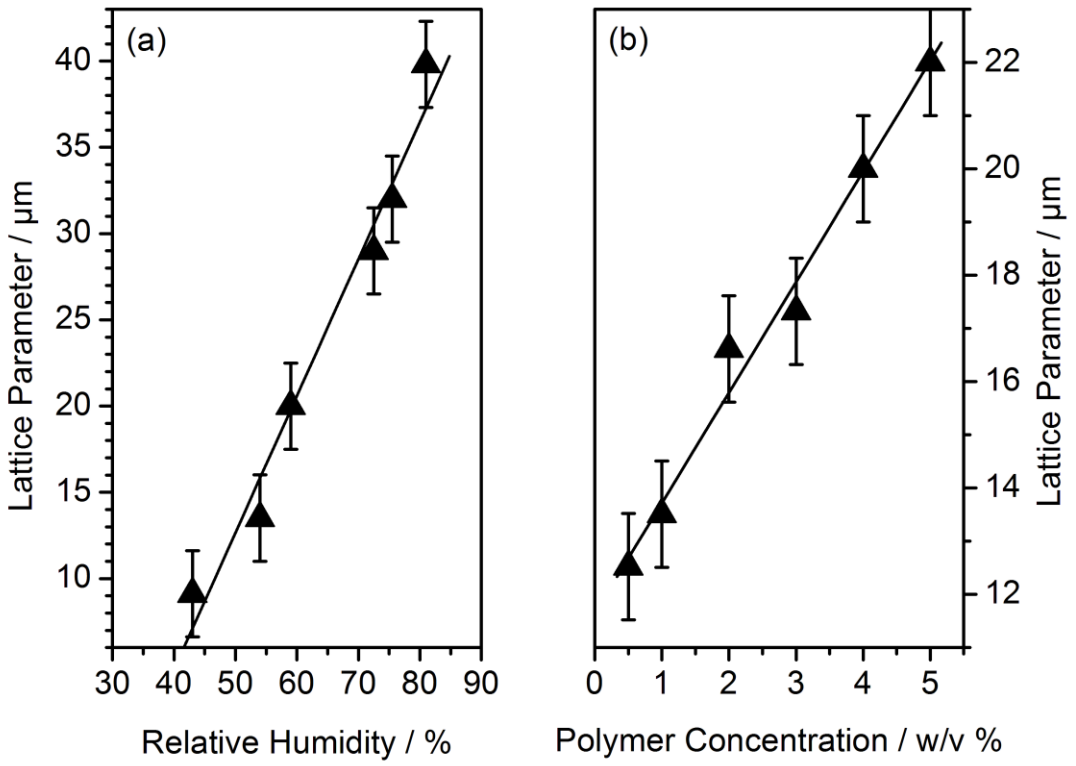

Figure 4.5: Lattice parameter of hexagonally ordered two-dimensional honeycomb array as a function of: (a) RH (1% w/v polybutadiene concentration); and (b) polybutadiene concentration (54% RH).

4.3.2 Plasmachemical Fluorination and Surface Texturing

XPS analysis of the polybutadiene honeycomb surfaces confirmed complete coverage of the glass slides with no Si(2p) signal detected from the underlying substrate, Table 4.1. The measured oxygen signal can be attributed to aerobic oxidation localised at the outer surface of the polymer film during annealing,[39] which disappears upon subsequent CF_4 plasma fluorination.[40]

Table 4.1: XPS elemental compositions for polybutadiene honeycomb surfaces: (a) untreated; (b) CF_4 plasma smooth (30 W, 60 s, downstream); and (c) CF_4 plasma textured (30 W, 5 min, glow).

XPS Elemental Composition / ± 0.5 %				
Honeycomb Polybutadiene		**% C**	**% F**	**% O**
(a) Untreated	Theoretical	100.0	0.0	0.0
	Experimental	87.8	0.0	12.2
(b) CF_4 plasma fluorinated (smooth)	Experimental	40.9	57.1	2.0
(c) CF_4 plasma fluorinated (textured)	Experimental	41.1	58.9	1.6

At room temperature, the as-prepared honeycomb structures gradually disappeared over a period of 48 h due to polymer chain relaxation;[41] whereas a short exposure to the CF_4 plasma was sufficient to lead to VUV-assisted sub-surface cross-linking[39,42,43] so as to stabilise the honeycomb structure, Figure 4.6.

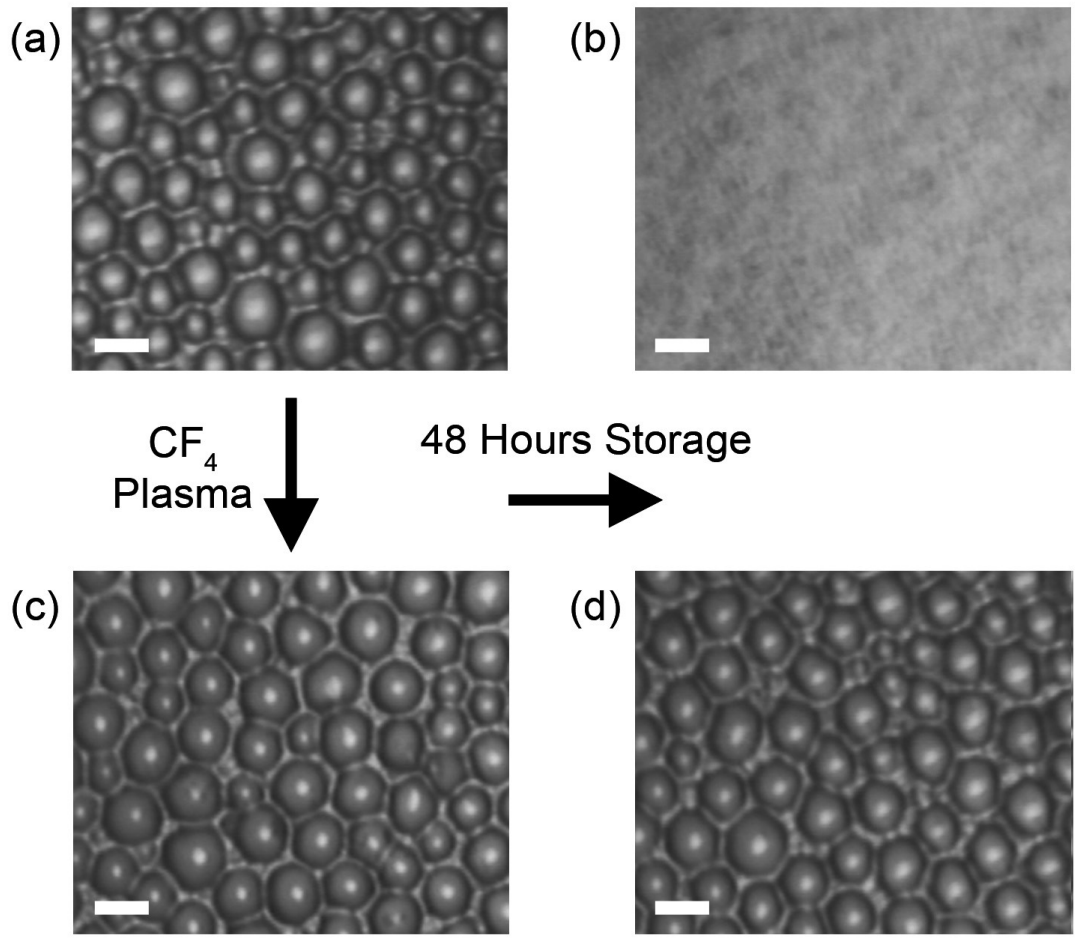

Figure 4.6: Optical microscope images of honeycomb polybutadiene surface: (a) solvent cast; (b) after storage for 48 h; (c) CF_4 plasma treatment of (a) (30 W, 60 s, downstream); and (d) following storage of (c) for 48 h. Scale bar = 50 μm.

Surface texture could be varied by altering the location of the polybutadiene substrate within the CF_4 plasma, Figure 4.7. A rougher surface was observed for the plasma glow region (due to ion bombardment[44,45]) as compared to the downstream region (absence of ion bombardment[44,45]), without any noticeable difference in surface chemistry as verified by XPS analysis, Table 4.1.

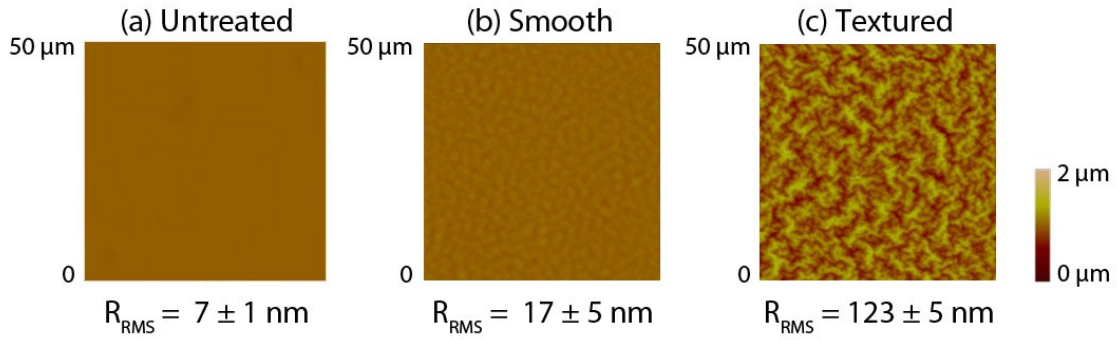

Figure 4.7: AFM height images of flat spin coated polybutadiene: (a) untreated; (b) CF_4 plasma smooth (30 W, 60 s, downstream); and (c) CF_4 plasma textured (30 W, 5 min, glow).

4.3.3 Water Droplet Impact

For sessile drops with microlitre volumes, water contact angles increase approximately linearly with average pore diameter for the solvent cast polybutadiene honeycomb surfaces, Figure 4.8. CF_4 plasma smooth (30 W, 60 s, downstream) honeycomb surfaces displayed enhanced hydrophobicity, with water contact angles rising to 172° for average pore diameters exceeding 20 µm, Figure 4.8. However, there remains significant contact angle hysteresis. Whereas for the case of CF_4 plasma textured (30 W, 5 min, glow) honeycomb surfaces, the very low contact angle hysteresis values are indicative of superhydrophobicity[46] (especially for pore sizes exceeding 12 µm), Table 4.2. This is consistent with CF_4 plasma textured flat polybutadiene surfaces (i.e. in the absence of pores) being sufficient to yield high water contact angle and low contact angle hysteresis values (as seen in Chapter 3).[40] It should be noted that an increase in the pore diameter does lead to a slight decrease in contact angle hysteresis value due to there being a greater amount of air trapped within the larger pores combined with a more irregular contact line.

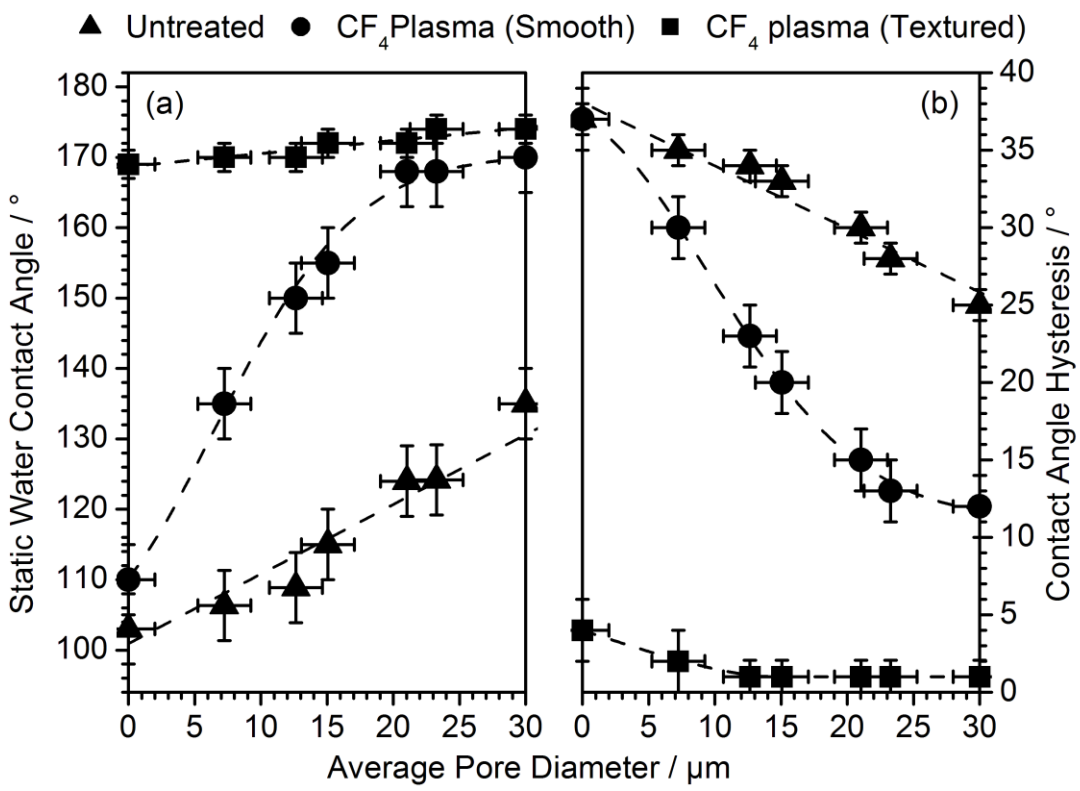

Figure 4.8: Microlitre sessile drop (a) static water contact angle and (b) contact angle hysteresis as a function of average pore diameter for untreated, CF_4 plasma treated smooth (30 W, 60 s, downstream) and CF_4 plasma treated textured (30 W, 5 min) honeycomb surfaces. Polymer films were cast from 1% w/v polybutadiene in dichloromethane (by variation in RH as described in Figure 4.2). Dashed lines are added for guides to the eye.

Table 4.2: Comparison of microlitre and picolitre water droplet behaviour on CF_4 plasma treated spin coated versus honeycomb polybutadiene surfaces (1% w/v concentration in dichloromethane, 54% RH, pore size = 12–14 μm). Where smooth corresponds to (30 W, 60 s, downstream) and textured to (30 W, 5 min, glow).

Polybutadiene	CF_4 Plasma Treatment	Microlitre		Picolitre		
		Static Contact Angle / ± 5°	Contact Angle Hysteresis / ± 1°	Static Contact Angle / ± 5°	Contact Angle Hysteresis / ± 1°	Impact Oscillation Frequency / ± 0.5 kHz
Spin Coated (Flat, Control)	Smooth	110	37	71	44	Spreading
	Textured	>170	4[†]	126[‡]	5	22.8
Honeycomb[§]	Smooth	150	23	126[‡]	28	17.9
	Textured	>170	1	Droplet bouncing		

[†] Lower microlitre contact angle hysteresis values (<1°) can be achieved be employing different CF_4 plasma conditions (30 W, 10 min, glow).[40]
[‡] The CF_4 plasma parameters for textured surfaces were chosen so as to give similar picolitre contact angles to those found for CF_4 plasma treated smooth honeycomb surface.
[§] 12–14 μm pore size was selected because it is sufficiently smaller than the diameter of the picolitre droplets (50 μm).

In the previous chapter, it was shown that the wetting of picolitre drops (the size delivered by modern inkjet printers) on plasma fluorinated surfaces can be quite different from microlitre drops[40] and consequently that the impact and spreading of picolitre drops cannot be extrapolated from studies on the microlitre scale. When a picolitre droplet strikes these (super)hydrophobic surfaces, the liquid first spreads outwards to a maximum diameter and then oscillates about its static position until the excess energy is lost by viscous dissipation. The amplitude and decay of the oscillations can be observed in the height or width of the drop or in the diameter of the contact line,[47] Figure 4.9 and Figure 4.10.

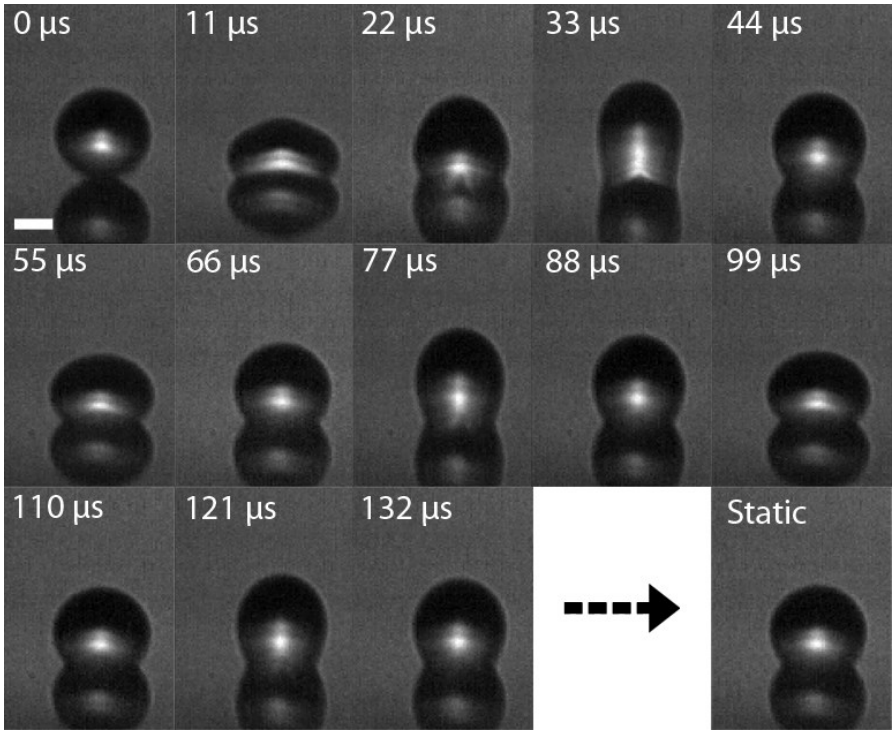

Figure 4.9: Typical high-speed video images of picolitre water droplet impact upon a superhydrophobic CF_4 plasma fluorinated polybutadiene honeycomb surface (showing lower reflection as well). White scale bar = 20 µm.

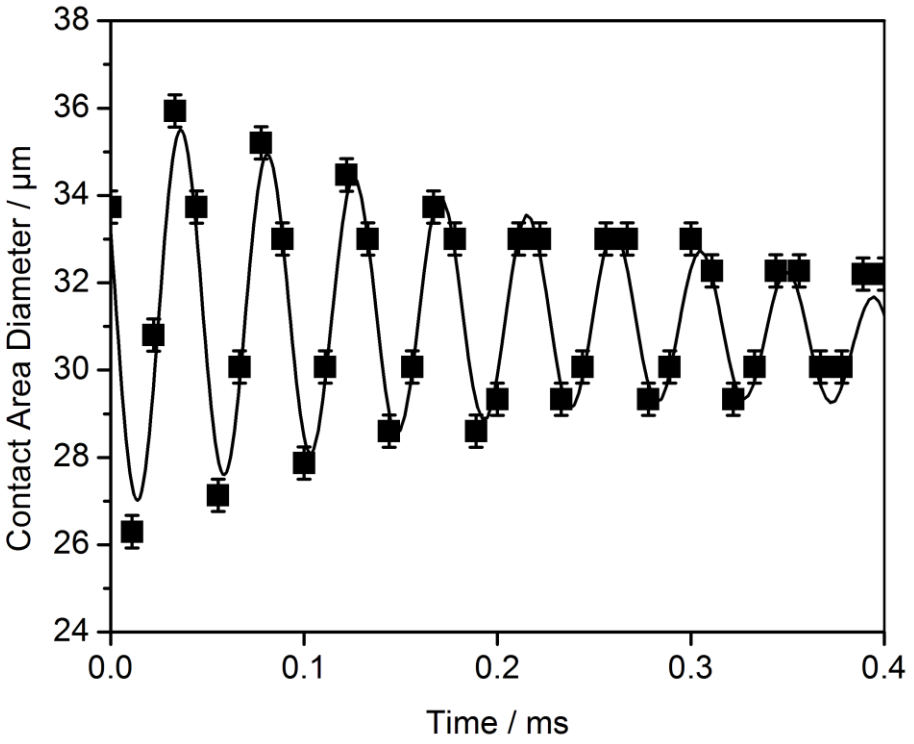

Figure 4.10: Typical damped oscillating curve fitted to the experimental data for picolitre water droplet fluctuation following impact.

This oscillatory motion of picolitre water droplets during impact was compared for the 4 different types of plasma fluorinated polybutadiene surface: smooth, textured, smooth honeycomb, and textured honeycomb, Table 4.2. The pore size of the honeycomb (12–14 µm) was chosen to be comparable to, but smaller than, the diameter of the water droplet (50 µm). The CF_4 plasma parameters for textured surfaces were chosen so as to give similar picolitre contact angles to those found for the smooth honeycomb surface. No oscillation was observed on the CF_4 plasma fluorinated smooth spin coated sample as all the excess surface free energy was dissipated during the initial spreading of the contact line. Water droplets impacting upon the textured spin coated polybutadiene oscillated at a higher frequency compared to those on the smooth honeycomb surfaces despite both surfaces exhibiting similar static picolitre contact angles and the same mode of oscillation (moving contact line), Table 4.2. Picolitre droplets striking the textured honeycomb surfaces bounced straight off in all cases (for 5–30 µm pore size range in present study).

4.4 Discussion

The pore sizes of these polybutadiene honeycomb arrays (up to 30 μm) are significantly larger than those previously reported for breath figure templating (typically 0.2–10 μm).[3] This difference may be attributed to the lower chain density of polybutadiene,[48] which leads to slower solidification around the water droplets and therefore increased droplet coalescence.[7] The polybutadiene solution concentration (and therefore viscosity) had little effect on this precipitation behaviour (average pore diameters remain similar) across the range studied, Figure 4.4. In contrast, earlier studies on other polymer systems showed that higher polymer concentrations stabilized smaller droplet arrays;[7] again, the lower chain density of polybutadiene might be a plausible contributing factor.

A key drawback encountered in prior studies of breath figure templating is the instability of the honeycomb structures in the presence of solvents or at elevated temperatures.[37] Indeed, the honeycomb polybutadiene surfaces formed in the present study are also seen to completely disappear at room temperature in 48 h, Figure 4.6. Stabilisation of these honeycomb surfaces is easily accomplished by CF_4 plasmachemical sub-surface cross-linking whilst concurrently lowering the surface energy via surface fluorination.[39] This should be contrasted with sulfur monochloride vulcanization, which is commonly employed for other honeycomb systems and suffers from drawbacks such as chemical entrapment and prolonged cross-linking times (typically 5 hours).[28,29]

Plasmachemical surface fluorination of polybutadiene follows earlier predicted structure–behaviour relationships.[39,40,49] The extent of plasma-induced surface roughening (texturing) can be decoupled from plasma fluorination by placement of the polybutadiene surfaces either in the electrical discharge glow region (plasma sheath bombardment[44,45]) or downstream (no ion bombardment,[44,45] thus smooth), Figure 4.7. The honeycomb structures, combined with non-texturing CF_4 plasma fluorination (30 W, 60 s, downstream), leads to an increase in hydrophobicity as observed by placing microlitre water droplets onto the surface, Figure 4.8. An average pore diameter of at least 20 μm is required to achieve contact angles greater than 170°. Smaller pores may be too shallow (assuming constant interfacial behaviour during pore formation[50])

to be capable of trapping air,[51,52,53,54,55] which is key to achieving a Cassie-Baxter state,[56] and therefore lead to lower contact angles more indicative of a Wenzel state of wetting.[57] Such smooth honeycomb samples also exhibit high contact angle hysteresis, Figure 4.8. This can be lowered if the polybutadiene samples are placed in the CF_4 plasma glow region (which generates a textured surface), which is consistent with the rationale that hierarchical surfaces (two length scales of roughness, in this case honeycomb structure plus plasma-induced surface roughening) can lead to true superhydrophobicity (high contact angles, low hysteresis).[40,58,59]

For the case of picolitre droplet impact on smooth plasma fluorinated polybutadiene, no oscillation was observed due to increased movement of the contact line during spreading, leading to an increase in the dissipation of the excess surface free energy of the droplet. Droplets impacting upon hierarchical plasma-textured honeycomb surfaces bounced due to the high contact angles and low hysteresis observed on these surfaces.

A comparison between CF_4 plasma fluorinated smooth honeycomb surfaces and CF_4 plasma fluorinated and textured spin coated polybutadiene films (with identical picolitre static contact angle values) shows that the picolitre droplet impact behaviour onto these two surfaces is markedly different. The droplet oscillation frequency is found to be much higher for the latter, Table 4.2. This is in disagreement with previous theoretical models, which suggest that droplets with similar contact angles should oscillate at similar frequencies.[60,61] This discrepancy may be due to the fact that the static contact angle is not an appropriate contact angle to use when predicting oscillation frequencies, and that contact angle hysteresis and the motion of the contact line should be taken into account.

These CF_4 plasma fluorinated polybutadiene honeycomb surfaces provide a quick and easy route to stable hierarchical superhydrophobicity. They are more superhydrophobic than conventional honeycomb arrays prepared from fluorinated polymers.[62] In addition, by utilising a solvent with a lower density than water it should be feasible to create a 3D honeycomb structure,[22] resulting in a highly porous polymer layer. Such low energy porous layers could find use in confined crystallization,[63] transportation,[64] templating,[65] or high surface area scaffolds.[66] Furthermore, droplet impact onto these hydrophobic surfaces is of

relevance to technological processes including rapid cooling,[67,68,69] delayed freezing,[70,71,72,73] crop spraying,[74] and inkjet printing (for microelectronics,[75,76,77,78] pharmaceutical dosing, or screening,[79,80,81] tissue engineering,[82,83] and optics[84,85]).

4.5 Conclusions

Solvent casting of linear polybutadiene under controlled humidity gives rise to the formation of two-dimensional hexagonally ordered honeycomb arrays. Pore aperture size and surface coverage can be independently controlled by varying the humidity and polymer concentration respectively. CF_4 plasmachemical modification imparts low surface energy functional groups in combination with surface texturing and sub-surface cross-linking of the honeycomb structures to yield superhydrophobicity (high contact angles and low hysteresis for microlitre droplets and bouncing for picolitre droplets).

4.6 References

[1] Rayleigh, L. Breath Figures. *Nature* **1911**, *86*, 416.

[2] Rayleigh, L. Breath Figures. *Nature* **1912**, *90*, 436.

[3] Widawski, G.; Rawiso, M.; François, B. Self-organized honeycomb morphology of star-polymer polystyrene film. *Nature* **1994**, *369*, 387.

[4] Beysens, D; Knobler, C. M. Growth of Breath Figures. *Phys. Rev. Lett.* **1986**, *57*, 1433.

[5] Reiss, H. The Growth of Uniform Colloidal Dispersions. *J. Chem. Phys.* **1951**, *19*, 482.

[6] Gray, J. J.; Klein, D. H.; Bonnecaze, R. T.; Korgel, B. A. Nonequilibrium Phase Behavior during the Random Sequential Adsorption of Tethered Hard Disks. *Phys. Rev. Lett.* **2000**, *85*, 4430.

[7] Stenzel, M. H.; Barner-Kowollik, C.; Davis, T. P. Formation of honeycomb-structured, porous films via breath figures with different polymer architectures. *J. Polym. Sci. Part A: Polym. Chem.* **2006**, *44*, 2363.

[8] Nishikawa, T.; Nishida, J.; Ookura, R.; Nishimura, S.-I.; Wada, S.; Karino, T.; Shimomura, M. Mesoscopic patterning of cell adhesive substrates as novel biofunctional interfaces. *Mater. Sci. Eng., C* **1999**, *10*, 141.

[9] Shastri, V. P.; Martin, I.; Langer, R. Macroporous polymer foams by hydrocarbon templating. *Proc. Natl. Acad. Sci. U.S.A.* **2000**, *97*, 1970.

[10] Wijnhoven, J. E. G. J.; Vos, W. L. Preparation of Photonic Crystals Made of Air Spheres in Titania. *Science* **1998**, *281*, 802.

[11] Imada, M.; Noda, S.; Chutinan, A.; Tokuda, T.; Murata, M.; Sasaki, G. Coherent two-dimensional lasing action in surface-emitting laser with triangular-lattice photonic crystal structure. *Appl. Phys. Lett.* **1999**, *75*, 316.

[12] Perez, J. M.; O'Loughin, T.; Simeone, F. J.; Weissleder, R.; Josephson, L. DNA-Based Magnetic Nanoparticle Assembly Acts as a Magnetic Relaxation Nanoswitch Allowing Screening of DNA-Cleaving Agents. *J. Am. Chem. Soc.* **2002**, *124*, 2856.

[13] Nam, J.-M.; Thaxton, C. S.; Mirkin, C. A. Nanoparticle-Based Bio-Bar Codes for the Ultrasensitive Detection of Proteins. *Science* **2003**, *301*, 1884.

[14] Böker, A.; Lin, Y.; Chiapperini, K.; Horowitz, R.; Thompson, M.; Carreon, V.; Xu, T.; Abetz, C.; Skaff, H.; Dinsmore, A. D.; Emrick, T.; Russell, T. P. Hierarchical nanoparticle assemblies formed by decorating breath figures. *Nat. Mater.* **2004**, *3*, 302.

[15] Karthaus, O.; Maruyama, N.; Cieren, X.; Shimomura, M.; Hasegawa, H.; Hashimoto, T. Water-Assisted Formation of Micrometer-Size Honeycomb Patterns of Polymers. *Langmuir* **2000**, *16*, 6071.

[16] François, B.; Ederlé, Y.; Mathis, C. Honeycomb membranes made from $C_{60}(PS)_6$. *Synth. Met.* **1999**, *103*, 2362.

[17] Pitois, O.; François, B. Formation of ordered micro-porous membranes. *Eur. Phys. J. B* **1999**, *8*, 225.

[18] Pitois, O.; François, B. Crystallization of condensation droplets on a liquid surface. *Colloid Polym. Sci.* **1999**, *277*, 574.
[19] Stenzel-Rosenbaum, M. H.; Davis, T. P.; Fane, A. G.; Chen, V. Porous Polymer Films and Honeycomb Structures Made by the Self-Organization of Well-Defined Macromolecular Structures Created by Living Radical Polymerization Techniques. *Angew. Chem., Int. Ed.* **2001**, *40*, 3428.
[20] Hernández-Guerrero, M.; Davis, T. P.; Barner-Kowollik, C.; Stenzel, M. H. Polystyrene comb polymers built on cellulose or poly(styrene-co-2-hydroxyethylmethacrylate) backbones as substrates for the preparation of structured honeycomb films. *Eur. Polym. J.* **2005**, *41*, 2264.
[21] Tian, Y.; Jiao, Q.; Ding, H.; Shi, Y.; Liu, B. The formation of honeycomb structure in polyphenylene oxide films. *Polymer* **2006**, *47*, 3866.
[22] Srinivasarao, M.; Collings, D.; Philips, A.; Patel, S. Three-Dimensionally Ordered Array of Air Bubbles in a Polymer Film. *Science* **2001**, *292*, 79.
[23] Peng, J.; Han, Y.; Yang, Y.; Li, B. The influencing factors on the macroporous formation in polymer films by water droplet templating. *Polymer* **2004**, *45*, 447.
[24] Ferrari, E.; Fabbri, P.; Pilati, F. Solvent and Substrate Contributions to the Formation of Breath Figure Patterns in Polystyrene Films. *Langmuir* **2011**, *27*, 1874.
[25] Karthaus, O.; Cieren, X.; Maruyama, N.; Shimomura, M. Mesoscopic 2-D ordering of inorganic/organic hybrid materials. *Mater. Sci. Eng., C* **1999**, *10*, 103.
[26] Yabu, H.; Tanaka, M.; Ijiro, K.; Shimomura, M. Preparation of Honeycomb-Patterned Polyimide Films by Self-Organization. *Langmuir* **2003**, *19*, 6297.
[27] Kabuto, T.; Hashimoto, Y.; Karthaus, O. Thermally Stable and Solvent Resistant Mesoporous Honeycomb Films from a Crosslinkable Polymer. *Adv. Funct. Mater.* **2007**, *17*, 3569.
[28] Li, L.; Zhong, Y.; Gong, J.; Li, J.; Chen, C.; Zheng, B.; Ma, Z. Constructing robust 3-dimensionally conformal micropatterns: vulcanization of honeycomb structured polymeric films. *Soft Matter* **2011**, *7*, 546.
[29] Li, L.; Zhong, Y.; Gong, J.; Li, J.; Huang, J.; Ma, Z. Fabrication of robust micro-patterned polymeric films via static breath-figure process and vulcanization. *J. Colloid Interface Sci.* **2011**, *354*, 758.
[30] Erdogan, B.; Song, L.; Wilson, J. N.; Park, J. O.; Srinivasarao, M.; Bunz, U. H. F. Permanent Bubble Arrays from a Cross-Linked Poly(para-phenyleneethynylene): Picoliter Holes without Microfabrication. *J. Am. Chem. Soc.* **2004**, *126*, 3678.
[31] Karikari, A. S.; Williams, S. R.; Heisey, C. L.; Rawlett, A. M.; Long, T. E. Porous Thin Films Based on Photo-Cross-Linked Star-Shaped Poly(d,l-lactide)s. *Langmuir* **2006**, *22*, 9687.
[32] Yabu, H.; Kojima, M.; Tsubouchi, M.; Onoue, S.; Sugitani, M.; Shimomura, M. Fabrication of photo-cross linked honeycomb-patterned films. *Colloids Surf., A* **2006**, *284–285*, 254.

[33] Li, L.; Chen, C.; Li, J.; Zhang, A.; Liu, X.; Xu, B.; Gao, S.; Jin, G.; Ma, Z. Robust and hydrophilic polymeric films with honeycomb pattern and their cell scaffold applications. *J. Mater. Chem.* **2009**, *19*, 2789.
[34] Lim, D.-K.; Do, H.-S.; Kim, H.-J.; Bang, J.-S.; Yoon, G.-H. Preparation of SIS/SBS-based UV-cross-linkable pressure-sensitive adhesives using the thiol-ene reaction. *J. Adhesion. Sci. Technol.* **2007**, *21*, 589.
[35] Greenspan, L. Humidity Fixed Points of Binary Saturated Aqueous Solutions. *J. Res., Natl. Bureau Standards* **1977**, *81A*, 89.
[36] Johnson, R. E. Jr.; Dettre, R. H. Wetting of Low-Energy Surfaces. In Wettability; Berg J. C., Ed.; Marcel Dekker, Inc.: New York, 1993; Chapter 1, p 13.
[37] Bunz, U. H. F. Breath Figures as a Dynamic Templating Method for Polymers and Nanomaterials. *Adv. Mater.* **2006**, *18*, 973.
[38] Maruyama, N.; Koito, T.; Nishida, J.; Sawadaishi, T.; Cieren, X.; Ijiro, K.; Karthaus, O.; Shimomura, M. Mesoscopic patterns of molecular aggregates on solid substrates. *Thin Solid Films* **1998**, *327–329*, 854-856.
[39] Woodward, I.; Schofield, W. C. E.; Roucoules, V.; Badyal, J. P. S. Super-hydrophobic Surfaces Produced by Plasma Fluorination of Polybutadiene Films. *Langmuir* **2003**, *19*, 3432.
[40] Brown, P. S.; Berson, A.; Talbot, E. L.; Wood, T. J.; Schofield, W. C. E.; Bain, C. D.; Badyal, J. P. S. Impact of Picoliter Droplets on Superhydrophobic Surfaces with Ultralow Spreading Ratios. *Langmuir* **2011**, 27, 13897.
[41] Edward, G. H.; O'Donnell, R. G. Relaxations in lightly crosslinked polymers. *J. Mater. Sci.* **1986**, *21*, 958.
[42] Clark, D. T.; Dilks, A. ESCA Applied to Polymers. XVIII. RF Glow Discharge Modification of Polymers in Helium, Neon, Argon, and Krypton. *J. Polym. Sci.: Polym. Chem. Ed.* **1978**, *16*, 911.
[43] Woodward, I. S.; Schofield, W. C. E.; Roucoules, V.; Bradley, T. J.; Badyal, J. P. S. Micropatterning of Plasma Fluorinated Super-hydrophobic Surfaces. *Plasma Chem. Plasma Process.* **2006**, *26*, 507.
[44] Harshbarger, W. R.; Porter, R. A.; Miller, T. A.; Norton, P. A Study of the Optical Emission from an rf Plasma during Semiconductor Etching. *Appl. Spectrosc.* **1977**, *31*, 201.
[45] Grill, V.; Walder, G.; Scheier, P.; Kurdel, M.; Märk, T. D. Absolute partial and total electron impact ionization cross sections for C2H6 from threshold up to 950 eV. *Int. J. Mass Spectrom. Ion Processes* **1993**, *129*, 31.
[46] Öner, D.; McCarthy, T. J. Ultrahydrophobic Surfaces. Effects of Topography Length Scales on Wettability. *Langmuir* **2000**, *16*, 7777.
[47] Kim, H.-Y.; Chun, J.-H. The recoiling of liquid droplets upon collision with solid surfaces. *Phys. Fluids* **2001**, *13*, 643.
[48] Fetters, L. J.; Lohse, D. J.; Richter, D.; Witten, T. A.; Zirkel, A. Connection between Polymer Molecular Weight, Density, Chain Dimensions, and Melt Viscoelastic Properties. *Macromolecules* **1994**, *27*, 4639.

[49] Hopkins, J.; Badyal, J. P. S. Nonequilibrium Glow Discharge Fluorination of Polymer Surfaces. *J. Phys. Chem.* **1995**, *99*, 4261.
[50] Wan, L.-S.; Ke, B.-B.; Zhang, J.; Xu, Z.-K. Pore Shape of Honeycomb-Patterned Films: Modulation and Interfacial Behavior. *J. Phys. Chem. B* **2012**, *116*, 40.
[51] Bico, J.; Marzolin, C.; Quére, D. Pearl drops. *Europhys. Lett.* **1999**, *47*, 220.
[52] Luo, B. H.; Shum, P. W.; Zhou, Z. F.; Li, K. Y. Surface geometrical model modification and contact angle prediction for the laser patterned steel surface. *Surf. Coat. Technol.* **2010**, *205*, 2597.
[53] Li, W.; Amirfazli, A. A thermodynamic approach for determining the contact angle hysteresis for superhydrophobic surfaces. *J. Colloid Interface Sci.* **2005**, *292*, 195.
[54] Li, W.; Amirfazli, A. Microtextured superhydrophobic surfaces: A thermodynamic analysis. *Adv. Colloid Interface Sci.* **2007**, *132*, 51.
[55] Tuteja, A.; Choi, W.; McKinley, G. H.; Cohen, R. E.; Rubner, M. F. Design Parameters for Superhydrophobicity and Superoleophobicity. *MRS Bull.* **2008**, *33*, 752.
[56] Cassie, A. B. D.; Baxter, S. Wettability of porous surfaces. *Trans. Faraday Soc.* **1944**, *40*, 546.
[57] Wenzel, R. N. Resistance of Solid Surfaces to Wetting by Water. *Ind. Eng. Chem.* **1936**, *28*, 988.
[58] Miwa, M.; Nakajima, A.; Fujishima, A.; Hashimoto, K.; Watanabe, T. Effects of the Surface Roughness on Sliding Angles of Water Droplets on Superhydrophobic Surfaces. *Langmuir* **2000**, *16, 5754.*
[59] Gao, L.; McCarthy, T. J. The “Lotus Effect” Explained: Two Reasons Why Two Length Scales of Topography Are Important. *Langmuir* **2006**, *22*, 2966.
[60] Strani, M.; Sabetta, F. Free vibrations of a drop in partial contact with a solid support. *J. Fluid Mech.* **1984**, *141*, 233.
[61] Strani, M.; Sabetta, F. Viscous oscillations of a supported drop in an immiscible fluid. *J. Fluid Mech.* **1988**, *189*, 397.
[62] Yabu, H.; Shimomura, M. Single-Step Fabrication of Transparent Superhydrophobic Porous Polymer Films. *Chem. Mater.* **2005**, *17*, 5231.
[63] Ha, J.-M.; Wolf, J. H.; Hillmyer, M. A.; Ward, M. D. Polymorph Selectivity under Nanoscopic Confinement. *J. Am. Chem. Soc.* **2004**, *126*, 3382.
[64] Hulteen, J. C.; Jirage, K. B.; Martin, C. R. Introducing Chemical Transport Selectivity into Gold Nanotubule Membranes. *J. Am. Chem. Soc.* **1998**, *120*, 6603.
[65] Cheng, C. X.; Tian, Y.; Qiao Shi, Y.; Pei Tang, R.; Xi, F. Porous Polymer Films and Honeycomb Structures Based on Amphiphilic Dendronized Block Copolymers. *Langmuir* **2005**, *21*, 6576.
[66] Mitchell, D. T.; Lee, S. B.; Trofin, L.; Li, N.; Nevanen, T. K.; Söderlund, H.; Martin, C. R. Smart Nanotubes for Bioseparations and Biocatalysis. *J. Am. Chem. Soc.* **2002**, *124*, 11864.
[67] Yao, S. C.; Choi, K. J. Heat transfer experiments of mono-dispersed vertically impacting sprays. *Int. J. Multiphase Flow* **1987**, *13*, 639.

[68] Pasandideh-Fard, M.; Aziz, S. D.; Chandra, S.; Mostaghimi, J. Cooling effectiveness of a water drop impinging on a hot surface. *Int. J. Heat and Fluid Flow* **2001**, *22*, 201.
[69] Chen, R.-H.; Chow, L. C.; Navedo, J. E. Effects of spray characteristics on critical heat flux in subcooled water spray cooling. *Int. J. Heat Mass Tran.* **2002**, *45*, 4033.
[70] Tourkine, P.; Le Merrer, M.; Quéré, D. Delayed Freezing on Water Repellent Materials. *Langmuir* **2009**, *25*, 7214.
[71] Kulinich, S. A.; Farzaneh, M. How Wetting Hysteresis Influences Ice Adhesion Strength on Superhydrophobic Surfaces. *Langmuir* **2009**, *25*, 8854.
[72] Cao, L.; Jones, A. K.; Sikka, V. K.; Wu, J.; Gao, D. Anti-Icing Superhydrophobic Coatings. *Langmuir* **2009**, *25*, 12444.
[73] Mishchenko, L.; Hatton, B.; Bahadur, V.; Taylor, J. A.; Krupenkin, T.; Aizenberg, J. Design of Ice-free Nanostructured Surfaces Based on Repulsion of Impacting Water Droplets. *ACS Nano* **2010**, *4*, 7699.
[74] Reichard, D. L. Drop Formation and Impaction on the Plant. *Weed Technol.* **1988**, *2*, 82.
[75] Sirringhaus, H.; Kawase, T.; Friend, R. H.; Shimoda, T.; Inbasekaran, M.; Wu, W.; Woo, E. P. High-Resolution Inkjet Printing of All-Polymer Transistor Circuits. *Science* **2000**, *290*, 2123.
[76] Wang, J. Z.; Zheng, Z. H.; Li, H. W.; Huck, W. T. S.; Sirringhaus, H. Dewetting of conducting polymer inkjet droplets on patterned surfaces. *Nat. Mater.* **2004**, *3*, 171.
[77] Sele, C. W.; von Werne, T.; Friend, R. H.; Sirringhaus, H. Lithography-Free, Self-Aligned Inkjet Printing with Sub-Hundred-Nanometer Resolution. *Adv. Mater.* **2005**, *17*, 997.
[78] Doggart, J.; Wu, Y.; Liu, P.; Zhu, S. Facile Inkjet-Printing Self-Aligned Electrodes for Organic Thin-Film Transistor Arrays with Small and Uniform Channel Length. *ACS Appl. Mater. Interfaces* **2010**, *2*, 2189.
[79] Barbulovic-Nad, I.; Lucente, M.; Sun, Y.; Zhang, M.; Wheeler, A. R.; Bussmann, M. Bio-Microarray Fabrication Techniques—A Review. *Crit. Rev. Biotechnol.* **2006**, *26*, 237.
[80] Tan, C. P.; Cipriany, R.; Lin, D. M.; Craighead, H. G. Nanoscale Resolution, Multicomponent Biomolecular Arrays Generated By Aligned Printing With Parylene Peel-Off. *Nano Lett.* **2010**, *10*, 719.
[81] Arrabito, G.; Pignataro, B. Inkjet Printing Methodologies for Drug Screening. *Anal. Chem.* **2010**, *82*, 3104.
[82] Mironov, V.; Boland, T.; Trusk, T.; Forgacs, G.; Markwald, R. R. Organ printing: computer-aided jet-based 3D tissue engineering. *Trends Biotechnol.* **2003**, *21*, 157.
[83] Xu, T.; Jin, J.; Gregory, C.; Hickman, J. J.; Boland, T. Inkjet printing of viable mammalian cells. *Biomaterials* **2005**, *26*, 93.
[84] Bharathan, J.; Yang, Y. Polymer electroluminescent devices processed by inkjet printing: I. Polymer light-emitting logo. *Appl. Phys. Lett.* **1998**, *72*, 2660.

[85] Chang, S.-C.; Bharathan, J.; Yang, Y.; Helgeson, R.; Wudl, F.; Ramey, M. B.; Reynolds, J. R. Dual-color polymer light-emitting pixels processed by hybrid inkjet printing. *Appl. Phys. Lett.* **1998**, *73*, 2561.

Chapter 5 Controlling Liquid Droplet Impact Dynamics by Tailoring the Solid Subsurface

5.1 Introduction

In the previous chapters, the impact and spreading of droplets of water was investigated on polymer surfaces with varying levels of surface roughness. However, the mechanical properties of the substrate are also known to affect the behaviour of impacting liquid droplets. The impact of liquid droplets onto soft surfaces is an important phenomenon underpinning a plethora of industrial processes including microfluidics,[1,2] electrowetting,[3] droplet condensation,[4] and inkjet printing (applications in microelectronics,[5,6,7,8] pharmaceutical dosing or screening,[9,10,11] tissue engineering,[12,13] and optics[14,15]).

Previous studies have shown that the vertical component of the surface tension resulting from a liquid droplet resting on a soft surface can induce the formation of a wetting ridge, Scheme 5.1, where the surface along the droplet contact line deforms.[16,17,18,19,20,21] These deformations can perturb the dynamics of droplet spreading[22] (viscoelastic braking) and have been seen to enhance contact line pinning in microlitre droplets.[23]

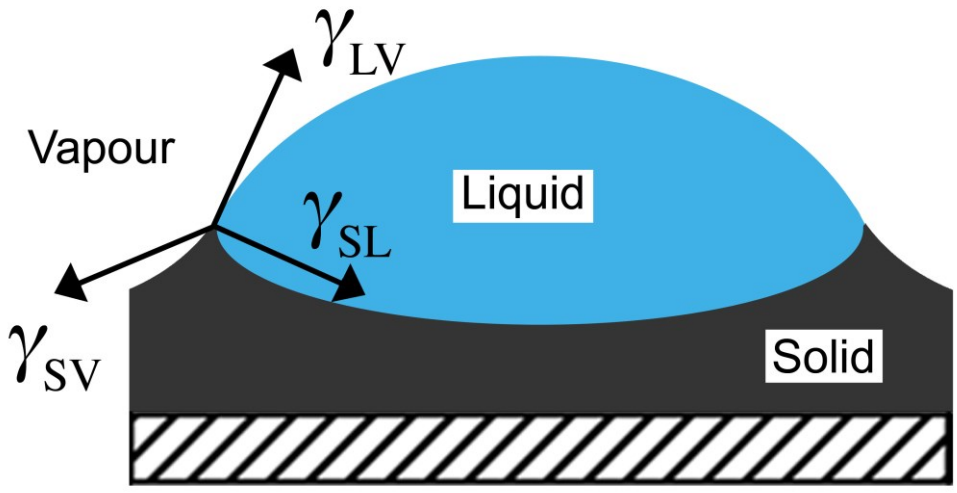

Scheme 5.1: Schematic diagram showing a wetting ridge formed on a soft surface due to the vertical component of the liquid-vapour surface tension, γ_{LV}.

A comparison of the oscillation of microlitre droplets following impact onto hard and soft surfaces has shown that droplets oscillate at a higher frequency on the latter.[24] This has been explained in terms of the deformed wetting ridge enhancing droplet pinning and reducing the amount of energy dissipation through contact line motion. However, the dependency of such behaviour upon the subsurface properties has not previously been investigated.

In this chapter, the impact dynamics of picolitre water droplets onto a range of different thickness films with controllable hardness and surface wettability has been studied, Scheme 5.2. Firstly, non-crosslinked and crosslinked plasma fluorinated polybutadiene films have been compared whilst maintaining the same hydrophobic surface chemistry.[25] An alternative system comprises surface initiated atom transfer radical polymerisation (ATRP)[26] growth of hydrophobic perfluorinated acrylate brushes with well-defined polymer chain length,[27] where pulsed plasma deposited vinylbenzyl chloride[28] and plasma chlorinated polybutadiene are utilised as ATRP initiator layers. These two different types of initiator layer permits any observed changes in droplet impact dynamics to be solely attributed to the mechanical properties of the underlying initiator layer. Furthermore, for a given initiator layer, the growth of two different perfluoroalkyl length brush layers enables the study of the effect of surface energy, and therefore droplet shape, upon impact dynamics whilst keeping the mechanical properties of the film constant.

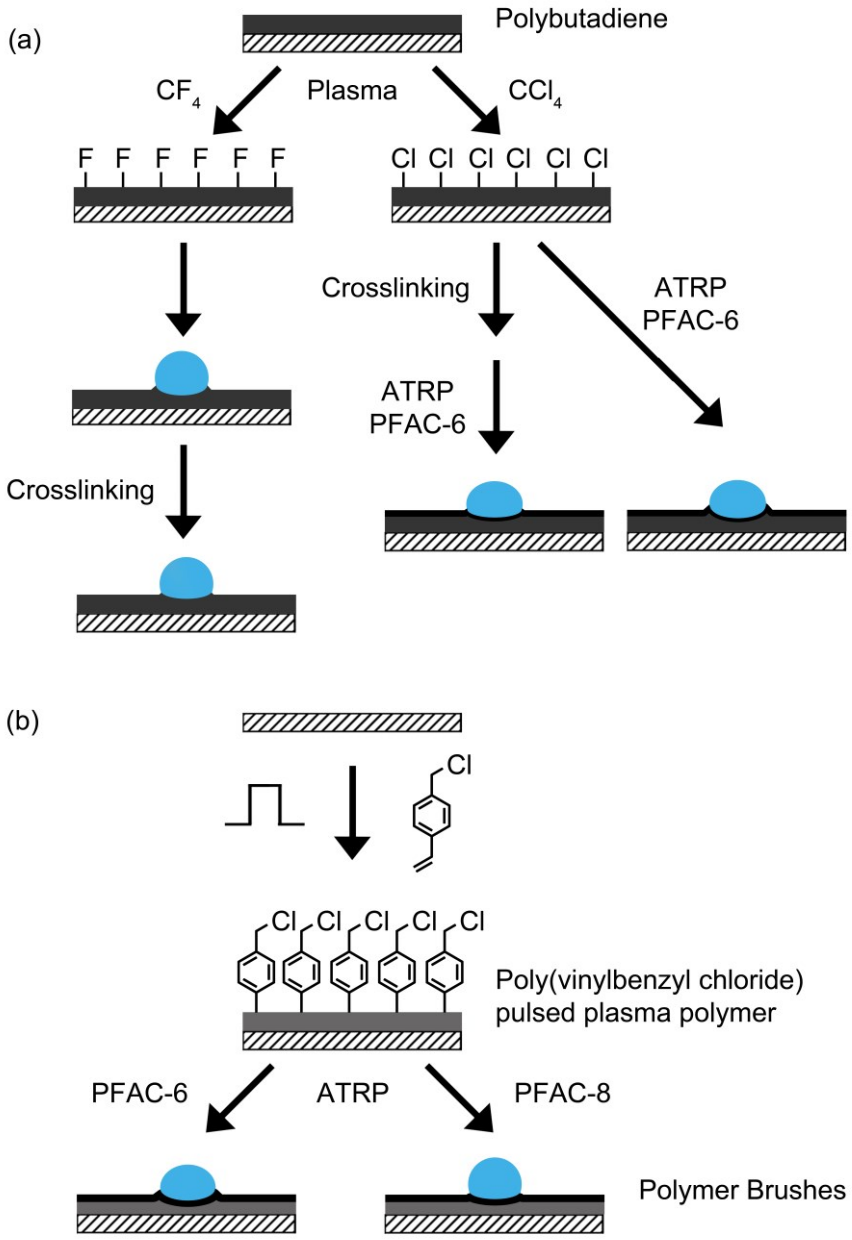

Scheme 5.2: Summary of functional surfaces investigated for water droplet impact: (a) spin coated polybutadiene; and (b) pulsed plasma deposited poly(vinylbenzyl chloride). PFAC-6 and PFAC-8 denote 1H,1H,2H,2H-perfluorooctyl acrylate and 1H,1H,2H,2H-perfluorodecyl acrylate monomers for ATRP respectively.

5.2 Experimental

5.2.1 Variable Thickness and Hardness Plasma Halogenated Polybutadiene Films

Polished silicon (100) wafers (Silicon Valley Microelectronics, Inc.) were used as substrates. Polybutadiene (M_w = 420,000, 36% cis 1,4 addition, 55% trans 1,4 addition, 9% 1,2 addition, Sigma-Aldrich Inc.) dissolved in toluene (+99.5%,

BDH) at various concentrations was spin coated using a photoresist spinner (Cammax Precima) operating at 3000 rpm. Any trapped solvent within these polymer films was then removed by annealing under vacuum at 90 °C for 60 min.

Plasmachemical fluorination (or chlorination for surface initiated ATRP) of the polybutadiene films was undertaken in a cylindrical glass reactor of similar design to that used in Section 3.2.1 (page 52). A piece of polybutadiene coated substrate was placed into the reactor (8 cm downstream to avoid surface texturing[29,30,31]), followed by evacuation to base pressure. CF_4 gas (+99.7%, Air Products) (or CCl_4 vapour (99.5%, May & Baker Ltd.)) was then admitted into the system via a needle valve at a pressure of 0.2 mbar and 2 cm^3 min^{-1} flow rate, and the electrical discharge ignited using a power of 50 W for 60 s. Upon completion of surface functionalization, the gas (vapour) feed was switched off and the chamber vented to atmosphere. Subsequent crosslinking of these plasma fluorinated (chlorinated) polybutadiene films entailed placing them in a vacuum oven at 155 °C for 60 min.[25]

5.2.2 Variable Thickness Plasma Deposited poly(vinylbenzyl chloride) ATRP Initiator Layers

Vinylbenzyl chloride monomer (97%, mixture of 3- and 4- isomers, Sigma Aldrich Ltd.) was loaded into a sealable glass tube and further purified using multiple freeze-pump-thaw cycles. Pulsed plasmachemical deposition of the poly(vinylbenzyl chloride) initiator layer was carried out in a cylindrical glass reactor of similar design to that used in Section 3.2.1 (page 52). Prior to each plasma deposition, the chamber was scrubbed with detergent, rinsed in propan-2-ol, and further cleaned using a 50 W air plasma for 30 min. Next, the substrate to be coated was placed into the center of the reactor, and the system pumped down to base pressure. Precursor vapor was introduced into the chamber at a pressure of 0.2 mbar for 5 min followed by ignition of the electrical discharge. The optimum duty cycle for structural retention of the vinylbenzyl chloride functionality corresponded to on-period = 100 μs and off-period = 4 ms in combination with peak power = 30 W. Upon completion of deposition, the precursor vapour was allowed to continue to flow through the system for a further 5 min in order to quench any trapped reactive sites in the deposited film.

5.2.3 Surface Initiated Atom Transfer Radical Polymerisation (ATRP)

The plasma chlorinated polybutadiene or pulsed plasma deposited poly(vinylbenzyl chloride) initiator coated silicon wafer pieces were loaded inside a sealable glass tube containing copper(I) bromide (5 mmol, 98%, Sigma Aldrich Ltd.), copper(II) bromide (0.01 mmol, 99%, Sigma Aldrich Ltd.), 2-2'-bipyridyl (10 mmol, ≥98%, Sigma Aldrich Ltd.), trifluorotoluene (4 mL, >99%, Sigma Aldrich Ltd.), and either 1H,1H,2H,2H-perfluorooctyl acrylate (0.05 mol, 95%, Fluorochem Ltd.) or 1H,1H,2H,2H-perfluorodecyl acrylate (0.05 mol, 98%, Fluorochem Ltd.).[27] The mixture was thoroughly degassed using several freeze-pump-thaw cycles and then the sample tube immersed into an oil bath maintained at 95 ºC for 16 h to allow polymerisation to take place. Finally, the cleaning and removal of any physisorbed polymer was undertaken by Soxhlet extraction with hot toluene for 5 h.

5.2.4 Surface Characterisation

Surface elemental compositions were determined by X-ray photoelectron spectroscopy (XPS) using a VG ESCALAB II electron spectrometer as described in Section 3.2.2 (page 52). Surface elemental compositions were calculated using sensitivity factors derived from chemical standards, C(1s): O(1s): F(1s): Cl(2p): Si(2p) equals 1.00: 0.36: 0.24: 0.39: 0.96.

Fourier transform infrared (FTIR) analysis of the deposited layers was undertaken using an FTIR spectrometer (Spectrum One, Perkin-Elmer Inc.) equipped with a liquid nitrogen cooled MCT detector. Spectra were recorded at a resolution of 4 cm^{-1} across the 700–4000 cm^{-1} wavelength range. Reflection absorption infrared spectroscopy (RAIRS) measurements were performed using a variable angle accessory (Specac Ltd.) set at 66° and fitted with a KRS-5 polarizer to remove the s-polarized component.

Thickness measurements of films deposited onto silicon wafers were made using a spectrophotometer (nkd-6000, Aquila Instruments Ltd). The obtained transmittance-reflectance curves (350–1000 nm wavelength range) were fitted to a Cauchy model for dielectric materials using a modified Levenberg-Marquardt algorithm.[32]

Microlitre sessile drop contact angle analysis was carried out with a video capture system (VCA2500XE, AST Products Inc.) using 1.0 µL dispensation of

de-ionised water. Picolitre drop impact studies were carried out using an imaging rig as described in Section 3.2.3 (page 53). The piezo-type nozzle (MicroFab MJ-ABP-01, Horizon Instruments Ltd.) had an aperture diameter of 30 μm, generating water drops of 30 μm diameter (14 pL). In addition to recordings made at 90,000 frames per second (fps), a faster frame rate of 180,000 fps was also employed in order to verify the droplet oscillation frequency. Images at the higher frame rate consisted of 128 x 32 with 0.73 μm pixel size.

Atomic force microscopy (AFM) images were collected in tapping mode at 20 °C in ambient air (Nanoscope III, Digital Instruments Inc.). The stiff silicon cantilever had a spring constant of 42–83 N m^{-1} (Nanoprobe, Digital Instruments Inc.). Root-mean-square (RMS) roughness values were calculated over 50 μm x 50 μm scan areas.

Hardness values were determined by microindentation (MVK-H2, Mitutoyo, Inc.) using a standard Vickers tip and a force of 20 mN (ASTM E384 - 11e1).[33]

5.3 Results

5.3.1 Non-Crosslinked Versus Crosslinked Plasma Halogenated Polybutadiene

The XPS elemental composition of spin coated polybutadiene showed the presence of some oxygen content, which can be attributed to aerobic oxidation at the polymer film surface during the annealing step to remove trapped solvent, Table 5.1.[25] Following CF_4 and CCl_4 plasma halogenation, virtually all of this surface oxygen is lost accompanied with a high level of halogen incorporation. The slight increase in surface oxygen concentration following thermal crosslinking of these CF_4 and CCl_4 plasma halogenated films arises from the reaction between atmospheric oxygen and any unreacted polybutadiene alkene bonds located in the near-surface region.[34] In the absence of the polybutadiene layer, no film deposition was detected following either CF_4 or CCl_4 plasma exposure to silicon wafer surfaces; thereby confirming that plasma assisted surface halogenation rather than plasma deposition occurs for polybutadiene.[35,36]

Table 5.1: XPS elemental compositions and static water contact angles for non-crosslinked and crosslinked: (a) untreated polybutadiene; (b) CF_4 plasma fluorinated polybutadiene; and (c) CCl_4 plasma chlorinated polybutadiene. Polybutadiene film thickness = 1 μm.

		XPS Elemental Composition / ±0.5%				Static Contact Angle†	
		% C	% F	% Cl	% O	Microlitre / ±2°	Picolitre / ±5°
(a) Untreated polybutadiene	Non-Crosslinked	87.8	0.0	0. 0	12.2	103	78
	Crosslinked	86.0	0.0	0.0	14.0	100	74
(b) CF_4 plasma fluorinated polybutadiene	Non-Crosslinked	40.9	57.1	0.0	2.0	134	106
	Crosslinked	41.0	54.6	0.0	4.4	133	105
(c) CCl_4 plasma chlorinated polybutadiene	Non-Crosslinked	56.5	0.0	43.5	0.0	88	74
	Crosslinked	55.3	0.0	43.0	1.7	85	72

† In all cases, picolitre droplet (30 μm diameter) static contact angles are lower than for microlitre droplets (1.2 mm diameter) due to either the smaller droplet size relative to surface features,[37] or the high-speed impact of the picolitre droplets pushing the contact line beyond its equilibrium position.[38]

Infrared assignments for non-crosslinked polybutadiene are as follows:[25,39] $CH=CH_2$ stretch (3010 cm^{-1}), $-CH_2$ stretch (2922 cm^{-1}), $-CH_2$ symmetric stretch (2845 cm^{-1}), $-CH_2$ deformation (1438 cm^{-1}), -CH bending (967 cm^{-1}), and $CH=CH_2$ bending (913 cm^{-1}), Figure 5.1. No change in the infrared spectrum was observed following plasmachemical halogenation, thereby indicating that only the outermost surface of the polybutadiene film is halogenated (i.e. limited to the XPS sampling depth of 2–5 nm).[25] Following thermal curing to crosslink these polybutadiene films, infrared analysis shows:[25] -OH stretch (3400 cm^{-1}), $-CH_2$ stretch (2922 cm^{-1}), aliphatic ester (1730 cm^{-1}), $-CH_2$ deformation (1438 cm^{-1}), and $CH=CH_2$ bending (913 cm^{-1}). The strong attenuation of the $CH=CH_2$ stretch (3010 cm^{-1}) confirms that bulk crosslinking has taken place, and the oxygenated species are attributable to aerial oxidation.[34]

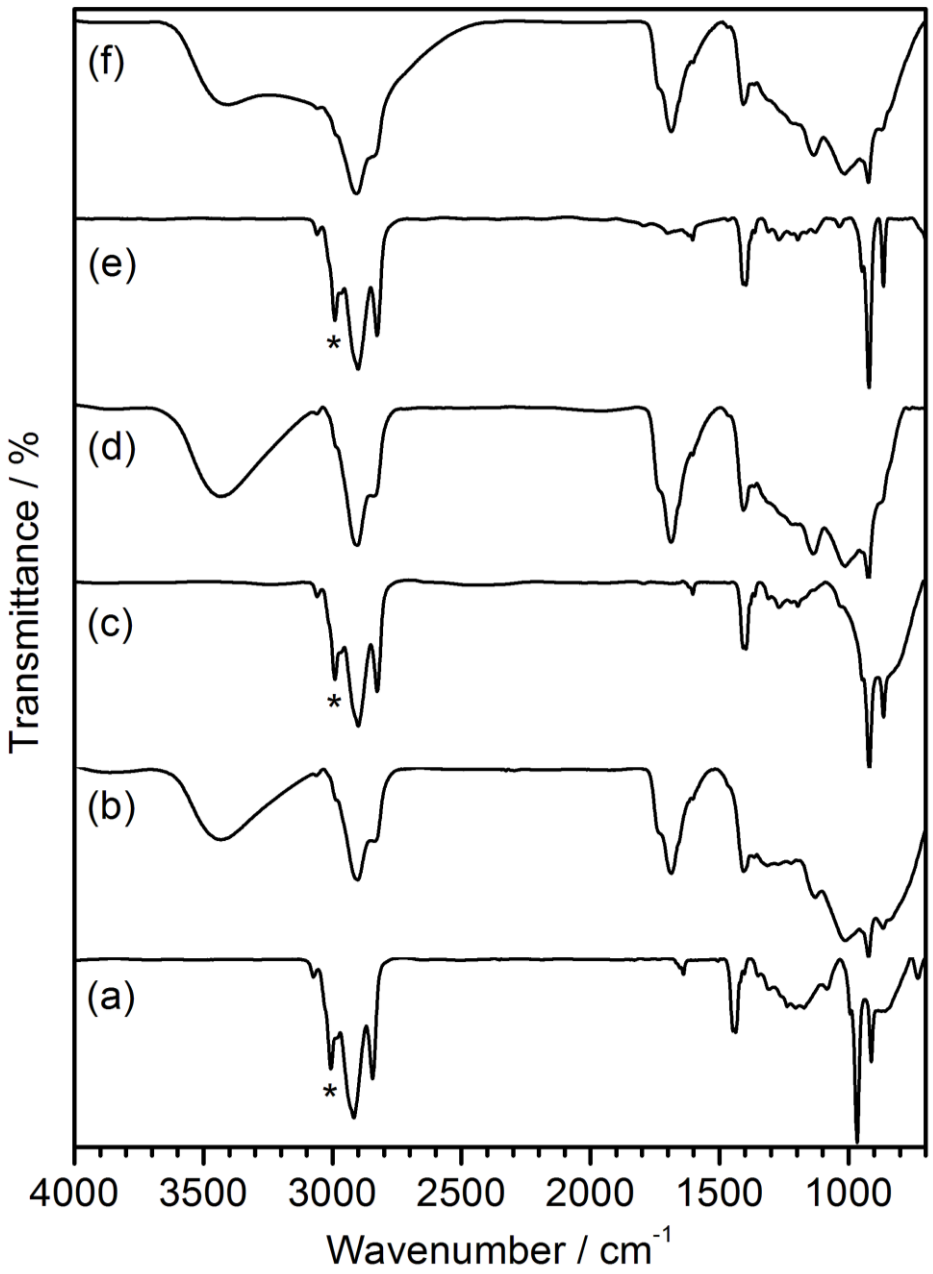

Figure 5.1: Infrared spectra of: (a) non-crosslinked polybutadiene; (b) crosslinked polybutadiene (c) non-crosslinked CF_4 plasma fluorinated polybutadiene; (d) crosslinked CF_4 plasma fluorinated polybutadiene; (e) non-crosslinked CCl_4 plasma chlorinated polybutadiene; and (f) crosslinked CCl_4 plasma chlorinated polybutadiene. * $CH=CH_2$ stretch (3010 cm^{-1}) for non-crosslinked polybutadiene.

In all cases, the AFM RMS surface roughness was measured to be less than 17 nm, which confirms the low level of plasmachemical roughening/texturing within the selected downstream plasma glow region due to the lack of surface bombardment by energetic electrical discharge species (e.g. ions),[29,30] Table 5.2.

Picolitre water droplet impact onto all of these surfaces displayed an initial spreading of the contact line to reach a maximum diameter. In the case of CF_4 plasma fluorinated polybutadiene, this was followed by dissipation of excess surface free energy observed as oscillations of the droplet height (stemming from lower energy dissipation during spreading across a more hydrophobic surface), whilst motion of the contact line was inhibited due to pinning, Figure 5.2(a).[40] The droplet oscillation frequency subsequent to impact was measured by monitoring the change in height of the drop over time, Figure 5.2(b). In the case of untreated and CCl_4 plasma chlorinated polybutadiene, no droplet oscillations were observed due to the excess surface free energy being more efficiently dissipated during the initial droplet impact and spreading[41] (much lower contact angles, Table 1).

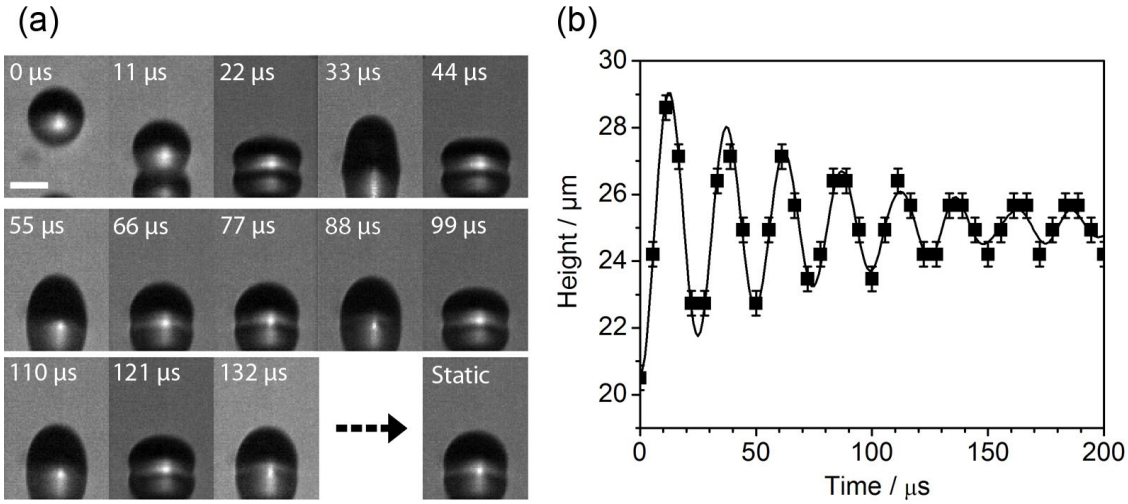

Figure 5.2: (a) High-speed video images (captured at 90,000 fps) of picolitre water droplet impact onto a hydrophobic CF_4 plasma fluorinated polybutadiene surface (reflection in substrate is seen in lower half, white scale bar = 20 µm); and (b) typical damped oscillation curve fitted to the experimental data for picolitre water droplet height fluctuation following impact. Oscillation frequencies were calculated from images captured at 180,000 fps.

The dynamics (oscillation frequency) of picolitre droplets following impact onto CF_4 plasma fluorinated polybutadiene were found to be dependent upon the film thickness, and film hardness (which could be altered by thermal crosslinking), Figure 5.3(a) and Table 5.2. A greater hardness reduces the influence of film thickness upon the change in oscillation frequency (despite the

droplets retaining similar static water contact angles across the entire film thickness range), Table 5.1 and Figure 5.3(a). The approximately linear relationship between oscillation frequency and film thickness was found to breakdowsn beyond 500 nm, with the measured oscillation frequency for the non-crosslinked and crosslinked CF_4 plasma fluorinated polybutadiene layers plateauing at 38.0 kHz and 33.6 kHz respectively.

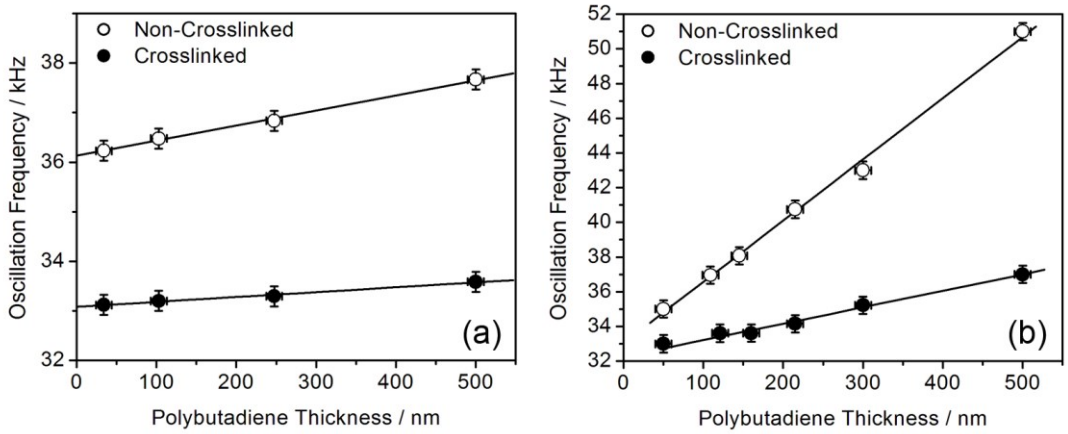

Figure 5.3: Oscillation frequencies of picolitre (30 μm diameter) water droplets following impact upon: (a) non-crosslinked and crosslinked CF_4 plasma fluorinated polybutadiene as a function of polybutadiene film thickness; and (b) 20 nm thick ATRP poly(perfluorooctyl acrylate) brushes grown from non-crosslinked and crosslinked CCl_4 plasma chlorinated polybutadiene as a function of polybutadiene film thickness. Microlitre and picolitre contact angles were not found to vary with film thickness, Table 5.1.

Table 5.2: AFM RMS roughness and microindentation hardness of 1 μm thick films.

Layer	AFM RMS Roughness / nm	Hardness / MPa
Non-crosslinked polybutadiene	7±1	17±2
Crosslinked polybutadiene	10±1	347±10
Non-crosslinked CF_4 plasma fluorinated polybutadiene	10±2	38±2
Crosslinked CF_4 plasma fluorinated polybutadiene	17±2	351±10
Non-crosslinked CCl_4 plasma chlorinated polybutadiene	6±1	21±2
Crosslinked CCl_4 plasma chlorinated polybutadiene	9±1	353±10
Pulsed plasma deposited poly(vinylbenzyl chloride)	5±1	92±1

3.2 Perfluoroalkyl Polymer Brushes Surface Grafted From CCl_4 Plasma Chlorinated Polybutadiene ATRP Initiator Layers

Both non-crosslinked and crosslinked CCl_4 plasma chlorinated polybutadiene layers were utilised for the surface initiated ATRP growth of 20 nm thick poly(perfluorooctyl acrylate) polymer brushes with a view to further investigating the role of the subsurface thickness upon droplet impact dynamics. ATRP growth of the poly(perfluorooctyl acrylate) polymer brushes from the plasma chlorinated polybutadiene surfaces was confirmed by XPS and infrared analysis, Table 5.3 and Figure 5.4. Elemental XPS compositions were found to be consistent with the growth of poly(perfluorooctyl acrylate) brushes containing an end capping chlorine as part of the ATRP mechanism.[42] Infrared assignments for the perfluorooctyl acrylate monomer are as follows:[39] C=O stretching (1734 cm^{-1}), C=C stretching (1640 cm^{-1}), C=CH_2 in plane stretching (1412 cm^{-1}), -CF_3 stretching (1325 cm^{-1}), -CF_2- antisymmetric stretching (1242 cm^{-1}), and -CF_2- symmetric stretching (1145 cm^{-1}), Figure 5.4. Following surface ATRP grafting, the alkene bond features (C=C stretching (1640 cm^{-1}) and C=CH_2 in plane stretching (1412 cm^{-1})) have disappeared due to polymerisation having taken place.

Table 5.3: XPS elemental compositions and static water contact angles for: (a) non-crosslinked and crosslinked CCl_4 plasma chlorinated polybutadiene; and (b) 20 nm thick ATRP poly(perfluorooctyl acrylate) brushes grown from (a).

		XPS Elemental Composition / ±0.5%				Static Contact Angle	
		% C	% F	% Cl	% O	Microlitre / ±2°	Picolitre / ±5°
(a) CCl_4 plasma chlorinated polybutadiene	Non-Crosslinked	56.5	0.0	43.5	0.0	88	74
	Crosslinked	55.3	0.0	43.0	1.7	85	72
(b) ATRP Poly($CF_3(CF_2)_5$ acrylate) brushes grown from (a)	Theoretical	40.7	48.2	3.7	7.4	–	–
	Non-Crosslinked	50.8	39.0	3.4	6.8	119	102
	Crosslinked	49.6	38.7	3.3	8.4	118	100

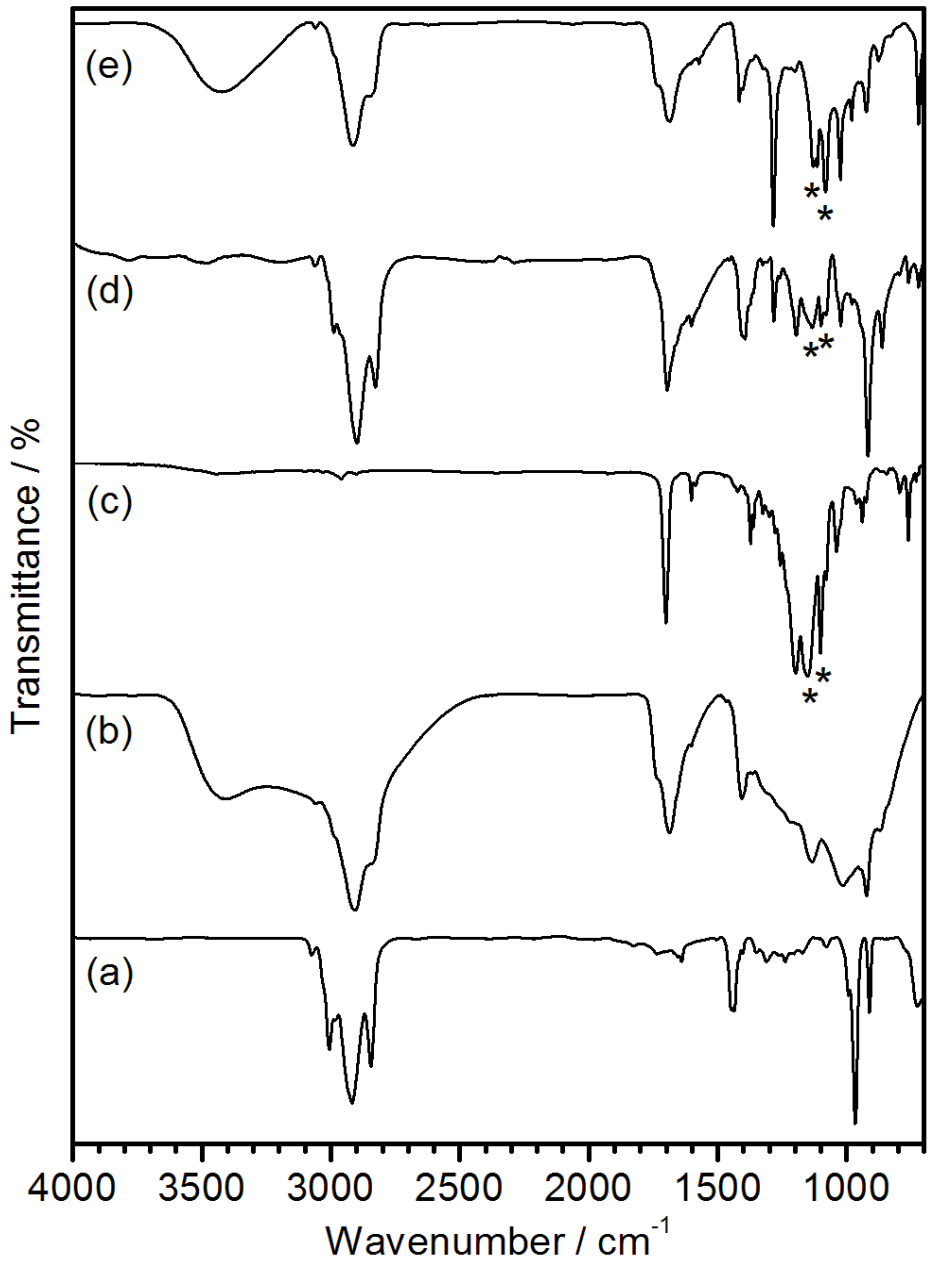

Figure 5.4: Infrared spectra of: (a) non-crosslinked CCl_4 plasma chlorinated polybutadiene; (b) crosslinked CCl_4 plasma chlorinated polybutadiene; (c) perfluorooctyl acrylate monomer; (d) 20 nm thick ATRP poly(perfluorooctyl acrylate) brushes grown from non-crosslinked CCl_4 plasma chlorinated polybutadiene; and (e) 20 nm thick ATRP poly(perfluorooctyl acrylate) brushes grown from crosslinked CCl_4 plasma chlorinated polybutadiene. * Perfluorooctyl acrylate CF_2 symmetric (1145 cm^{-1}) and antisymmetric (1242 cm^{-1}) stretching peaks.

Droplet oscillation frequencies following impact upon 20 nm thick ATRP poly(perfluorooctyl acrylate) brush layers grown from non-crosslinked and crosslinked CCl_4 plasma chlorinated polybutadiene were found to be governed by both the thickness and hardness of the underlying CCl_4 plasma chlorinated

polybutadiene initiator layer, Table 5.2 and Figure 5.3(b). This was in conjunction with the picolitre droplet static contact angle remaining constant (around 100°) for both the non-crosslinked and crosslinked underlayer across the entire thickness range, Table 5.3. The approximately linear relationship between the underlayer thickness and oscillation frequency was found to breakdown for both the non-crosslinked and crosslinked CCl_4 plasma chlorinated polybutadiene underlayer beyond 500 nm, with the measured oscillation frequency plateauing at 53.8 kHz and 38.2 kHz respectively. Control experiments showed that water droplets impacting upon CCl_4 plasma chlorinated polybutadiene in the absence of the ATRP poly(perfluorooctyl acrylate) brush layer gave rise to spreading with no measurable oscillatory behaviour.

Following picolitre droplet (30 μm diameter) impact experiments, the surfaces were analysed by atomic force microscopy (AFM). For all samples, approximately 30 μm diameter rings were observed, which are consistent with the formation of a wetting ridge, Figure 5.5. The ridge height exceeds the 20 nm thickness of the ATRP poly(perfluorooctyl acrylate) brush, thereby indicative of subsurface deformation. The extent of lateral and vertical surface deformation during droplet impact was found to depend upon the thickness and hardness of the underlying CCl_4 plasma chlorinated polybutadiene ATRP initiator layer. Water droplet impact upon 20 nm thick ATRP poly(perfluorooctyl acrylate) brush layers grown from crosslinked (harder) CCl_4 plasma chlorinated polybutadiene exhibited a wetting ridge that was smaller in height and width compared to that measured following droplet impact onto ATRP poly(perfluorooctyl acrylate) brush layers grown from non-crosslinked (softer) CCl_4 plasma chlorinated polybutadiene of the same thickness, Figure 5.5. The ridge height of the surface deformation following droplet impact increased in a linear fashion as a function of underlayer thicknesses upto 500 nm, Figure 5.5(d). For underlayer thicknesses exceeding 500 nm, the deformation ridge height levelled off to 130–140 nm for non-crosslinked and 50–55 nm for crosslinked CCl_4 plasma chlorinated polybutadiene underlayer (which is consistent with the aforementioned plateauing of oscillation frequency beyond 500 nm polybutadiene film thickness).

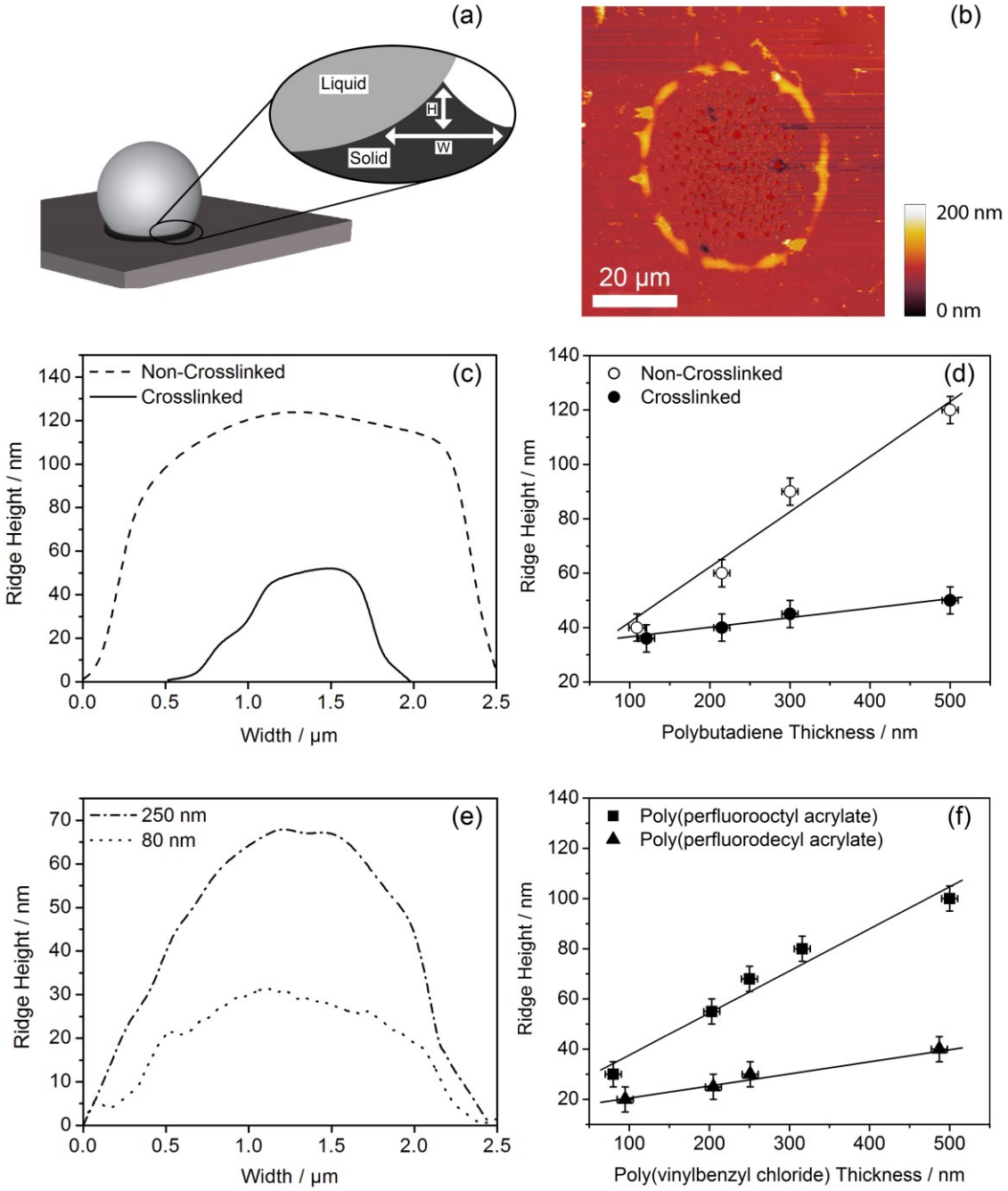

Figure 5.5: (a) Schematic of surface deformation induced by a 30 µm diameter water droplet impacting onto a soft surface; (b) AFM height image of surface after droplet impact upon poly(perfluorooctyl acrylate) brushes grown from 500 nm thick non-crosslinked CCl_4 plasma chlorinated polybutadiene; (c) height and width of wetting ridge following droplet impact upon poly(perfluorooctyl acrylate) brushes grown from 500 nm thick non-crosslinked and crosslinked CCl_4 plasma chlorinated polybutadiene; (d) ridge height of surface deformation as a function of CCl_4 plasma chlorinated polybutadiene underlayer thickness for poly(perfluorooctyl acrylate) brushes; (e) height and width of wetting ridge following droplet impact upon poly(perfluorooctyl acrylate) brushes grown from pulsed plasma deposited poly(vinylbenzyl chloride) initiator layers of different thicknesses; and (f) ridge height of surface deformation as a function of

pulsed plasma deposited poly(vinylbenzyl chloride) underlayer thickness for poly(perfluorooctyl acrylate) and poly(perfluorodecyl acrylate) brushes.

3.3 Perfluoroalkyl Polymer Brushes Surface Grafted From Pulsed Plasma Deposited poly(vinylbenzyl chloride) ATRP Initiator Layers

XPS analysis of the pulsed plasma deposited poly(vinylbenzyl chloride) layer confirmed complete coverage of the silicon substrate with no Si(2p) signal detected. In addition, the elemental composition correlates well to the predicted theoretical values based on the vinylbenzyl chloride precursor, thereby confirming good structural retention of the benzyl chloride functionality,[28] Table 5.4. Infrared spectroscopy provided further verification with the main fingerprint features closely matching those of the monomer:[28,39] CH_2-Cl wag (1263 cm^{-1}), benzyl ring stretches (1495 and 1603 cm^{-1}), Figure 5.6. Disappearance of the vinyl double bond (1629 cm^{-1}) is consistent with polymerisation having taken place during pulsed plasma deposition.[28]

Table 5.4: XPS elemental compositions and static water contact angles for: (a) pulsed plasma deposited poly(vinylbenzyl chloride); (b) ATRP poly(perfluorooctyl acrylate) brushes grown from (a); and (c) ATRP poly(perfluorodecyl acrylate) brushes grown from (a).

		XPS Elemental Composition / ±0.5%				Static Contact Angles	
		% C	% F	% Cl	% O	Microlitre / ±2°	Picolitre / ±5°
(a) Pulsed plasma deposited poly(vinylbenzyl chloride)	Theoretical	90.0	0.0	10.0	0.0	–	–
	Experimental	86.8	0.0	9.6	3.6	80	65
(b) ATRP Poly($CF_3(CF_2)_5$ acrylate) brushes grown from (a)	Theoretical	40.7	48.2	3.7	7.4	–	–
	Experimental	51.0	40.5	1.5	7.0	118	102
(c) ATRP Poly($CF_3(CF_2)_7$ acrylate) brushes grown from (a)	Theoretical	39.4	51.5	3.0	6.1	–	–
	Experimental	41.9	49.8	2.7	5.6	124	114

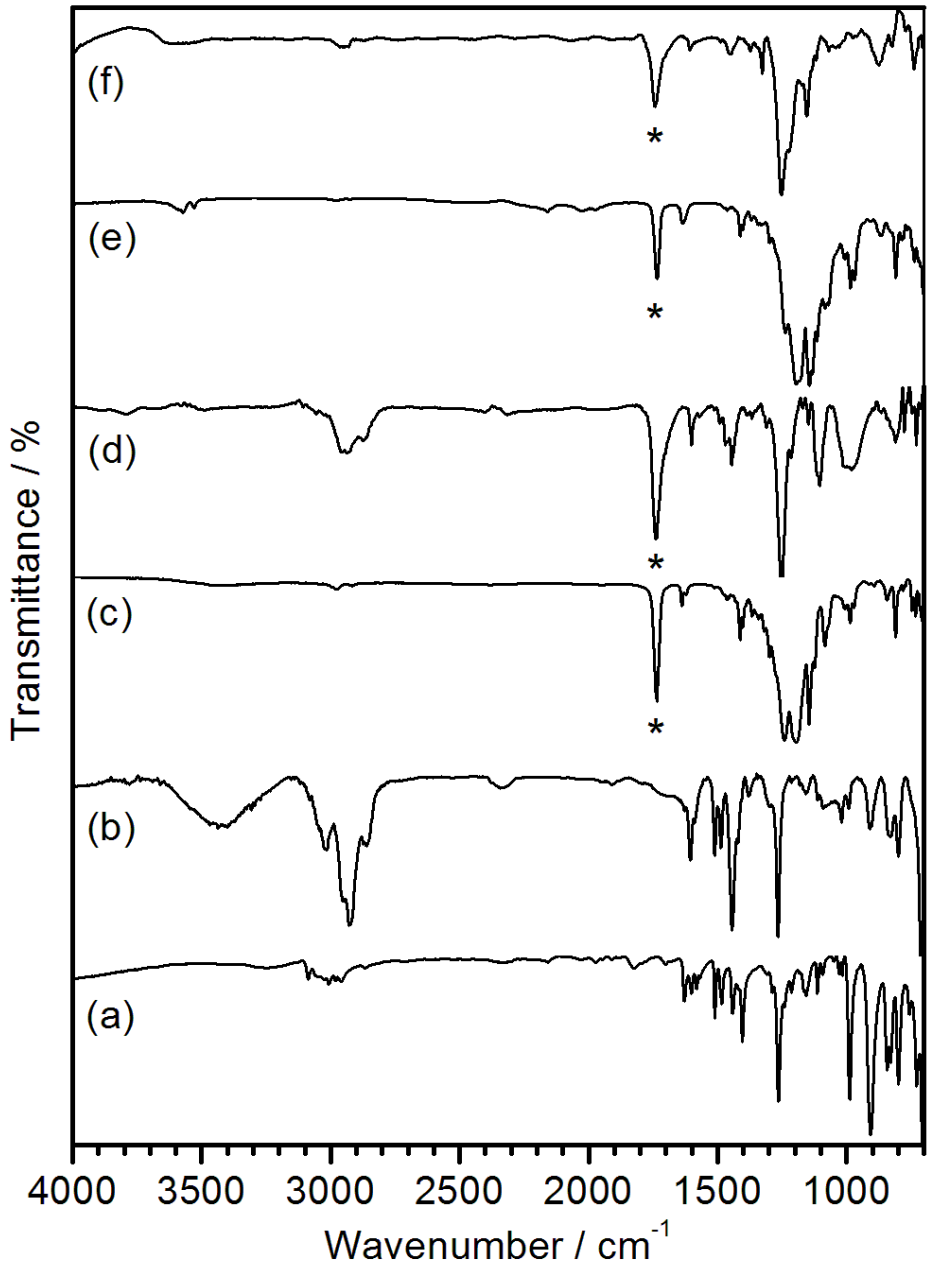

Figure 5.6: Infrared spectra of: (a) vinylbenzyl chloride monomer; (b) pulsed plasma deposited poly(vinylbenzyl chloride) (c) perfluorooctyl acrylate monomer; (d) 20 nm thick ATRP poly(perfluorooctyl acrylate) brushes grown from pulsed plasma deposited poly(vinylbenzyl chloride); (e) perfluorodecyl acrylate monomer; and (f) 20 nm thick ATRP poly(perfluorodecyl acrylate) brushes grown from pulsed plasma deposited poly(vinylbenzyl chloride). * Perfluoroalkyl acrylate carbonyl C=O peaks stretching (1734/1735 cm^{-1}) peaks.

Pulsed plasma deposited poly(vinylbenzyl chloride) was used as an initiator layer for the ATRP growth of poly(perfluorinated acrylate) brushes. ATRP growth of the poly(perfluorooctyl acrylate) polymer brushes from the pulsed plasma deposited poly(vinylbenzyl chloride) was confirmed by XPS and

infrared analysis, Table 5.4 and Figure 5.6. Elemental XPS compositions were found to be consistent with the growth of poly(perfluorooctyl acrylate) brushes containing an end capping chlorine as part of the ATRP mechanism.[42] Infrared assignments for perfluorooctyl acrylate monomer are as follows:[39] C=O stretching (1734 cm^{-1}), C=C stretching (1640 cm^{-1}), $C=CH_2$ in plane stretching (1412 cm^{-1}), $-CF_3$ stretching (1325 cm^{-1}), $-CF_2-$ antisymmetric stretching (1242 cm^{-1}), and $-CF_2-$ symmetric stretching (1145 cm^{-1}), Figure 5.6. Following surface ATRP grafting, the polymerisable alkene bond features (C=C stretching (1640 cm^{-1}) and $C=CH_2$ in plane stretching (1412 cm^{-1})) had disappeared.

ATRP growth of the poly(perfluorodecyl acrylate) polymer brushes from the pulsed plasma deposited poly(vinylbenzyl chloride) was confirmed by XPS and infrared analysis, Table 5.4 and Figure 5.6. Elemental XPS compositions were found to be consistent with the growth of poly(perfluorodecyl acrylate) brushes containing an end capping chlorine as part of the ATRP mechanism.[42] Infrared assignments for perfluorodecyl acrylate monomer are as follows:[39] C=O stretching (1735 cm^{-1}), C=C stretching (1636 cm^{-1}), $C=CH_2$ in plane stretching (1412 cm^{-1}), $-CF_3$ stretching (1327 cm^{-1}), $-CF_2-$ antisymmetric stretching (1195 cm^{-1}), and $-CF_2-$ symmetric stretching (1144 cm^{-1}), Figure 5.6. Following surface ATRP grafting, the alkene bond features (C=C stretching (1636 cm^{-1}) and $C=CH_2$ in plane stretching (1412 cm^{-1})) have disappeared due to polymerisation having taken place.

The oscillation frequency of picolitre droplets following impact onto these surfaces was found to be dependent upon the thickness of the underlying poly(vinylbenzyl chloride) ATRP initiator layer. By changing the perfluorinated acrylate monomer used for ATRP, the surface energy could be altered independently (higher water contact angle value for longer perfluorodecyl acrylate versus perfluorooctyl acrylate polymer brush side groups, Table 5.4). This showed that the dependence of oscillation frequency on the ATRP initiator layer thickness diminishes for droplets impacting upon surfaces with higher static contact angles, Figure 5.7. In both cases, the linear relationship between oscillation frequency and film thickness was found to breakdown beyond 500 nm, with the measured oscillation frequency plateauing at 51.6 kHz and 34.4 kHz for poly(perfluorooctyl acrylate) and poly(perfluorodecyl acrylate) brush surfaces respectively.

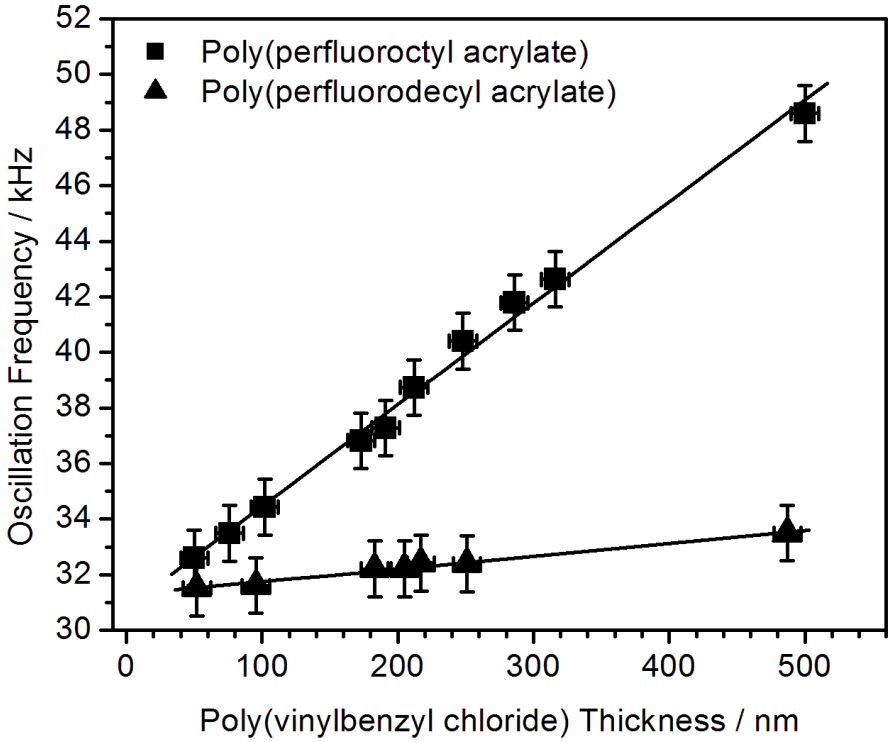

Figure 5.7: Oscillation frequencies of 30 μm diameter picolitre droplets following impact onto 20 nm thick poly(perfluorooctyl acrylate) brushes (picolitre contact angle = 102±5°) and 20 nm thick poly(perfluorodecyl acrylate) brushes (picolitre contact angle = 114±5°) grown from pulsed plasma deposited poly(vinylbenzyl chloride) ATRP initiator layers as a function of poly(vinylbenzyl chloride) underlayer thickness.

Following picolitre droplet impact experiments, the surface deformation was analysed by AFM. The height of the wetting ridge was found to increase with poly(vinylbenzyl chloride) ATRP initiator layer thicknesses upto 500 nm, Figure 5.5(d) and (f). For layer thicknesses above 500 nm, the deformation ridge height was 100–110 nm for poly(perfluorooctyl acrylate) ATRP brush surfaces and 40–45 nm for poly(perfluorodecyl acrylate) ATRP brush surfaces (which is consistent with the aforementioned plateauing of oscillation frequency beyond 500 nm poly(vinylbenzyl chloride) underlayer thickness).

The effect of underlayer thickness on the oscillation frequency of impacting picolitre droplets onto ATRP grown poly(perfluorooctyl acrylate) brushes was found to be dependent on the underlayer hardness, Figure 5.8(a). Impact onto softer films resulted in a larger surface deformation that is more dependent upon the underlayer thickness, Figure 5.8(b).

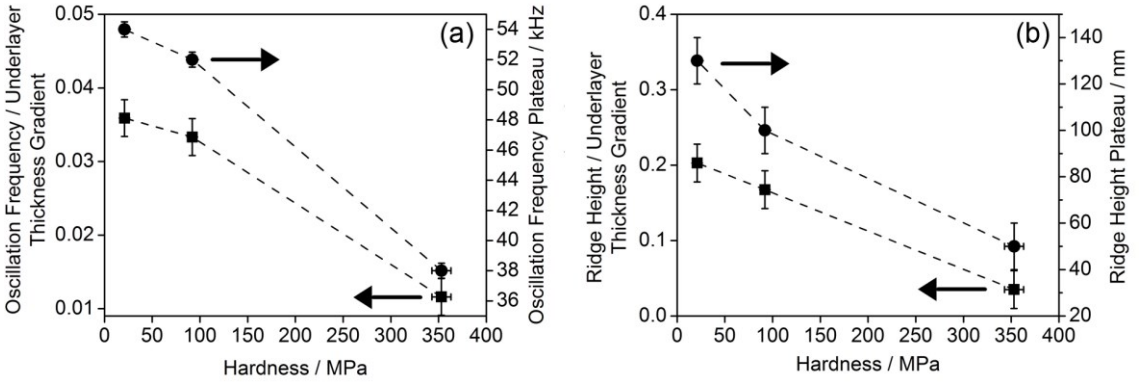

Figure 5.8: Effect of underlayer hardness upon: (a) drop oscillation frequency dependence on underlayer thickness and plateau and (b) surface deformation ridge height dependence on underlayer thickness and plateau after picolitre droplet impact upon 20 nm thick ATRP poly(perfluorooctyl acrylate)* brushes grown from initiator layers with varying underlayer hardness values. * Assuming similar polymer brush densities.

5.4 Discussion

Picolitre droplet impact has been studied for a range of hydrophobic surfaces with variable underlayer hardness. CF_4 plasma fluorinated polybutadiene provides a hydrophobic surface and can be crosslinked to alter its mechanical properties, Table 5.2.[25] Picolitre droplet impact onto these hydrophobic surfaces results in oscillation of the droplet height about a final static value, caused by excess energy not being fully dissipated through spreading. Unlike in the studies on rougher, superhydrophobic surfaces (Chapters 3 and 4),[31,38] the contact line remains pinned during the majority of the oscillation cycle, with only a small retraction evidenced after the initial spreading, Figure 5.2 (compared to Figure 3.4 (page 57) and Figure 4.9 (page 85)). The oscillation frequency of droplets after impact on these surfaces was found to depend upon the polybutadiene thickness and hardness. On soft (non-crosslinked) CF_4 plasma fluorinated polybutadiene, the oscillation frequency increased with increasing polymer film thickness. Whilst drop impact on a harder (crosslinked) polymer layer gives rise to lower oscillation frequencies and there is relatively little change in frequency observed across a range of thicknesses, Figure 5.3(a).

Surface initiated ATRP growth of hydrophobic poly(perfluoroalkyl acrylate) polymer brushes has been undertaken on CCl_4 plasma chlorinated polybutadiene (non-crosslinked and crosslinked) and pulsed plasma deposited

poly(vinylbenzyl chloride). By utilising the same poly(perfluorooctyl acrylate) ATRP polymer brushes (constant contact angle), the thickness dependence of the picolitre droplet dynamics of impact observed for the two different initiator layers (CCl_4 plasma chlorinated polybutadiene and pulsed plasma poly(vinylbenzyl chloride)) can be directly attributable to their mechanical properties, Table 5.2 and Figures 5.3, 5.7, and 5.8(a). The oscillation frequency on non-crosslinked polybutadiene is higher than on pulsed plasma deposited poly(vinylbenzyl chloride) at similar film thickness, Figures 5.3(b) and 5.7, because the polybutadiene layer is softer, Table 5.2.

Water droplet impact onto soft surfaces can lead to the formation of a wetting ridge. The extent of surface deformation is dependent upon the elastic shear modulus of the film and the contact angle of the droplet[43]

$$\zeta \propto \frac{\gamma \sin\theta}{G}, \qquad (5.1)$$

where ζ is the vertical displacement, γ is the liquid/vapour interfacial tension, θ is the equilibrium contact angle of the droplet, and G is the elastic shear modulus of the solid. In the present study, the vertical surface displacement following picolitre droplet impact upon ATRP polymer brush surfaces is found to be dependent upon the mechanical properties of the underlying ATRP initiator layer, Figure 5.8(b); harder films give rise to a smaller wetting ridge as predicted using Equation 5.1 (assuming linear relationship with elastic shear modulus[44]). This wetting ridge has a negligible effect on the static contact angles of picolitre droplets, which are found to remain constant within error across a wide range of underlayer thicknesses. However, the size of this ridge does affect the droplet dynamics. The observed rise in droplet oscillation frequency following impact with increasing film thickness for all of the surfaces investigated correlates to greater surface deformation (ridge height) for thicker films,[23,45,46,47] Figures 5.5 and 5.8.

By utilising different perfluoroalkyl chain length (hydrophobicity) ATRP polymer brushes grown from the same type of initiator layer (thereby ensuring similar mechanical properties of the bulk film), the effect of a change in the droplet shape shows that the frequency values are lower for the droplets with higher contact angles, as previously seen in Chapter 3.[38] In addition, the dependence of the oscillation frequency on the film thickness is found to be less

for droplets with higher static contact angles. Equation 5.1 shows that the degree of surface deformation is dependent upon the sine of the contact angle of the droplet, therefore, above 90°, a droplet with a higher contact angle would be expected to induce the formation of a smaller wetting ridge on a film with the same mechanical properties, resulting in a smaller change in frequency as the film thickness increases, Figure 5.7.

In all cases, oscillation frequency and extent of surface deformation are found to plateau above 500 nm underlayer thicknesses, regardless of the contact angle of the droplet or the mechanical properties of the film. This is most likely due to the size of the droplet (consistently 30 μm diameter) being able to induce the formation of a deformation of a certain height as suggested by theoretical studies.[48] Above 500 nm, the underlying film can be considered semi-infinite and further increases in thickness do not lead to a greater surface deformation.[46,49]

The dynamics of picolitre droplets following impact on soft surfaces and the resulting deformation are of relevance to microfluidics and inkjet printing.[50] Furthermore, such droplet impact studies provide a novel means to probe the mechanical properties of ultrathin films.[51]

5.5 Conclusions

The dynamics of picolitre water droplets following impact onto thin films is governed by the underlayer film thickness and mechanical hardness. Thicker films give rise to higher oscillation frequencies due to greater surface deformation (ridge formation) around the contact line.

5.6 References

[1] Gervais, T.; El-Ali, J.; Günther, A.; Jensen, K. F. Flow-induced deformation of shallow microfluidic channels. *Lab Chip* **2006**, *6*, 500.

[2] Pu, G.; Ai, J.; Severtson, S. J. Drop Behavior on a Thermally-Stripped Acrylic Polymer: Influence of Surface Tension Induced Wetting Ridge Formation on Retention and Running. *Langmuir* **2010**, *26*, 12696.

[3] Li, C.; Jiang, H. Electrowetting-driven variable-focus microlens on flexible surfaces. *Appl. Phys. Lett.* **2012**, *100*, 231105.

[4] Sokuler, M.; Auernhammer, G. K.; Roth, M.; Liu, C.; Bonacurrso, E.; Butt, H.-J. The Softer the Better: Fast Condensation on Soft Surfaces. *Langmuir* **2010**, *26*, 1544.

[5] Sirringhaus, H.; Kawase, T.; Friend, R. H.; Shimoda, T.; Inbasekaran, M.; Wu, W.; Woo, E. P. High-Resolution Inkjet Printing of All-Polymer Transistor Circuits. *Science* **2000**, *290*, 2123.

[6] Wang, J. Z.; Zheng, Z. H.; Li, H. W.; Huck, W. T. S.; Sirringhaus, H. Dewetting of conducting polymer inkjet droplets on patterned surfaces. *Nat. Mater.* **2004**, *3*, 171.

[7] Sele, C. W.; von Werne, T.; Friend, R. H.; Sirringhaus, H. Lithography-Free, Self-Aligned Inkjet Printing with Sub-Hundred-Nanometer Resolution. *Adv. Mater.* **2005**, *17*, 997.

[8] Doggart, J.; Wu, Y.; Liu, P.; Zhu, S. Facile Inkjet-Printing Self-Aligned Electrodes for Organic Thin-Film Transistor Arrays with Small and Uniform Channel Length. *ACS Appl. Mater. Interfaces* **2010**, *2*, 2189.

[9] Barbulovic-Nad, I.; Lucente, M.; Sun, Y.; Zhang, M.; Wheeler, A. R.; Bussmann, M. Bio-Microarray Fabrication Techniques—A Review. *Crit. Rev. Biotechnol.* **2006**, *26*, 237.

[10] Tan, C. P.; Cipriany, R.; Lin, D. M.; Craighead, H. G. Nanoscale Resolution, Multicomponent Biomolecular Arrays Generated By Aligned Printing With Parylene Peel-Off. *Nano Lett.* **2010**, *10*, 719.

[11] Arrabito, G.; Pignataro, B. Inkjet Printing Methodologies for Drug Screening. *Anal. Chem.* **2010**, *82*, 3104.

[12] Mironov, V.; Boland, T.; Trusk, T.; Forgacs, G.; Markwald, R. R. Organ printing: computer-aided jet-based 3D tissue engineering. *Trends Biotechnol.* **2003**, *21*, 157.

[13] Xu, T.; Jin, J.; Gregory, C.; Hickman, J. J.; Boland, T. Inkjet printing of viable mammalian cells. *Biomaterials* **2005**, *26*, 93.

[14] Bharathan, J.; Yang, Y. Polymer electroluminescent devices processed by inkjet printing: I. Polymer light-emitting logo. *Appl. Phys. Lett.* **1998**, *72*, 2660.

[15] Chang, S.-C.; Bharathan, J.; Yang, Y.; Helgeson, R.; Wudl, F.; Ramey, M. B.; Reynolds, J. R. Dual-color polymer light-emitting pixels processed by hybrid inkjet printing. *Appl. Phys. Lett.* **1998**, *73*, 2561.

[16] Shanahan, M. E. R. The influence of solid micro-deformation on contact angle equilibrium. *J. Phys. D: Appl. Phys.* **1987**, *20*, 945.

[17] Shanahan, M. E. R. The spreading dynamics of a liquid drop on a viscoelastic solid. *J. Phys. D: Appl. Phys.* **1988**, *21*, 981.

[18] Extrand, C. W.; Kumagai, Y. Contact Angles and Hysteresis on Soft Surfaces. *J. Colloid Interface Sci.* **1996**, *184*, 191.
[19] White, L. R. The contact angle on an elastic substrate. 1. The role of disjoining pressure in the surface mechanics. *J. Colloid Interface Sci.* **2003**, *258*, 82.
[20] Pericet-Cámara, R.; Best, A.; Butt, H.-J.; Bonaccurso, E. Effect of Capillary Pressure and Surface Tension on the Deformation of Elastic Surfaces by Sessile Liquid Microdrops: An Experimental Investigation. *Langmuir* **2008**, *24*, 10565.
[21] Pericet-Camara, R.; Auernhammer, G. K.; Koynov, K.; Lorenzoni, S.; Raiteri, R.; Bonaccurso, E. Solid-supported thin elastomer films deformed by microdrops. *Soft Matter* **2009**, *5*, 3611.
[22] Shanahan, M. E. R.; Carré, A. Viscoelastic Dissipation in Wetting and Adhesion Phenomena. *Langmuir* **1995**, *11*, 1396.
[23] Pu, G.; Severtson, S. J. Dependence of Wetting Behavior on the Thickness of Highly Viscoelastic Films. *J. Phys. Chem. C* **2011**, *115*, 18729.
[24] Rioboo, R.; Voué, M.; Adão, Conti, J.; Vaillant, A.; Seveno, D.; De Coninck, J. Drop Impact on Soft Surfaces: Beyond the Static Contact Angles. *Langmuir* **2010**, *26*, 4873.
[25] Woodward, I.; Schofield, W. C. E.; Roucoules, V.; Badyal, J. P. S. Super-hydrophobic Surfaces Produced by Plasma Fluorination of Polybutadiene Films. *Langmuir* **2003**, *19*, 3432.
[26] Wang, J.-S.; Matyjaszewski, K. Controlled/"living" radical polymerization. atom transfer radical polymerization in the presence of transition-metal complexes. *J. Am. Chem. Soc.* **1995**, *117*, 5614.
[27] Granville, A. M.; Brittain, W. J. Stimuli-Responsive Semi-Fluorinated Polymer Brushes on Porous Silica Substrates. *Macromol. Rapid Commun.* **2004**, *25*, 1298.
[28] Teare, D. O. H.; Barwick, D. C.; Schofield, W. C. E.; Garrod, R. P.; Ward, L. J.; Badyal, J. P. S. Substrate-Independent Approach for Polymer Brush Growth by Surface Atom Transfer Radical Polymerization. *Langmuir* **2005**, *21*, 11425.
[29] Harshbarger, W. R.; Porter, R. A.; Miller, T. A.; Norton, P. A Study of the Optical Emission from an rf Plasma during Semiconductor Etching. *Appl. Spectrosc.* **1977**, *31*, 201.
[30] Grill, V.; Walder, G.; Scheier, P.; Kurdel, M.; Märk, T. D. Absolute partial and total electron impact ionization cross sections for C_2H_6 from threshold up to 950 eV. *Int. J. Mass Spectrom. Ion Processes* **1993**, *129*, 31.
[31] Brown, P. S.; Talbot, E. L.; Wood, T. J.; Bain, C. D.; Badyal, J. P. S. Superhydrophobic Hierarchical Honeycomb Surfaces. *Langmuir* **2012**, *28*, 13712.
[32] Tabet, M. F.; McGahan, W. A. Use of artificial neural networks to predict thickness and optical constants of thin films from reflectance data. *Thin Solid Films* **2000**, *370*, 122.
[33] ASTM Standard E384 - 11e1, " Standard Test Method for Knoop and Vickers Hardness of Materials," ASTM International, West

Conshohocken, PA, 2011, DOI: 10.1520/E0384-11E01, www.astm.org (accessed Jul. 29 2013).
[34] Raghavan, D.; Gu, X.; Nguyen, T.; VanLandingham, M.; Karim, A. Mapping Polymer Heterogeneity Using Atomic Force Microscopy Phase Imaging and Nanoscale Indentation. *Macromolecules* **2000**, *33*, 2573.
[35] Strobel, M.; Corn, S.; Lyons, C. S.; Korba, G. A. Plasma fluorination of polyolefins. *J. Polym. Sci. Part A: Polym. Chem.* **1987**, *25*, 1295.
[36] Inagaki, N.; Tasaka, S.; Imai, M. Hydrophilic surface modification of polypropylene films by CCl_4 plasma. *J. Appl. Polym. Sci.* **1993**, *48*, 1963.
[37] Good, R. J.; Koo, M. N. The effect of drop size on contact angle. *J. Colloid Inter. Sci.* **1979**, *71*, 283.
[38] Brown, P. S.; Berson, A.; Talbot, E. L.; Wood, T. J.; Schofield, W. C. E.; Bain, C. D.; Badyal, J. P. S. Impact of Picoliter Droplets on Superhydrophobic Surfaces with Ultralow Spreading Ratios. *Langmuir* **2011**, *27*, 13897.
[39] Lin-Vien, D.; Colthrup, N. B.; Fateley, W. G.; Grasselli, J. G. *The Handbook of Infrared and Raman Characteristic Frequencies of Organic Molecules*; Academic Press, Inc.: San Diego, 1991.
[40] Gao, L.; McCarthy, T. J. Contact Angle Hysteresis Explained. *Langmuir* **2006**, *22*, 6234.
[41] Mao, T.; Kuhn, D. C. S.; Tran, H. Spread and rebound of liquid droplets upon impact on flat surfaces. *AIChE J.* **1997**, *43*, 2169.
[42] Zhang, H.; Schubert, U. S. *J. Polym. Sci., Part A: Polym. Chem.* **2004**, *42*, 4882.
[43] Shanahan, M. E. R.; Carré, A. Spreading and dynamics of liquid drops involving nanometric deformations on soft substrates. *Colloids Surf., A* **2002**, *206*, 115.
[44] Gubicza, J.; Juhász, A.; Tasnádi, P.; Arató, P.; Vörös, G. Determination of the hardness and elastic modulus from continuous Vickers indentation testing. *J. Mater. Sci.* **1996**, *31*, 3109.
[45] Voué, M.; Rioboo, R.; Bauthier, C.; Conti, J.; Charlot, M.; De Coninck, J. Dissipation and moving contact lines on non-rigid substrates. *J. Eur. Ceram. Soc.* **2003**, *23*, 2769.
[46] Yu, Y.-S.; Yang, Z.; Zhao, Y.-P. Role of Vertical Component of Surface Tension of the Droplet on the Elastic Deformation of PDMS Membrane. *J. Adhes. Sci. Technol.* **2008**, *22*, 687.
[47] Yu, Y.-S.; Zhao, Y.-P. Elastic deformation of soft membrane with finite thickness induced by a sessile liquid droplet. *J. Colloid. Interface. Sci.* **2009**, *339*, 489.
[48] Style, R. W.; Dufresne, E. R. Static Wetting On Deformable Substrates, from Liquid to Soft Solids. *Soft Matter* **2012**, *8*, 7177.
[49] Yu, Y.-S. Substrate elastic deformation due to vertical component of liquid-vapor interfacial tension. *Appl. Math. Mech. -Engl. Ed.* **2012**, *33*, 1095.
[50] Calvert, P. Inkjet Printing for Materials and Devices. *Chem. Mater.* **2001**, *13*, 3299.
[51] Long, D.; Ajdari, A.; Leibler, L. Static and Dynamic Wetting Properties of Thin Rubber Films. *Langmuir* **1996**, *12*, 5221.

Chapter 6 Droplet Impact onto Charged Polymer Surfaces

6.1 Introduction

The role of substrate surface chemistry, roughness, and subsurface mechanical properties on droplet impact has been outlined in the previous chapters. Another property that can affect droplet impact and spreading is the presence of surface charge. The impact and spreading of liquid droplets upon plastic surfaces is of increasing importance in microfluidics,[1,2,3] filtration,[4] and inkjet printing[5] with the latter finding use in microelectronics,[6,7,8,9] pharmaceutical dosing or screening,[10,11,12] tissue engineering,[13,14] and optics.[15,16] Due to their non-conducting nature, such substrates are prone to charge build-up on their surfaces,[17] which has been found to be detrimental to printing process, causing electrostatic attraction of the ink droplets and leading to unexpected results.[18,19,20,21] Droplets on superhydrophobic silane surfaces have been observed to move against gravity to a region of higher charge density; such behaviour is dependent upon the degree of surface charge and the contact angle hysteresis of the droplet.[22]

The interaction of water droplets and charged surfaces is also of importance for filtration products.[4] Porous polymer networks are found to exhibit improved filtration abilities if they contain surface charges due to the electrostatic attraction of particulates and water droplets.[23,24] Despite this, the effect on impact of a liquid droplet upon a charged polymer surface has received little focus, the majority of work being on the behaviour of static droplets on conducting surfaces for use in optical switches[25] and electrowetting;[26] or droplet impact on conducting surfaces for use in continuous inkjet[27] and electrospray[28,29] deposition techniques.[30]

In this chapter, the effect of surface charge on the impact of picolitre droplets of water upon polystyrene, PTFE, and O_2 plasma treated PTFE was investigated. Variation of O_2 plasma treatment has been shown to result in varying levels of surface roughness,[31,32,33] resulting in different static contact angles and contact angle hysteresis.[31] The presence of surface charge was

found to cause an increase in picolitre droplet impact velocity resulting in a change in the static contact angle, depending upon the hysteresis.

6.2 Experimental

Polystyrene (Goodfellow Cambridge Ltd.) and polytetrafluoroethylene sheets (PTFE, Goodfellow Cambridge Ltd.) were used as substrates. Plasmachemical treatment of PTFE was undertaken in a cylindrical glass reactor of similar design to that used in Section 3.2.1 (page 52). A piece of PTFE was placed into the reactor at ambient temperature, followed by evacuation to base pressure. O_2 gas (+99.5% purity, BOC Ltd.) was then admitted into the system via a needle valve at a pressure of 0.2 mbar and 2 cm^3 min^{-1} flow rate, and the electrical discharge ignited at various powers for 2 min. Upon completion of surface functionalization, the gas feed was switched off and the chamber vented to atmosphere.

Surface elemental compositions were determined by X-ray photoelectron spectroscopy (XPS) using a VG ESCALAB II electron spectrometer as described in Section 3.2.2 (page 52). Surface elemental compositions were calculated using sensitivity factors derived from chemical standards, C(1s): O(1s): F(1s) equals 1.00: 0.34: 0.26.

Atomic force microscopy (AFM) images were collected in tapping mode at 20 °C in ambient air (Digital Instruments Nanoscope III, Santa Barbara, CA). The stiff silicon cantilever had a spring constant of 42–83 N m^{-1} (Nanoprobe). Root-mean-square (RMS) roughness values were calculated over 10 μm x 10 μm scan areas.

Microlitre sessile drop contact angle analysis was carried out with a video capture system (VCA2500XE, AST Products Inc.) using 1.0 μL dispensation of de-ionised water (BS 3978 grade 1). Advancing and receding angles were measured by respectively increasing and decreasing the droplet size until the contact line was observed to move.[34]

Surface charge was applied to substrates through the use of a piezo-electric anti-static gun (Zerostat® 3, Structure Probe, Inc.). By pressing the trigger, the piezo crystal is compressed generating a voltage, which is applied to a sharp tip at the end of the gun causing ionisation of the surrounding atmosphere. When the trigger is released the piezo expands and a potential of

opposite polarity is generated.[35] Placing an uncharged, non-conducting substrate within range of the gun causes the induction of a surface potential.[36] Pressing or releasing the trigger in close proximity to the substrate surface achieved positive and negative surface potentials respectively. By holding the gun at different heights above the substrate it is possible to achieve different surface potentials, which were measured using an electrostatic voltmeter (Isoprobe® 244, Monroe Electronics, Inc.) with a probe–surface spacing of 5 mm.

Picolitre drop impact studies were carried out using an imaging rig as described in Section 3.2.3 (page 53). The piezo-type nozzle (MicroFab MJ-ABP-01, Horizon Instruments Ltd.) had an aperture diameter of 30 μm, generating water drops of 30 μm diameter (14 pL).

6.3 Results

6.3.1 Polystyrene

XPS elemental compositions of polystyrene surfaces were found to be consistent with theoretical and literature[37,38] values, Table 6.1. Flat polystyrene substrate surfaces were charged by exposure to a piezo-electric gun. Charging the substrate was not found to alter the surface chemistry, Table 6.1. Bringing a microlitre droplet of water into close proximity led to attraction and eventually the jumping of the microlitre droplet from the syringe needle to the surface, Figure 6.1. The height at which the droplet snapped to the surface (d_s) was found to be dependent upon the magnitude of the surface potential on the substrate, Figure 6.2.

Table 6.1: XPS elemental composition of uncharged and charged polystyrene.

Polystyrene	XPS Elemental Composition / ±0.5%	
	% C	% O
Theoretical	100.00	0.0
Uncharged	99.7	0.3
Charged	99.6	0.4

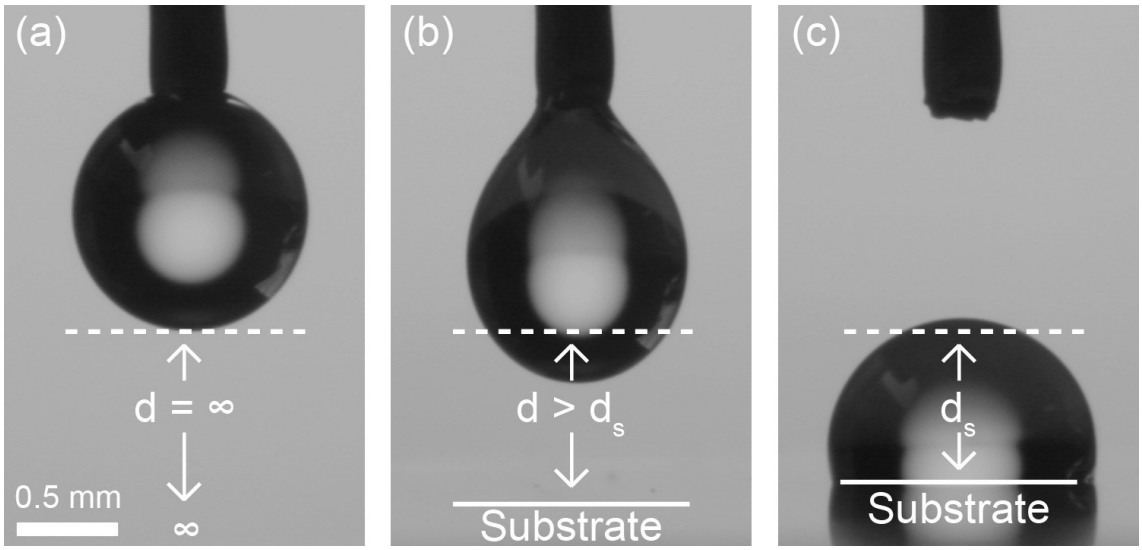

Figure 6.1: Charged substrate moving towards a microlitre (1 μL) droplet of water: (a) in air; (b) deformation due to attraction between charged surface and electrostatically induced charge on the droplet; and (c) following detachment from the syringe occurring at a 'snap distance', d_s. Where d is the distance from the substrate to the original position of the bottom of the drop.

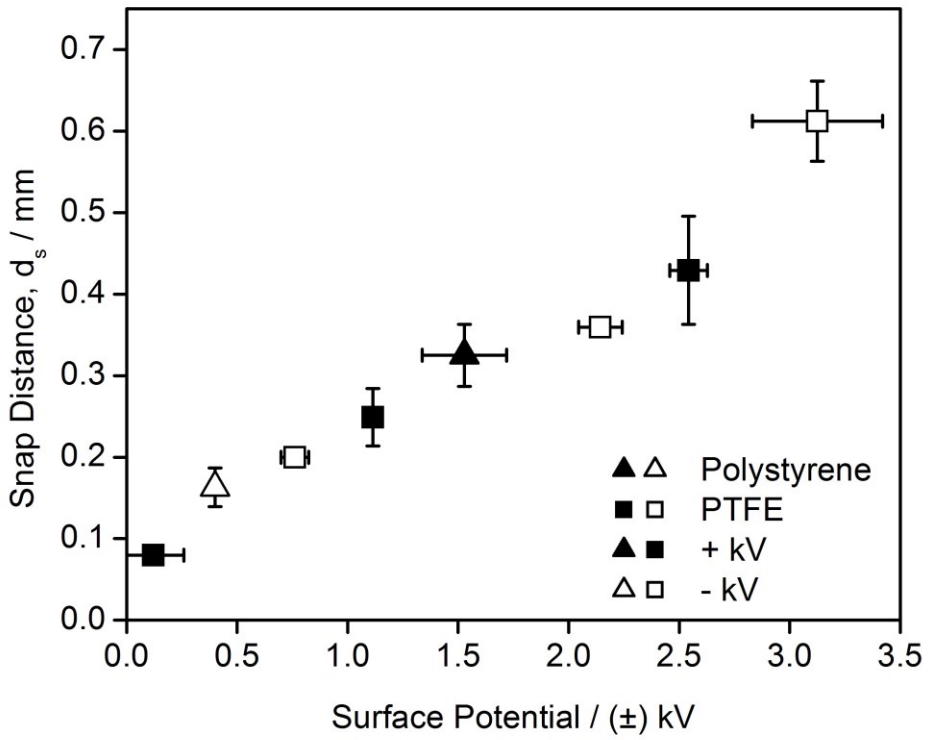

Figure 6.2: Snap distance (separation between bottom of water droplet in air (d=∞) and position of surface at threshold for droplet jumping, d_s) as a function of surface potential for flat polystyrene and PTFE substrates (other substrates such as polyvinylchloride (Goodfellow Cambridge Ltd.) and Nylon-6 (Goodfellow Cambridge Ltd.) fit this trend). Uncharged substrates were not found to induce deformation or jumping of the droplet (d_s = 0).

Picolitre droplet impact onto uncharged polystyrene surfaces yielded a static contact angle of 92±3°, Table 6.2. Upon charging, droplet impact velocities were found to increase with rising surface potential resulting in larger static contact angles, Figures 6.3 and 6.4. Droplet impact velocities exceeding 3 m s^{-1} gave static contact angles of 118±2°, Figure 6.4.

Table 6.2: AFM RMS roughness and water contact angles for uncharged: (a) flat polystyrene; (b) untreated PTFE; (c) 30 W O_2 plasma treated PTFE; and (d) 80 W O_2 plasma treated PTFE.

	AFM RMS Roughness / nm	**Microlitre Contact Angle / °**				**Picolitre Static Contact Angle / °**
		Static	**Advancing**	**Receding**	**Hysteresis**	
(a) Polystyrene	7.4±1	91±1	95±1	87±1	8±1	92±3
(b) Untreated PTFE	59.7±5	111±1	115±1	102±1	13±1	120±3
(c) 30 W O_2 plasma treated PTFE	89.3±5	123±1	126±2	97 ±2	29±2	118±3
(d) 80 W O_2 plasma treated PTFE	174.7±5	133±1	138±1	22±2	116±2	110±3

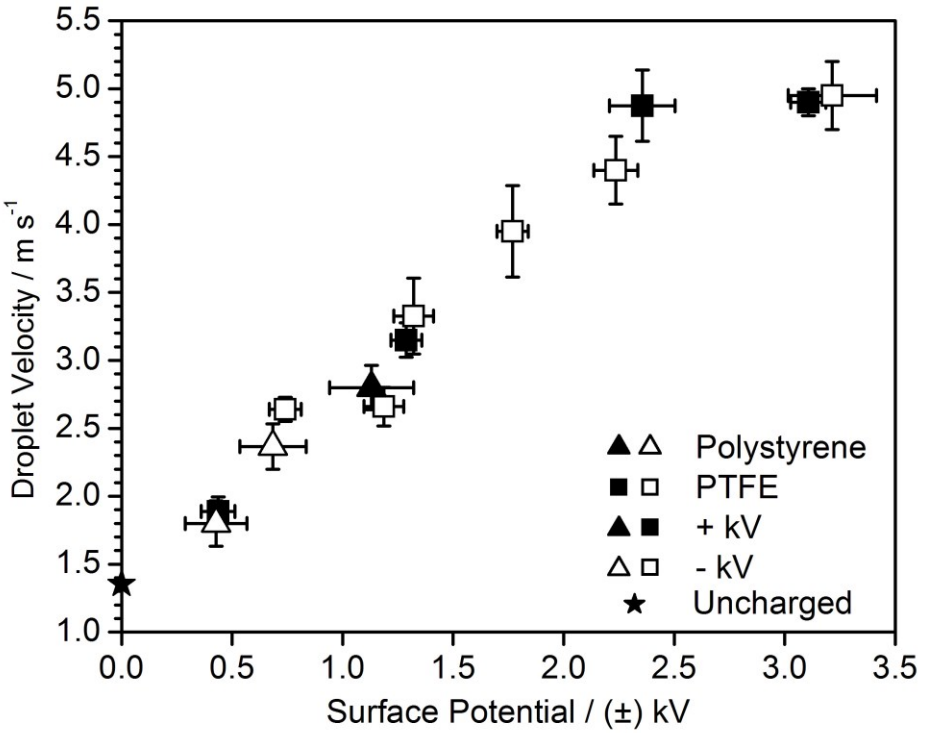

Figure 6.3: Picolitre droplet velocity prior to impact as a function of surface potential on flat polystyrene and PTFE substrates (other substrates such as polyvinylchloride (Goodfellow Cambridge Ltd.) and Nylon-6 (Goodfellow Cambridge Ltd.) fit this trend). Drop velocities prior to impact on uncharged surfaces were 1.2–1.5 m s^{-1}.

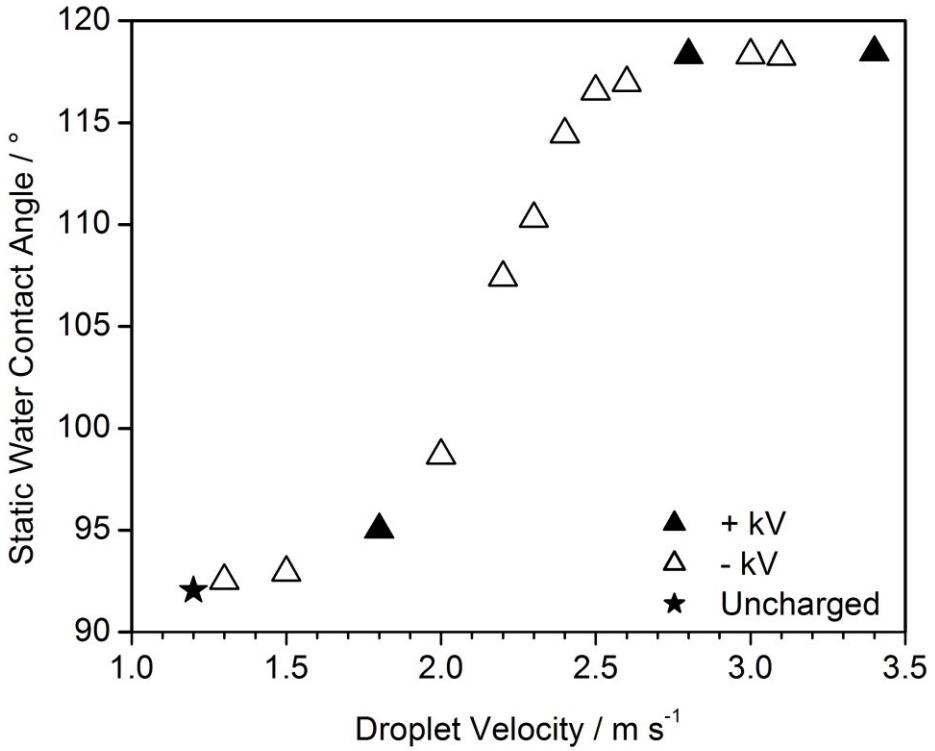

Figure 6.4: Picolitre static contact angle as a function of water droplet velocity prior to impact onto charged, flat polystyrene.

6.3.2 PTFE

XPS elemental compositions of untreated PTFE surfaces were found to be consistent with theoretical values, Table 6.3. Following O_2 plasma roughening, the elemental composition remained relatively unchanged, as found in previous studies.[31,32,33]

Table 6.3: XPS elemental composition of untreated and O_2 plasma treated PTFE.

PTFE	XPS Elemental Composition / ±0.5%		
	% C	% F	% O
Theoretical	33.3	66.7	0.0
Untreated	33.1	66.7	0.2
30 W O_2 Plasma Treated	33.7	65.1	1.2
80 W O_2 Plasma Treated	33.2	65.3	1.5

Atomic force microscopy (AFM) was carried out to determine the extent of O_2 plasma texturing of the PTFE surfaces, Figure 6.5. A higher plasma treatment power was found to result in greater RMS roughness and enhanced hydrophobicity,[31,32,33] in conjunction with larger contact angle hysteresis, Table 6.2. This trend for contact angle hysteresis is consistent with previous work[31] and theoretical studies[39] showing hysteresis increases with roughness when the droplets are in the Wenzel state.[40] Similar behaviour could be achieved through roughening the PTFE via sonication for 2 h in a cyclohexane (>99% purity, Fisher Scientific UK Ltd.)–propan-2-ol (>99.5% purity, Fisher Scientific UK Ltd.) mixture. These roughened surfaces (RMS = 130.9±5 nm) were also found to exhibit increased static contact angles (130±2°) and contact angle hysteresis (63±2°).

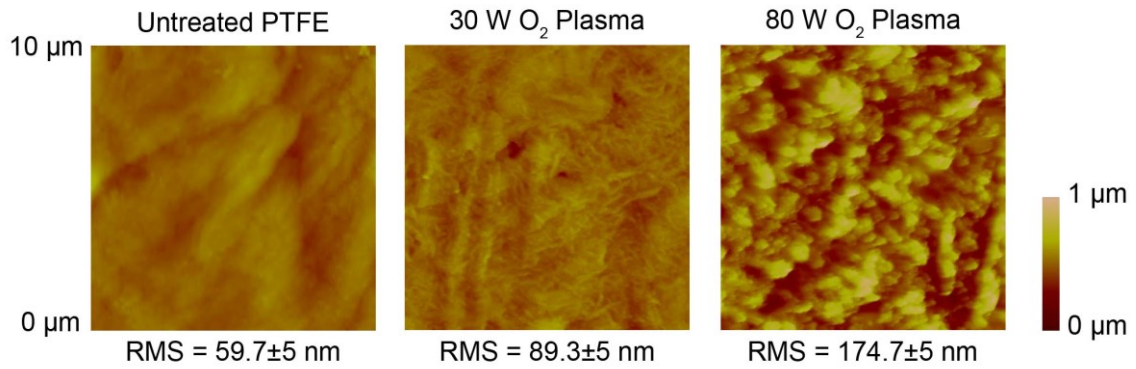

Figure 6.5: AFM images and RMS roughness values for untreated PTFE and O_2 plasma textured PTFE.

Picolitre water droplets impacting onto uncharged, O_2 plasma textured PTFE showed that increased surface roughness leads to a lower static contact angle, Table 6.2. By charging the PTFE substrates, the impact velocity of picolitre water droplets was enhanced, Figure 6.3. The picolitre droplet static contact angle was found to be influenced by the droplet velocity and the roughness of the PTFE substrate, Figure 6.6. For the untreated PTFE substrate, the static contact angles were found to be independent of impact velocities for droplet speeds below 3 m s^{-1}. Above 3 m s^{-1} the static contact angle was found to increase rapidly until droplets were observed to bounce after impact at velocities exceeding 4 m s^{-1}, Figure 6.6(a). For O_2 plasma textured PTFE substrates, the effect of droplet impact speed on static contact angle was influenced by surface roughness (and therefore droplet hysteresis which was seen in Chapter 4 (page 84) to be similar for microlitre and picolitre droplets[41]). In the case of 90 nm RMS roughness, the static contact angle is found to decrease as the droplet velocity increases upto 3 m s^{-1}. However above 3 m s^{-1}, further increases in the droplet velocity results in an increase in the static water contact angle, Figure 6.6(b). For the 175 nm RMS roughness plasma treated PTFE substrates, the static contact angle decreases with increasing droplet velocity across the entire range of velocities studied, Figure 6.6(c).

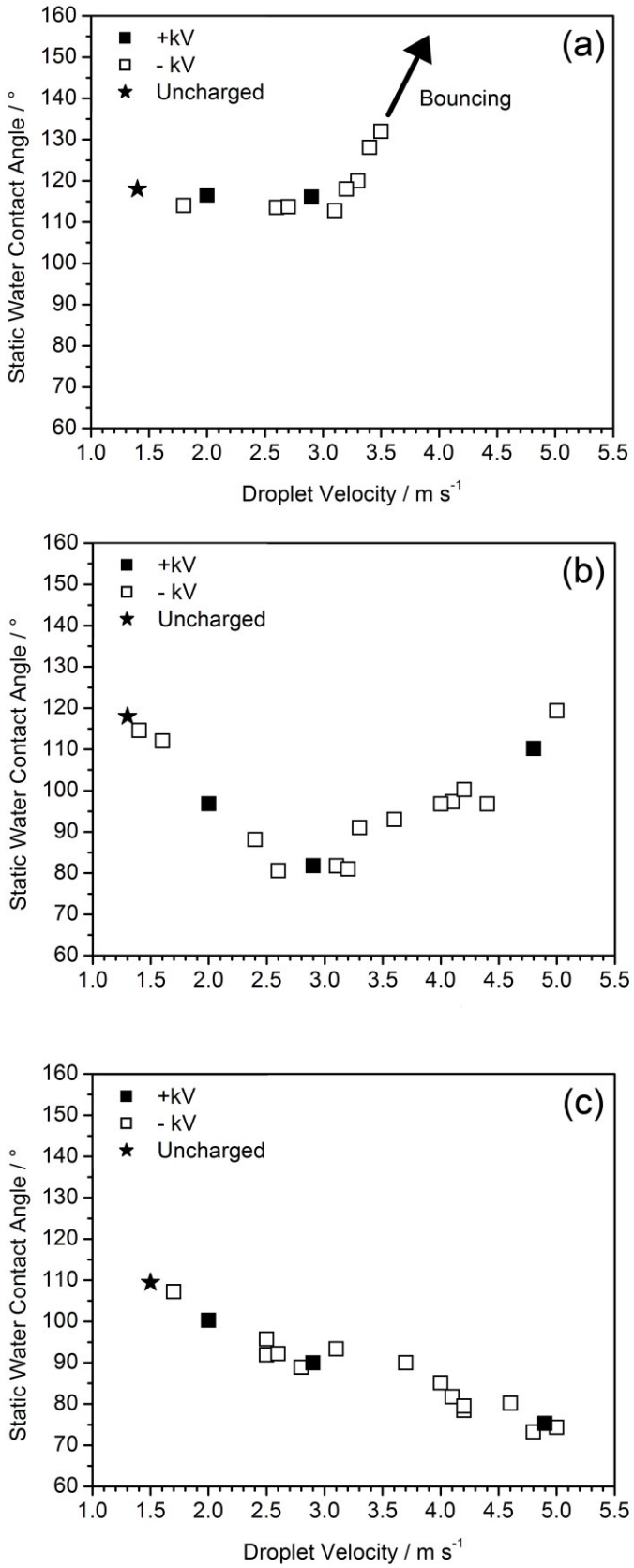

Figure 6.6: Picolitre static contact angle as a function of drop velocity prior to impact onto charged: (a) untreated PTFE; (b) 30 W O_2 plasma treated PTFE; and (c) 80 W O_2 plasma treated PTFE.

6.4 Discussion

Polystyrene and PTFE surfaces can be charged via treatment with an anti-static gun.[36] Microlitre water contact angle analysis of charged surfaces was found to result in the electrostatic induction of the droplet as the surface is brought into close proximity. This induced charge is attracted to the substrate surface charge, causing deformation and eventual jumping of the droplet from the syringe to the surface, Figure 6.1. By increasing the surface potential, the height from the substrate at which a droplet would snap to the surface increased, Figure 6.2. This behaviour was found to be independent of the surface chemistry and topography and was confirmed to occur for other polymer surfaces (Nylon-6 (Goodfellow Cambridge Ltd.) and polyvinylchloride (Goodfellow Cambridge Ltd.)) charged in a similar manner.

O_2 plasma treatment of PTFE causes surface texturing without alteration of the chemistry of the polymer, resulting in an increase in the static contact angle of microlitre droplets of water.[31,32,33] The resulting surfaces also exhibit varying levels of contact angle hysteresis, dependent upon the extent of surface roughness, Table 6.2 and Figure 6.5. For uncharged substrates, the static contact angle of impacting picolitre droplets of water was dependent upon the surface roughness and therefore hysteresis. A higher hysteresis resulted in a lower static contact angle due to the contact line being unable to retract after initial spreading following droplet impact, Table 6.2.

The impact of picolitre droplets onto polystyrene, untreated PTFE, and O_2 plasma treated PTFE substrates was also found to be dependent upon the magnitude of the surface potential. Droplets were attracted to the charged surfaces, causing droplet acceleration and resulting in an increase in the impact velocity with increasing surface potential, Figure 6.3.

The higher impact speeds caused by this attraction to a charged substrate were found to result in a change in the impact behaviour. For polystyrene substrates an increase in droplet velocity resulted in an increase in the static contact angle, Figure 6.4. This is due to the greater amount of inertial energy available after initial spreading of the droplet causing an increase in contact line retraction and therefore a higher contact angle. For the case of the untreated PTFE substrates, the change in velocity had little effect on the static

contact angle upto speeds of 3 m s^{-1} due to the higher hysteresis compared to polystyrene, Table 6.2. However above 3 m s^{-1} droplets were found to display higher static contact angles after impact and above 4 m s^{-1} the amount of excess energy not dissipated during spreading (due to the lower surface energy of PTFE compared to polystyrene) is sufficient to cause the droplets to bounce, Figure 6.6(a).

For O_2 plasma treated PTFE substrates, the effect of increased droplet velocities is dependent upon the degree of hysteresis experienced by the water droplets. For low power treatments (30 W), there is an increase in hysteresis compared to that on the untreated PTFE surface, Table 6.2. The higher hysteresis means that there is an initial decrease in static contact angles as a function of droplet velocity (upto 3 m s^{-1}) due to the greater impact speed causing an increase in the maximum spreading diameter of the droplet but not sufficiently enough for the droplet to reach the receding contact angle (i.e. droplet contact line becomes pinned).[42] However, at higher impact velocities (over 3 m s^{-1}) there is sufficient energy after initial droplet spreading for the bulk of the droplet to pull the contact angle to below the receding angle, which allows for retraction of the contact line and therefore an increase in static contact angle with increasing impact velocity, Figure 6.6(b) and Scheme 6.1.

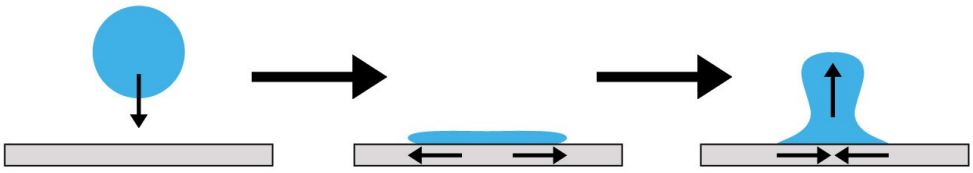

Scheme 6.1: Schematic of droplet impact. At higher velocities, the droplet retains sufficient energy after initial spreading to pull the contact angle to below the receding angle allowing contact line retraction, which results in a higher static contact angle.

For higher power treatments (80 W), the surface roughness is much greater and the receding angle is lower, Table 6.2. For the entire range of velocities studied, the static contact angle decreases with increasing impact velocity, Figure 6.6(c) as there is no retraction of the contact line after impact. A similar change in static contact angle was possible by increasing the dropping height of microlitre droplets pipetted onto uncharged PTFE surfaces (higher dropping heights leading to higher velocities and lower static contact angles).

In the current study, the parameters used to generate the droplet are kept constant and any variation in droplet impact velocities is achieved through changing the substrate surface potential, causing a varying degree of droplet attraction and acceleration. Similar results were obtained for both positive and negatively charged surfaces; with the droplet acceleration towards the substrate suggesting that the droplet undergoes charging during drop generation in the nozzle. The presence of a negatively charged surface results in the electrostatic induction of a positive charge in the droplets as they are jetted from the bulk liquid in the nozzle.[43,44,45] These positively charged droplets are then accelerated towards the negatively charged substrate after jetting. The exact nature of the migrating charged species (for example, dissolved ions in water) is unknown and requires further study.

The surface potentials utilised are below what is generally considered an acceptable level of surface charge for applications such as inkjet printing,[20] however this work has demonstrated that issues caused by electrostatic attraction of ink drops can still arise even at these low surface potentials (similar behaviour has been found for more ink-relevant solvents such as alcohols and glycol ethers, though the impact speeds onto uncharged substrates were lower than those typically used in industry). With greater focus on the inkjet printing of materials onto plastic substrates,[46,47] the issue of static build-up on the substrate (common during roll-to-roll processing[48]) and its effect on drop impact and spreading will become increasingly important.

6.5 Conclusions

Increased droplet velocities due to electrostatic attraction between charged polymer substrates and picolitre droplets of water results in varying impact behaviour that can depend upon the degree of surface roughness and therefore contact angle hysteresis. Higher surface potentials result in higher droplet velocities giving rise to unexpected behaviour such as a decrease in print resolution or droplet bouncing.

6.6 References

[1] Barker, S. L. R.; Tarlov, M. J.; Canavan, H.; Hickman, J. J.; Locascio, L. E. Plastic Microfluidic Devices Modified with Polyelectrolyte Multilayers. *Anal. Chem.* **2000**, *72*, 4899.

[2] Becker, H.; Locascio, L. E. Polymer microfluidic devices. *Talanta* **2002**, *56*, 267.

[3] Geissler, M.; Roy, E.; Diaz-Quijada, G. A.; Galas, J.-C.; Veres, T. Microfluidic Patterning of Miniaturized DNA Arrays on Plastic Substrates. *ACS Appl. Mater. Interfaces* **2009**, *1*, 1387.

[4] Angadjivand, S. A.; Jones, M. E.; Meyer, D. E. Method of charging electret filter media. U.S. Patent US5496507 A, Mar. 5, 1996.

[5] Calvert, P. Inkjet Printing for Materials and Devices. *Chem. Mater.* **2001**, *13*, 3299.

[6] Sirringhaus, H.; Kawase, T.; Friend, R. H.; Shimoda, T.; Inbasekaran, M.; Wu, W.; Woo, E. P. High-Resolution Inkjet Printing of All-Polymer Transistor Circuits. *Science* **2000**, *290*, 2123.

[7] Wang, J. Z.; Zheng, Z. H.; Li, H. W.; Huck, W. T. S.; Sirringhaus, H. Dewetting of conducting polymer inkjet droplets on patterned surfaces. *Nat. Mater.* **2004**, *3*, 171.

[8] Sele, C. W.; von Werne, T.; Friend, R. H.; Sirringhaus, H. Lithography-Free, Self-Aligned Inkjet Printing with Sub-Hundred-Nanometer Resolution. *Adv. Mater.* **2005**, *17*, 997.

[9] Doggart, J.; Wu, Y.; Liu, P.; Zhu, S. Facile Inkjet-Printing Self-Aligned Electrodes for Organic Thin-Film Transistor Arrays with Small and Uniform Channel Length. *ACS Appl. Mater. Interfaces* **2010**, *2*, 2189.

[10] Barbulovic-Nad, I.; Lucente, M.; Sun, Y.; Zhang, M.; Wheeler, A. R.; Bussmann, M. Bio-Microarray Fabrication Techniques—A Review. *Crit. Rev. Biotechnol.* **2006**, *26*, 237.

[11] Tan, C. P.; Cipriany, R.; Lin, D. M.; Craighead, H. G. Nanoscale Resolution, Multicomponent Biomolecular Arrays Generated By Aligned Printing With Parylene Peel-Off. *Nano Lett.* **2010**, *10*, 719.

[12] Arrabito, G.; Pignataro, B. Inkjet Printing Methodologies for Drug Screening. *Anal. Chem.* **2010**, *82*, 3104.

[13] Mironov, V.; Boland, T.; Trusk, T.; Forgacs, G.; Markwald, R. R. Organ printing: computer-aided jet-based 3D tissue engineering. *Trends Biotechnol.* **2003**, *21*, 157.

[14] Xu, T.; Jin, J.; Gregory, C.; Hickman, J. J.; Boland, T. Inkjet printing of viable mammalian cells. *Biomaterials* **2005**, *26*, 93.

[15] Bharathan, J.; Yang, Y. Polymer electroluminescent devices processed by inkjet printing: I. Polymer light-emitting logo. *Appl. Phys. Lett.* **1998**, *72*, 2660.

[16] Chang, S.-C.; Bharathan, J.; Yang, Y.; Helgeson, R.; Wudl, F.; Ramey, M. B.; Reynolds, J. R. Dual-color polymer light-emitting pixels processed by hybrid inkjet printing. *Appl. Phys. Lett.* **1998**, *73*, 2561.

[17] Piérart, F.; Wildhaber, J. H.; Vrancken, I.; Devadason, S. G.; Le Souëf, P. N. Washing plastic spaces in household detergent reduces

electrostatic charge and greatly improves delivery. *Eur. Respir. J.* **1999**, *13*, 673.
[18] Roland. http://tipsandtricks.rolanddga.com/print-cut/managing-static-for-improved-image-quality-and-maximum-printer-performance (accessed August 20, 2013).
[19] Sign & Digital Graphics. http://sdgmag.com/article/printing-finishing/fighting-static (accessed August 20, 2013).
[20] Industrial + Specialty Printing. http://industrial-printing.net/content/eliminating-printing-defects-caused-static-electricity, (accessed August, 20 2013).
[21] Docan Digital Printing System. http://www.uvflatbedprinter.com.cn/technical/29.html (accessed August, 20 2013).
[22] Wu, Y.; Saito, N.; Nae, F. A.; Inoue, Y.; Takai, O. Water droplets interaction with super-hydrophobic surfaces. *Surf. Sci.* **2006**, *600*, 3710.
[23] Smith, P. A.; East, G. C.; Brown, R. C.; Wake, D. Generation of Triboelectric Charge in Textile Fibre Mixtures, and their use as Air Filters. *J. Electrostat.* **1988**, *21*, 81.
[24] Tsai, P. P.; Schreuder-Gibson, H.; Gibson, P. Different electrostatic methods for making electret filters. *J. Electrostat.* **2002**, *54*, 333.
[25] Karadag, Y.; Jonáš, A.; Kiraz, A. Determination of microdroplet contact angles using electrically driven droplet oscillations. *Appl. Phys. Lett.* **2011**, *98*, 194101.
[26] Janocha, B.; Bauser, H.; Oehr, C.; Brunner, H.; Göpel, W. Competitive Electrowetting of Polymer Surfaces by Water and Decane. *Langmuir* **2000**, *16*, 3349.
[27] Martin, G. D.; Hoath, S. D.; Hutchings, I. M. Inkjet printing - the physics of manipulating liquid jets and drops. *J. Phys.: Conf. Ser.* **2008**, *105*, 012001.
[28] Cloupeau, M.; Prunet-Foch, B. Electrostatic spraying of liquids in cone-jet mode. *J. Electrost.* **1989**, *22*, 135.
[29] Giglio, E.; Gervais, B.; Rangama, J.; Manil, B.; Huber, B. A.; Duft, D.; Müller, R.; Leisner, T.; Guet, C. Shape deformations of surface-charged microdroplets. *Phys. Rev. E* **2008**, *77*, 036319.
[30] Ryu, S. U.; Lee, S. Y. Maximum spreading of electrically charged droplets impacting on dielectric substrates. *Int. J. Multiphase Flow* **2009**, *35*, 1.
[31] Morra, M,; Occhiello, E.; Garbassi, F. Surface characterization of plasma-treated PTFE. *Surf. Interface. Anal.* **1990**, *16*, 412.
[32] Ryan, M. E.; Badyal, J. P. S. Surface Texturing of PTFE Film Using Non-equilibrium Plasmas. *Macromolecules* **1995**, *28*, 1377.
[33] Coulson, S. R.; Woodward, I.; Badyal, J. P. S.; Brewer, S. A.; Willis, C. Super-Repellent Composite Fluoropolymer Surfaces. *J. Phys. Chem. B* **2000**, *104*, 8836.
[34] Johnson, R. E. Jr.; Dettre, R. H. Wetting of Low-Energy Surfaces. In Wettability; Berg J. C., Ed.; Marcel Dekker, Inc.: New York, 1993; Chapter 1, p 13.

[35] Secker. E. S. Device for Neutralizing the Charge on Statically-Charged Surfaces. U.S. Patent US3997817, Dec. 14, 1976.
[36] Soh, S.; Kwok, S. W.; Liu, H.; Whitesides, G. M. Contact De-electrification of Electrostatically Charged Polymers. *J. Am. Chem. Soc.* **2012**, *134*, 20151.
[37] Paynter, R. W. XPS studies of the ageing of plasma-treated polymer surfaces. *Surf. Interface Anal.* **2000**, *29*, 56.
[38] Browne, M. M.; Lubarsky, G. V.; Davidson, M. R.; Bradley, R. H. Protein adsorption onto polystyrene surfaces studied by XPS and AFM. *Surf. Sci.* **2004**, *553*, 155.
[39] Johnson, R. E., Jr.; Dettre, R. H. TITLE. In *Contact Angle, Wettability and Adhesion*; Fowkes, F. M., Ed.; Adv. Chem. Ser. 43; American Chemical Society: Washington, DC, 1964; 112.
[40] Wenzel, R. N. Resistance of Solid Surfaces to Wetting by Water. *Ind. Eng. Chem.* **1936**, *28*, 988.
[41] Brown, P. S.; Talbot, E. L.; Wood, T. J.; Bain, C. D.; Badyal, J. P. S. Superhydrophobic Hierarchical Honeycomb Surfaces. *Langmuir* **2012**, *28*, 13712.
[42] Rioboo, R.; Marengo, M.; Tropea, C. Time evolution of liquid drop impact onto solid, dry surfaces. *Exp. Fluids.* **2002**, *33*, 112.
[43] Thomson, W. On a Self-acting Apparatus for multiplying and maintaining Electric Charges, with applications to illustrate the Voltaic Theory. *Proc. Roy. Soc. London* **1867**, *16*, 67.
[44] Lee, S.; Byun, D.; Jung, D.; Choi, J.; Kim, Y.; Yang, J. H.; Son, S. U.; Tran, S. B. Q.; Ko, H. S. Pole-type ground electrode in nozzle for electrostatic field induced drop-on-demand inkjet head. *Sens. Actuators, A* **2008**, *141*, 506.
[45] Marín, Á. G.; van Hoeve, W.; García-Sánchez, P.; Shui, L.; Xie, Y.; Fontelos, M. A.; Eijkel, J. C. T.; van den Berg, A.; Lohse, D. The microfluidic Kelvin water dropper. *Lab Chip* **2013**, *13*, 4503.
[46] Scandurra, A.; Indelli, G. F.; Spartà, N. G.; Galliano, F.; Ravesi, S.; Pignataro, S. Low-temperature sintered conductive silver patterns obtained by inkjet printing for plastic electronics. *Surf. Interface Anal.* **2010**, *42*, 1163.
[47] Singh, M.; Haverinen, H. M.; Dhagat, P.; Jabbour, G. E. Inkjet Printing—Process and Its Applications. *Adv. Mater.* **2010**, *22*, 673.
[48] Jain, K.; Klosner, M.; Zemel, M.; Raghunandan, S. Flexible Electronics and Displays: High-Resolution, Roll-to-Roll, Projection Lithography and Photoablation Processing Technologies for High-Throughput Production. *Proc. IEEE* **2005**, *93*, 1500.

Chapter 7 Tuning the Imbibition Behaviour of Porous Membranes for Oil–Water Separation

7.1 Introduction

In the previous chapters, focus has been on the impact of picolitre droplets on solid surfaces. However, the impact, spreading, and imbibition of liquid droplets into porous media is of relevance to many applications including liquid packaging,[1,2] water distribution in soil,[3] inkjet printing,[4] and oil recovery. Due to the frequency of off-shore oil spillages,[5,6] and the emergence of fracking (where water-based fluids are used to fracture rocks for the release of oil and gas), the separation of oil and water is an important environmental challenge.[7,8,9,10,11,12] Existing methods for the removal or collection of oils from an oil–water mixture utilise absorbent materials[13] such as zeolites,[14,15] organoclays,[16] non-woven polypropylene,[17,18] or natural fibres[19] (such as straw,[20] cellulose,[18] or wool[21]). However, these materials tend to also absorb water, thereby reducing their efficiency.[22] In addition, extra steps are necessary to remove the absorbed oil from the material, which makes such methods highly incompatible with continuous flow systems (e.g. attached to clean-up vessels).

There also exist separation membranes that repel one liquid phase whilst allowing the other to pass through. For example, these can be made out of hydrophobic and oleophilic materials,[23,24,25,26] causing water to run off the surface whilst allowing oil to permeate through. However creation of such membranes typically involves wet chemical processes where the modifications necessary to ensure water repellency (superhydrophobicity) dictate the formation of the porous material[27] (meaning only certain pore sizes and porous network types may be achievable) or an additional coating is applied to an existing porous material, which can reduce flow.[23,28]

In this chapter, the behaviour of picolitre droplets after impact was compared on untreated and CF_4 plasma fluorinated polyethersulfone membranes. This method of creating a superhydrophobic membrane is favourable as it is applied to existing membranes and does not affect the physical properties of the material (e.g. pore size, network type, porosity etc).

By varying the pore size within the membranes, the imbibition behaviour of liquids could be altered. CF_4 plasma fluorinated polyethersulfone membranes were used for the separation of oil and water.

7.2 Experimental

Polished silicon (100) wafers (Silicon Valley Microelectronics, Inc.) were used as flat substrates. Polyethersulfone (Goodfellow Cambridge Ltd.) was dissolved in dichloromethane (99.99% purity, Fisher Scientific UK Ltd.) at a concentration of 2% (w/v) and spin coated using a photoresist spinner (Cammax Precima) operating at 2000 rpm. Porous polyethersulfone membranes (Supor-100 membrane (0.1 μm pore size), Supor-1200 membrane (1.2 μm pore size), and Supor-5000 membrane (5 μm pore size), 130±3 μm thickness, Pall Corp.) were used as received.

Plasmachemical fluorination of the polyethersulfone was undertaken in a cylindrical glass reactor of similar design to that used in Section 3.2.1 (page 52). A piece of polyethersulfone was placed into the reactor at ambient temperature (8 cm downstream to avoid surface texturing[29,30,31]), followed by evacuation to base pressure. CF_4 gas (+99.7% purity, Air Products) was then admitted into the system via a needle valve at a pressure of 0.2 mbar and 2 cm^3 min^{-1} flow rate, and the electrical discharge ignited at a power of 30 W for 60 s. Upon completion of surface functionalization, the gas feed was switched off and the chamber vented to atmosphere.

To prepare cross-sections of the CF_4 plasma treated polyethersulfone membranes for XPS analysis the membranes were mounted onto a rotary microtome (RM 2165, Leica Biosystems Ltd.) and 20 μm thick slices were cut off the top to reveal the cross-sections.

Surface elemental compositions were determined by X-ray photoelectron spectroscopy (XPS) using a VG ESCALAB II electron spectrometer as described in Section 3.2.2 (page 52). Elemental compositions were calculated using sensitivity factors derived from chemical standards, C(1s): O(1s): S(2p): F(1s) equals 1.00: 0.34: 0.57: 0.26.

Scanning electron microscopy (SEM) images of gold-coated membrane samples were acquired using a Cambridge Stereoscan 240.

Microlitre sessile drop contact angle analysis was carried out with a video

capture system (VCA2500XE, AST Products Inc.) using 1.0 μL dispensation of de-ionised water (BS 3978 grade 1). Advancing and receding angles were measured by respectively increasing and decreasing the droplet size until the contact line was observed to move.[32]

Picolitre drop impact studies were carried out using an imaging rig as described in Section 3.2.3 (page 53). The piezo-type nozzle (MicroFab MJ-ABP-01, Horizon Instruments Ltd.) had an aperture diameter of 30 μm, generating water drops of 30 μm diameter (14 pL).

Oil imbibition times were calculated by measuring the time taken for a 2 μL drop of decane (+99%, Sigma Aldrich Ltd.), dodecane (99%, Sigma Aldrich Ltd.), tetradecane (+99%, Sigma Aldrich Ltd.), or hexadecane (99%, Sigma Aldrich Ltd.) to imbibe. Oil–water separation was tested by pouring an agitated mixture of hexadecane and water over the porous membrane and measuring the time taken for complete separation to occur. Oil Red O (≥75% dye content, Sigma Aldrich Ltd) and Procion® Blue MX-R (35% dye content, Sigma Aldrich Ltd.) were used as oil and water dispersible dyes respectively.

7.3 Results

7.3.1 Surface Characterisation

XPS elemental compositions of untreated, flat polyethersulfone surfaces were found to be consistent with theoretical values for the parent polymer structure, Table 6.3. Following CF_4 plasma fluorination of the flat polyethersulfone surfaces, the level of fluorine incorporation was comparable to previous studies.[33,34] In the case of the porous polyethersulfone membranes, the extent of surface CF_4 plasma fluorination is difficult to determine quantitatively between different pore sizes due to the influence of roughness upon the surface sensitivity of the XPS technique (variable electron take-off angles alter the sampling depth[35,36,37]), Table 6.3. Cross-sectional analysis was carried out using a microtome to progressively slice the membranes from the outer surface towards the underlying bulk. XPS characterisation after removal of each 20 μm thick section confirmed that CF_4 plasma fluorination penetrates throughout the membrane pore structure.[38]

Table 7.1: XPS elemental compositions of untreated and CF_4 plasma fluorinated polyethersulfone.

Polyethersulfone		XPS Elemental Composition / ±0.5%			
		% C	% F	% O	% S
Untreated	Theoretical	75.0	0.0	18.8	6.2
	Flat Non-porous	75.4	0.0	18.8	5.8
CF_4 plasma fluorinated	Theoretical	50.0	33.3	12.5	4.2
	Flat Non-porous	40.6	48.7	9.1	1.6
	0.1 μm pore membrane	44.9	45.4	8.2	1.5
	1.2 μm pore membrane	42.8	47.9	7.5	1.8
	5 μm pore membrane	40.7	52.4	5.7	1.2

SEM characterisation showed surface pore morphology typical of polyethersulfone membranes prepared by non-solvent-induced phase separation.[39] CF_4 plasma modification did not lead to any significant etching of the porous membrane surfaces, Figure 7.1.

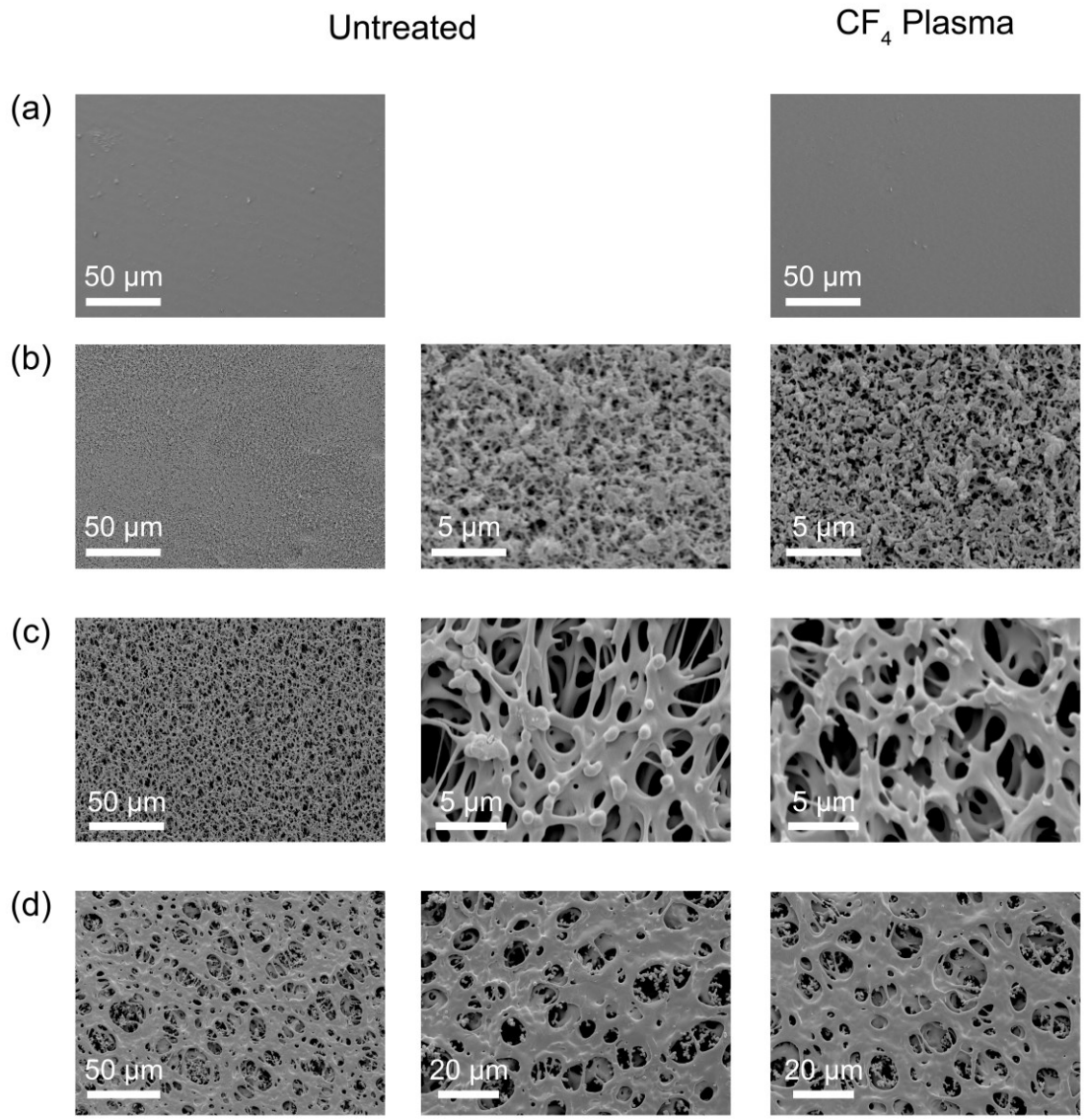

Figure 7.1: SEM images of polyethersulfone: (a) flat non-porous; (b) 0.1 µm pore membranes; (c) 1.2 µm pore membranes; and (d) 5 µm pore membranes. Pore morphology remains unchanged following CF_4 plasma exposure (30 W, 60 s).

7.3.2 Water Droplet Impact

Water contact angle analysis showed a change from hydrophilic to hydrophobic following CF_4 plasma fluorination of flat, non-porous polyethersulfone, Table 7.2. In the case of untreated polyethersulfone membranes, their hydrophilic nature leads to rapid imbibition of water into the membrane for all pore sizes, Table 7.2. CF_4 plasma fluorination makes the membranes hydrophobic and 1 µL water droplets are unable to imbibe into the substrate. Static water contact angles are found to increase with decreasing pore size, reaching 165° for the 0.1 µm pore sized membrane.

Table 7.2: Water contact angles for untreated and CF_4 plasma fluorinated polyethersulfone.

Polyethersulfone		**Microlitre Contact Angle / °**				**Picolitre Static Contact Angle / °**
		Static	**Advancing**	**Receding**	**Hysteresis**	
Flat Non-porous	Untreated	80±1	83±1	71±1	12±1	74±2
	Treated	112±1	120±1	88±1	32±1	108±2
0.1 µm pore membrane	Untreated	*Imbibes*	–	–	–	*Imbibes*
	Treated	165±1	168±1	158±1	10±1	138±5
1.2 µm pore membrane	Untreated	*Imbibes*	–	–	–	*Imbibes*
	Treated	161±1	164±1	144±1	20±1	116±2
5 µm pore membrane	Untreated	*Imbibes*	–	–	–	*Imbibes*
	Treated	130±1	140±1	84±1	56±1	*Imbibes*

The imbibition behaviour of picolitre droplets impacting on porous polyethersulfone membranes was studied by monitoring the change in droplet contact line diameter over time. In the case of untreated (hydrophilic) membranes, the water droplet quickly imbibes into the material leading to a decrease in the contact line diameter of the visible drop on the surface. The time taken for a droplet to imbibe decreases with decreasing membrane pore size, Figure 7.2(a).

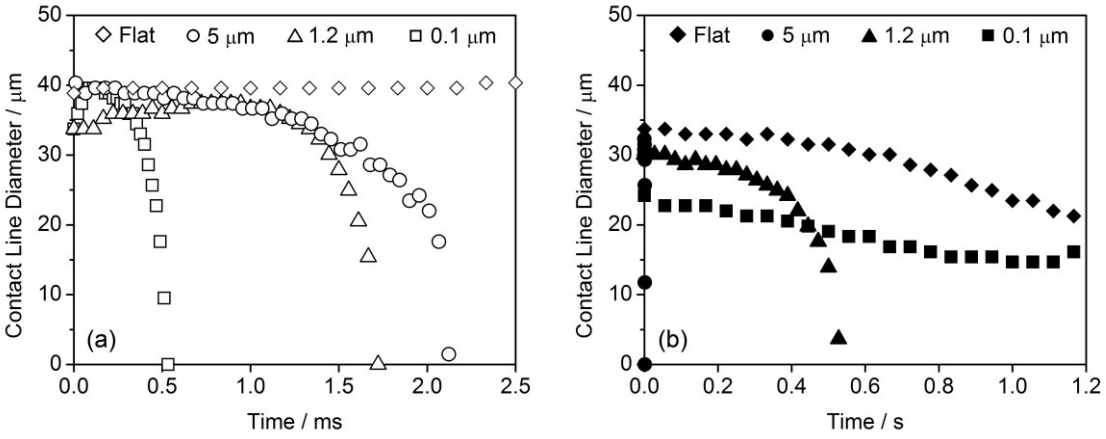

Figure 7.2: Evolution of picolitre droplet (30 μm diameter in air) contact line diameter over time following impact upon: (a) untreated polyethersulfone surfaces (time in ms) and (b) CF_4 plasma fluorinated polyethersulfone surfaces (time in s).

Following CF_4 plasma fluorination, the maximum contact line diameter achieved for picolitre droplets was measured to be smaller across the range of pore sizes (inhibiting spreading), Figure 7.2(b). The smallest pore membranes (0.1 μm) yield the most hydrophobic surface (smallest contact line diameter). In addition, the imbibition behaviour (decrease in contact line diameter over time) of picolitre droplets on CF_4 plasma fluorinated membranes was found to be different compared to the untreated membranes. Imbibition time is fastest for CF_4 plasma fluorinated membranes with the largest pores (5 μm), remaining relatively unchanged compared to the time observed for the untreated 5 μm pore membrane, Figures 7.2 and 7.3. The imbibition of droplets on CF_4 plasma fluorinated membranes slows down with decreasing pore size (in contrast to the untreated membranes, where imbibition increases with decreasing pore size). In fact, the contact line of droplets on CF_4 plasma fluorinated membranes with the smallest pores (0.1 μm) decreases slowly over the course of several seconds

suggesting the droplets were merely drying and that no imbibition occurs. This drying time (over 2 s) is measured to be longer than that for a drop on the CF_4 plasma fluorinated flat surface (about 1.6 s) due to the larger contact angle in the former case (138° vs 108° for flat).[40,41]

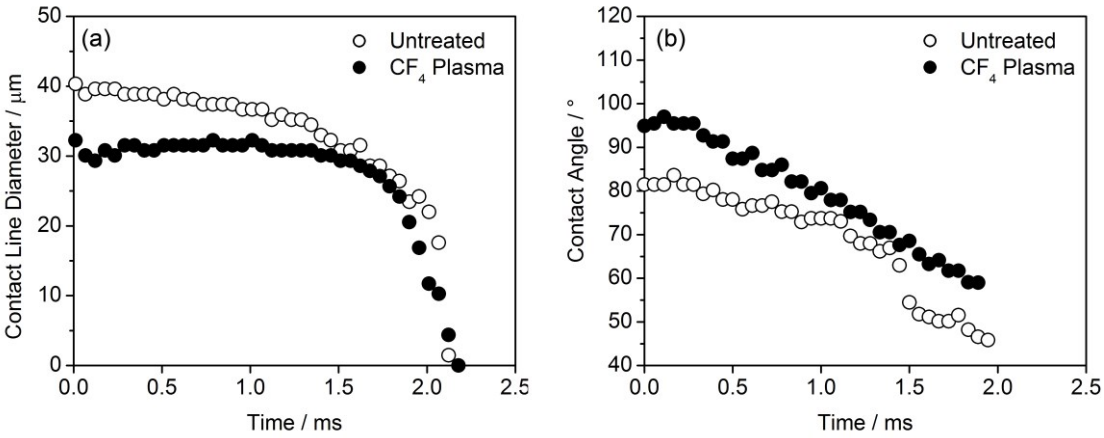

Figure 7.3: Evolution of picolitre droplet (30 µm diameter in air): (a) contact line diameter and (b) contact angle over time following impact upon untreated and CF_4 plasma fluorinated (30 W, 60 s) polyethersulfone membrane surfaces (5 µm pore size).

7.3.3 Oil–Water Separation

Dispensation of low surface tension liquids onto the untreated polyethersulfone membranes leads to their imbibition. The time taken for a 2 µL drop of oil to imbibe into the membrane decreases with increasing membrane pore size and shorter hydrocarbon chain length of the oil (lower viscosity and surface tension), Figure 7.4(a).

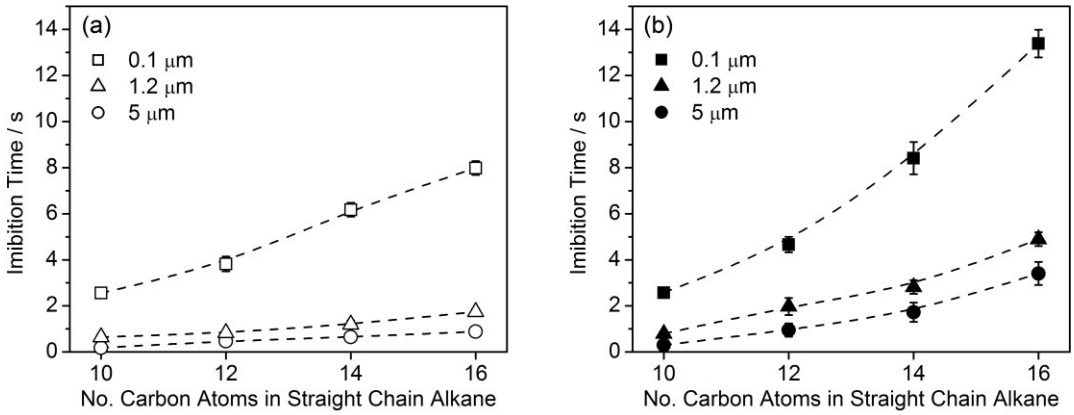

Figure 7.4: Imbibition time of 2 μL drops of oil as a function of hydrocarbon chain length and pore size on: (a) untreated polyethersulfone membranes and (b) CF_4 plasma fluorinated (30 W, 60 s) polyethersulfone membranes.

Following CF_4 plasma fluorination, all three membranes were found to become hydrophobic, Table 7.2. However, these membranes are still able to absorb oils, with only a slight increase in imbibition time compared to the untreated membranes, Figure 7.4. Such behaviour makes these CF_4 plasma fluorinated membranes suitable for use in the separation of oil and water. The fluorinated membranes were found to block the permeation of water, whilst hexadecane passed straight through, resulting in high separation efficiencies (>99%) for all membrane pore sizes, Figure 7.5. The time taken to separate an oil–water mixture is dependent upon the pore size of the membrane with the separation time increasing with decreasing membrane pore size (same trend as observed for imbibition of single oil drops, Figure 7.4).

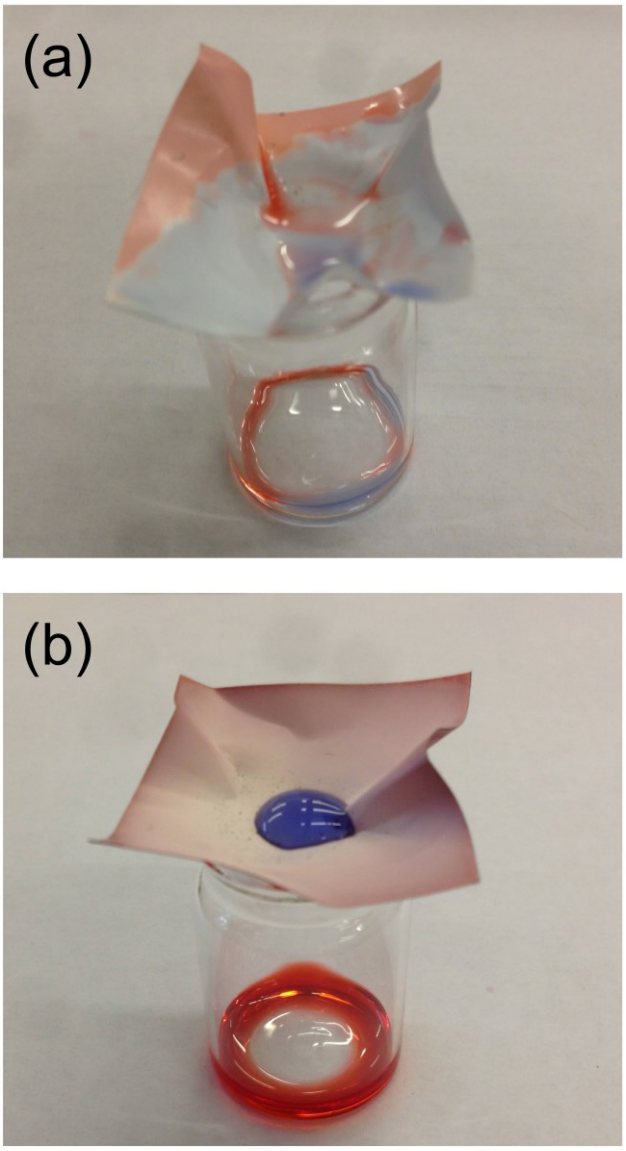

Figure 7.5: Hexadecane–water mixture dispensed onto: (a) untreated polyethersulfone membrane (5 μm pore size); and (b) CF_4 plasma fluorinated polyethersulfone membrane (5 μm pore size) where the water collects on top whilst the oil passes through. Hexadecane was dyed with Oil Red O (Sigma Aldrich Ltd.) whilst water was dyed with Procion® Blue MX-R (Sigma Aldrich Ltd.). Similar results were obtained for decane–water mixtures, 1.2 μm and 0.1 μm pore membranes, and also in the absence of dyes.

7.4 Discussion

CF_4 plasma fluorination of polyethersulfone was found to result in a high level of surface fluorination. This is consistent with previous studies, where hydrogen abstraction and atomic fluorine addition are major reaction pathways.[34] In the case of the flat, non-porous surfaces, there is a change from hydrophilicity (80°) to hydrophobicity (112°).

Fast imbibition of microlitre water droplets is observed on the untreated, porous polyethersulfone membranes, Table 7.2. Following CF_4 plasma fluorination, the membranes became hydrophobic with microlitre contact angles of upto 165°. The level of hydrophobicity is enhanced by the membrane surface roughness,[42] with the 0.1 μm pores exhibiting the highest static contact angle for the microlitre droplets, Table 7.2 and Figure 7.1. This results in no imbibition behaviour in the case of microlitre droplets of water following CF_4 plasma fluorination of the membranes.

Picolitre droplets were found to quickly imbibe into the untreated polyethersulfone membrane surfaces, Figure 7.2. This imbibition behaviour is fastest for 0.1 μm pore size, and is inconsistent with the equation most commonly used to describe imbibition into porous materials (modelled as a bundle of straight, non-connecting capillaries), the Lucas–Washburn equation[43]

$$x^2 = \left(\frac{rt}{2\eta}\right)\gamma\cos\theta, \qquad (7.1)$$

where x is the distance travelled in the capillary, r is the radius of the capillary, t is the time, η is the fluid dynamic viscosity, γ is the interfacial surface tension, and θ is the contact angle between the walls of the capillary and the fluid. This predicts that wider pores fill quicker than narrower ones. However, it has been shown that at shorter time scales, especially in small length capillaries, it is the narrower ones that fill faster.[44,45] This disagreement with the Lucas–Washburn equation is thought to be due to the acceleration experienced by a fluid as it enters a capillary, something not considered in Equation 7.1. This inertial flow regime is described as[46]

$$x^2 = \frac{2\gamma\cos\theta\, t^2}{r\rho}, \qquad (7.2)$$

where ρ is the fluid density. In this case, the distance travelled by the liquid at time t is inversely proportional to the square root of the pore radius i.e. narrower pores fill quicker. This inertial regime is short but can result in high distances travelled,[47] it has been found to be most important under conditions of limited fluid supply (such as in droplets[48]) and in real porous substrates, potentially due to the summing effect of inertia in an interconnected porous network.[48] The inertial term is also of greater importance for short capillaries such as those typically found in porous membranes.[44] In the current study, the membranes used have average thicknesses of 130±3 μm. Assuming straight channels (and similar aspect ratios), this capillary length is below that where the inertial regime is considered increasingly important.[44,45] The inertial regime could therefore explain why the imbibition times for picolitre water droplets decrease with decreasing pore size (a similar trend was observed for the imbibition of microlitre water droplets).

Following CF_4 plasma fluorination of the porous membranes, picolitre droplets display lower maximum spreading diameters for all pore sizes compared to the untreated membranes, Figure 7.2. However, picolitre droplet imbibition behaviour was found to be dependent upon the pore size. CF_4 plasma fluorinated polyethersulfone membranes with 5 μm pores show little difference in imbibition behaviour of water droplets relative to the untreated membrane, whereas no imbibition of impacting picolitre water droplets is observed for fluorinated 0.1 μm pore membranes, and they remain visible on the surface (the decrease in contact line diameter is due to drying). For the 0.1 μm pore surface, the average pore size is much smaller than the drop diameter (30 μm before impact) and the pore surface morphology combined with CF_4 plasma fluorination results in a hydrophobic surface (picolitre water droplet static contact angles of 138°). The surface roughness is less for the 1.2 μm pore surface and therefore the contact angle is lower (stabilising at 116°). This trend extends to the 5 μm pore surface (locally smoother in relation to the 30 μm drop) to give a lower contact angle (95° before quickly decreasing). This variation in apparent contact angle (contact angle between drop and porous surface, which takes into account effect of roughness[49]) coincides with a change in the imbibition behaviour.[50,51,52] Increased hydrophobicity creates a greater barrier against spontaneous imbibition. This barrier must be overcome

for imbibition to occur, at which point the behaviour is dictated by the contact angle between the walls of the pores and the fluid, which will differ from the apparent contact angle of the visible droplet on the surface[53] (and would need to be below 90° if imbibition is to proceed). The differing behaviour between microlitre and picolitre droplets on the same membrane surface can be explained on the basis of the relative size of the surface features in the relation to the size of the drop resulting in different apparent contact angles[54] and therefore barrier to imbibition, Table 7.2.[51,52] Droplets with lower apparent contact angles were found to be more likely to imbibe into porous media.[55,56] Picolitre droplets may also be more likely to imbibe due to the increased droplet inertia during impact overcoming the hydrophobic barrier.

Minimising spreading whilst ensuring adequate imbibition into porous materials is of relevance to inkjet printing where the spreading of a drop on the substrate defines the print resolution and imbibition into a porous material can aid print quality and durability.[57,58] Furthermore, imbibition of water droplets on the CF_4 plasma treated 5 μm pore surfaces shows a decrease in contact angle at constant contact area diameter for the majority of the imbibition, Figure 7.3. This is in contrast to droplet imbibition on the untreated 5 μm pore surfaces, which resulted in a decrease in both contact diameter and contact angle. Such contact line pinning in the case of the treated membrane should lead to a more even imbibition into the membrane to give more uniform printed features.[59]

In the case of low surface tension liquids, the CF_4 plasma treatment was not found to adversely affect the imbibition behaviour for droplets of straight chain alkanes due to the polyethersulfone surfaces still exhibiting oleophilicity following CF_4 plasma treatment (static contact angles on flat, CF_4 treated polyethersulfone 58–71° across oil range studied). This results in only a small increase in the imbibition rate of microlitre oil droplets compared to the untreated membranes, Figure 7.4. Oil imbibition is found to be quickest on membranes with the largest (5 μm) pores. This may be due to the time taken to transition from the initial inertial regime (Equation 7.2) to the viscous regime (Lucas–Washburn, Equation 7.1) being shorter for high-viscosity, low-density fluids.[47] Oil imbibition time is also dependent upon the hydrocarbon chain length of the oil with longer chain length oils taking longer to imbibe, most likely due to increasing viscosity and higher contact angles, Equation 7.1.[60]

These CF_4 plasma fluorinated membranes are efficient as oil–water separators; oils were found to imbibe into the porous network, passing through to be collected on the other side, whilst water droplets remained on the surface and could easily be rolled off, Figure 7.5. Their use in continuous flow systems may be limited as the oil imbibition time (lowest for 5 μm pore sized membranes) must be balanced against the water repellency (highest for 0.1 μm pore membranes), however such systems could potentially be utilised downstream of continuous flow separators to help maximise separation efficiencies. Such oil–water separators could prove extremely useful in reducing the environmental impact of the oil, gas, metal, textile, and food processing industries.[61]

7.5 Conclusions

CF_4 plasma fluorination of polyethersulfone membranes results in changing imbibition behaviour dependent upon the pore size in relation to the drop diameter. It is possible to inhibit the spreading of picolitre droplets of water with little change in imbibition behaviour. In the case of microlitre droplets, water was found to remain on the surface whilst oils passed straight through. Such a membrane could be utilised in the separation of oil–water mixtures.

7.6 References

[1] Tufvesson, H.; Lindström, T. The effect of sizing and paper structure on paperboard for retortable packaging. *Nord. Pulp Paper Res. J.* **2007**, *22*, 200.

[2] Koivu, V.; Seppänen, R.; Turpeinen, T.; Mattila, K.; Hyväluoma, J.; Kataja, M. Combining X-ray micro-tomography and image analysis to study imbibition and void space in liquid packaging board. *J. Pulp Paper Sci.* **2010**, *36*, 170.

[3] Pechenkina, N. V.; Zakirov, A. G.; Koposov, G. F. Analysis of the Distribution of Moisture Imbibition Velocity in Heavy-Textured Soils. *Eurasian Soil Sci.* **2008**, *41*, 623.

[4] Anderson, D. M. Imbibition of a liquid droplet on a deformable porous substrate. *Phys. Fluids* **2005**, *17*, 087104.

[5] Schaum, J.; Cohen, M.; Perry, S.; Artz, R.; Draxler, R.; Frithsen, J. B.; Heist, D.; Lorber, M.; Phillips, L. Screening Level Assessment of Risks Due to Dioxin Emissions from Burning Oil from the BP Deepwater Horizon Gulf of Mexico Spill. *Environ. Sci. Technol.* **2010**, *44*, 9383.

[6] Cheng, Y.; Li, X.; Xu, Q.; Garcia-Pineda, O.; Andersen, O. B.; Pichel, W. G. SAR observation and model tracking of an oil spill event in coastal waters. *Mar. Pollut. Bull.* **2011**, *62*, 350.

[7] Kota, A. K.; Kwon, G.; Choi, W.; Mabry, J. M.; Tuteja, A. Hygro-responsive membranes for effective Oil–Water separation. *Nat. Commun.* **2012**, *3*, 1025.

[8] Kwon, G.; Kota, A. K.; Li, Y.; Sohani, A.; Mabry, J. M.; Tuteja, A. On-Demand Separation of Oil–Water Mixtures. *Adv. Mater.* **2012**, *24*, 3666.

[9] Li, J.; Shi, L.; Chen, Y.; Zhang, Y.; Guo, Z.; Su, B.; Liu, W. Stable superhydrophobic coatings from thiol-ligand nanocrystals and their application in oil/water separation. *J. Mater. Chem.* **2012**, *22*, 9774.

[10] Yang, H.; Lan, Y.; Zhu, W.; Li, W.; Xu, D.; Cui, J.; Shen, D.; Li, G. Polydopamine-coated nanofibrous mats as a versatile platform for producing porous functional membranes. *J. Mater. Chem.* **2012**, *22*, 16994.

[11] Tian, D.; Zhang, X.; Tian, Y.; Wu, Y.; Wang, X.; Zhai, J.; Jiang, L. Photo-induced water–oil separation based on switchable superhydrophobicity–superhydrophilicity and underwater superoleophobicity of the aligned ZnO nanorod array-coated mesh films. *J. Mater. Chem.* **2012**, *22*, 19652.

[12] Brown, V. J. Industry Issues: Putting the Heat on Gas. *Environ. Health Perspect.* **2007**, *115*, A76.

[13] Adebajo, M. O.; Frost, R. J.; Kloprogge, J. T.; Carmody, R.; Kokot, S. Porous Materials for Oil Spill Cleanup: A Review of Synthesis and Absorbing Properties. *J. Porous Mater.* **2003**, *10*, 159.

[14] Küntzel, J.; Ham, R.; Melin, Th. Regeneration of Hydrophobic Zeolites with Steam. *Chem. Eng. Technol.* **1999**, *22*, 991.

[15] Meininghuas, C. K. W.; Prins, R. Sorption of volatile organic compounds on hydrophobic zeolites. *Micropor. Mesopor. Mater.* **2000**, *35–36*, 349.
[16] Alther, G. R. Organically modified clay removes oil from water. *Waste Manag.* **1995**, *15*, 623.
[17] Bayat, A.; Aghamiri, S. F.; Moheb, A.; Vakili-Nezhaad, G. R. Oil Spill Cleanup from Sea Water by Sorbent Materials. *Chem. Eng. Technol.* **2005**, *28*, 1525.
[18] Teas, Ch.; Kalligeros, S.; Zanikos, F.; Stournas, S.; Lois, E.; Anastopoulos, G. Investigation of the effectiveness of absorbent materials in oil spills clean up. *Desalination* **2001**, *140*, 259.
[19] Annunciado, T. R.; Sydenstricker, T. H. D.; Amico, S. C. Experimental investigation of various vegetable fibers as sorbent materials for oil spills. *Mar. Pollut. Bull.* **2005**, *50*, 1340.
[20] Sun, X.-F.; Sun, R.; Sun, J.-X. Acetylation of Rice Straw with or without Catalysts and Its Characterization as a Natural Sorbent in Oil Spill Cleanup. *J. Agric. Food Chem.* **2002**, *50*, 6428.
[21] Radetić, M. M.; Jocić, D. M.; Jovančić, P. M.; Petrović, Z. L. J.; Thomas, H. F. Recycled Wool-Based Nonwoven Material as an Oil Sorbent. *Environ. Sci. Technol.* **2003**, *37*, 1008.
[22] Zhu, Q.; Pan, Q.; Liu, F. Facile Removal and Collection of Oils from Water Surfaces through Superhydrophobic and Superoleophilic Sponges. *J. Phys. Chem. C* **2011**, *115*, 17464.
[23] Feng, L.; Zhang, Z.; Mai, Z.; Ma, Y.; Liu, B.; Jiang, L.; Zhu, D. A Super-Hydrophobic and Super-Oleophilic Coating Mesh Film for the Separation of Oil and Water. *Angew. Chem. Int. Ed.* **2004**, *43*, 2012.
[24] Wang, S.; Li, M.; Lu, Q. Filter Paper with Selective Absorption and Separation of Liquids that Differ in Surface Tension. *ACS Appl. Mater. Interfaces* **2010**, *2*, 677.
[25] Lee, C. H.; Johnson, N.; Drelich, J.; Yap, Y. K. The performance of superhydrophobic and superoleophilic carbon nanotube meshes in water–oil filtration. *Carbon* **2011**, *49*, 669.
[26] Zhang, W.; Shi, Z.; Zhang, F.; Liu, X.; Jin, J.; Jiang, L. Superhydrophobic and Superoleophilic PVDF Membranes for Effective Separation of Water-in-Oil Emulsions with High Flux. *Adv. Mater.* **2013**, *25*, 2071.
[27] Lin, D.-J.; Beltsios, K.; Chang, C.-L.; Cheng, L.-P. Fine Structure and Formation Mechanism of Particulate Phase-Inversion Poly(vinylidene fluoride) Membranes. *J. Polym. Sci., Part B: Polym. Phys.* **2003**, *41*, 1578.
[28] Li, J.; Chen, Y.; Zhang, Y.; Guo, Z.; Su, B.-L.; Liu, W. Stable superhydrophobic coatings from thiol-ligand nanocrystal and their applications in oil/water separation. **2012**, *22*, 9774.
[29] Harshbarger, W. R.; Porter, R. A.; Miller, T. A.; Norton, P. A Study of the Optical Emission from an rf Plasma during Semiconductor Etching. *Appl. Spectrosc.* **1977**, *31*, 201.

[30] Grill, V.; Walder, G.; Scheier, P.; Kurdel, M.; Märk, T. D. Absolute partial and total electron impact ionization cross sections for C2H6 from threshold up to 950 eV. *Int. J. Mass Spectrom. Ion Processes* **1993**, *129*, 31.
[31] Brown, P. S.; Talbot, E. L.; Wood, T. J.; Bain, C. D.; Badyal, J. P. S. Superhydrophobic Hierarchical Honeycomb Surfaces. *Langmuir* **2012**, *28*, 13712.
[32] Johnson, R. E. Jr.; Dettre, R. H. Wetting of Low-Energy Surfaces. In Wettability; Berg J. C., Ed.; Marcel Dekker, Inc.: New York, 1993; Chapter 1, p 13.
[33] Hopkins, J.; Badyal, J. P. S. Plasma Modification of Poly(ether sulfone). *Macromolecules* **1994**, *27*, 5498.
[34] Hopkins, J.; Badyal, J. P. S. Nonequilibrium Glow Discharge Fluorination of Polymer Surfaces. *J. Phys. Chem.* **1995**, *99*, 4261.
[35] Shen, W.; Li, Z.; Liu, Y. Surface Chemical Functional Groups Modification of Porous Carbon. *Recent Pat. Chem. Eng.* **2008**, *1*, 27.
[36] Powell, C. J.; Jablonski, A. Progress in quantitative surface analysis by X-ray photoelectron spectroscopy: Current status and perspectives. *J. Electron Spectrosc. Relat. Phenom.* **2010**, *178–179*, 331.
[37] Baird, R. J.; Fadley, C. S.; Kawamoto, S. K.; Mehta, M. Concentration Profiles for Irregular Surfaces from X-ray Photoelectron Angular Distributions. *Anal. Chem.* **1976**, *48*, 843.
[38] Godfrey, S. P.; Kinmond, E. J.; Badyal, J. P. S. Plasmachemical Functionalization of Porous Polystyrene Beads. *Chem. Mater.* **2001**, *13*, 513.
[39] Ulbricht, M.; Schuster, O.; Ansorge, W.; Ruetering, M.; Steiger, P. Influence of the strongly anisotropic cross-section morphology of a novel polyethersulfone microfiltration membrane on filtration performance. *Sep. Purif. Technol.* **2007**, *57*, 63.
[40] Picknett, R. G.; Bexon, R. The evaporation of sessile or pendant drops in still air. *J. Colloid Interface Sci.* **1977**, *61*, 336.
[41] Talbot, E. L.; Berson, A.; Brown, P. S.; Bain, C. D. Evaporation of picoliter droplets on surfaces with a range of wettabilities and thermal conductivities. *Phys. Rev. E* **2012**, *85*, 061604.
[42] Wenzel, R. N. Resistance of Solid Surfaces to Wetting by Water. *Ind. Eng. Chem.* **1936**, *28*, 988.
[43] Washburn, E. W. The Dynamics of Capillary Flow. *Phys. Rev.* **1921**, *17*, 273.
[44] Sorbie, K. S.; Wu, Y. Z.; McDougall, S. R. The Extended Washburn Equation and Its Application to the Oil/Water Pore Doublet Problem. *J. Colloid Interface Sci.* **1995**, *174*, 289.
[45] Ridgway, C. J.; Gane, P. A. C.; Schoelkopf, J. Effect of Capillary Element Aspect Ratio on the Dynamic Imbibition within Porous Networks. *J. Colloid Interface Sci.* **2002**, *252*, 373.
[46] Bosanquet, C. H. On the flow of liquids into capillary tubes. *Philos. Mag. Ser. 6* **1923**, *45*, 525.
[47] Quéré, D. Inertial capillarity. *Europhys. Lett.* **1997**, *39*, 533.

[48] Schoelkopf, J.; Gane, P. A. C.; Ridgway, C. J.; Matthews, G. P. Practical observation of deviation from Lucas–Washburn scaling in porous media. *Colloids Surf., A.* **2002**, *206*, 445.
[49] Ouali, F. F.; McHale, G.; Javed, H.; Trabi, C.; Shirtcliffe, N. J.; Newton, M. I. Wetting considerations in capillary rise and imbibition in closed square tubes and open rectangular cross-section channels. *Microfluid Nanofluid* **2013***, 15*, 309.
[50] Dumoré, J. M.; Schols, R. S. Drainage Capillary-Pressure Functions and the Influence of Connate Water. *Soc. Pet. Eng. J.* **1974**, *14*, 437.
[51] Clarke, A.; Blake, T. D.; Carruthers, K.; Woodward, A. Spreading and Imbibition of Liquid Droplets on Porous Surfaces. *Langmuir* **2002**, *18*, 2980.
[52] Hilpert, M.; Ben-David, A. Infiltration of liquid droplets into porous media: Effects of dynamic contact angle and contact angle hysteresis. *Int. J. Multiphase Flow* **2009**, *35*, 205.
[53] Philip, J. R. Limitations on Scaling by Contact Angle. *Soil Sci. Soc. Am. J.* **1971**, *35*, 507.
[54] Brown, P. S.; Berson, A.; Talbot, E. L.; Wood, T. J.; Schofield, W. C. E.; Bain, C. D.; Badyal, J. P. S. Impact of Picoliter Droplets on Superhydrophobic Surfaces with Ultralow Spreading Ratios. *Langmuir* **2011**, 27, 13897.
[55] Denesuk, M.; Smith, G. L.; Zelinski, B. J. J.; Kreidl, N. J.; Uhlmann, D. R. Capillary Penetration of Liquid Droplets into Porous Materials. *J. Colloid Interface Sci.* **1993**, *158*, 114.
[56] Bico, J.; Tordeux, C.; Quéré, D. Rough Wetting. *Europhys. Lett.* **2001**, *55*, 214.
[57] Ridgway, C. J.; Gane, P. A. C. Ink-Coating Adhesion; The Importance of Pore Size and Pigment Surface Chemistry. *J. Dispersion Sci. Technol.* **2004**, *25*, 469.
[58] Chen, T.; Pidding, T.; Vaidyanathan, R. Multi-layered porous ink-jet recording media. World Patent WO 2008137343 A1, Nov. 13, 2008.
[59] Kettle, J.; Lamminmäki, T.; Gane, P. A review of modified surfaces for high speed inkjet coating. *Surf. Coat. Technol.* **2010**, *204*, 2103.
[60] Murphy, J. B.; Noland, T. L. Temperature Effects on Seed Imbibition and Leakage Mediated by Viscosity and Membranes. *Plant Physiol.* **1982**, *69*, 428.
[61] Cheryan, M.; Rajagopalan, N. Membrane processing of oily streams. Wastewater treatment and waste reduction. *J. Membr. Sci.* **1998**, *151*, 13.

Chapter 8 Ultra-Fast Oleophobic–Hydrophilic Switching Surfaces for Anti-Fogging, Self-Cleaning, and Oil–Water Separation

8.1 Introduction

In the previous chapter, a porous membrane was CF_4 plasma treated resulting in an efficient oil–water separator. The membranes were hydrophobic–oleophilic and therefore were found to repel water whilst allowing oil to permeate through. The main drawback of such separation membranes tends to be surface contamination with oil culminating in a drop in separation efficiency.[1,2] Such separation membranes are also difficult to integrate into gravity-driven, continuous flow systems due to the tendency for oils to be less dense than water, resulting in a situation where separation cannot occur due to a water barrier layer between the hydrophobic–oleophilic membrane and the oil.[3] A more attractive approach appears to be the utilisation of oleophobic–hydrophilic surfaces where the oil and oil-based contaminants are repelled and water passes through.[4] Such surfaces are also of interested for self-cleaning,[5,6,7] anti-fog,[5,8,9] and anti-fouling[10,11] applications.

One important and common method for creating oleophobic–hydrophilic surfaces is through the use of polyelectrolyte–surfactant complexes,[12,13] where the surfactant is attached to the polyelectrolyte via an oppositely charged electrostatic interaction.[14,15] In the case of polyelectrolyte–fluorosurfactant complexes, the fluorinated alkyl chains can orientate towards the air–solid interface to provide a low surface energy film. Such alignment localises hydrophilic portions of the polyelectrolyte in the near-surface region due to electrostatic attraction.[16] This means that when water is placed onto the surface, it penetrates through defects in the fluorinated outermost layer towards the hydrophilic sub-surface to provide hydrophilicity.[17] Whilst larger oil molecules are unable to penetrate through this top layer to leave the surface oleophobic.[17] Earlier polyelectrolyte–surfactant complex oleophobic–hydrophilic surfaces have been impeded from more widespread usage due to several factors: it can take several minutes for the water to penetrate through the

fluorinated top layer, resulting in a surface that is initially hydrophobic;[18,19] and the level of oil repellency is quite poor, (hexadecane contact angles of only 70° or less[20,21,22]). Pulsed plasma deposited poly(maleic anhydride) and poly(acrylic acid) surfaces that were subsequently complexed to fluorosurfactant displayed improved oleophobicity,[12,13] however the two step process is unsuitable for many industrial applications.

In this chapter, fast-switching oleophobic–hydrophilic polyelectrolyte–fluorosurfactant surfaces are created by utilising three different maleic anhydride copolymers, Scheme 8.1. In order to systematically investigate the role of polymer backbone structure, these comprised poly(ethylene-*alt*-maleic anhydride) alternating copolymer as a reference standard (based on previously reported polyelectrolyte–fluorosurfactant switching studies[12]), poly(styrene-*alt*-maleic anhydride) where the aforementioned alternating copolymer ethylene segments are replaced with styrene segments, and finally poly(styrene-*co*-maleic anhydride) which is a copolymer comprising single maleic anhydride units alternating with styrene block segments (because maleic anhydride does not homopolymerise[23]).

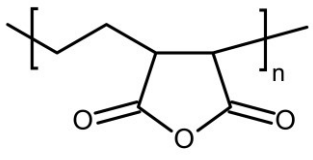

Poly(ethylene-*alt*-maleic anhydride)

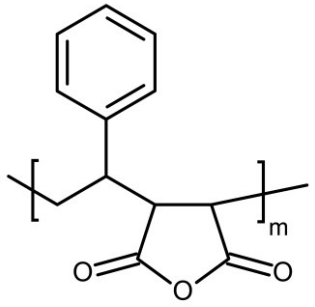

Poly(styrene-*alt*-maleic anhydride)

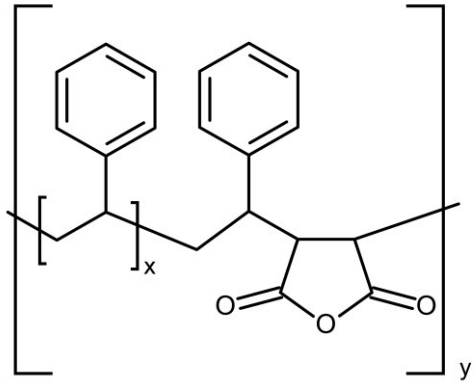

Poly(styrene-*co*-maleic anhydride)
(where x=0 for alternating copolymer)

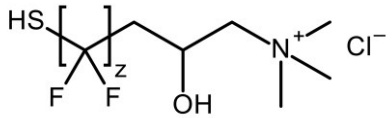

Zonyl® FSD cationic fluorosurfactant (where z = 6–20)

Scheme 8.1: Copolymers and cationic fluorosurfactant used to prepare copolymer–fluorosurfactant complexes.

8.2 Experimental

Polished silicon (100) wafers (Silicon Valley Microelectronics, Inc.) and glass slides (Academy Science Ltd.) were used as flat substrates. Poly(ethylene-*alt*-maleic anhydride) (Vertellus Specialties Inc.), poly(styrene-*alt*-maleic anhydride) (Apollo Scientific Ltd.), or poly(styrene-*co*-maleic anhydride) (Polyscope Polymers BV) were dissolved in acetone (+99.8%, Sigma Aldrich Ltd.) at a concentration of 2% (w/v). The cationic fluorosurfactant (Zonyl® FSD, DuPont Ltd.) employed for complexation was dissolved in high purity water at a concentration of 5% (v/v) and then added to the copolymer solution. The precipitated solid was collected from the liquid phase and dissolved at a concentration of 2% (w/v) in dimethylformamide (99%, Fisher Scientific UK Ltd.) for preparation of smooth surfaces and, in the case of the poly(styrene-*co*-maleic anhydride)–fluorosurfactant complex, varying composition dimethylformamide–methanol (99%, Sigma Aldrich Ltd.) solvent mixtures were utilised to produce rough surfaces. Spin coating was carried out using a photoresist spinner (Cammax Precima) operating at 2000 rpm. For the oil–water separation experiments, stainless steel mesh (0.16 mm wire diameter, 0.20 mm square holes, The Mesh Company Ltd.) was dip coated in the copolymer–fluorosurfactant complex solution and the solvent allowed to evaporate.

Glass transition temperatures of the copolymer and copolymer–fluorosurfactant complexes were measured by differential scanning calorimetry (DSC, Pyris 1, Perkin Elmer Inc.).

Microlitre sessile drop contact angle analysis was carried out with a video capture system (VCA2500XE, AST Products Inc.) using 1.0 μL dispensation of de-ionised water (BS 3978 grade 1), hexadecane (99%, Sigma Aldrich Ltd.), tetradecane (+99%, Sigma Aldrich Ltd.), dodecane (99%, Sigma Aldrich Ltd.), decane (+99%, Sigma Aldrich Ltd.), octane (+99%, Sigma Aldrich Ltd.), heptane (99%, Sigma Aldrich Ltd.), hexane (+99%, Sigma Aldrich Ltd.), and pentane (+99%, Sigma Aldrich Ltd.). Advancing and receding contact angles were measured by respectively increasing and decreasing the droplet size until the contact line was observed to move.[24] Oil repellency was further tested using motor engine oil (GTX 15W-40, Castrol Ltd.) and olive cooking oil (Tesco PLC).

Switching parameters were determined by calculating the difference between equilibrium hexadecane and water contact angles.

Atomic force microscopy (AFM) images were collected in tapping mode at 20 °C in ambient air (Nanoscope III, Digital Instruments, Santa Barbara, CA) using a tapping mode tip with a spring constant of 42–83 N m^{-1} (Nanoprobe). Root-mean-square (RMS) roughness values were calculated over 100 x 100 μm scan areas.

Anti-fogging was tested by exposing the coated surfaces to a high purity water spray from a pressurised nozzle (RG-3L, Anest Iwata Inc.).[25] Self-cleaning was tested by dispensing oil droplets onto a surface followed by rinsing with high purity water. Oil–water separation was tested by pouring an agitated mixture of oil and water over stainless steel mesh which has been dip coated with copolymer–fluorosurfactant complex. Oil Red O (≥75% dye content, Sigma Aldrich Ltd) and Procion® Blue MX-R (35% dye content, Sigma Aldrich Ltd.) were employed as oil and water dispersible dyes respectively in order to enhance visual contrast (similar results were obtained in absence of dye).

8.3 Results

8.3.1 Surface Switching

Differential scanning calorimetry (DSC) showed that the poly(ethylene-*alt*-maleic anhydride) copolymer has a higher glass transition temperature compared to the poly(styrene-*alt*-maleic anhydride), which can be attributed to the larger molecular weight of the former and less ordering due to the stiff and bulky styrene groups[26] for the latter, Table 8.1. In the case of the poly(styrene-*co*-maleic anhydride) copolymer, the presence of a single glass transition temperature is consistent with block styrene segments alternating with single maleic anhydride units (since a plausible alternative diblock copolymer structure should display two respective glass transition temperatures[27]), Scheme 8.1. Also, its higher glass transition temperature compared to the poly(styrene-*alt*-maleic anhydride) alternating copolymer stems from a combination of higher molecular weight and favourable intermolecular interactions between adjacent styrene units contained within the block styrene segments.[28]

Table 8.1: Glass transition temperatures of copolymers and copolymer–fluorosurfactant complexes.

Copolymer	Maleic Anhydride Content / wt. %	Molecular Weight / g mol^{-1}	Glass Transition Temperature / °C	
			Copolymer	Copolymer–Fluorosurfactant Complex
Poly(ethylene-*alt*-maleic anhydride)	50	60,000	155	157
Poly(styrene-*alt*-maleic anhydride)	50	50,000	120	131
Poly(styrene-*co*-maleic anhydride)	26	80,000	160	138

Following fluorosurfactant complexation, both the poly(ethylene-*alt*-maleic anhydride) and poly(styrene-*alt*-maleic anhydride) copolymer–fluorosurfactant complexes display raised glass transition temperatures, which suggests a greater degree of ordering upon surfactant complexation, and is consistent with previous studies relating to copolymer–surfactant complex systems, Table 8.1.[29,30] In contrast, for the poly(styrene-*co*-maleic anhydride)–fluorosurfactant complex, the glass transition temperature is lower compared to that of the parent copolymer; this may be due to disruption of the favourable intermolecular interactions between adjacent styrene units contained within the block segments (something which is absent for the parent alternating copolymers).[28,31]

Spin coating of all three copolymer–fluorosurfactant complexes dissolved in dimethylformamide (DMF) onto silicon wafers and glass slides produced smooth films (AFM RMS roughness = 1–5 nm), Table 8.2. In all cases, a time period of 10 s was sufficient for the water contact angles to reach their final static values (in fact, the poly(styrene-*alt*-maleic anhydride)–fluorosurfactant system underwent instantaneous water wetting); whereas hexadecane droplets remained stationary, Figure 8.1 and Table 8.2. Copolymer–fluorosurfactant complex surfaces prepared using an alternative quaternary ammonium cationic fluorosurfactant (S-106A, Chemguard) displayed similar oleophobic–hydrophilic switching behaviour. This was also found to be the case for copolymer–fluorosurfactant complex surfaces created using a cationic copolymer (poly(styrene-*alt*-maleimide), SMA® 1000I, Cray Valley HSC) and an anionic

fluorosurfactant (Capstone® FS-63, Dupont Ltd.). Control experiments utilising any of the parent copolymers (in the absence of fluorosurfactant complexation) showed the converse trend, with an absence of superhydrophilicity and instantaneous spreading of hexadecane droplets, Table 8.2.

Table 8.2: Microlitre water and hexadecane static contact angles for copolymer spin coated from acetone solvent; copolymer–fluorosurfactant complex surfaces (smooth) spin coated from dimethylformamide (DMF) solvent; and poly(styrene-*co*-maleic anhydride)–fluorosurfactant complex surfaces (rough) spin coated from 33 vol % DMF–66 vol % methanol. Water droplets were allowed to relax for 10 s to reach equilibrium prior to final static contact angle measurement. No relaxation in contact angle was observed for hexadecane droplets. AFM surface roughness values are included for comparison.

	AFM RMS Roughness / nm	**Static Water Contact Angle / °**		**Hexadecane Contact Angle / °**			
		0 s	**10 s**	**Static**	**Advancing**	**Receding**	**Hysteresis**
Poly(ethylene-*alt*-maleic anhydride)	4.4±1	38±2	22±2	Wets	–	–	–
Poly(ethylene-*alt*-maleic anhydride)–fluorosurfactant	1.1±0.3	88±2	<10	74±1	76±2	72±2	4±2
Poly(styrene-*alt*-maleic anhydride)	6.7±1	68±2	66±2	Wets	–	–	–
Poly(styrene-*alt*-maleic anhydride)–fluorosurfactant	2.7±0.3	<10	<10	80±2	85±2	66±2	19±2
Poly(styrene-*co*-maleic anhydride)	10.3±1	90±2	90±2	Wets	–	–	–
Poly(styrene-*co*-maleic anhydride)–fluorosurfactant	5.3±1	36±2	23±2	80±2	88±2	66±2	22±2
Poly(styrene-*co*-maleic anhydride)–fluorosurfactant 33 vol % DMF– 66 vol % methanol	246±3	<10	<10	112±5	125±5	<10	>115

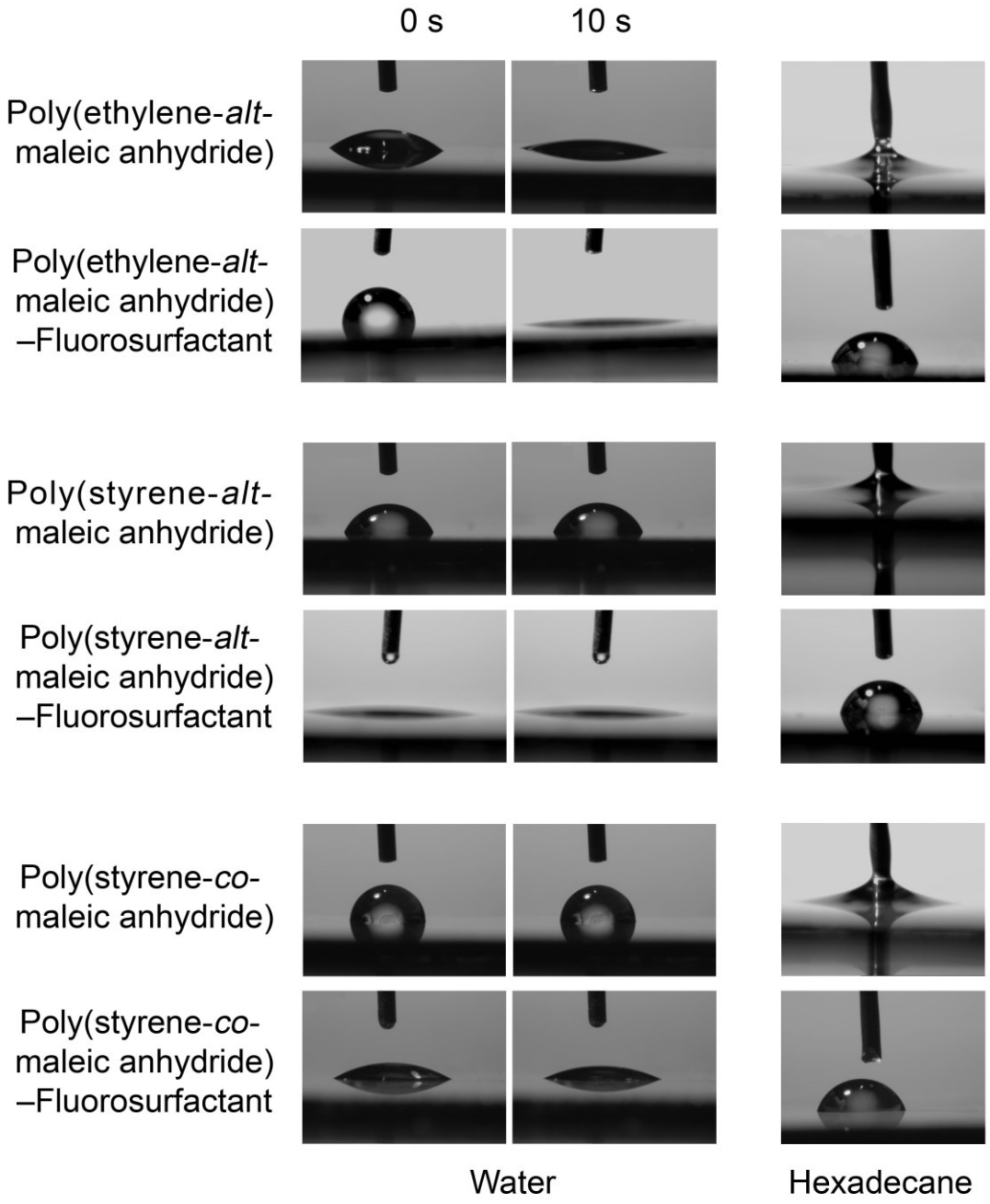

Figure 8.1: Microlitre water and hexadecane droplets dispensed onto copolymer spin coated from acetone solvent and copolymer–fluorosurfactant complex surfaces spin coated from dimethylformamide solvent. No relaxation in contact angle value was observed for hexadecane droplets.

Oil repellency of the poly(ethylene-*alt*-maleic anhydride)–fluorosurfactant complex surfaces was found to improve (higher contact angle and lower hysteresis) with increasing hydrocarbon length of straight chain alkane droplets, Figure 8.2. A similar trend was observed for both of the poly(styrene-maleic anhydride)–fluorosurfactant complex surfaces. Furthermore, olive oil and motor engine oil spreading were shown to be inhibited on all three types of copolymer–fluorosurfactant complex surfaces, Figure 8.3.

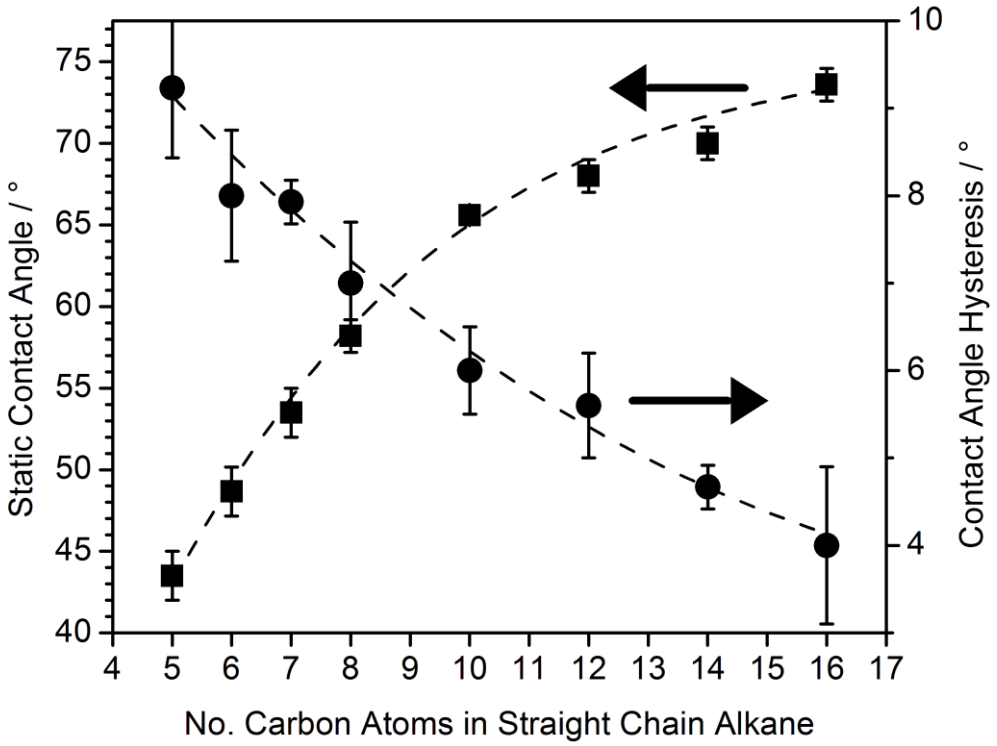

Figure 8.2: Static contact angles and contact angle hysteresis of microlitre droplets of oil on poly(ethylene-*alt*-maleic anhydride)–fluorosurfactant complex surfaces spin coated from dimethylformamide solvent as a function of liquid alkane chain length. A similar trend was noted for poly(styrene-*alt*-maleic anhydride)–fluorosurfactant and poly(styrene-*co*-maleic anhydride)–fluorosurfactant surfaces spin coated from dimethylformamide solvent.

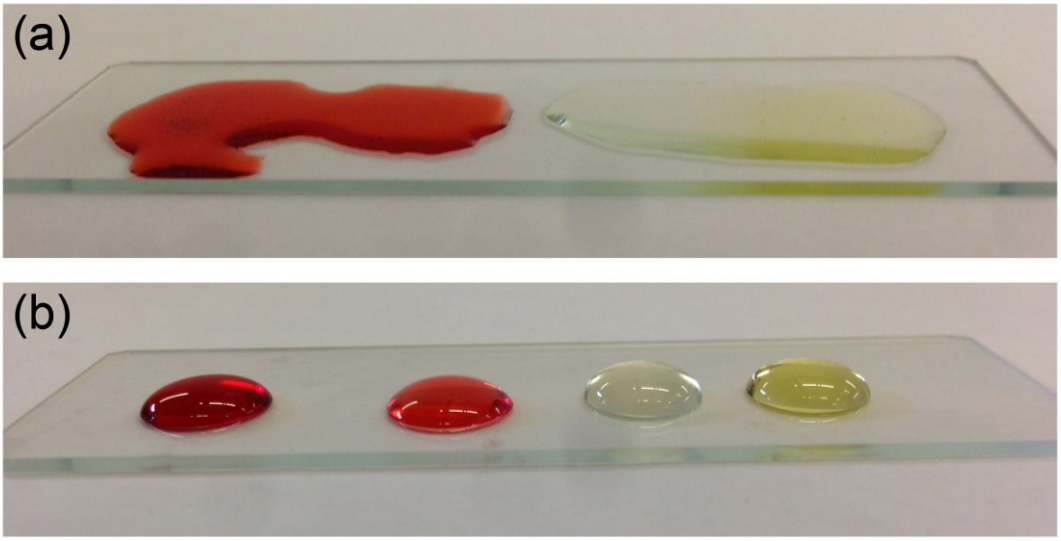

Figure 8.3: Hexadecane, octane, olive oil, and motor oil droplets (left to right) on: (a) uncoated glass slide; and (b) poly(ethylene-*alt*-maleic anhydride)–fluorosurfactant complex surface solvent cast from dimethylformamide. A similar trend was noted for poly(styrene-*alt*-maleic anhydride)–fluorosurfactant and poly(styrene-*co*-maleic anhydride)–fluorosurfactant surfaces spin coated from dimethylformamide solvent. Hexadecane and octane droplets are dyed with Oil Red O (Sigma Aldrich Ltd.) to show contrast (similar results were obtained in the absence of dye).

8.3.2 Anti-Fogging and Self-Cleaning

Extremely low water contact angles are highly desirable for anti-fogging applications.[32] Copolymer–fluorosurfactant complex dip coated glass slides using dimethylformamide solvent were found to retain their transparency (anti-fogging) during water vapour exposure, Figure 8.4.

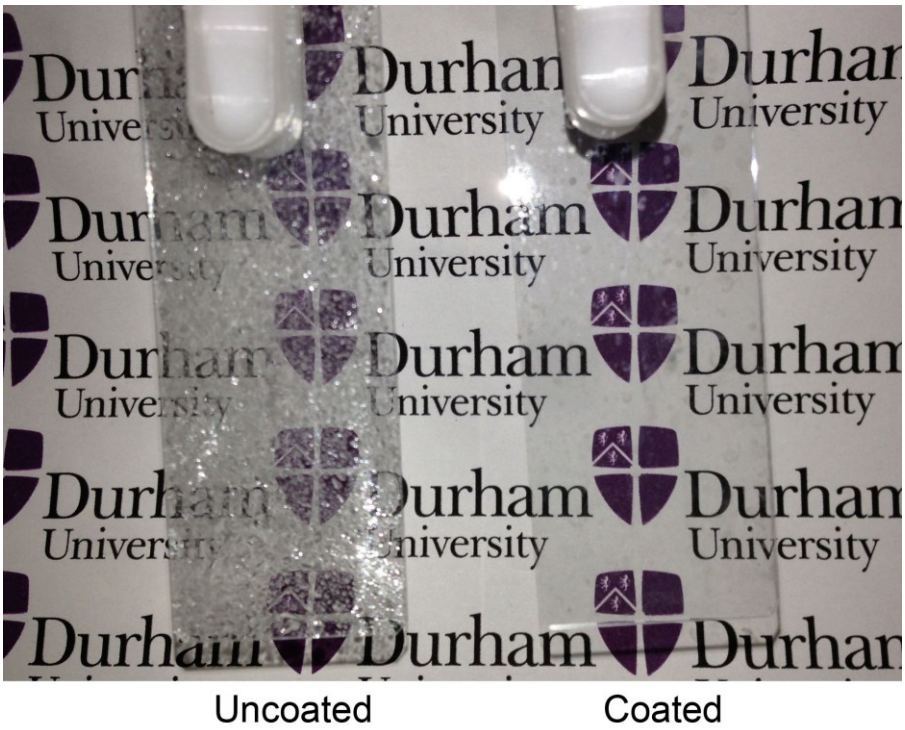

Figure 8.4: Demonstration of anti-fogging following exposure to water vapour (fogging): on uncoated glass slide and poly(ethylene-*alt*-maleic anhydride)–fluorosurfactant complex solvent cast from dimethylformamide. Similar behaviour was observed for poly(styrene-*alt*-maleic anhydride)–fluorosurfactant and poly(styrene-*co*-maleic anhydride)–fluorosurfactant complex dip coated glass slides using dimethylformamide solvent.

Self-cleaning properties were demonstrated by rinsing off fouling oils with just water, Figure 8.5. This is consistent with the high receding contact angle measured for hexadecane, Table 8.2.[33]

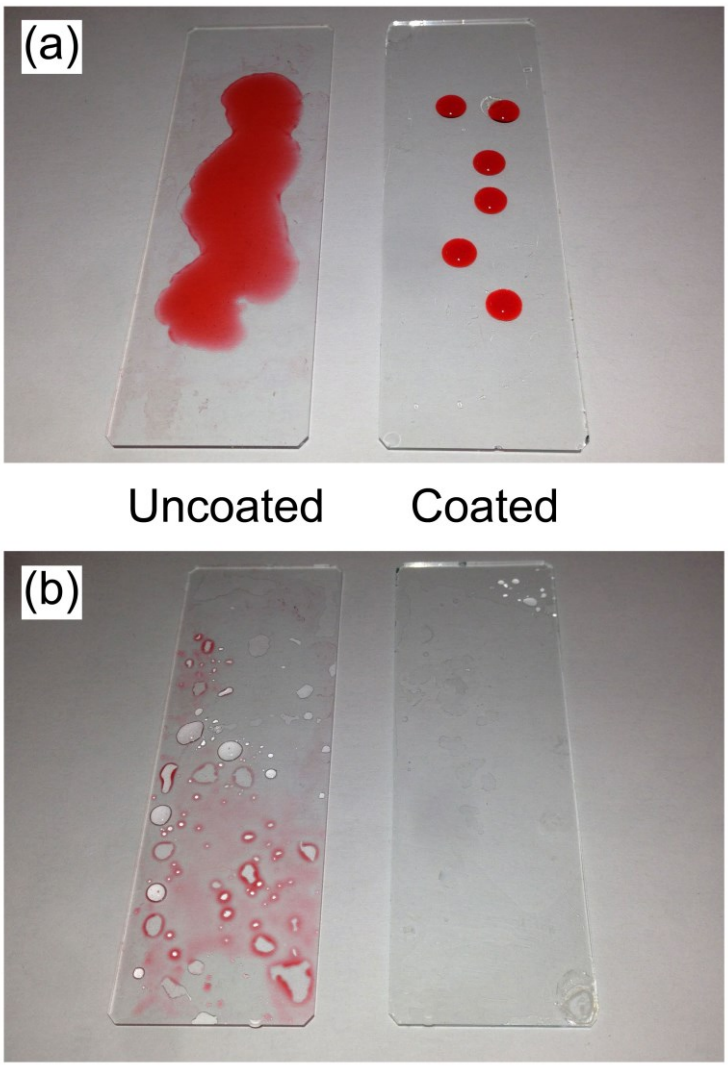

Figure 8.5: Demonstration of self-cleaning: (a) uncoated glass slide and poly(ethylene-*alt*-maleic anhydride)–fluorosurfactant complex coating solvent cast from dimethylformamide fouled with hexadecane; and (b) after quick rinse with water. Similar behaviour was observed for poly(styrene-*alt*-maleic anhydride)–fluorosurfactant and poly(styrene-*co*-maleic anhydride)–fluorosurfactant complex surfaces solvent cast from dimethylformamide. Hexadecane droplets are dyed with Oil Red O (Sigma Aldrich Ltd.) to show contrast (similar results were obtained in the absence of dye).

8.3.3 Solvent-Induced Roughening to Enhance Switching Parameter

Further enhancement of the oleophobic–hydrophilic surface switching behaviour was investigated for the poly(styrene-*co*-maleic anhydride)–fluorosurfactant system by varying the casting solvent mixture composition, Figure 8.6. Diluting dimethylformamide with methanol gives rise to an increase in surface roughness, which is attributable to the poor solubility of the styrene block segments in methanol.[34] This solvent-induced roughness lowers the static water contact angle (<10°) whilst concurrently raising the static hexadecane contact angle (>110°), to yield a hexadecane–water switching parameter exceeding 100°, Figure 8.6. Control experiments showed a lack of surface roughness enhancement by varying the dimethylformamide–methanol solvent composition for poly(ethylene-*alt*-maleic anhydride)–fluorosurfactant and the poly(styrene-*alt*-maleic anhydride)–fluorosurfactant complex solutions, which is consistent with the absence of low methanol solubility styrene block segments being present in the alternating copolymer structures, Scheme 8.1.

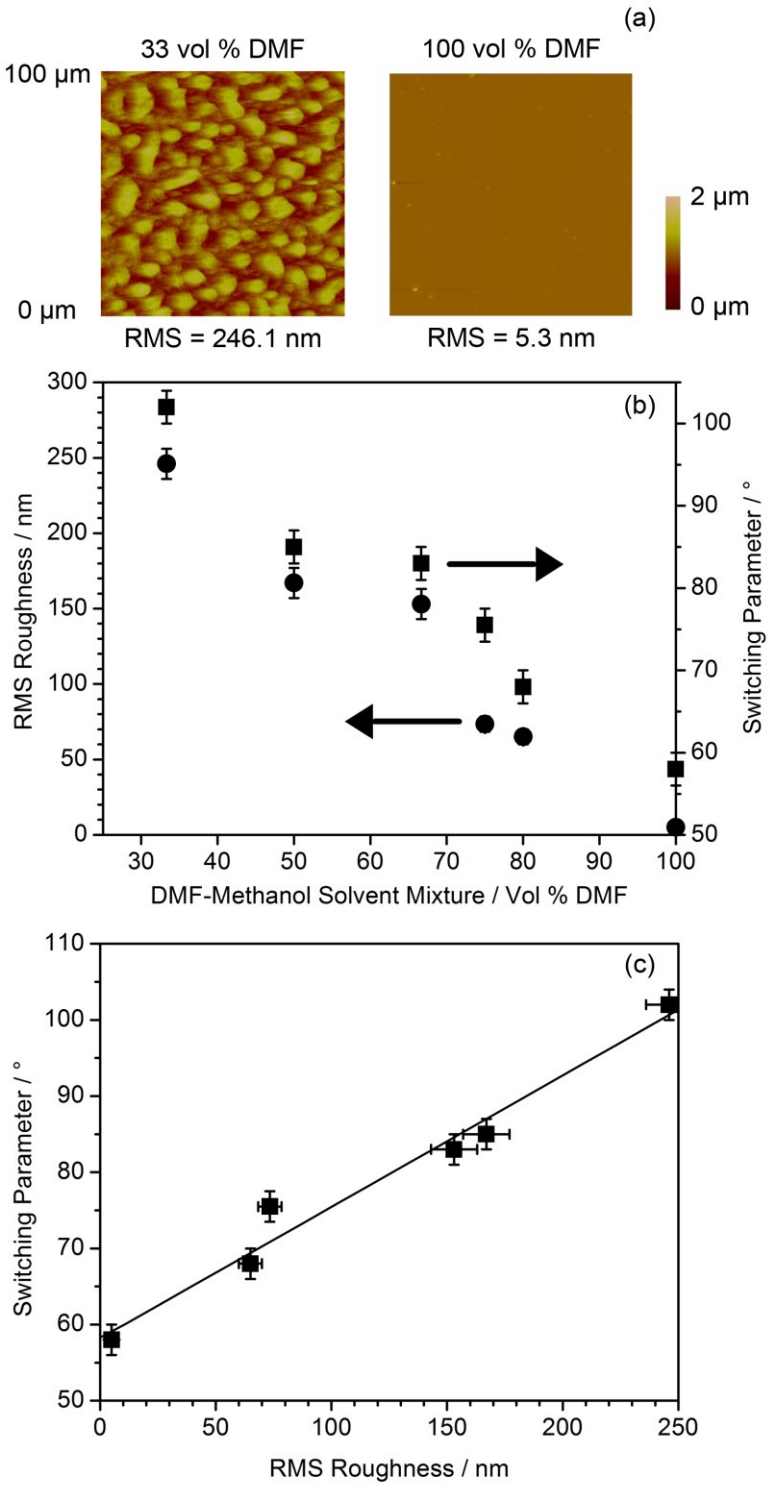

Figure 8.6: (a) AFM height images and RMS roughness values for poly(styrene-*co*-maleic anhydride)–fluorosurfactant complex surfaces spin coated from different vol % dimethylformamide–methanol solutions; (b) AFM RMS roughness and hexadecane–water static contact angle switching parameter of poly(styrene-*co*-maleic anhydride)–fluorosurfactant complex surfaces as a function of dimethylformamide–methanol solvent mixture composition; and (c) correlation between hexadecane–water static contact angle switching parameter of poly(styrene-*co*-maleic anhydride)–fluorosurfactant complex surfaces and AFM RMS roughness.

8.3.4 Oil–Water Separation

Oil–water separation efficacy was tested using copolymer–fluorosurfactant complex coatings dip coated onto stainless steel mesh. These were then suspended over a sample vial followed by dispensing an agitated oil–water mixture. The water component was observed to pass through the mesh whilst the oil (hexadecane) remained suspended on the mesh surface, Figure 8.7. These meshes were then inclined at an angle, and pouring the oil–water mixture over them yielded separation efficiencies as high as 98% in the case of the poly(styrene-*co*-maleic anhydride)–fluorosurfactant complex surface (attributable to the dimethylformamide–methanol solvent mixture induced roughness enhancement of the oil–water switching parameter), Figure 8.7 and Table 8.3. The absence of solvent induced roughness resulted in lower oil–water separation efficiencies for the two alternating copolymer–fluorosurfactant complex systems.

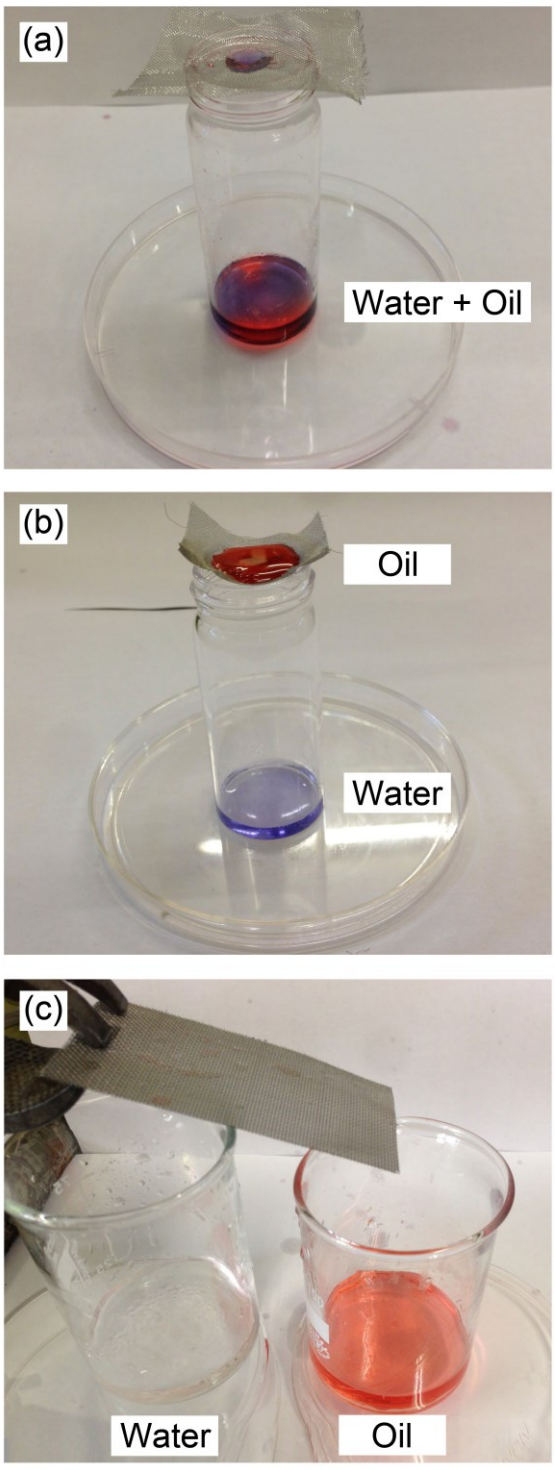

Figure 8.7: Demonstration of oil–water separation: hexadecane–water mixture dispensed onto (a) uncoated stainless steel mesh; (b) stainless steel mesh dip coated with poly(styrene-*co*-maleic anhydride)–fluorosurfactant complex in 33 vol % dimethylformamide–66 vol % methanol solvent mixture; and (c) inclined coated stainless steel mesh dip coated with poly(styrene-*co*-maleic anhydride)–fluorosurfactant complex in 33 vol % dimethylformamide–66 vol % methanol solvent mixture acting as oil–water separator (oil and water are shown to be collected into separate beakers). Similar behaviour was observed for octane– and motor oil–water mixtures. Hexadecane is dyed with Oil Red O (Sigma Aldrich Ltd.) to show contrast (similar results were obtained in the absence of dye).

Table 8.3: Oil–water separation efficiencies for copolymer–fluorosurfactant complex dip coated stainless steel mesh from 33 vol % dimethylformamide–66 vol % methanol solvent mixtures.

Switching Surface	AFM RMS Roughness / nm	Oil–Water Separation Efficiency[a] / %
Poly(ethylene-*alt*-maleic anhydride) + fluorosurfactant	1.1±0.3	0
Poly(styrene-*alt*-maleic anhydride) + fluorosurfactant	2.7±0.3	48±4
Poly(styrene-*co*-maleic anhydride) + fluorosurfactant	246±3	98±2

[a]100% efficiency corresponds to complete separation of water from hexadecane.

8.4 Discussion

Previously reported polymer–fluorosurfactant complex surfaces that display oleophobic–hydrophilic switching behaviour rely on the inherent hydrophilicity of the base polymer.[17] For instance, in the case of solvent cast ionic polymer–fluorosurfactant complex surfaces, the fluorinated surfactant tails segregate at the air–solid interface, thereby aligning the hydrolysed counterionic groups towards the near-surface region as a consequence of their strong electrostatic attraction towards the ionic surfactant head.[16,35,36] This interfacial interaction leads to an enhanced concentration of hydrophilic groups in the near-surface region compared to the parent polymer. It has been proposed that such polymer–fluorosurfactant surfaces are able to exhibit oleophobic–hydrophilic switching behaviour due to the existence of defect sites or "holes" at the fluorinated surfactant tail air–solid interface through which water molecules can penetrate down towards the complexing counterion hydrophilic sub-surface.[17] This description helps to explain why all three copolymer–fluorosurfactant complex systems in the present study display lower final static water contact angles compared to their parent base copolymers, Figure 8.1 and Table 8.2.

The oleophobic–hydrophilic behaviour of such polymer–fluorosurfactant complex surfaces can be quantified in terms of a switching parameter (for instance, the difference in measured static contact angle between hexadecane and water droplets), Figure 8.8. Most previous studies have tended to quote

water contact angles only after allowing the droplet to stabilise over several minutes on the surface because of the slow rate at which water molecules penetrate through towards the hydrophilic sub-surface to manifest surface switching (although the surface initially is hydrophobic).[18,19,21] In the present investigation, the time taken to reach a final static water contact angle is much shorter (<10 s) for all copolymer–fluorosurfactant systems. Furthermore, both styrene-containing copolymer–fluorosurfactant complex surfaces reach a final static water contact angle value much quicker than their ethylene-containing copolymer counterpart due to the bulky styrene side group providing a lower packing efficiency for the former, and thereby facilitating a faster penetration of water into the hydrophilic sub-surface, Figure 8.1. This explanation is consistent with the styrene-based copolymer–fluorosurfactant complexes having lower glass transition temperatures, Table 8.1. In addition, for the case of the poly(styrene-*alt*-maleic anhydride) copolymer, the more disordered nature of the alternating styrene side groups provides a greater level of polymer chain mobility,[37,38] which allows the fluorinated alkyl chains to reorient themselves more readily at the solid–air interface (culminating in instantaneous water wetting and high hexadecane contact angle values, Figure 8.1 and Table 8.2).

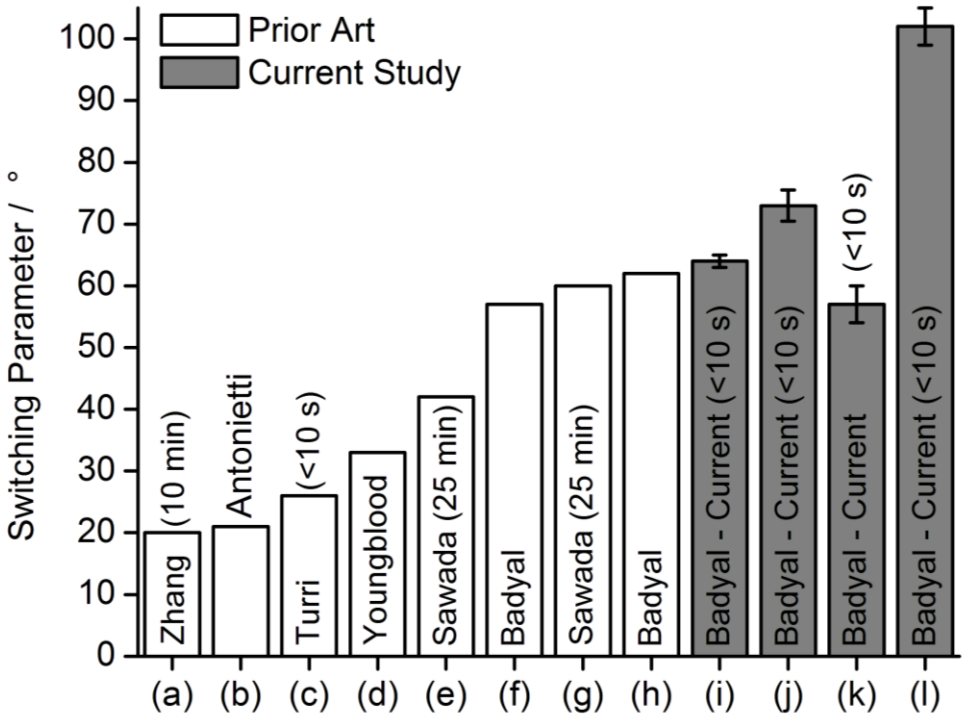

Figure 8.8: Oleophobic–hydrophilic switching parameters for nominally flat surfaces reported in the literature: (a) Zhang,[19] (b) Antonietti,[20] (c) Turri,[22] (d) Youngblood,[6] (e) Sawada,[18] (f) Badyal,[12] (g) Sawada,[21] (h) Badyal,[13] (i) poly(ethylene-*alt*-maleic anhydride)–fluorosurfactant (RMS = 1.1±0.3 nm), (j) poly(styrene-*alt*-maleic anhydride)–fluorosurfactant (RMS = 2.7±0.3 nm), (k) poly(styrene-co-maleic anhydride)–fluorosurfactant (smooth, RMS = 5.3±1 nm), and (l) poly(styrene-*co*-maleic anhydride)–fluorosurfactant (rough, RMS = 246±3 nm). Switching parameters are calculated from the difference between hexadecane and water static contact angles. Time taken for water to reach final static water contact angle value is given in brackets if reported.

The high receding hexadecane contact angle and low surface roughness of copolymer–fluorosurfactant complex surfaces spin coated from dimethylformamide solvent make them ideal for self-cleaning and anti-fog applications, Table 8.2 and Figures 8.3–8.5. Such surfaces are easily cleaned by rinsing in water (which replaces the oil–solid interaction with a much more favourable water–solid interaction, i.e. switching).

Dissolving the poly(styrene-*co*-maleic anhydride)–fluorosurfactant complex in a dimethylformamide–methanol solvent mixture prior to film formation enhances surface roughness due to the poor solubility of the styrene block segments in methanol.[34] This surface roughness is capable of improving hydrophilicity due to increased surface area (Wenzel wetting[39]) and oleophobicity due to the ability to trap air (Cassie-Baxter wetting[40]), Table

8.2.[41,42,43] A key advantage of this approach is that it circumvents the need for introducing roughness as a separate step through the incorporation of additional materials[19,41,44] or by mixing roughening particles into the copolymer–fluorosurfactant complex solution. It is envisaged that a range of different solvents or coating methods (e.g. spray coating[45]) may be used to introduce surface roughness for the enhancement of the switching parameter for other types of polymer–surfactant complex systems.

Coating of steel mesh with such roughened poly(styrene-*co*-maleic anhydride)–fluorosurfactant complex surfaces (prepared from dimethylformamide–methanol solvent mixtures) provides two length scales of roughness (steel mesh pores plus solvent-induced film roughness) both of which help to lower oil contact angle hysteresis (improve oil repellency).[46,47] When combined with the inherent high switching parameter, oil–water separation with >98% efficiency is attained, Table 8.3. This performance matches existing oleophobic–hydrophilic systems for oil–water separation (which however tend to be far more complex in nature and fabrication methods).[7] Although there are more efficient separation processes (99.999% efficiency[48]) based on membrane filtration where small pores allow the passage of water whilst blocking oils,[49] such filters have low volume throughput and can be easily clogged with excess oil (requiring cleaning or replacement). Other membranes, such as those investigated in Chapter 7 are hydrophobic–oleophilic. One embodiment of the current methodology would be to deploy it for pre-treatment filters installed upstream of conventional membrane filters, thereby ensuring removal of the majority of oil-based contaminants so as to minimise the amount of oil reaching the membrane filters (and therefore avoid blockage as well as maximise efficiency). Such oil–water separators could potentially help to tackle the environmental impact of the gas, oil, metal, textile, and food processing industries.[50]

8.5 Conclusions

Solvent cast copolymer–fluorosurfactant complexes have been found to display large magnitude oleophobic–hydrophilic switching behaviour as well as rapid switching speeds. Further enhancement in switching performance is achieved by combining surface chemical functionality and roughness. These ultra-fast

switching oleophobic–hydrophilic surfaces have been shown to display excellent anti-fog, self-cleaning, and oil–water separation properties.

8.6 References

[1] Jin, M.; Wang, J.; Yao, X.; Liao, M.; Zhao, Y.; Jiang, L. Underwater Oil Capture by a Three-Dimensional Network Architectured Organosilane Surface. *Adv. Mater.* **2011**, *23*, 2861.

[2] Xue, Z.; Wang, S.; Lin, L.; Chen, L.; Liu, M.; Feng, L.; Jiang, L. A Novel Superhydrophilic and Underwater Superoleophobic Hydrogel-Coated Mesh for Oil/Water Separation. *Adv. Mater.* **2011**, *23*, 4270.

[3] Kota, A. K.; Kwon, G.; Choi, W.; Mabry, J. M.; Tuteja, A. Hygro-responsive membranes for effective Oil–Water separation. *Nat. Commun.* **2012**, *3*, 1025.

[4] Howarter, J. A.; Youngblood, J. P. Amphiphile grafted membranes for the separation of oil-in-water dispersions. *J. Colloid Interface Sci.* **2009**, *329*, 127.

[5] Howarter, J. A.; Youngblood, J. P. Self-Cleaning and Anti-Fog Surfaces via Stimuli-Responsive Polymer Brushes. *Adv. Mater.* **2007**, *19*, 3838.

[6] Howarter, J. A.; Genson, K. L.; Youngblood, J. P. Wetting Behavior of Oleophobic Polymer Coatings Synthesized from Fluorosurfactant-Macromers. *ACS Appl. Mater. Interfaces* **2011**, *3*, 2022.

[7] Leng, B.; Shao, Z.; de With, G.; Ming, W. Superoleophobic Cotton Textiles. *Langmuir* **2009**, *25*, 2456.

[8] Wang, Y.; Dong, Q.; Wang, Y.; Wang, H.; Li, G.; Bai, R. Investigation on RAFT Polymerization of a Y-Shaped Amphiphilic Fluorinated Monomer and Anti-Fog and Oil-Repellent Properties of the Polymers. *Macromol. Rapid Commun.* **2010**, *31*, 1816.

[9] Briscoe, B. J.; Galvin, K. P. The effect of surface fog on the transmittance of light. *Sol. Energy* **1991**, *46*, 191.

[10] Xu, F. J.; Neoh, K. G.; Kang, E. T. Bioactive surfaces and biomaterials via atom transfer radical polymerization. *Prog. Polym. Sci.* **2009**, *34*, 719.

[11] Kobayashi, M.; Terayama, Y.; Yamaguchi, H.; Terada, M.; Murakami, D.; Ishihara, K.; Takahara, A. Wettability and Antifouling Behavior on the Surfaces of Superhydrophilic Polymer Brushes. *Langmuir* **2012**, *28*, 7212.

[12] Lampitt, R. A.; Crowther, J. M.; Badyal, J. P. S. Switching Liquid Repellent Surfaces. *J. Phys. Chem. B* **2000**, *104*, 10329.

[13] Hutton, S. J.; Crowther, J. M.; Badyal, J. P. S. Complexation of Fluorosurfactants to Functionalized Solid Surfaces: Smart Behavior. *Chem. Mater.* **2000**, *12*, 2282.

[14] Goddard, E. D. Polymer–surfactant interaction part II. Polymer and surfactant of opposite charge. *Colloids Surf.* **1986**, *19*, 301.

[15] Thünemann, A. F.; Lochhaas, K. H. Surface and Solid-State Properties of a Fluorinated Polyelectrolyte–Surfactant Complex. *Langmuir* **1999**, *15*, 4867.

[16] Vaidya, A.; Chaudhury, M. K. Synthesis and Surface Properties of Environmentally Responsive Segmented Polyurethanes. *J. Colloid Interface Sci.* **2002**, *249*, 235.

[17] Li, L.; Wang, Y.; Gallaschun, C.; Risch, T.; Sun, J. Why can a nanometer-thick polymer coated surface be more wettable to water than to oil? *J. Mater. Chem.* **2012**, *22*, 16719.

[18] Sawada, H.; Yoshioka, H.; Kawase, T.; Takahashi, H.; Abe, A.; Ohashi, R. Synthesis and Applications of a Variety of Fluoroalkyl End-Capped Oligomers/Silica Gel Polymer Hybrids. *J. Appl. Polym. Sci.* **2005**, *98*, 169.

[19] Yang, J.; Zhang, Z.; Xu, X.; Zhu, X.; Men, X.; Zhou, X. Superhydrophilic-superoleophobic coatings. *J. Mater. Chem.* **2012**, *22*, 2834.

[20] Antonietti, M.; Henke, S.; Thünemann, A. F. Highly ordered materials with ultra-low surface energies: Polyelectrolyte–surfactant, complexes with fluorinated surfactants. *Adv. Mater.* **1996**, *8*, 41.

[21] Sawada, H.; Ikematsu, Y.; Kawase, T.; Hayakawa, Y. Synthesis and Surface Properties of Novel Fluoroalkylated Flip-Flop-Type Silane Coupling Agents. *Langmuir* **1996**, *12*, 3529.

[22] Turri, S.; Valsecchi, R.; Viganò, M.; Levi, M. Hydrophilic–oleophobic behaviour in thin films from fluoromodified nanoclays and polystyrene. *Polym. Bull.* **2009**, *63*, 235.

[23] Bartlett, P. D.; Nozaki, K. The Polymerization of Allyl Compounds. III. The Peroxide-induced Copolymerization of Allyl Acetate with Maleic Anhydride. *J. Am. Chem. Soc.* **1946**, *68*, 1495.

[24] Johnson, R. E. Jr.; Dettre, R. H. Wetting of Low-Energy Surfaces. In Wettability; Berg J. C., Ed.; Marcel Dekker, Inc.: New York, 1993; Chapter 1, p 13.

[25] Mochizuki, C.; Hara, H.; Takano, I.; Hayakawa, T.; Sato, M. Application of carbonated apatite coating on a Ti substrate by aqueous spray method. *Mater. Sci. Eng., C* **2013**, *33*, 951.

[26] Kunal, K.; Robertson, C. G.; Pawlus, S.; Hahn, S. F.; Sokolov, A. P. Role of Chemical Structure in Fragility of Polymers: A Qualitative Picture. *Macromolecules* **2008**, *41*, 7232.

[27] Kraus, G.; Childers, C. W.; Gruver, J. T. Properties of random and block copolymers of butadiene and styrene. I. Dynamic properties and glassy transition temperatures. *J. Appl. Polym. Sci.* **1967**, *11*, 1581.

[28] López-Díaz, D.; Velázquez, M. M. Evidence of glass transition in thin films of maleic anhydride derivatives: Effect of the surfactant coadsorption. *Eur. Phys. J. E* **2008**, *26*, 417.

[29] Kokufuta, E.; Zhang, Y.-Q.; Tanaka, T.; Mamada, A. Effects of Surfactants on the Phase Transition of Poly(N-isopropylacrylamide) Gel. *Macromolecules* **1993**, *26*, 1053.

[30] Antonietti, M.; Conrad, J. Synthesis of Very Highly Ordered Liquid Crystalline Phases by Complex Formation of Polyacrylic Acid with Cationic Surfactants. *Angew. Chem. Int. Ed. Engl.* **1994**, *33*, 1869.

[31] Ghebremeskel, A. N.; Vemavarapu, C.; Lodaya, M. Use of surfactants as plasticizers in preparing solid dispersions of poorly soluble API: Selection of polymer–surfactant combinations using solubility parameters and testing the processability. *Int. J. Pharm.* **2007**, *328*, 119.

[32] Grosu, G.; Andrzejewski, L.; Veilleux, G.; Ross, G. G. Relation between the size of fog droplets and their contact angles with CR39 surfaces. *J. Phys. D: Appl. Phys.* **2004**, *37*, 3350.

[33] Howarter, J. A.; Youngblood, J. P. Self-Cleaning and Next Generation Anti-Fog Surfaces and Coatings. *Macromol. Rapid Commun.* **2008**, *29*, 455.

[34] Spatz, J. P.; Möller, M.; Noeske, M; Behm, R. J.; Pietralla, M. Nanomosaic Surfaces by Lateral Phase Separation of a Diblock Copolymer. *Macromolecules* **1997**, *30*, 3874.

[35] Su, Z.; Wu, D.; Hsu, S. L.; McCarthy, T. J. Adsorption of End-Functionalized Poly(ethylene oxide)s to the Poly(ethylene oxide)–Air Interface. *Macromolecules* **1997**, *30*, 840.

[36] Walters, K. B.; Schwark, D. W.; Hirt, D. E. Surface Characterization of Linear Low-Density Polyethylene Films Modified with Fluorinated Additives. *Langmuir* **2003**, *19*, 5851.

[37] Qiu, G.-M.; Zhu, L.-P.; Zhu, B.-K.; Xu, Y.-Y.; Qiu, G.-L. Grafting of styrene/maleic anhydride copolymer onto PVDF membrane by supercritical carbon dioxide: Preparation, characterization and biocompatibility. *J. Supercrit. Fluids* **2008**, *45*, 374.

[38] Reiter, G. Dewetting as a Probe of Polymer Mobility in Thin Films. *Macromolecules* **1994**, *27*, 3046.

[39] Wenzel, R. N. Resistance Of Solid Surfaces To Wetting By Water. *Ind. Eng. Chem.* **1936**, *28*, 988.

[40] Cassie, A. B. D.; Baxter, S. Wettability of porous surfaces. *Trans. Faraday Soc.* **1944**, *40*, 546.

[41] Tuteja, A.; Choi, W.; Ma, M.; Mabry, J. M.; Mazzella, S. A.; Rutledge, G. C.; McKinley, G. H.; Cohen, R. E. Designing Superoleophobic Surfaces. *Science* **2007**, *318*, 1618.

[42] Steele, A.; Bayer, I.; Loth, E. Inherently Superoleophobic Nanocomposite Coatings by Spray Atomization. *Nano Lett.* **2009**, *9*, 501.

[43] Choi, W.; Tuteja, A.; Chhatre, S.; Mabry, J. M.; Cohen, R. E.; McKinley, G. H. Fabrics with Tunable Oleophobicity. *Adv. Mater.* **2009**, *21*, 2190.

[44] Tuteja, A.; Kota, A. K.; Kwon, G.; Mabry, J. M. Superhydrophilic and oleophobic porous materials and methods for making and using the same. U.S. Patent US 2012/0000853 A1, Jan. 5, 2012.

[45] Badyal, J. P. S.; Woodward, I. S. Method and apparatus for the formation of hydrophobic surfaces. World Patent WO 2003080258 A2, Oct. 2, 2003.

[46] Gao, L.; McCarthy, T. J. The “Lotus Effect” Explained: Two Reasons Why Two Length Scales of Topography Are Important *Langmuir* **2006**, *22*, 2966.

[47] Zhao, H.; Park, K.-C.; Law, K.-Y. Effect of Surface Texturing on Superoleophobicity, Contact Angle Hysteresis, and “Robustness”. *Langmuir* **2012**, *28*, 14925.

[48] Compass Water Solutions. http://www.cworldwater.com/ultrasep.html (accessed July 1, 2013).

[49] Hydration Technology Innovations. http://www.htiwater.com/technology/ultrafiltration.html (accessed July 1, 2013).

[50] Cheryan, M.; Rajagopalan, N. Membrane processing of oily streams. Wastewater treatment and waste reduction. *J. Membr. Sci.* **1998**, *151*, 13.

Chapter 9 Conclusions and Further Work

The impact, spreading, and imbibition of picolitre droplets of water is dependent upon a range of surface properties including chemistry, roughness, charge, and porosity. In Chapter 3, it was found that the impact and spreading of picolitre droplets of water onto superhydrophobic CF_4 plasma fluorinated polybutadiene surfaces is strongly influenced by the length scale of surface topography (for similar RMS roughness values). Large differences are observed between the behaviour of microlitre and picolitre drops, implying that measurements made with conventional contact angle instruments are unlikely to be good predictors of inkjet behaviour. The droplet oscillation frequency following impact was found to be a good parameter to differentiate the different droplet dynamics arising from different surfaces topographies. The superhydrophobic surfaces were found to inhibit spreading, resulting in a static spreading ratio of 0.63. Such surfaces could be utilised for high-resolution inkjet printing. Further work could entail studying the impact and spreading of inkjet-relevant droplets such as glycol ethers or alcohols. Issues such as droplet bouncing could be mitigated by utilising a patterned substrate featuring hydrophilic spots on a superhydrophobic background, increasing droplet adhesion whilst improving feature size and printed line formation.

Plasma texturing of polybutadiene was found to result in two length scales of surface roughness. A further level of morphology can be added via solvent templating. In Chapter 4, solvent casting of polybutadiene under controlled humidity gives rise to the formation of two-dimensional hexagonally ordered honeycomb arrays. Pore aperture size and surface coverage can be independently controlled by varying the humidity and polymer concentration respectively. CF_4 plasmachemical modification imparts low surface energy functional groups in combination with surface texturing and sub-surface cross-linking of the honeycomb structures to yield superhydrophobicity (high contact angles and low hysteresis for microlitre droplets and bouncing for picolitre droplets). Further control of the honeycomb structures could be achieved through altering the molecular weight or chemistry of the polymer. Other polymer systems could give rise to different pore sizes more suitable for

picolitre droplet impact and so a more systematic study of pore size and distribution could be carried out. Other polymer–solvent systems could also give rise to 3D porous networks.

The dynamics of droplet impact are also found to be governed by the mechanical properties of the substrate. In Chapter 5, it was found that the dynamics of picolitre water droplets following impact onto thin films is governed by the underlayer film thickness and mechanical hardness. Thicker films give rise to higher oscillation frequencies due to greater surface deformation (ridge formation) around the contact line. Further work could entail curing the polymer films at different temperatures to achieve different levels of crosslinking. In addition, by altering the plasma deposition parameters of poly(vinylbenzyl chloride) it may also be possible to control the mechanical properties of this layer.

Plastic substrates are susceptible to charging, which can affect droplet impact. In Chapter 6, it was found that increased droplet velocities due to electrostatic attraction between charged polymer substrates and picolitre droplets resulted in variable impact behaviour that can depend upon the degree of surface roughness and therefore contact angle hysteresis. Higher surface potentials result in higher droplet velocities and can give rise to unexpected behaviour such as a decrease in print resolution or droplet bouncing. Further work in this area could involve the introduction of patterned charge on the surface, which may enable the ability to observe lateral droplet movement either on the surface or in air. The addition of electrolytes to the jetted fluid may help to determine the nature of the charged species involved.

The previous work in this thesis was concerned with the impact and spreading on solid surfaces. However droplet impact upon porous materials is also relevant to a variety of applications. In Chapter 7, the CF_4 plasma fluorination of polyethersulfone membranes resulted in alteration of the imbibition behaviour dependent upon the membrane pore size in relation to the drop diameter. It is possible to inhibit the spreading of picolitre droplets of water with little change in imbibition behaviour, which could be of use in inkjet printing where increased print resolution and ink adhesion are important. In the case of microlitre droplets, water was found to remain on the surface whilst oils passed straight through. Such a membrane could therefore utilised in the separation of

oil–water mixtures. Further work on porous materials could involve altering the plasma treatment parameters to introduce plasma-induced roughness to the porous materials, which will affect the imbibition. It would also be possible to acquire straight channel polyethersulfone membranes and compare them to the interconnected pore membranes featured in the current work.

The separation of oil and water is an important challenge with many applications. In Chapter 8, solvent cast copolymer–fluorosurfactant complexes were found to display large magnitude oleophobic–hydrophilic switching behaviour as well as rapid switching speeds. Further enhancement in switching performance is achieved by combining surface chemical functionality and roughness. These ultra-fast switching oleophobic–hydrophilic surfaces have been shown to display excellent anti-fog, self-cleaning, and oil–water separation properties. Further work could entail the addition of roughening particles to the copolymer–fluorosurfactant complex solution prior to deposition in order to enhance the oleophobic–hydrophilic properties of this coating. A study of the effect of polymer and fluorosurfactant properties on the switching speed (the time taken for water to penetrate down to the hydrophilic subsurface) could be carried out through the utilisation of the picolitre droplet rig from earlier chapters.

Throughout this thesis, it has been demonstrated that a range of substrate properties can govern the impact and spreading of picolitre water droplets; the behaviour of which can be found to differ from larger droplets typically used to characterise the wettability of a surface. This work will be applicable to a range of applications including microfluidics, oil–water separation, and inkjet printing.